

Wensheng Luo · Yunfei Yin ·
Xiangyu Shao · Jianxing Liu · Ligang Wu

Advanced Control Methodologies For Power Converter Systems

Studies in Systems, Decision and Control

Volume 413

Series Editor

Janusz Kacprzyk, Systems Research Institute, Polish Academy of Sciences,
Warsaw, Poland

The series “Studies in Systems, Decision and Control” (SSDC) covers both new developments and advances, as well as the state of the art, in the various areas of broadly perceived systems, decision making and control—quickly, up to date and with a high quality. The intent is to cover the theory, applications, and perspectives on the state of the art and future developments relevant to systems, decision making, control, complex processes and related areas, as embedded in the fields of engineering, computer science, physics, economics, social and life sciences, as well as the paradigms and methodologies behind them. The series contains monographs, textbooks, lecture notes and edited volumes in systems, decision making and control spanning the areas of Cyber-Physical Systems, Autonomous Systems, Sensor Networks, Control Systems, Energy Systems, Automotive Systems, Biological Systems, Vehicular Networking and Connected Vehicles, Aerospace Systems, Automation, Manufacturing, Smart Grids, Nonlinear Systems, Power Systems, Robotics, Social Systems, Economic Systems and other. Of particular value to both the contributors and the readership are the short publication timeframe and the worldwide distribution and exposure which enable both a wide and rapid dissemination of research output.

Indexed by SCOPUS, DBLP, WTI Frankfurt eG, zbMATH, SCImago.

All books published in the series are submitted for consideration in Web of Science.

More information about this series at <https://link.springer.com/bookseries/13304>

Wensheng Luo · Yunfei Yin · Xiangyu Shao ·
Jianxing Liu · Ligang Wu

Advanced Control Methodologies For Power Converter Systems

Wensheng Luo
Harbin Institute of Technology
Harbin, Heilongjiang, China

Yunfei Yin
School of Astronautics
Harbin Institute of Technology
Harbin, Heilongjiang, China

Xiangyu Shao
School of Astronautics
Harbin Institute of Technology
Harbin, Heilongjiang, China

Jianxing Liu
School of Astronautics
Harbin Institute of Technology
Harbin, Heilongjiang, China

Ligang Wu
School of Astronautics
Harbin Institute of Technology
Harbin, Heilongjiang, China

ISSN 2198-4182 ISSN 2198-4190 (electronic)
Studies in Systems, Decision and Control
ISBN 978-3-030-94288-5 ISBN 978-3-030-94289-2 (eBook)
<https://doi.org/10.1007/978-3-030-94289-2>

© The Editor(s) (if applicable) and The Author(s), under exclusive license to Springer Nature Switzerland AG 2022

This work is subject to copyright. All rights are solely and exclusively licensed by the Publisher, whether the whole or part of the material is concerned, specifically the rights of translation, reprinting, reuse of illustrations, recitation, broadcasting, reproduction on microfilms or in any other physical way, and transmission or information storage and retrieval, electronic adaptation, computer software, or by similar or dissimilar methodology now known or hereafter developed.

The use of general descriptive names, registered names, trademarks, service marks, etc. in this publication does not imply, even in the absence of a specific statement, that such names are exempt from the relevant protective laws and regulations and therefore free for general use.

The publisher, the authors and the editors are safe to assume that the advice and information in this book are believed to be true and accurate at the date of publication. Neither the publisher nor the authors or the editors give a warranty, expressed or implied, with respect to the material contained herein or for any errors or omissions that may have been made. The publisher remains neutral with regard to jurisdictional claims in published maps and institutional affiliations.

This Springer imprint is published by the registered company Springer Nature Switzerland AG
The registered company address is: Gewerbestrasse 11, 6330 Cham, Switzerland

To Our Families

Preface

Power electronic converters have become indispensable devices for plenty of industrial applications over the last decades. Composed by controllable power switches, they can be controlled by effective strategies to achieve desirable transient response and steady-state performance, to ensure the stability, reliability and safety of the system. Due to the limits of conventional proportional-integral control which is adopted as an industry standard, many advanced control methodologies and techniques have been developed to improve the converter performance. This book presents the research work on some advanced control methodologies for several types of power converters, including three-phase two-level ac/dc power converter, three-phase Neutral-Point-Clamped (NPC) ac/dc power converter, dc/dc buck converter and boost converter. Specifically, the disturbance observer-based control strategies are investigated, including disturbance observer-based sliding mode control strategies, \mathcal{H}_∞ control strategies and model predictive control strategies. Based on these works, intelligent control strategies have been investigated. Specifically, adaptive control strategies have been explored to facilitate the self-tuning ability of the converter system. Some sufficient conditions for system variables such as the voltage, current, active and reactive power are obtained. Moreover, to improve the robustness against the system uncertainties, neural network-based control strategies are investigated. The effectiveness and advantage of the proposed control strategies are verified via simulations and experiments.

This book aims to present some advanced control methodologies for power converters. The content of this book can be divided into two parts. The first part focuses on disturbance observer-based control methods for power converters under investigation. The second part investigates intelligent control methods. These methodologies provide a framework for controller design, observer design, stability and performance analysis for the considered power converter systems.

The brief content structure of the book is as follows. The main contents of the first part include: Chap. 2 investigates the disturbance observer-based sliding mode control strategy for three-phase two-level ac/dc power converter; Chap. 3 designs a linear disturbance observer-based proportional-integral control to regulate the dc-link voltage of the three-phase two-level ac/dc power converter; Chap. 4 designs

a sliding mode observer-based sliding mode control strategy to regulate the dc-link voltage of three-phase two-level ac/dc power converter; Chap. 5 investigates the disturbance observer-based control strategies for three-phase three-level neutral-point-clamped ac/dc power converter; Chap. 6 proposes the disturbance observer-based control strategy for dc/dc buck converter; Chap. 7 designs a model predictive control strategy for three-phase two-level ac/dc power converter. The main contents of the second part include: Chap. 8 designs two adaptive control strategies for dc/dc buck converter, which are single-loop adaptive control strategy and double-loop adaptive control strategy; Chap. 9 proposes a control strategy consisting of adaptive control and \mathcal{H}_∞ technique for three-phase two-level ac/dc power converter; Chap. 10 investigates adaptive super-twisting sliding mode control-based \mathcal{H}_∞ control method, taking into account both the load variation and component parameter uncertainty of three-phase two-level ac/dc power converter; Chap. 11 investigates radial basis function neural network-based control strategy for three-phase three-level neutral-point-clamped ac/dc power converter.

This book is a research monograph whose intended audience is graduate, post-graduate students, researchers, as well as engineers in power converter control fields.

Harbin, China

June 2021

Wensheng Luo

Yunfei Yin

Xiangyu Shao

Jianxing Liu

Ligang Wu

Acknowledgements

There are numerous individuals without whose constructive suggestions, insightful comments and constant supports this monograph could not have been completed. Special thanks go to Profs. Leopoldo G. Franquelo, Sergio Vazquez, Jose I. Leon, Francisco Gordillo, Dr. Abraham Marquez from the University of Seville and Prof. Dianguo Xu from Harbin Institute of Technology, for their valuable academic ideas and continuous encouragement. The authors are deeply grateful to their families for the understanding and unconditional supports. Finally, we would like to thank the editors at Springer for their professional and efficient handling of this project.

The writing of this book was supported in part by the National Key R&D Program of China (No. 2019YFB1312001), National Natural Science Foundation of China (62033005, 62022030, 62003114), the State Grid Heilongjiang Electric Power Company Limited funded project (No. 522417190057), the China Postdoctoral Science Foundation (2020M681097) and the Heilongjiang Postdoctoral Fund (LBH-Z20134).

Contents

1	Introduction	1
1.1	Power Electronic Converters	1
1.2	Control Methods for Power Converters	3
1.2.1	Linear Control Methods	3
1.2.2	Nonlinear Control Methods	4
1.2.3	Disturbance Rejection Control Methods	15
1.3	Outline of the Book	18
References		21
 Part I Disturbance Observer Based Control Methods		
2	Sliding Mode Control of Three-Phase Two-Level Converters	33
2.1	Mathematical Model and Control Objectives	33
2.1.1	Mathematical Model	33
2.1.2	Control Objectives	35
2.2	Control Scheme	37
2.2.1	Voltage Regulation Loop	38
2.2.2	Observer Design	39
2.2.3	Current Tracking Loop	42
2.3	Simulation Verification	43
2.4	Summary	47
References		48
3	Proportional-Integral Control of Three-Phase Two-Level Converters	49
3.1	Control Scheme	50
3.1.1	Voltage Regulation Loop	50
3.1.2	Observer Design	51
3.1.3	Current Tracking Loop	51
3.1.4	Voltage Loop Analysis	52
3.2	Experiment Verification	55
3.3	Summary	63

4 State Estimation and Control of Three-Phase Two-Level Converters via Sliding Mode	65
4.1 Control Scheme	66
4.1.1 Voltage Regulation Loop	66
4.1.2 Observer Design	67
4.1.3 Voltage Loop Analysis	67
4.1.4 Current Tracking Loop	71
4.2 Simulation Verification	72
4.3 Experiment Verification	74
4.4 Summary	80
References	80
5 Proportional-Integral Control of Three-Phase Neutral-Point-Clamped Converters	81
5.1 Mathematical Model and Control Objectives	86
5.1.1 Converter Model	86
5.1.2 Control Objectives	90
5.2 Voltage Oriented Control	91
5.2.1 Voltage Regulation Loop	91
5.2.2 Current Tracking Loop	92
5.2.3 Voltage Balancing Loop	93
5.2.4 Simulation Verification	93
5.3 Direct Power Control	99
5.3.1 Voltage Regulation Loop	99
5.3.2 Power Tracking Loop	102
5.3.3 Voltage Balancing Loop	109
5.3.4 Simulation Verification	112
5.4 Summary	115
References	117
6 Sliding Mode Control of Buck Converters	119
6.1 Mathematical Model and Control Objectives	120
6.1.1 Mathematical Model	120
6.1.2 Control Objectives	121
6.2 Control Scheme	121
6.2.1 Voltage Regulation Loop	122
6.2.2 Current Tracking Loop	124
6.3 Simulation Verification	125
6.4 Summary	130
References	130
7 Model Predictive Control of Three-Phase Two-Level Converters	131
7.1 Control Scheme	131
7.1.1 Voltage Regulation Loop	133
7.1.2 Power Tracking Loop	133

7.2	Simulation Verification	135
7.3	Summary	135
	References	139
 Part II Intelligent Control Methods		
8	Adaptive Control of Buck Converters	143
8.1	Control Scheme	143
8.1.1	Single-Loop Adaptive Control	144
8.1.2	Double-Loop Adaptive Control	146
8.2	Experiment Verification	147
8.3	Summary	150
9	Adaptive \mathcal{H}_∞ Control of Three-Phase Two-Level Converters	151
9.1	Control Scheme	151
9.1.1	Voltage Regulation Loop	152
9.1.2	Current Tracking Loop	154
9.2	Simulation Verification	158
9.3	Summary	166
	References	168
10	Adaptive Sliding Mode Control of Three-Phase Two-Level Converters	169
10.1	Control Scheme	170
10.1.1	Voltage Regulation Loop	170
10.1.2	Current Tracking Loop	172
10.1.3	Stability Analysis	174
10.2	Simulation Verification	177
10.3	Summary	180
	References	181
11	Adaptive Neural Network Control of Three-Phase Neutral-Point-Clamped Converters	183
11.1	Control Scheme	184
11.1.1	Voltage Regulation Loop	184
11.1.2	Power Tracking Loop	185
11.1.3	Voltage Balancing Loop	189
11.2	Experiment Verification	193
11.3	Summary	197
	References	198
12	Conclusion and Further Work	201
12.1	Conclusion	201
12.2	Further Work	203

Notations and Acronyms

■	end of proof
◆	end of remark
\triangleq	is defined as
\in	belongs to
\forall	for all
\sum	sum
\mathbb{C}	field of complex numbers
\mathbb{R}	field of real numbers
\mathbb{R}^n	space of n -dimensional real vectors
$\mathbb{R}^{n \times m}$	space of $n \times m$ real matrices
\mathbb{Z}	field of integral numbers
\mathbb{Z}^+	field of positive integral numbers
lim	limit
max	maximum
min	minimum
sup	supremum
inf	infimum
rank(\cdot)	rank of a matrix
det(\cdot)	determinant of a matrix
trace(\cdot)	trace of a matrix
deg(\cdot)	degree of a polynomial
$\lambda_i(\cdot)$	i th eigenvalue of a matrix
$\lambda_{\min}(\cdot)$	minimum eigenvalue of a matrix
$\lambda_{\max}(\cdot)$	maximum eigenvalue of a matrix
$\text{Re}(\cdot)$	real part of a complex number
I	identity matrix
I_n	$n \times n$ identity matrix
0	zero matrix
$0_{n \times m}$	zero matrix of dimension $n \times m$
X^T	transpose of matrix X
X^*	conjugate transpose of matrix X

X^{-1}	inverse of matrix X
X^+	Moore-Penrose inverse of matrix X
X^\perp	full row rank matrix satisfying $X^\perp X = 0$ and $X^\perp X^{\perp T} > 0$
diag	block diagonal matrix with blocks $\{X_1, \dots, X_m\}$
$\text{sym}(A)$	$A + A^T$
$X > (<)0$	X is real symmetric positive (negative) definite
$X \geq (\leq)0$	X is real symmetric positive (negative) semi-definite
$\mathcal{L}_2\{[0, \infty), [0, \infty)\}$	space of square summable sequences on $\{[0, \infty), [0, \infty)\}$ (continuous case)
$\ell_2\{[0, \infty), [0, \infty)\}$	space of square summable sequences on $\{[0, \infty), [0, \infty)\}$ (discrete case)
$ \cdot $	Euclidean vector norm
$\ \cdot\ $	Euclidean matrix norm (spectral norm)
$\ \cdot\ _2$	\mathcal{L}_2 – norm : $\sqrt{\int_0^\infty \cdot ^2 dt}$ (continuous case) ℓ_2 – norm : $\sqrt{\sum_0^\infty \cdot ^2}$ (discrete case)
$\ \cdot\ _{E_2}$	$\mathbf{E}\{\ \cdot\ _2\}$
$\ \mathbf{T}\ _\infty$	\mathcal{H}_∞ norm of transfer function \mathbf{T} : $\sup_{\omega \in [0, \infty)} \ \mathbf{T}(j\omega)\ $ (continuous case) $\sup_{\omega \in [0, 2\pi)} \ \mathbf{T}(e^{j\omega})\ $ (discrete case)
*	symmetric terms in a symmetric matrix
LMI	Linear matrix inequality
PD	Positive definite
ND	Negative definite
SMC	Sliding mode control
SRF	Synchronous rotating frame
PWM	Pulse width modulation
PLL	Phase locked loop
VOC	Voltage oriented control
DPC	Direct power control
THD	Total harmonic distortion
ADRC	Active disturbance rejection control
SMO	Sliding mode observer
LDO	Linear disturbance observer
ESO	Extended state observer
LESO	Linear extended state observer
NESO	Nonlinear extended state observer
NN	Neural network
T-S	Takagi-Sugeno
MPC	Model predictive control

List of Figures

Fig. 1.1	Operating principle of power converters	2
Fig. 1.2	PI control	3
Fig. 1.3	PR control	4
Fig. 1.4	Conventional SMC	6
Fig. 1.5	System trajectories under SMC	7
Fig. 1.6	System trajectories under delayed SMC	7
Fig. 1.7	Chattering of system trajectory	8
Fig. 1.8	System trajectory under second-order SMC	9
Fig. 1.9	Structure of the super-twisting algorithm	10
Fig. 1.10	Adaptive control diagram	12
Fig. 1.11	Model referenced adaptive control system	13
Fig. 1.12	Self-tuning control system	13
Fig. 1.13	Observer	16
Fig. 1.14	Principle of active disturbance rejection control	16
Fig. 1.15	Main contents of the book	19
Fig. 2.1	Circuit diagram of grid-connected three-phase two-level power converter	34
Fig. 2.2	Control diagram of PLL	37
Fig. 2.3	Control process of three-phase two-level power converter	38
Fig. 2.4	Overall control diagram of three-phase two-level power converter	38
Fig. 2.5	Voltage regulation loop without disturbance observer	39
Fig. 2.6	Voltage regulation loop with disturbance observer	40
Fig. 2.7	Current tracking loop	42
Fig. 2.8	DC-link voltage transient response of super-twisting SMC without observer	44
Fig. 2.9	DC-link voltage transient responses of super-twisting SMC with observers	45
Fig. 2.10	DC-link voltage steady errors of super-twisting SMC with observers	46
Fig. 2.11	i_d tracking performance	46

Fig. 2.12	i_q tracking performance	47
Fig. 2.13	Obtained grid current wave	47
Fig. 3.1	Voltage regulation loop: PI control based on LDO	50
Fig. 3.2	Current tracking loop: PI control	52
Fig. 3.3	State response with different observer gains	55
Fig. 3.4	State response under different loads	56
Fig. 3.5	Experiment setup	57
Fig. 3.6	Grid voltage waveform	57
Fig. 3.7	Grid voltage harmonic spectrum	58
Fig. 3.8	V_{dc} response of nominal load case	58
Fig. 3.9	Obtained current harmonic spectrum with nominal case: LDO-PI	59
Fig. 3.10	Obtained current harmonic spectrum with nominal case: conv. PI	59
Fig. 3.11	V_{dc} response of nominal load with reduced capacitor	60
Fig. 3.12	V_{dc} response of large load case	61
Fig. 3.13	V_{dc} response of large load with reduced capacitor	61
Fig. 3.14	V_{dc} response of small load case	62
Fig. 3.15	V_{dc} response of small load with reduced capacitor	62
Fig. 4.1	Voltage regulation loop: super-twisting SMC based on SMO	66
Fig. 4.2	Simulation verification of SMO-SMC: nominal capacitor	73
Fig. 4.3	Simulation verification of SMO-SMC: small capacitor	73
Fig. 4.4	Grid voltage waveform	74
Fig. 4.5	Grid voltage harmonic spectrum	74
Fig. 4.6	V_{dc} response of nominal condition	75
Fig. 4.7	Obtained current harmonic spectrum of nominal condition: SMO-SMC	76
Fig. 4.8	Obtained current harmonic spectrum of nominal condition: conv. PI	76
Fig. 4.9	V_{dc} response of nominal load with reduced capacitor	77
Fig. 4.10	V_{dc} response of large load condition	77
Fig. 4.11	V_{dc} response of large load with reduced capacitor	78
Fig. 4.12	V_{dc} response of small load condition	78
Fig. 4.13	V_{dc} response of small load with reduced capacitor	78
Fig. 5.1	Modulated voltage of a two-level, b three-level and c nine-level converters	82
Fig. 5.2	VOC control process of three-phase three-level NPC power converter	84
Fig. 5.3	Overall VOC diagram of three-phase three-level NPC power converter	84
Fig. 5.4	DPC control process of three-phase three-level NPC power converter	85
Fig. 5.5	Overall DPC diagram of three-phase three-level NPC power converter	85

Fig. 5.6	Topology of three-phase three-level NPC	87
Fig. 5.7	Voltage regulation loop compensated by LESO	91
Fig. 5.8	Capacitor voltage balance control	93
Fig. 5.9	DC-link voltage transient response of case 1	94
Fig. 5.10	Stead-state current THD of case 1: conv. PI	95
Fig. 5.11	Stead-state current THD of case 1: LESO-PI	95
Fig. 5.12	AC currents in steady-state	96
Fig. 5.13	Capacitor voltages	96
Fig. 5.14	DC-link voltage transient response of case 2	97
Fig. 5.15	Stead-state current THD of case 2: conv. PI	97
Fig. 5.16	Stead-state current THD of case 2: LESO-PI	98
Fig. 5.17	DC-link voltage transient response of case 3	98
Fig. 5.18	Voltage regulation loop: H_{∞} control based on LESO	99
Fig. 5.19	Power tracking loop: super-twisting SMC	102
Fig. 5.20	Equivalent control point	103
Fig. 5.21	Power tracking loop: detailed diagram	104
Fig. 5.22	Capacitor voltage balancing loop: super-twisting SMC	109
Fig. 5.23	DC-link voltage transient response: a LESO- H_{∞} control, b PI control	113
Fig. 5.24	Active power tracking: a LESO- H_{∞} control, b PI control	113
Fig. 5.25	Reactive power tracking: a LESO- H_{∞} control, b PI control	114
Fig. 5.26	Tracking errors of instantaneous active and reactive power	114
Fig. 5.27	Grid voltage and current: a LESO- H_{∞} control, b PI control	115
Fig. 5.28	Current harmonic spectrum: a LESO- H_{∞} control, b PI control	116
Fig. 5.29	Capacitor voltage difference.eps	116
Fig. 6.1	Circuit diagram of dc/dc buck converter	121
Fig. 6.2	Proposed cascaded control structure	121
Fig. 6.3	Voltage regulation loop	123
Fig. 6.4	Current tracking loop	124
Fig. 6.5	Output voltage regulation: a SMC control, b PI control	126
Fig. 6.6	Inductor current tracking: a SMC control, b PI control	126
Fig. 6.7	LESO performance	127
Fig. 6.8	Output voltage regulation: a SMC control, b PI control	128
Fig. 6.9	Inductor current tracking: a SMC control, b PI control	128
Fig. 6.10	Output voltage regulation: a SMC control, b PI control	129
Fig. 6.11	Inductor current tracking: a SMC control, b PI control	129
Fig. 7.1	Proposed control structure for grid connected power converters	132
Fig. 7.2	Flow diagram of MPC	134
Fig. 7.3	DC-link capacitor voltage: a conv. MPC control, b LESO-MPC control	136
Fig. 7.4	Active power response: a conv. MPC control, b LESO-MPC control	136

Fig. 7.5	Reactive power response: a conv. MPC control, b LESO-MPC control	137
Fig. 7.6	Load estimation	137
Fig. 7.7	Grid voltage and current: a conv. MPC control, b LESO-MPC control	138
Fig. 7.8	Current harmonic spectrum: a conv. MPC control, b LESO-MPC control	138
Fig. 8.1	Control structure of single-loop adaptive strategy	145
Fig. 8.2	Control structure of double-loop adaptive strategy	147
Fig. 8.3	Laboratory prototype of dc-dc buck converter	148
Fig. 8.4	Output voltage with load changes	149
Fig. 8.5	Output voltage with voltage reference changes	150
Fig. 9.1	Adaptive controller structure	154
Fig. 9.2	\mathcal{H}_∞ controller structure	157
Fig. 9.3	Output voltage response: a ESO-SOSM control, b Adaptive \mathcal{H}_∞ control	160
Fig. 9.4	Output voltage response with load steps	160
Fig. 9.5	i_d response: a ESO-SOSM control, b Adaptive \mathcal{H}_∞ control	161
Fig. 9.6	i_q response: a ESO-SOSM control, b Adaptive \mathcal{H}_∞ control	161
Fig. 9.7	Responses of grid current and grid voltage: a ESO-SOSM control, b Adaptive \mathcal{H}_∞ control	162
Fig. 9.8	Responses of grid current and grid voltage: a ESO-SOSM control at first load step, b Adaptive \mathcal{H}_∞ control at first load step, c ESO-SOSM control at second load step, d Adaptive \mathcal{H}_∞ control at second load step	162
Fig. 9.9	Current THD: a ESO-SOSM control, b Adaptive \mathcal{H}_∞ control	163
Fig. 9.10	Responses of adaptive law	163
Fig. 9.11	Active power and reactive power responses under adaptive \mathcal{H}_∞ control	164
Fig. 9.12	Responses of grid current and grid voltage under adaptive \mathcal{H}_∞ control: a from 0.3 to 0.9 s, b from 0.4 to 0.45 s; c from 0.8 to 0.85 s	164
Fig. 9.13	$i_{dq}(t)$ responses under adaptive \mathcal{H}_∞ control strategy	165
Fig. 9.14	$i_{dq}(t)$ error transients under adaptive \mathcal{H}_∞ control strategy	166
Fig. 9.15	v_{dc} response under parameter uncertainties and external disturbances	166
Fig. 9.16	i_d response: a ESO-SOSM control, b Adaptive \mathcal{H}_∞ control	167
Fig. 9.17	i_q response: a ESO-SOSM control, b Adaptive \mathcal{H}_∞ control	167
Fig. 10.1	Voltage regulation loop: H_∞ control based on LESO	170
Fig. 10.2	Current tracking loop with adaptive super-twisting SMC	172
Fig. 10.3	DC-link capacitor voltage transient response	179
Fig. 10.4	i_d transient response: a Adp. ST-SMC, b PI control	179
Fig. 10.5	i_q transient response: a Adp. ST-SMC, b PI control	180

Fig. 10.6	Phase current and source voltage: a Adp. ST-SMC, b PI control	180
Fig. 10.7	Adaptive gains of Γ_d and Γ_q	181
Fig. 11.1	Control diagram	184
Fig. 11.2	Adaptive controller in the voltage regulation loop	186
Fig. 11.3	Adaptive sliding mode controller structure based on the RBF neural network technology	190
Fig. 11.4	\mathcal{H}_∞ controller structure based on the reduced-order observer	193
Fig. 11.5	Laboratory prototype of three-phase three-level NPC power converter	193
Fig. 11.6	Grid voltage: a waveform, b harmonic spectrum	194
Fig. 11.7	v_{c1} and v_{c2} responses: a ANN control, b PI control	195
Fig. 11.8	x_1 and x_2 responses: a , b ANN control, c , d PI control	195
Fig. 11.9	p and q responses: a , b ANN control, c , d PI control	196
Fig. 11.10	Grid voltage and current responses: a , b ANN control, c , d PI control	197
Fig. 11.11	Current harmonic spectrum, active and reactive power and power factor: a , b ANN control, c , d PI control	198

List of Tables

Table 2.1	System parameters	43
Table 2.2	Parameters of super-twisting SMC without observer	44
Table 2.3	Parameters of super-twisting SMC with observers	44
Table 2.4	Parameters of observers	45
Table 2.5	THD Value of different observers	46
Table 3.1	System parameters	56
Table 3.2	Control parameters	57
Table 3.3	Summary of experiment results with nominal capacitor	63
Table 3.4	Summary of experiment results with small capacitor	64
Table 4.1	System parameters	72
Table 4.2	Control parameters	72
Table 4.3	Summary of experiment results with bulk capacitor	79
Table 4.4	Summary of experiment results with small capacitor	79
Table 5.1	System parameters	94
Table 5.2	Control parameters	94
Table 5.3	System parameters	112
Table 5.4	Control parameters	112
Table 6.1	Topologies of three basic converters	120
Table 6.2	System parameters	125
Table 6.3	Control parameters	125
Table 7.1	Switch positions in (α, β) model	132
Table 7.2	System parameters	135
Table 8.1	System parameters	148
Table 8.2	Control parameters	148
Table 8.3	Results with load changes	149
Table 8.4	Results with reference voltage changes	150
Table 9.1	System parameters	159
Table 9.2	Control parameters	159
Table 9.3	Comparisons of proposed control strategy with other strategies	165
Table 10.1	System parameters	178

Table 10.2	Control parameters	178
Table 11.1	System parameters	193
Table 11.2	Control parameters	194

Chapter 1

Introduction



Abstract This chapter presents the preliminary backgrounds for power converter control strategies, including the linear control strategies such as proportional-integral-derivative control, nonlinear control strategies such as sliding mode control, adaptive control, fuzzy logic control, etc., and the disturbance observer based control strategies. Finally, the outline of the book is listed.

1.1 Power Electronic Converters

The power system is the most important infrastructure for economic and social development, which commissions energy conversion, transmission and distribution. Due to the non-renewability of fossil energy and the deterioration of global climate environment, the modern power system is transitioning to a stage of sustainability and intelligence. On one hand, in order to achieve long-term sustainability, large-scale development of clean renewable energy sources, such as wind and solar energy, is required [1, 2]. At the same time, considering the intermittent nature of such energy sources, it is necessary to equip corresponding energy storage devices [3–7]. Therefore, the grid integration of renewable energy and the energy conversion of energy storage devices are the main tasks of the power system's transition toward sustainability. On the other hand, in order to intelligentize the power system, corresponding control measures need to be taken to enable the power to flow intelligently on demand, thereby improving energy utilization, optimizing power quality and enhancing system reliability [8–11]. Therefore, the bi-directional power flow the fundamental feature and basic task of the intelligent power system. The realization of these tasks all depend on the development of power electronics technology [12–19].

Power electronics technology refers to the electronic technology applied in the power field, involving three major fields such as power, electronics and control, and mainly realizes the conversion of electric energy. Common power conversion methods include ac/dc, dc/ac, ac/ac, dc/dc, etc. The purpose of power conversion is to enable people to use the power more conveniently and effectively. Power electronic converters based on power electronics technology are indispensable devices in modern power systems. Without power electronic converters, the modernization of the

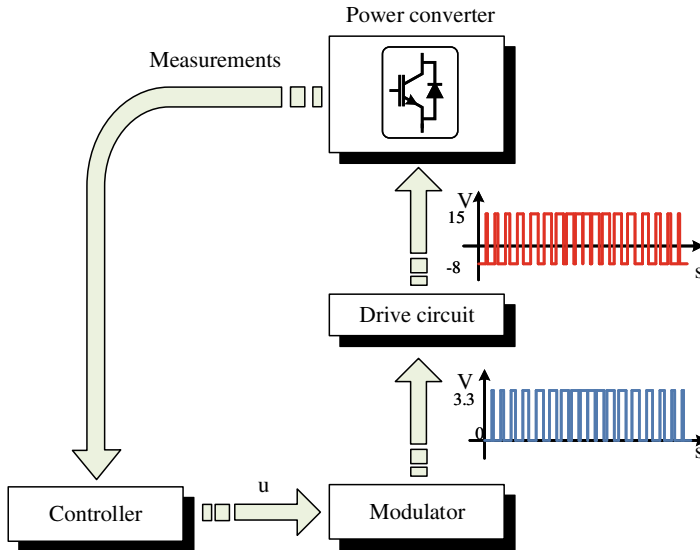


Fig. 1.1 Operating principle of power converters

power system will be difficult to achieve. Taking power transmission as an example, in order to reduce the loss of power transmission lines, dc transmission methods are mostly adopted, in this case both the transmitting terminal rectifier and the receiving terminal inverter adopt power electronic converters. Not only that, efficient and reliable flexible ac transmission can only be realized through electronic converters [20–26].

As shown in Fig. 1.1, a complete power converter system consists of the power converter plant, controller, modulator and drive circuit. The operating principle is as follows: the controller receives the measurement signal, and then generates a control signal according to the control target, then the control signal is converted into digital switching signal by the modulator, which is transformed to some certain level by the drive circuit, to control the power switches (such as IGBT) to be on and off as required to achieve the corresponding control objectives.

It can be seen that in order to make the power converter operate normally and meet the performance requirements, it is necessary to adopt an effective control strategy and modulation technology. Considering that the modulation signal is generated based on the control signal, the controller is the core component of power converter system, and the performance of controller directly affects the converter performance. Therefore, research on advanced power converter control strategies is the key to improving converter performance. As mentioned above, power converters are the fundamental devices of power system modernization, therefore high-performance power converters under advanced control strategies are of great significance to enable the power system with high efficiency, reliability and intelligence.

1.2 Control Methods for Power Converters

1.2.1 Linear Control Methods

The most classic and widely used control scheme is the linear proportional-integral-derivative (PID) series of controllers, which have been used in the industrial field since the 1950s and have the advantages of simple concept, mature theory, and clear physical meaning, and it is considered to be the most reliable control solution in the industrial field. According to different control requirements, there can be different combinations, such as pure proportional control, PI control, PD control, PID control, etc. [27]. It should be noted that the above-mentioned control algorithms are mostly used in the (d, q) coordinate system. When controlling in the (α, β) coordinate system, its changed form, proportional-Resonance (PR) controller is adopted.

(1) PI Control

Since the three-phase ac variable (voltage/current) is converted to a two-phase dc variable (with constant reference) in the (d, q) coordinate system, the PI controller is mostly used in the (d, q) control situation. Because it is a first-order controller, and is able to track a constant signal without steady-state error. Figure 1.2 is the algorithm structure of the PI controller. The transfer function from the error signal e_{dq} to the control signal u_{dq} is:

$$G_{PI}^{dq}(s) = k_p + \frac{k_i}{s}, \quad (1.1)$$

where k_p and k_i are respectively the proportional and integral parameters.

(2) PR Control

In the (α, β) coordinate system, the three-phase ac variable is converted to the two-phase ac variable. In this case, the PI controller cannot achieve good tracking. Therefore, a PR controller is required to track the reference signal with a specific frequency. Figure 1.3 is the algorithm structure of PR controller. The transfer function from the error signal $e_{\alpha\beta}$ to the control signal $u_{\alpha\beta}$ is:

Fig. 1.2 PI control

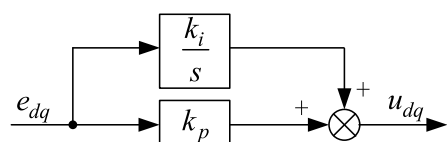
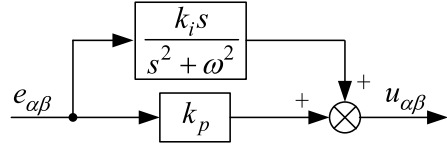


Fig. 1.3 PR control

$$G_{PR}(s) = k_p + \frac{k_i s}{s^2 + \omega^2}, \quad (1.2)$$

where k_p and k_i are respectively the proportional and integral parameters, ω is the grid voltage angular frequency.

Linear controllers also can be in the form of state feedback, that is, the controller is designed based on the state space expression of the system [28, 29]. In fact, the state feedback control is to put proportional control on each state quantity. Taking into account the derivative relationship between the state quantities, the state feedback control can be converted to PID control. It should be noted that when the adopted converter model is non-linear, the system must be linearized before designing the state feedback controller.

It should be pointed out that the above-mentioned linear PID series controllers require accurate linear models. Therefore, when there exist parameter changes, nonlinearities and load disturbances in the system, the performance of the controller will be significantly degraded. For power converters, these undesirable factors all exist. First of all, the parameters of all components inside the converter will drift within a certain range, including the filter inductance value and parasitic resistance value of each phase, the turn-on and turn-off time of each phase power switch, and the dc-link capacitance value. Secondly, in a switching cycle, the internal circuit connection mode will change many times, and the converter also has the phenomenon of inductance saturation and voltage clamping, all of which make the power converter a nonlinear system in nature. Thirdly, the converter always faces unpredictable load changes on the input side and the output side, which causes disturbance to the system.

1.2.2 Nonlinear Control Methods

In order to make up for the shortcomings of linear controllers, many advanced nonlinear control methods have been investigated for power converter control in recent years, including sliding mode control [30, 31, 31–55], adaptive control [56–67], fuzzy control [68–74], model predictive control [75–97], deadbeat control [98–100], passive control [101, 102], back-stepping control [103, 104], differential smoothing control [105, 106], and neural network control [107–111], etc. Among these nonlinear control algorithms, sliding mode control is an effective method to deal with complex nonlinearities and uncertainties in actual systems due to its insensitivity to external disturbances and finite time convergence [112–115]; adaptive control can

automatically adjust the controller parameters, so that the controller has good adaptability to system uncertainty and has good engineering practicability; fuzzy logic control is an effective method for dealing with complex systems because it does not require precise mathematical models and can deal with system nonlinearities and uncertainties. Therefore, sliding mode control and adaptive control methods are currently the hotspots in the design of power converter controllers.

(1) Sliding Mode Control (SMC)

Sliding mode control (SMC) was brought up in the 1950s by researchers including Emelyanov, Utkin and etc., and the control idea originated from the switching action of electromagnetic relays [116]. Sliding mode control is also called variable structure control, which implies that the form of the control signal changes according to the state of the system. The sliding mode controller consists of two signals that switch each other:

$$u = \begin{cases} u^+(x), & s(x) > 0 \\ u^-(x), & s(x) < 0 \end{cases}, \quad (1.3)$$

where x is the system state variable, and $s(x)$ is the control signal switching function, which satisfies $s(0) = 0$ and is differentiable.

It can be seen that sliding mode control is a kind of nonlinear control method with discontinuous control signal. Due to the discontinuity of control signal, the dynamic differential equation of the system trajectory is discontinuous at the right side, as follows:

$$\dot{x} = f(x), \quad (1.4)$$

$$f(x) = \begin{cases} f^+(x), & s(x) > 0 \\ f^-(x), & s(x) < 0 \end{cases}, \quad (1.5)$$

In state space, the hyperplane satisfying $s(x) = 0$ is expressed as

$$S = \{x \mid s(x) = 0\}. \quad (1.6)$$

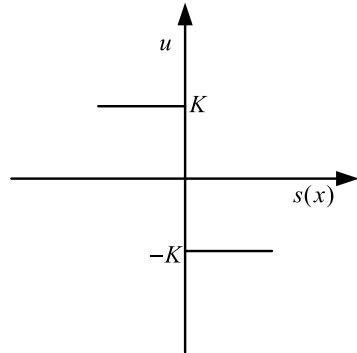
Definition 1.1 [116] Sliding mode refers the movement of a dynamic system

$$\dot{x} = f(x, t), x \in \mathbf{R}^n \quad (1.7)$$

that occurs on the hyperplane S , which satisfies: if the initial state $x_0(t_0)$ is on the hyperplane S , then the movement from this state will remain on the hyperplane, that is,

$$x_0 \in S \rightarrow x(t, x_0) \in S, \quad (1.8)$$

the hyperplane S is called sliding surface.

Fig. 1.4 Conventional SMC

The design of sliding mode controller consists of two steps:

- Step 1: design the sliding surface S so that the system state can be asymptotically stable at the origin after reaching the sliding surface.
- Step 2: design the sliding mode controller so that the state of the system can reach the sliding mode surface from the initial state.

◆ Traditional sliding mode control

As shown in Fig. 1.4, the traditional sliding mode control is essentially a switching control, and the control signal form is as follows:

$$u = -K \operatorname{sign}(s(x)) = \begin{cases} -K, & s(x) > 0 \\ K, & s(x) < 0 \end{cases}. \quad (1.9)$$

Therefore, under the control signal u , the system will reach the sliding surface of $s(x) = 0$.

Take the second-order system as an example, suppose the dynamic equation of the system is:

$$\begin{cases} \dot{x}_1 = x_2 \\ \dot{x}_2 = x_2 + u \end{cases}. \quad (1.10)$$

Design the sliding surface S as:

$$S = \{x \mid s(x) = x_1 + \beta x_2 = 0\}. \quad (1.11)$$

As shown in Fig. 1.5, the system state will eventually reach the sliding surface S . On the sliding surface S , it satisfies:

$$x_1 = -\beta x_2 = -\beta \dot{x}_1. \quad (1.12)$$

As can be seen, as long as $\beta > 0$, x_1 can asymptotically converge to the origin.

Fig. 1.5 System trajectories under SMC

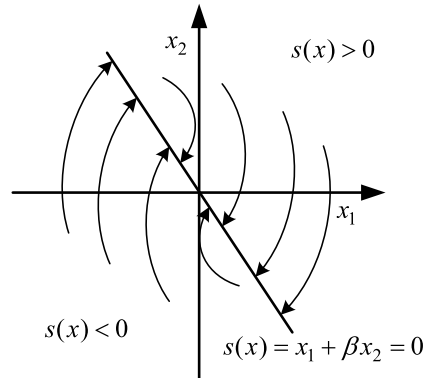
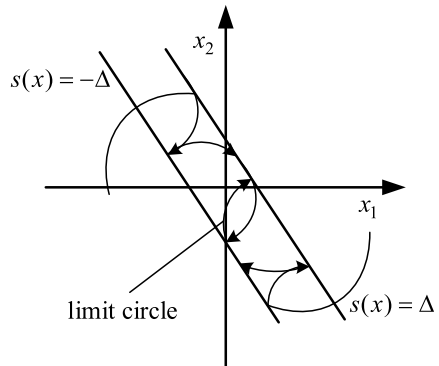


Fig. 1.6 System trajectories under delayed SMC



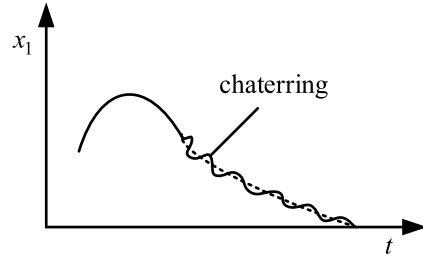
It is worth noting that on the sliding surface, the system dynamic only depends on the form of switching function $s(x)$. If $s(x)$ is designed to be independent of system perturbation and external interference (such as in (1.11)), the sliding mode of the system is completely robust to the perturbation and external interference.

The major drawback of traditional sliding mode control is the chattering phenomenon. The cause of chattering is the delay in the switching of control signal, as shown in (1.13), the control signal cannot be switched immediately when $s(x) = 0$, but is delayed for a period of time until $s(x) > |\Delta|$.

$$u = -K \operatorname{sign}(s(x)) = \begin{cases} -K, & s(x) > \Delta \\ K, & s(x) < -\Delta \end{cases}. \quad (1.13)$$

The effect of this delay is that the system trajectory will not converge to the sliding surface S , but move back and forth between two hyperplanes $s(x) = \Delta$ and $s(x) = -\Delta$, forming a limit cycle, as shown in Fig. 1.6. In time domain, the limit cycle results in that the trajectory of the system cannot smoothly converge to the origin, but converges to the vicinity of the origin with a small oscillation, as shown in Fig. 1.7.

Fig. 1.7 Chattering of system trajectory



The main causes for the delay are: (1) the delay caused by the inertia of components, for example, it takes time for power switch to open and close; (2) the delay caused by the fixed space, such as the empty range in the hydraulic device; (3) the delay caused by the sampling of discrete system. In this case, the delay from sampling to generating control signal is of at least one sampling period; (4) the delay caused by unmodeled dynamics, for example, some unmodeled dynamic of the system is much faster, causing the control process to appear relatively lagging. For real systems, one or more of the above causes always exist, and delay cannot be avoided, therefore chattering is also inevitable.

In practical applications, if it cannot be eliminated or reduced to acceptable range, chattering may cause problems. For example, in robot control, the chattering of drive motor will cause the joints of the robot to shake; in the machining process, the chattering of tool will cause the cutting surface of parts to be unsatisfactory and produce waste; in the control of power electronic system, the controlled voltage or current cannot be stabilized at the reference value, resulting in steady-state error. Moreover, under certain circumstances, chattering may even cause high-frequency resonance which leads to system instability.

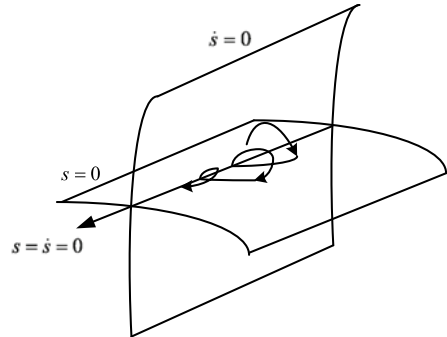
In order to reduce or eliminate chattering, researchers have proposed various methods, including quasi-sliding mode methods, filtering methods, observer methods, and high-order sliding mode methods [117–121]. Among them, the high-order sliding mode algorithm is the most attractive to researchers. The high-order sliding mode algorithm not only can guarantee the continuity of the sliding mode control function, but also the finite time convergence and strong robustness. The high-order sliding mode algorithm means that it is not only required to ensure that the switching function $s(x) = 0$, but also that the derivatives of the switching function are also required to be 0. For example, the sliding mode of order r satisfies:

$$s = \dot{s} = \ddot{s} = \dots = s^{(r-1)} = 0. \quad (1.14)$$

Correspondingly, a control algorithm with a relative degree of r needs to be adopted, that is, the control signal u_s with the sign function explicitly appears in the r th derivative of s :

$$s^{(r)}(t, x) = h(t, x) + g(t, x)u_s. \quad (1.15)$$

Fig. 1.8 System trajectory under second-order SMC



In this case, the chattering effect is transferred to the r th derivative of the switching function s , so that the trajectory of s is smooth and converges to the origin. Note that the general nonlinear system is considered here, the switching function is related to the time t , and the related results are also applicable to linear time-invariant systems.

Based on the consideration of high-order sliding mode algorithm, Levant proposed a second-order sliding mode algorithm. Consider following system:

$$\dot{x} = f(t, x, u), \quad (1.16)$$

$$u = U(t, x), \quad (1.17)$$

$$\dot{u} = \Phi(t, x), \quad (1.18)$$

where U is a continuous function, and Φ is a bounded discontinuous function.

Taking the derivative of the switching function $s(t, x)$ yields:

$$\dot{s}(t, x) = \frac{\partial s}{\partial t} + \frac{\partial s}{\partial x} f(t, x, u), \quad (1.19)$$

$$\ddot{s}(t, x) = \frac{\partial \dot{s}}{\partial t} + \frac{\partial \dot{s}}{\partial x} f(t, x, u) + \frac{\partial \dot{s}}{\partial u} \Phi(t, x), \quad (1.20)$$

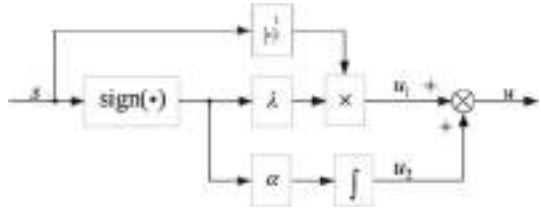
Let $h(t, x) = \frac{\partial \dot{s}}{\partial t} + \frac{\partial \dot{s}}{\partial x} f(t, x, u)$, $g(t, x) = \frac{\partial \dot{s}}{\partial u}$, $u_s = \Phi(t, x)$, then (1.20) is consistent with (1.15).

Based on (1.18), a second-order sliding mode algorithm can be designed as:

$$\Phi(t, x) = \begin{cases} -\alpha_m \text{sign}(s(t, x)), & ss \leq 0, \\ -\alpha_M \text{sign}(s(t, x)), & ss > 0, \end{cases} \quad (1.21)$$

where α_m and α_M are the controller parameters to be designed, which are determined according to the system parameters and initial conditions, and $\alpha_M > \alpha_m > 0$. With the second-order sliding mode controller, the system trajectory will converge to the hyperplane of $s = \dot{s} = 0$, as shown in Fig. 1.8.

Fig. 1.9 Structure of the super-twisting algorithm



Remark 1.2 The higher-order sliding mode algorithm is also effective for systems with lower relative degrees, that is, the second-order sliding mode algorithm can control systems with a relative degree of 1. More importantly, compared to the first-order sliding mode algorithm, the second-order sliding mode algorithm eliminates the effect of chattering.

It can be seen that the second-order sliding mode algorithm (1.21) needs to use the derivative of the switching function to design the control signal, but the derivative information is often difficult to directly measure, and needs to be calculated through numerical calculations, which not only increases the computational burden, but also causes a loss of accuracy. For this consideration, Levant proposed a super-twisting second-order sliding mode algorithm, the algorithm structure of which is shown in Fig. 1.9.

The expression of the super-twisting sliding mode algorithm is:

$$\begin{cases} u = u_1 + u_2 \\ u_1 = -\lambda |s|^{\frac{1}{2}} \text{sign}(s) \\ \dot{u}_2 = -\alpha \text{sign}(s) \end{cases} . \quad (1.22)$$

It can be seen that the controller design of the super-twisting algorithm only needs the information of switching function, but not its derivative information. Assuming $0 < G_m < g(t, x) < G_M$, $-H < h(t, x) < H$, the parameters of the super-twisting sliding mode algorithm should satisfy

$$\alpha > \frac{H}{G_m}, \quad \lambda^2 \geq \frac{4H}{G_m^2} \frac{G_M}{G_m} \frac{\alpha + H}{\alpha - H}. \quad (1.23)$$

Regarding (1.18), then

$$\Phi(t, x) = -\frac{\lambda}{2} |s|^{-\frac{1}{2}} \dot{s} - \alpha \text{sign}(s), \quad (1.24)$$

as can be seen, $\Phi(t, x)$ derived by the super-twisting algorithm is also a discontinuous function, which ensures that the system trajectory reaches the hyperplane of $s = \dot{s} = 0$ [122].

At present, the first-order sliding mode control and second-order sliding mode control for power converters are mostly used in dc/dc power converters [30, 31,

[33–35, 123, 124], and there are fewer applications in three-phase ac/dc converters [125]. In these literatures, the systems under first-order sliding mode control all suffer from the chattering effect. Although some technologies (such as harmonic injection technology and control signal shrinking technology) can suppress the impact of chattering to some extent, they cannot be totally eliminated. In order to avoid the chattering problem of the first-order sliding mode, researchers gradually adopt the second-order sliding mode algorithm to control power converters. The second-order sliding mode algorithm includes the forms of twisting second-order sliding mode, suboptimal second-order sliding mode, terminal second-order sliding mode, super-twisting second-order sliding mode, etc. In [33, 123], a suboptimal second-order sliding mode algorithm has been employed to control a dc/dc step-down power converter, where the second-order sliding mode algorithm needs to use the first derivative of sliding mode variable. Regarding that it is difficult to directly measure this value, the author used a state machine to switch the control signal according to the sign of the sliding mode variable, and finally achieved system stability. However, the existence of state machine complicated the control structure of the system, leading to more processing time in practical applications. In [34, 35], terminal second-order sliding mode control has been adopted for dc/dc step-down converter control, which also requires the derivative information of the sliding mode variable, thus brings inconvenience to the control. In [124], twisting second-order sliding mode algorithm has been used to control a dc/dc buck converter. The disadvantage is also that the derivative information of the sliding mode variable is required.

As can be seen, most second-order sliding mode algorithms need to obtain the first derivative information of the sliding mode variable in real time during the control process, for which purpose the system needs to have corresponding sensing and measuring devices. When the derivative cannot be directly measured, either an observer is used to estimate it, or suboptimal second-order sliding mode control is used. The former will increase the complexity of the control system, also the selection and design of the derivative observer will directly affect the control performance. The latter adopts quadrant control, that is, the corresponding controller is selected according to the quadrant of the sliding mode variable and its derivative, thus the convergence speed is slower than directly using the derivative, which is why it is called suboptimal.

◆ Adaptive control

Adaptive control was firstly proposed by Draper et al. in 1951, aiming to make the internal combustion engine control system with performance uncertainty automatically reach the optimal operating point [126]. In 1958, Whitaker et al. designed an adaptive flight control system to adjust the control parameters to achieve the most ideal flight characteristics, by using the deviation between the actual flight characteristics and the expected characteristics of the reference model [127]. This is the original application of the famous model reference adaptive control system. This type of system was later prosperously developed with the contributions of Parks and Landaud in stability and hyperstability theory, and became a basic adaptive system [128, 129]. In 1970s, Astrom, Wittenmark et al. proposed and developed another

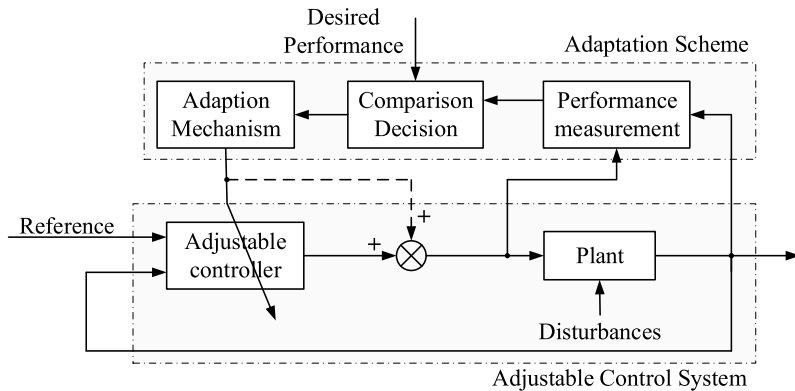


Fig. 1.10 Adaptive control diagram

important adaptive control method, namely self-tuning control [130]. The main feature of this adaptive system is to online estimate the mathematical model parameters or uncertain external disturbance, and use these estimated values to modify the control parameters. Because this method is easy to implement in microprocessor, it has aroused the attention and interest of researchers from all over the world. Various new self-tuning control methods have emerged, and their application range has become wider.

The goal of adaptive control is that the system can achieve and maintain acceptable performance when system parameters and external disturbance are unknown or time-varying. Specifically, an adaptive control system should have the following functions:

- online identify system parameters and measure the performance, to obtain the changes in system states.
- determine current control strategy according to a certain law (the adaptive law).
- online modify controller parameters or system input signals.

In order to meet these functions, the general adaptive control system structure is shown in Fig. 1.10. It includes modules of performance index measurement, performance comparison and decision-making, adaptive mechanism and adaptive controller, with which the goal of adaptive control can be achieved [131].

The main feature of adaptive control is that no matter how large the uncertainty or disturbance is, the control goal can be achieved. In contrast, robust control requires uncertainty to be bounded and relatively small. Adaptive control technology provides a systematic method for automatically adjusting controller parameters online. Although the system parameters and external disturbance are unknown or time-varying, the controller can still be adjusted accurately to meet high performance requirements.

The adaptive control system is mainly divided into two categories: one is model reference adaptive control system, and the other is self-tuning control system.

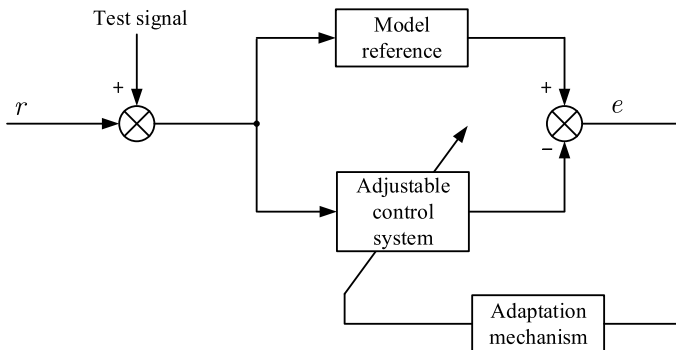


Fig. 1.11 Model referenced adaptive control system

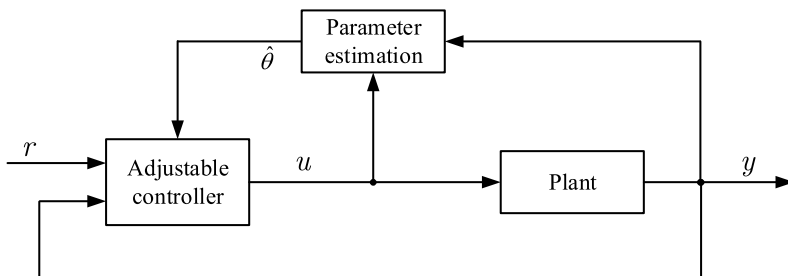


Fig. 1.12 Self-tuning control system

Figure 1.11 shows the typical structure of model reference adaptive control system. This system uses a reference model as an auxiliary system, and its output or state can be designed with expected performance indexes. The input signal enters the reference model and the adaptive control system at the same time, and then the output of the two systems is differenced to obtain the error signal e . This error signal enters the adaptive control system according to an adaptive mechanism, and is used to adjust controller parameters or generate an auxiliary input signal to minimize a functional index of the error. In this way, the output of the adaptive control system can asymptotically approach the output of the ideal model.

Figure 1.12 shows the typical structure of self-tuning control system. This type of system estimates the uncertain parameters, including unknown or time-varying model characteristics and external disturbance. Then the estimated value of uncertain parameters $\hat{\theta}$ is input into the controller, and the controller adjusts the control parameters according to the estimated value and the predetermined performance index, and the resulted control signal acts on the system. After several times of parameter estimation and control parameter adjustment, the system performance index can be reached.

Here is a simple example to illustrate the working process of the self-tuning control system. Consider following scalar system:

$$\dot{x} = \theta x + u, \quad (1.25)$$

where x is the system state, u is the control signal, and θ is a constant but unknown. The control target is as $t \rightarrow \infty$, $x(t) \rightarrow 0$. The design of the adaptive law is as follows:

$$\dot{\hat{\theta}} = x^2, \quad (1.26)$$

$$u = -(\hat{\theta} + 1)x, \quad (1.27)$$

where $\hat{\theta}$ is the estimated value of θ . The obtained closed loop system is:

$$\dot{x} = (\theta - \hat{\theta} - 1)x, \quad (1.28)$$

$$\dot{\hat{\theta}} = x^2. \quad (1.29)$$

As can be seen, the growth of $\hat{\theta}$ dominates the growth of x , so the feedback gain $\hat{\theta} + 1$ has a value large enough to overcome the uncertainty, and the system is stabilized.

At present, there are some applications of adaptive control in power converters [56–61, 68, 132, 133].

Regarding the adaptive control of ac/dc converters, in the term of model reference adaptive control, in [56], in order to cope with the parameter uncertainty of the inductance and grid frequency, the model adaptive control method was used to realize the direct power control of the converter. Reference [57] adopted an adaptive observer to estimate the dc voltage of the converter, where the observer design is based on the idea of model reference adaptive control. In the term of self-tuning control, [58] adopted an adaptive first-order sliding mode algorithm to achieve the control and ripple suppression of the converter. Reference [59] used adaptive PR control for the converter, where the resonance frequency control parameters were automatically adjusted according to the current error. Reference [60] employed adaptive back-stepping sliding mode control, where the control structure was complicated and not convenient for engineering applications.

There are also some applications of adaptive control in dc/dc converters. For model reference adaptive control, [61] used an adaptive law to estimate the load value; [132] designed an adaptive observer to estimate the system output. In the aspect of self-tuning control, [64] obtained the ideal pole position by adaptively adjusting the PI parameters to enhance the system stability; [133] used an adaptive observer to estimate the output error, which is then provided to the PI controller.

◆ Fuzzy Logic Control

Regarding the fuzzy logic control of power converters, most of the research work focuses on dc/dc converters [74, 134–139], and relatively less work for ac/dc converters [68–70, 140, 141].

For ac/dc converter control, fuzzy logic has two main uses, one is for adjusting control parameters, and the other is for fuzzy model modeling. Among the two, fuzzy

logic has more applications in adjusting control parameters. For example, [140, 141] adopted conventional I-type Mamdani fuzzy logic to adjust the parameters of the sliding mode controller, resulting in a fuzzy sliding mode controller; similarly, [68, 69] adjusted the PI controller parameters via Mamdani fuzzy logic, resulting in a fuzzy PI control. In the aspect of fuzzy model modeling, [70] adopted conventional I-type Takagi-Sugeno (T-S) fuzzy logic modeling for the ac/dc converter wind power systems. The conventional I-type referred to here means that the membership functions are definite.

For dc/dc converters, the application of fuzzy logic is more diverse, including fuzzy modeling, direct fuzzy control, type II fuzzy control and so on. For example, in the aspect of fuzzy modeling, [74, 134] used T-S fuzzy logic to model the converter; in the aspect of direct fuzzy control, [135–138] adopted Mamdani fuzzy logic to directly generate the control signal; in the aspect of type II fuzzy control, [139] employed type II Mamdani fuzzy logic to design a fuzzy sliding mode controller.

Up to this point, the types of existing power converter controllers have been reviewed. The above-mentioned controllers have advantages or disadvantages in terms of tracking performance, robustness, and complexity. They can be employed alone or in combination to avoid the shortcomings.

1.2.3 Disturbance Rejection Control Methods

For ac/dc and dc/dc power converters, one of the main control problems is from the unpredictable time-varying load disturbance connected to the dc side, which causes dc voltage fluctuation. The value of this load is unknown and shall vary in a large range. The magnitude of load and the robustness of controller determine whether the dc voltage can be restored to its reference. Normally, the controller parameters are adjusted based on a nominal operating condition. These parameters have a certain stability margin and can resist external interference to some extent. However, when the disturbance continues to increase, the control parameters of the nominal operating condition shall not be able to maintain the control performance. A thought is, if this load is known to the controller, then it can be included in the controller design and the system is robust against it. In order to achieve this, an effective method is to add a disturbance observer in the voltage control loop to compensate the controller. In this case, when the external disturbance value changes, the estimated disturbance value compensated to the controller also changes. Therefore, the controller becomes more flexible and can adapt to changes in external disturbances, thus the robustness is improved.

Observers, usually also called filters or estimators, are used to extract unmeasurable variables from the system through available information, as shown in Fig. 1.13. The early famous observers include the classic Luenberger observer [142] and Kalman filter [143]. According to the purpose of observer, observers can be divided into two categories: (1) state observers that reconstruct the internal state of system; (2) disturbance observers that obtain external interference information.

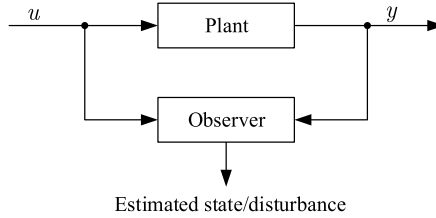


Fig. 1.13 Observer

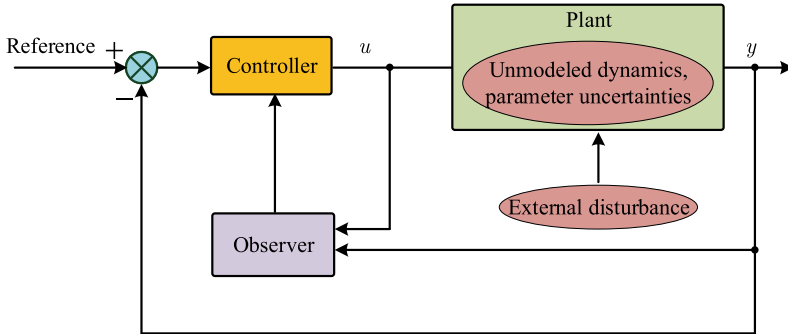


Fig. 1.14 Principle of active disturbance rejection control

The control method based on disturbance observer is also called active disturbance rejection control (ADRC) method. It was originated by Jingqing Han in 1995 [144], and systematically organized in 2009 [145–149]. As shown in Fig. 1.14, the ADRC principle is: put the unknown system dynamics, external interference and nonlinearity all together as a lumped disturbance term of the system, design an observer to estimate the disturbance term in real time, then put the estimated value to the controller to perform a feedforward compensation [150–152]. Therefore, the core idea of ADRC is to use the disturbance information to eliminate its influence. The ADRC is a forward compensation method, that is, the disturbance observer estimates the disturbance value, and the estimated disturbance is compensated to the controller in forward channel. This method is fairly effective in dealing with internal nonlinearity, uncertainty and external disturbance. Meanwhile, due to the inherent practicality of its design concept, ADRC has advantages in solving practical engineering problems, such as turbofan engines, MEMS gyroscopes, etc. [153–157].

Up to now, there are some works that adopted ADRC for converter control. In these works, in aspects of different types of disturbance observers, different types of controllers, and different circuit topologies, ADRC is realized with different methods. According to the algorithm form, interference observers can be divided into two categories, i.e., linear disturbance observer [91, 125, 155, 158–162], and nonlinear disturbance observer [163–165].

◆ Linear Disturbance Observer

As the analysis of linear systems is mature, linear disturbance observers are more common in the literature. Among the linear disturbance observers, a commonly used one is the linear state extended observer (LESO). When constructing LESO, the external disturbance is regarded as an augmented state of the system, thus it is an indirect form of disturbance observer. The extended state observer (ESO) is an effective observation technique, which expands the lumped disturbance (including parameter uncertainty, unmodeled dynamics and load changes) into a new state variable, and estimate the total disturbance and the original system state at the same time. The linear ESO means that the designed observer dynamic equation has a linear form, in contrast to which there is nonlinear extended state observer (NESO) [166, 167]. ESO is the most important research result of professor Jingqing Han in ADRC technology, which is briefly introduced below.

Consider following nonlinear system:

$$\begin{cases} \dot{x}_1 = x_2 \\ \dot{x}_2 = bu + f(x_1, x_2) \\ y = x_1 \end{cases}, \quad (1.30)$$

where $f(x_1, x_2)$ is an unknown function, which reflects the impact of system uncertainty and unknown disturbance.

Extend $f(x_1, x_2)$ to a new state variable x_3 , that is, $x_3 = f(x_1, x_2)$, and define its derivative as $\dot{x}_3 = h(t)$, then the extended system is:

$$\begin{cases} \dot{x}_1 = x_2 \\ \dot{x}_2 = x_3 + bu \\ \dot{x}_3 = h(t) \\ y = x_1 \end{cases}, \quad (1.31)$$

Then design a state observer for the extended system:

$$\begin{cases} e = z - y \\ \dot{z}_1 = z_2 - \beta_1 g_1(e) \\ \dot{z}_2 = z_3 - \beta_2 g_2(e) + bu \\ \dot{z}_3 = -\beta_3 g_3(e) \end{cases}, \quad (1.32)$$

where $g_i(e)$ ($i = 1, 2, 3$) is the observer correction function, which can be designed as a linear or nonlinear function, and the obtained observer is called a linear or nonlinear ESO, respectively. If the parameters β_i ($i = 1, 2, 3$) are appropriately selected, this observer can have a good estimate of the variables x_1, x_2 of the original system (1.30) and the variable x_3 extended from the disturbance.

In existing works, LESO has been used to estimate the dc-link load disturbance of the power converter [125, 160]. Reference [125] employed LESO in the voltage regulation loop to estimate the load disturbance connected to dc-link, and compensate the estimated value to the second-order sliding mode controller of the voltage loop;

the current tracking loop was controlled in (d, q) synchronous rotating frame (SRF), two second-order sliding mode controllers are used to track d and q axis currents. In [160], the voltage control loop adopted a proportional controller based on LESO, and the current tracking loop used two proportional-resonance in (α, β) stationary coordinate system. The results show that the system control performance has been significantly improved after the disturbance observer is applied.

In addition to ESO, some direct forms of linear disturbance observers are also designed for power converter control [91, 161, 162]. This type of observers directly make use of the system dynamic equation to obtain the dynamic expression of disturbance, without the need to extend the disturbance to a new system state. The disturbance dynamic can be designed based on different algorithms, including Luenberger observer [91], PI observer [161], Kalman observer [162] and so on. However, these works mainly aimed at the disturbance caused by internal parameter uncertainty. Up to now, there is no direct form of linear disturbance observer adopted for dc-link load disturbance estimation of power converter.

1.3 Outline of the Book

The general layout of presentation of this book is divided into two parts. Part I: disturbance observer based control methods, and Part II: intelligent control methods. The main contents of this book are shown in Fig. 1.15.

Part I focuses on disturbance observer based control methods for power converters. Part I which begins with Chap. 2 consists of six chapters as follow.

- **Chapter 2** investigates the disturbance observer based sliding mode control strategy for grid-connected three-phase two-level ac/dc power converter. The control target is to regulate the dc-link voltage. The voltage oriented control with two cascaded loops is adopted. In the outer voltage regulation loop, a super twisting sliding mode controller is employed, which is compensated by a disturbance observer. In the inner current tracking loop, the control is carried out in dq synchronous reference frame (SRF), and two super twisting sliding mode controllers are used to track the d -axis and q -axis currents. For the disturbance observer, four different disturbance observers are designed for comparison, which are linear observer, second-order sliding mode observer, linear extended state observer and nonlinear extended observer. Then the performance of the observers is compared according to the transient response of the dc-link voltage.
- **Chapter 3** designs a linear disturbance observer (LDO) based PI control to regulate the dc-link voltage of the three-phase two-level ac/dc power converter. The control structure is the same as in Chap. 2, i.e., the voltage loop consists of a disturbance observer. The LDO is designed based on a similar one in that chapter, but with better performance. By adopting LDO based PI control in voltage regulation loop, the outer loop is a pure linear system, in which way the classical control theory can be used to analyze the system. The current tracking loop adopts the conventional

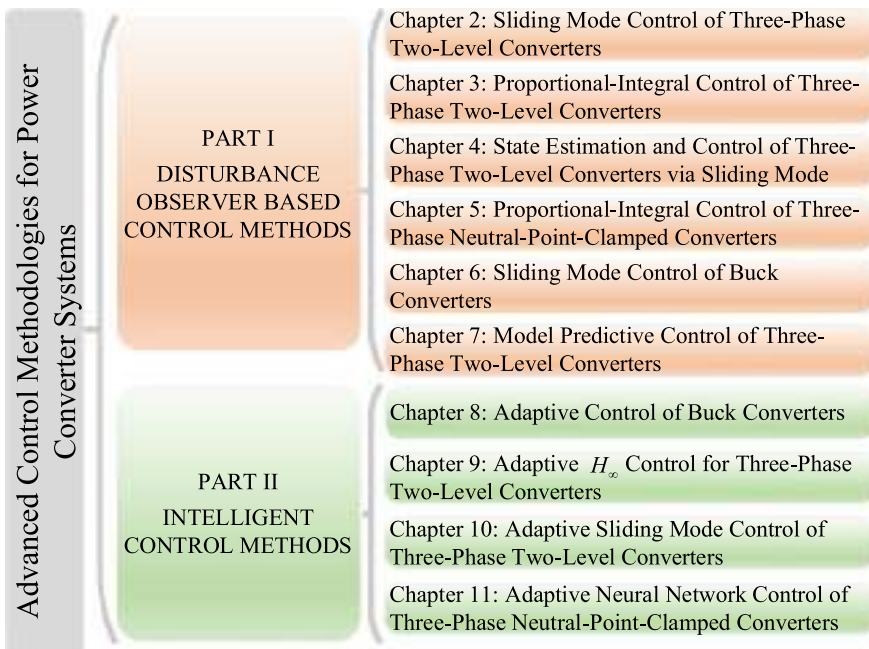


Fig. 1.15 Main contents of the book

SRF-PI control. The proposed control strategy is first theoretically verified to be effective and advantageous than conventional PI control. Then experiments are conducted on a 5kW grid-connected power converter, to validate the correctness of theoretical deduction and test converter's performance in real application.

- **Chapter 4** designs a sliding mode observer (SMO) based SMC strategy to regulate the dc-link voltage of the three-phase two-level ac/dc power converter. The control structure is the same as in Chap. 2, and the SMO is derived from a similar one in that chapter. The SMO has similar characteristics as the LDO in Chap. 3, since it has parameters to tune the transient process and the performance of steady state, but it converges faster and is more robust against external disturbance. The stability of voltage regulation loop under SMO-SMC control is first proved via Lyapunov method. Then the effectiveness and advantage of the proposed control strategy is verified via simulation, using the conventional PI control as comparison baseline. At last, experiments are carried out on a 5kW grid-connected power converter, to validate the theoretical and simulation results.
- **Chapter 5** investigates the disturbance observer based control strategies for three-phase three-level neutral point clamped (NPC) ac/dc power converter. The control target is to regulate the dc-link voltage. Two control modes are investigated, i.e., voltage oriented control (VOC) and direct power control (DPC). VOC has three control loops, which are voltage regulation loop, current tracking loop, and capacitor voltage balance loop. DPC also has three control loops, which are voltage reg-

ulation loop, power tracking loop, and capacitor voltage balance loop. This chapter firstly investigates the performance improvement brought by linear extended state observer (LESO) under VOC, where the LESO is adopted in voltage regulation loop to compensate the PI controller. The effectiveness and advantage of LESO is verified via simulation. After this, the LESO is further adopted under DPC, where LESO based H_∞ control is designed for voltage regulation loop, adaptive super-twisting SMC is adopted for power tracking loop and capacitor voltage balance loop. The effectiveness of proposed strategy under DPC is verified via simulation.

- **Chapter 6** proposes the disturbance observer based control strategy for dc/dc buck converter. The control target is to regulate the dc out voltage. Cascaded two loop control structure is adopted, i.e., voltage regulation loop as outer loop and current tracking loop as inner loop. For voltage regulation loop, LESO based second-order SMC strategy is designed. For current tracking loop, a second-order sliding mode controller is employed. The effectiveness of proposed strategy is verified by simulation.
- **Chapter 7** designs a model predictive control strategy for three-phase two-level ac/dc power converter. For power tracking loop, the finite-set model predictive control (MPC) is adopted for power tracking loop to directly drive the active and reactive powers of the system to their reference values with fast dynamics. For voltage regulation loop, a linear extended state observer based PI controller is designed to regulate the dc-link voltage. The effectiveness of proposed strategy is verified through simulation, and its advantage is shown by using conventional MPC as comparison baseline.

Part II investigates intelligent control methods for power converters. Part II which begins with Chap. 8 consists of four chapters as follows.

- **Chapter 8** designs two adaptive control strategies for dc/dc buck converter, which are single-loop adaptive control strategy and double-loop adaptive control strategy. The single-loop adaptive control strategy directly regulates the output voltage, and is designed based on adaptive and back-stepping control approach. The double-loop adaptive control strategy has voltage regulation loop as outer loop and current tracking loop as inner loop, and is designed with adaptive and sliding mode control approach. This chapter compares and analyzes the advantages and disadvantages of the two proposed adaptive control strategies, and give a guideline for selecting appropriate control strategy for buck converter under specific requirements.
- **Chapter 9** proposes a control strategy consisting of adaptive control and H_∞ technique for three-phase two-level ac/dc power converter. An efficient adaptive controller is designed to regulate dc-link output voltage to its reference in the presence of external disturbances. Two H_∞ controllers are designed in dq SRF to force the grid currents to track their reference values generated from the voltage loop. The effectiveness of proposed strategy is verified through simulation, and its advantage is shown by using sliding mode control as comparison baseline.
- **Chapter 10** investigates adaptive super-twisting SMC based H_∞ control method, taking into account both the load variation and component parameter uncertainty of three-phase two-level ac/dc power converter. Two adaptive super-twisting slid-

ing mode controllers are designed for current tracking, to drive the grid currents to their references in finite time. For voltage regulation, linear extended state observer based H_∞ control strategy is designed. The finite-time convergence of the closed-loop system is proved via Lyapunov method. By adopting the adaptive super-twisting algorithm, the upper bound of the external disturbance derivative is not required to be provided a priori. The effectiveness and advantage of the proposed strategy is verified through simulation, using conventional PI control as comparison baseline.

- **Chapter 11** investigates radial basis function (RBF) neural network based control strategy for three-phase three-level neutral-point-clamped (NPC) ac/dc power converter. In power tracking loop, two RBF neural network based adaptive controllers are designed to respectively drive the active and reactive power to their reference values. In voltage regulation loop, an adaptive controller is designed to regulate the dc-link voltage where the load is regarded as external disturbance. In voltage balance loop, a reduced-order observer based controller is developed for the voltage balance loop to ensure there is no voltage difference between two dc-link capacitors. The effectiveness and advantage of the proposed control strategy for the NPC power converter are verified through experiments.
- **Chapter 12** summarizes the results of the book and then proposes some related topics for the future research work.

References

1. Romero-Cadaval, E., Francois, B., Malinowski, M., Zhong, Q.C.: Grid-connected photovoltaic plants: an alternative energy source, replacing conventional sources. *IEEE Ind. Electron. Mag.* **9**(1), 18–32 (2015)
2. Owusu, P.A., Asumadu-Sarkodie, S.: A review of renewable energy sources, sustainability issues and climate change mitigation. *Cogent Eng.* **3**(1), 1167990 (2016)
3. Tan, X., Li, Q., Wang, H.: Advances and trends of energy storage technology in microgrid. *Int. J. Electr. Power Energy Syst.* **44**(1), 179–191 (2013)
4. Suberu, M.Y., Mustafa, M.W., Bashir, N.: Energy storage systems for renewable energy power sector integration and mitigation of intermittency. *Renew. Sustain. Energy Rev.* **35**, 499–514 (2014)
5. Vazquez, S., Lukic, S.M., Galvan, E., Franquelo, L.G., Carrasco, J.M.: Energy storage systems for transport and grid applications. *IEEE Trans. Ind. Electron.* **57**(12), 3881–3895 (2010)
6. Styński S., Luo W., Chub A., Franquelo L. G., Malinowski M., D. Vinnikov: Utility-scale energy storage systems: converters and control. *IEEE Ind. Electron. Mag.* **14**(4), 32–52 (2020)
7. Luo, W., Styński, S., Chub, A., Franquelo, L.G., Malinowski, M., Vinnikov, D.: Utility-scale energy storage systems: A comprehensive review of their applications, challenges, and future directions. *IEEE Ind. Electron. Mag.* (2020). <https://doi.org/10.1109/MIE.2020.3026169>
8. El-Hawary, M.E.: The smart grid-state-of-the-art and future trends. *Electr. Power Compon. Syst.* **42**(3–4), 239–250 (2014)
9. Stoustrup, J., Annaswamy, A., Chakrabortty, A., Qu, Z.: Smart grid control: overview and research opportunities. Springer (2019)
10. Luo, A., Xu, Q., Ma, F., Chen, Y.: Overview of power quality analysis and control technology for the smart grid. *J. Mod. Power Syst. Clean Energy* **41**, 1–9 (2016)

11. Hossain, M.S., Madlool, N.A., Rahim, N.A., Selvaraj, J., Pandey, A.K., Khan, A.F.: Role of smart grid in renewable energy: an overview. *Renew. Sustain. Energy Rev.* **60**, 1168–1184 (2016)
12. Leon, J.I., Kouro, S., Franquelo, L.G., Rodriguez, J., Wu, B.: The essential role and the continuous evolution of modulation techniques for voltage-source inverters in the past, present, and future power electronics. *IEEE Trans. Ind. Electron.* **63**(5), 2688–2701 (2016)
13. Blaabjerg, F., Teodorescu, R., Liserre, M., Timbus, A.V.: Overview of control and grid synchronization for distributed power generation systems. *IEEE Trans. Ind. Electron.* **53**(5), 1398–1409 (2006)
14. Guerrero, J.M., Vasquez, J.C., Matas, J., De Vicuña, L.G., Castilla, M.: Hierarchical control of droop-controlled AC and DC microgrids-A general approach toward standardization. *IEEE Trans. Ind. Electron.* **58**(1), 158–172 (2010)
15. Carrasco, J.M., Franquelo, L.G., Bialasiewicz, J.T., Galván, E., PortilloGuisado, R.C., Prats, M.M., Leon, J.I., Moreno-Alfonso, N.: Power-electronic systems for the grid integration of renewable energy sources: a survey. *IEEE Trans. Ind. Electron.* **53**(4), 1002–1016 (2006)
16. Colak, I., Kabalci, E., Fulli, G., Lazarou, S.: A survey on the contributions of power electronics to smart grid systems. *Renew. Sustain. Energy Rev.* **47**, 562–579 (2015)
17. Chakraborty, S., Simoes, M.G., Kramer, W.E.: Power Electronics for Renewable and Distributed Energy Systems. Springer (2013)
18. Molina, M.G.: Energy storage and power electronics technologies: a strong combination to empower the transformation to the smart grid. *Proc. IEEE* **105**(11), 2191–2219 (2017)
19. Blaabjerg, F., Liserre, M., Ma, K.: Power electronics converters for wind turbine systems. *IEEE Trans. Ind. Appl.* **48**(2), 708–719 (2011)
20. Bidram, A., Davoudi, A.: Hierarchical structure of microgrids control system. *IEEE Trans. Smart Grid* **3**(4), 1963–1976 (2012)
21. Li, Y.W., Kao, C.N.: An accurate power control strategy for power-electronics-interfaced distributed generation units operating in a low-voltage multibus microgrid. *IEEE Trans. Power Electron.* **24**(12), 2977–2988 (2009)
22. Liserre, M., Sauter, T., Hung, J.Y.: Future energy systems: integrating renewable energy sources into the smart power grid through industrial electronics. *IEEE Ind. Electron. Mag.* **4**(1), 18–37 (2010)
23. Strasser, T., Andren, F., Kathan, J., Cecati, C., Buccella, C., Siano, P., Leitao, P., Zhabelova, G., Vyatkin, V., Vrba, P., Marik, V.: A review of architectures and concepts for intelligence in future electric energy systems. *IEEE Trans. Ind. Electron.* **62**(4), 2424–2438 (2014)
24. Ellabban, O., Abu-Rub, H., Blaabjerg, F.: Renewable energy resources: current status, future prospects and their enabling technology. *Renew. Sustain. Energy Rev.* **39**, 748–764 (2014)
25. Zhong, Q.C., Hornik, T.: Control of Power Inverters in Renewable Energy and Smart Grid Integration, vol. 97. Wiley (2012)
26. Blaabjerg, F., Chen, Z., Kjaer, S.B.: Power electronics as efficient interface in dispersed power generation systems. *IEEE Trans. Power Electron.* **19**(5), 1184–1194 (2004)
27. Teodorescu, R., Liserre, M., Rodriguez, P.: Grid Converters for Photovoltaic and Wind Power Systems. Wiley (2011)
28. Panten, N., Hoffmann, N., Fuchs, F.W.: Finite control set model predictive current control for grid-connected voltage-source converters with LCL filters: a study based on different state feedbacks. *IEEE Trans. Power Electron.* **31**(7), 5189–5200 (2015)
29. Wang, J., Zhang, C., Li, S., Yang, J., Li, Q.: Finite-time output feedback control for PWM-based DC-DC buck power converters of current sensorless mode. *IEEE Trans. Control Syst. Technol.* **25**(4), 1359–1371 (2016)
30. Cid-Pastor, A., Giral, R., Calvente, J., Utkin, V.I., Martinez-Salamero, L.: Interleaved converters based on sliding-mode control in a ring configuration. *IEEE Trans. Circuits Syst. I Regul. Pap.* **58**(10), 2566–2577 (2011)
31. Wai, R.J., Shih, L.C.: Design of voltage tracking control for dc-dc boost converter via total sliding-mode technique. *IEEE Trans. Ind. Electron.* **58**(6), 2502–2511 (2010)

32. Sebaaly, F., Vahedi, H., Kanaan, H.Y., Moubayed, N., Al-Haddad, K.: Sliding mode fixed frequency current controller design for grid-connected NPC inverter. *IEEE J. Emerg. Sel. Top. Power Electron.* **4**(4), 1397–1405 (2016)
33. Ling, R., Shu, Z., Hu, Q., Song, Y.D.: Second-order sliding-mode controlled three-level buck DC-DC converters. *IEEE Trans. Ind. Electron.* **65**(1), 898–906 (2017)
34. Ma, L., Zhang, Y., Yang, X., Ding, S., Dong, L.: Quasi-continuous second-order sliding mode control of buck converter. *IEEE Access* **6**, 17859–17867 (2018)
35. Ding, S., Zheng, W.X., Sun, J., Wang, J.: Second-order sliding-mode controller design and its implementation for buck converters. *IEEE Trans. Ind. Inf.* **14**(5), 1990–2000 (2017)
36. Hu, J., Shang, L., He, Y., Zhu, Z.Q.: Direct active and reactive power regulation of grid-connected DC/AC converters using sliding mode control approach. *IEEE Trans. Power Electron.* **26**(1), 210–222 (2010)
37. Tan, S.C., Lai, Y.M., Chi, K.T.: Indirect sliding mode control of power converters via double integral sliding surface. *IEEE Trans. Power Electron.* **23**(2), 600–611 (2008)
38. Qureshi, M.A., Ahmad, I., Munir, M.F.: Double integral sliding mode control of continuous gain four quadrant quasi-Z-source converter. *IEEE Access* **6**, 77785–77795 (2018)
39. Tan, S.C., Lai, Y.M., Tse, C.K., Cheung, M.K.: Adaptive feedforward and feedback control schemes for sliding mode controlled power converters. *IEEE Trans. Power Electron.* **21**(1), 182–192 (2006)
40. Zou, S., Mallik, A., Lu, J., Khaligh, A.: Sliding mode control scheme for a CLLC resonant converter. *IEEE Trans. Power Electron.* **34**(12), 12274–12284 (2019)
41. Pradhan, R., Subudhi, B.: Double integral sliding mode MPPT control of a photovoltaic system. *IEEE Trans. Control Syst. Technol.* **24**(1), 285–292 (2015)
42. Wang, Z., Li, S., Li, Q.: Discrete-time fast terminal sliding mode control design for DC-DC buck converters with mismatched disturbances. *IEEE Trans. Ind. Inf.* **16**(2), 1204–1213 (2019)
43. Wu, J., Lu, Y.: Adaptive backstepping sliding mode control for boost converter with constant power load. *IEEE Access* **7**, 50797–50807 (2019)
44. Shtessel, Y., Baev, S., Biglari, H.: Unity power factor control in three-phase AC/DC boost converter using sliding modes. *IEEE Trans. Ind. Electron.* **55**(11), 3874–3882 (2008)
45. Labbe, B., Allard, B., Lin-Shi, X., Chesneau, D.: An integrated sliding-mode buck converter with switching frequency control for battery-powered applications. *IEEE Trans. Power Electron.* **28**(9), 4318–4326 (2012)
46. Haroun, R., Cid-Pastor, A., El Aroudi, A., Martinez-Salamero, L.: Synthesis of canonical elements for power processing in dc distribution systems using cascaded converters and sliding-mode control. *IEEE Trans. Power Electron.* **29**(3), 1366–1381 (2013)
47. Monteiro, J., Silva, J.F., Pinto, S.F., Palma, J.: Linear and sliding-mode control design for matrix converter-based unified power flow controllers. *IEEE Trans. Power Electron.* **29**(7), 3357–3367 (2013)
48. Sadeghi, R., Madani, S.M., Ataei, M., Kashkooli, M.A., Ademi, S.: Super-twisting sliding mode direct power control of a brushless doubly fed induction generator. *IEEE Trans. Ind. Electron.* **65**(11), 9147–9156 (2018)
49. Yang, Q., Saeedifard, M., Perez, M.A.: Sliding mode control of the modular multilevel converter. *IEEE Trans. Ind. Electron.* **66**(2), 887–897 (2018)
50. Vidal-Idiarte, E., Carrejo, C.E., Calvente, J., Martinez-Salamero, L.: Two-loop digital sliding mode control of DC-DC power converters based on predictive interpolation. *IEEE Trans. Ind. Electron.* **58**(6), 2491–2501 (2010)
51. Mokhtar, M., Marei, M.I., El-Sattar, A.A.: An adaptive droop control scheme for DC microgrids integrating sliding mode voltage and current controlled boost converters. *IEEE Trans. Smart Grid* **10**(2), 1685–1693 (2017)
52. Martins, L.T., Stefanello, M., Pinheiro, H., Vieira, R.P.: Current control of grid-tied LCL-VSI with a sliding mode controller in a multiloop approach. *IEEE Trans. Power Electron.* **34**(12), 12356–12367 (2019)

53. Lopez-Santos, O., Martinez-Salamero, L., Garcia, G., Valderrama-Blavi, H., Sierra-Polanco, T.: Robust sliding-mode control design for a voltage regulated quadratic boost converter. *IEEE Trans. Power Electron.* **30**(4), 2313–2327 (2014)
54. Morales, J., de Vicuna, L.G., Guzman, R., Castilla, M., Miret, J.: Modeling and sliding mode control for three-phase active power filters using the vector operation technique. *IEEE Trans. Ind. Electron.* **65**(9), 6828–6838 (2018)
55. Zhao, Y., Qiao, W., Ha, D.: A sliding-mode duty-ratio controller for DC/DC buck converters with constant power loads. *IEEE Trans. Ind. Appl.* **50**(2), 1448–1458 (2013)
56. Portillo, R., Vazquez, S., Leon, J.I., Prats, M.M., Franquelo, L.G.: Model based adaptive direct power control for three-level NPC converters. *IEEE Trans. Ind. Inf.* **9**(2), 1148–1157 (2012)
57. Pahlevani, M., Jain, P.: A fast DC-bus voltage controller for bidirectional single-phase AC/DC converters. *IEEE Trans. Power Electron.* **30**(8), 4536–4547 (2014)
58. Gautam, A.R., Gourav, K., Guerrero, J.M., Fulwani, D.M.: Ripple mitigation with improved line-load transients response in a two-stage DC-DC-AC converter: adaptive SMC approach. *IEEE Trans. Ind. Electron.* **65**(4), 3125–3135 (2017)
59. Eren, S., Pahlevani, M., Bakhtshai, A., Jain, P.: A digital current control technique for grid-connected AC/DC converters used for energy storage systems. *IEEE Trans. Power Electron.* **32**(5), 3970–3988 (2016)
60. Li, J., Liu, Z., Su, Q.: Improved adaptive backstepping sliding mode control for a three-phase PWM AC-DC converter. *IET Control Theory Appl.* **13**(6), 854–860 (2019)
61. Chan, C.Y., Chincholkar, S.H., Jiang, W.: Adaptive current-mode control of a high step-up DC-DC converter. *IEEE Trans. Power Electron.* **32**(9), 7297–7305 (2016)
62. Bellinaso, L.V., Figueira, H.H., Basquera, M.F., Vieira, R.P., Gründling, H.A., Michels, L.: Cascade control with adaptive voltage controller applied to photovoltaic boost converters. *IEEE Trans. Ind. Appl.* **55**(2), 1903–1912 (2018)
63. He, J., Ruan, X., Zhang, L.: Adaptive voltage control for bidirectional converter in flicker-free electrolytic capacitor-less AC-DC LED driver. *IEEE Trans. Ind. Electron.* **64**(1), 320–324 (2016)
64. Kasicheyanula, S., John, V.: Adaptive control strategy for ultracapacitor based bidirectional DC-DC converters. *IEEE Trans. Ind. Appl.* **55**(2), 1717–1728 (2018)
65. Hernandez-Gomez, M., Ortega, R., Lamnabhi-Lagarrigue, F., Escobar, G.: Adaptive PI stabilization of switched power converters. *IEEE Trans. Control Syst. Technol.* **18**(3), 688–698 (2009)
66. Massing, J.R., Stefanello, M., Grundling, H.A., Pinheiro, H.: Adaptive current control for grid-connected converters with LCL filter. *IEEE Trans. Ind. Electron.* **59**(12), 4681–4693 (2011)
67. Hogan, D.J., Gonzalez-Espin, F.J., Hayes, J.G., Lightbody, G., Foley, R.: An adaptive digital-control scheme for improved active power filtering under distorted grid conditions. *IEEE Trans. Ind. Electron.* **65**(2), 988–999 (2017)
68. Kanthaphayao, Y., Chunkag, V.: Current-sharing bus and fuzzy gain scheduling of proportional-integral controller to control a parallel-connected AC/DC converter. *IET Power Electron.* **7**(10), 2525–2532 (2014)
69. Bayhan, S., Demirbas, S., Abu-Rub, H.: Fuzzy-PI-based sensorless frequency and voltage controller for doubly fed induction generator connected to a DC microgrid. *IET Renew. Power Gener.* **10**(8), 1069–1077 (2016)
70. Harrabi, N., Souissi, M., Aitouche, A., Chaabane, M.: Intelligent control of grid-connected AC-DC-AC converters for a WECS based on T-S fuzzy interconnected systems modelling. *IET Power Electron.* **11**(9), 1507–1518 (2018)
71. El Khateb, A., Abd Rahim, N., Selvaraj, J., Uddin, M.N.: Fuzzy-logic-controller-based SEPIC converter for maximum power point tracking. *IEEE Trans. Ind. Appl.* **50**(4), 2349–2358 (2014)
72. Chiu, C.S.: TS fuzzy maximum power point tracking control of solar power generation systems. *IEEE Trans. Energy Convers.* **25**(4), 1123–1132 (2010)
73. Bouafia, A., Krim, F., Gaubert, J.P.: Fuzzy-logic-based switching state selection for direct power control of three-phase PWM rectifier. *IEEE Trans. Ind. Electron.* **56**(6), 1984–1992 (2009)

74. Lian, K.Y., Liou, J.J., Huang, C.Y.: LMI-based integral fuzzy control of DC-DC converters. *IEEE Trans. Fuzzy Syst.* **14**(1), 71–80 (2006)
75. Vazquez, S., Aguilera, R.P., Acuna, P., Pou, J., Leon, J.I., Franquelo, L.G., Agelidis, V.G.: Model predictive control for single-phase NPC converters based on optimal switching sequences. *IEEE Trans. Ind. Electron.* **63**(12), 7533–7541 (2016)
76. Vazquez, S., Rodriguez, J., Rivera, M., Franquelo, L.G., Norambuena, M.: Model predictive control for power converters and drives: advances and trends. *IEEE Trans. Ind. Electron.* **64**(2), 935–947 (2016)
77. Kwak, S., Moon, U.C., Park, J.C.: Predictive-control-based direct power control with an adaptive parameter identification technique for improved AFE performance. *IEEE Trans. Power Electron.* **29**(11), 6178–6187 (2014)
78. Oettmeier, F.M., Neely, J., Pekarek, S., DeCarlo, R., Uthaichana, K.: MPC of switching in a boost converter using a hybrid state model with a sliding mode observer. *IEEE Trans. Ind. Electron.* **56**(9), 3453–3466 (2008)
79. Rodriguez, J., Kazmierkowski, M.P., Espinoza, J.R., Zanchetta, P., Abu-Rub, H., Young, H.A., Rojas, C.A.: State of the art of finite control set model predictive control in power electronics. *IEEE Trans. Ind. Inf.* **9**(2), 1003–1016 (2012)
80. Kouro, S., Cortes, P., Vargas, R., Ammann, U., Rodriguez, J.: Model predictive control-A simple and powerful method to control power converters. *IEEE Trans. Ind. Electron.* **56**(6), 1826–1838 (2008)
81. Cortes, P., Rodriguez, J., Silva, C., Flores, A.: Delay compensation in model predictive current control of a three-phase inverter. *IEEE Trans. Ind. Electron.* **59**(2), 1323–1325 (2011)
82. Cortes, P., Ortiz, G., Yuz, J.I., Rodriguez, J., Vazquez, S., Franquelo, L.G.: Model predictive control of an inverter with output LC filter for UPS applications. *IEEE Trans. Ind. Electron.* **56**(6), 1875–1883 (2009)
83. Rodriguez, J., Pontt, J., Silva, C.A., Correa, P., Lezana, P., Cortes, P., Ammann, U.: Predictive current control of a voltage source inverter. *IEEE Trans. Ind. Electron.* **54**(1), 495–503 (2007)
84. Preindl, M., Schaltz, E., Thogersen, P.: Switching frequency reduction using model predictive direct current control for high-power voltage source inverters. *IEEE Trans. Ind. Electron.* **58**(7), 2826–2835 (2010)
85. Barros, J.D., Silva, J.F.: Optimal predictive control of three-phase NPC multilevel converter for power quality applications. *IEEE Trans. Ind. Electron.* **55**(10), 3670–3681 (2008)
86. Barros, J.D., Silva, J.F.: Multilevel optimal predictive dynamic voltage restorer. *IEEE Trans. Ind. Electron.* **57**(8), 2747–2760 (2009)
87. Chaves, M., Margato, E., Silva, J.F., Pinto, S.F., Santana, J.: Fast optimum-predictive control and capacitor voltage balancing strategy for bipolar back-to-back NPC converters in high-voltage direct current transmission systems. *IET Gener., Transm. Distrib.* **5**(3), 368–375 (2011)
88. Perez, M.A., Rodriguez, J., Fuentes, E.J., Kammerer, F.: Predictive control of AC-AC modular multilevel converters. *IEEE Trans. Ind. Electron.* **59**(7), 2832–2839 (2011)
89. Rivera, M., Rojas, C., Rodriguez, J., Wheeler, P., Wu, B., Espinoza, J.: Predictive current control with input filter resonance mitigation for a direct matrix converter. *IEEE Trans. Power Electron.* **26**(10), 2794–2803 (2011)
90. Villarreal, F., Espinoza, J.R., Rojas, C.A., Rodriguez, J., Rivera, M., Sbarbaro, D.: Multi-objective switching state selector for finite-states model predictive control based on fuzzy decision making in a matrix converter. *IEEE Trans. Ind. Electron.* **60**(2), 589–599 (2012)
91. Xia, C., Wang, M., Song, Z., Liu, T.: Robust model predictive current control of three-phase voltage source PWM rectifier with online disturbance observation. *IEEE Trans. Ind. Inf.* **8**(3), 459–471 (2012)
92. Quevedo, D.E., Aguilera, R.P., Perez, M.A., Cortes, P., Lizana, R.: Model predictive control of an AFE rectifier with dynamic references. *IEEE Trans. Power Electron.* **27**(7), 3128–3136 (2011)
93. Rivera, M., Wilson, A., Rojas, C.A., Rodriguez, J., Espinoza, J.R., Wheeler, P.W., Empringham, L.: A comparative assessment of model predictive current control and space vector modulation in a direct matrix converter. *IEEE Trans. Ind. Electron.* **60**(2), 578–588 (2012)

94. Aguilera, R.P., Lezana, P., Quevedo, D.E.: Finite-control-set model predictive control with improved steady-state performance. *IEEE Trans. Ind. Inf.* **9**(2), 658–667 (2012)
95. Thielemans, S., Vyncke, T.J., Melkebeek, J.: Weight factor selection for model-based predictive control of a four-level flying-capacitor inverter. *IET Power Electron.* **5**(3), 323–333 (2012)
96. Ahmed, K.H., Massoud, A.M., Finney, S.J., Williams, B.W.: A modified stationary reference frame-based predictive current control with zero steady-state error for LCL coupled inverter-based distributed generation systems. *IEEE Trans. Ind. Electron.* **58**(4), 1359–1370 (2010)
97. Kakosimos, P.E., Kladas, A.G.: Implementation of photovoltaic array MPPT through fixed step predictive control technique. *Renew. Energy* **36**(9), 2508–2514 (2011)
98. Zhang, Y., Xie, W., Zhang, Y.: Deadbeat direct power control of three-phase pulse-width modulation rectifiers. *IET Power Electron.* **7**(6), 1340–1346 (2014)
99. Song, W., Ma, J., Zhou, L., Feng, X.: Deadbeat predictive power control of single-phase three-level neutral-point-clamped converters using space-vector modulation for electric railway traction. *IEEE Trans. Power Electron.* **31**(1), 721–732 (2015)
100. Wang, B., Zhang, X., Ye, J., Gooi, H.B.: Deadbeat control for a single-inductor multiple-input multiple-output DC-DC converter. *IEEE Trans. Power Electron.* **34**(2), 1914–1924 (2018)
101. Hassan, M.A., Li, E.P., Li, X., Li, T., Duan, C., Chi, S.: Adaptive passivity-based control of DC-DC buck power converter with constant power load in dc microgrid systems. *IEEE J. Emerg. Sel. Top. Power Electron.* **7**(3), 2029–2040 (2018)
102. Harnefors, L., Yépes, A.G., Vidal, A., Doval-Gandoy, J.: Passivity-based controller design of grid-connected VSCs for prevention of electrical resonance instability. *IEEE Trans. Ind. Electron.* **62**(2), 702–710 (2014)
103. Zuniga-Ventura, Y.A., Langarica-Cordoba, D., Leyva-Ramos, J., Diaz-Saldivaria, L.H., Ramirez-Rivera, V.M.: Adaptive backstepping control for a fuel cell/boost converter system. *IEEE J. Emerg. Sel. Top. Power Electron.* **6**(2), 686–695 (2018)
104. Allag, A., Hammoudi, M.Y., Mimoune, S.M., Ayad, M.Y.: Adaptive backstepping voltage controller design for an PWM AC-DC converter. *Int. J. Electr. Power Eng.* **1**(1), 62–69 (2007)
105. Pahlevaninezhad, M., Das, P., Drobnik, J., Jain, P.K., Bakhshai, A.: A new control approach based on the differential flatness theory for an AC/DC converter used in electric vehicles. *IEEE Trans. Power Electron.* **27**(4), 2085–2103 (2011)
106. Thounthong, P.: Control of a three-level boost converter based on a differential flatness approach for fuel cell vehicle applications. *IEEE Trans. Veh. Technol.* **61**(3), 1467–1472 (2012)
107. Bose, B.K.: Neural network applications in power electronics and motor drives—an introduction and perspective. *IEEE Trans. Ind. Electron.* **54**(1), 14–33 (2007)
108. Li, S., Fairbank, M., Johnson, C., Wunsch, D.C., Alonso, E., Proao, J.L.: Artificial neural networks for control of a grid-connected rectifier/inverter under disturbance, dynamic and power converter switching conditions. *IEEE Trans. Neural Netw. Learn. Syst.* **25**(4), 738–750 (2013)
109. Lin, W.M., Hong, C.M., Chen, C.H.: Neural-network-based MPPT control of a stand-alone hybrid power generation system. *IEEE Trans. Power Electron.* **26**(12), 3571–3581 (2011)
110. Gheisarnejad, M., Khooban, M.H.: IoT-Based DC/DC deep learning power converter control: real-time implementation. *IEEE Trans. Power Electron.* **35**(12), 13621–13630 (2020)
111. Singh, B., Jayaprakash, P., Kumar, S., Kothari, D.P.: Implementation of neural-network-controlled three-leg VSC and a transformer as three-phase four-wire DSTATCOM. *IEEE Trans. Ind. Appl.* **47**(4), 1892–1901 (2011)
112. Levant, A.: Higher-order sliding modes, differentiation and output-feedback control. *Int. J. Control.* **76**(9–10), 924–941 (2003)
113. Zhai, D.H., Xia, Y.: Finite-time control of teleoperation systems with input saturation and varying time delays. *IEEE Trans. Syst., Man, Cybern.: Syst.* **47**(7), 1522–1534 (2016)
114. Song, J., Niu, Y., Zou, Y.: Finite-time stabilization via sliding mode control. *IEEE Trans. Autom. Control* **62**(3), 1478–1483 (2016)

115. Yan, X.G., Spurgeon, S.K., Edwards, C.: Memoryless static output feedback sliding mode control for nonlinear systems with delayed disturbances. *IEEE Trans. Autom. Control* **59**(7), 1906–1912 (2013)
116. Gao, W., Hung, J.C.: Variable structure control of nonlinear systems: a new approach. *IEEE Trans. Ind. Electron.* **40**(1), 45–55 (1993)
117. Acary, V., Brogliato, B., Orlov, Y.V.: Chattering-free digital sliding-mode control with state observer and disturbance rejection. *IEEE Trans. Autom. Control* **57**(5), 1087–1101 (2011)
118. Gonzalez, T., Moreno, J.A., Fridman, L.: Variable gain super-twisting sliding mode control. *IEEE Trans. Autom. Control* **57**(8), 2100–2105 (2011)
119. Albiol-Tendillo, L., Vidal-Idiarte, E., Maixe-Altes, J., Mendez-Prince, S., Martinez-Salamero, L.: Seamless sliding-mode control for bidirectional boost converter with output filter for electric vehicles applications. *IET Power Electron.* **8**(9), 1808–1816 (2015)
120. Zhang, J., Liu, X., Xia, Y., Zuo, Z., Wang, Y.: Disturbance observer-based integral sliding-mode control for systems with mismatched disturbances. *IEEE Trans. Ind. Electron.* **63**(11), 7040–7048 (2016)
121. Xu, W., Jiang, Y., Mu, C.: Novel composite sliding mode control for PMSM drive system based on disturbance observer. *IEEE Trans. Appl. Supercond.* **26**(7), 1–5 (2016)
122. Levant, A.: Sliding order and sliding accuracy in sliding mode control. *Int. J. Control.* **58**(6), 1247–1263 (1993)
123. Ling, R., Maksimovic, D., Leyva, R.: Second-order sliding-mode controlled synchronous buck DC-DC converter. *IEEE Trans. Power Electron.* **31**(3), 2539–2549 (2015)
124. RakhtAla, S.M., Yasoubi, M., HosseinNia, H.: Design of second order sliding mode and sliding mode algorithms: a practical insight to DC-DC buck converter. *IEEE/CAA J. Autom. Sin.* **4**(3), 483–497 (2017)
125. Liu, J., Vazquez, S., Wu, L., Marquez, A., Gao, H., Franquelo, L.G.: Extended state observer-based sliding-mode control for three-phase power converters. *IEEE Trans. Ind. Electron.* **64**(1), 22–31 (2016)
126. Draper, C.S., Li, Y.T.: Principles of Optimizing Control Systems and an Application to the Internal Combustion Engine. American Society of Mechanical Engineers (1951)
127. Whitaker, H.P., Yamron, J., Kezer, A.: Design of model-reference adaptive control systems for aircraft. Massachusetts Institute of Technology, Instrumentation Laboratory (1958)
128. Parks, P.: Liapunov redesign of model reference adaptive control systems. *IEEE Trans. Autom. Control* **11**(3), 362–367 (1966)
129. Landau, I.: A hyperstability criterion for model reference adaptive control systems. *IEEE Trans. Autom. Control* **14**(5), 552–555 (1969)
130. Åström, K.J., Wittenmark, B.: On self tuning regulators. *Automatica* **9**(2), 185–199 (1973)
131. Landau, I.D., Lozano, R., M'Saad, M., Karimi, A.: Adaptive Control: Algorithms, Analysis and Applications. Springer (2011)
132. Oucheriah, S., Guo, L.: PWM-based adaptive sliding-mode control for boost DC-DC converters. *IEEE Trans. Ind. Electron.* **60**(8), 3291–3294 (2012)
133. Babazadeh, A., Maksimovic, D.: Hybrid digital adaptive control for fast transient response in synchronous buck DC-DC converters. *IEEE Trans. Power Electron.* **24**(11), 2625–2638 (2009)
134. Lam, H.K., Tan, S.C.: Stability analysis of fuzzy-model-based control systems: application on regulation of switching DC-DC converter. *IET Control Theory Appl.* **3**(8), 1093–1106 (2009)
135. Ofoli, A.R., Rubaai, A.: Real-time implementation of a fuzzy logic controller for switch-mode power-stage DC-DC converters. *IEEE Trans. Ind. Appl.* **42**(6), 1367–1374 (2006)
136. Guo, L., Hung, J.Y., Nelms, R.M.: Evaluation of DSP-based PID and fuzzy controllers for DC-DC converters. *IEEE Trans. Ind. Electron.* **56**(6), 2237–2248 (2009)
137. So, W.C., Tse, C.K., Lee, Y.S.: Development of a fuzzy logic controller for DC/DC converters: design, computer simulation, and experimental evaluation. *IEEE Trans. Power Electron.* **11**(1), 24–32 (1996)

138. Perry, A.G., Feng, G., Liu, Y.F., Sen, P.C.: A design method for PI-like fuzzy logic controllers for DC-DC converter. *IEEE Trans. Ind. Electron.* **54**(5), 2688–2696 (2007)
139. Lin, P.Z., Lin, C.M., Hsu, C.F., Lee, T.T.: Type-2 fuzzy controller design using a sliding-mode approach for application to DC-DC converters. *IEE Proc.-Electr. Power Appl.* **152**(6), 1482–1488 (2005)
140. Chang, E.C., Liang, T.J., Chen, J.F., Chang, F.J.: Real-time implementation of grey fuzzy terminal sliding mode control for PWM DC-AC converters. *IET Power Electron.* **1**(2), 235–244 (2008)
141. Zhu, Y., Fei, J.: Disturbance observer based fuzzy sliding mode control of PV grid connected inverter. *IEEE Access* **6**, 21202–21211 (2018)
142. Luenberger, D.: Observers for multivariable systems. *IEEE Trans. Autom. Control* **11**(2), 190–197 (1966)
143. Kalman, R.E.: A new approach to linear filtering and prediction problems. *J. Basic Eng.* **82**(1), 35–45 (1960)
144. Han, J.: A class of extended state observers for uncertain systems. *Control Decis.* **10**(1), 85–88 (1995)
145. Han, J.: From PID to active disturbance rejection control. *IEEE Trans. Ind. Electron.* **56**(3), 900–906 (2009)
146. Zheng, Q., Gao, L.Q., Gao, Z.: On validation of extended state observer through analysis and experimentation. *J. Dyn. Syst. Meas. Contr.* **134**(2), 24505–24510 (2012)
147. Guo, B.Z., Zhao, Z.L.: On the convergence of an extended state observer for nonlinear systems with uncertainty. *Syst. Control Lett.* **60**(6), 420–430 (2011)
148. Vasiljevic, L.K., Khalil, H.K.: Error bounds in differentiation of noisy signals by high-gain observers. *Syst. Control Lett.* **57**(10), 856–862 (2008)
149. Xia, Y., Shi, P., Liu, G.P., Rees, D., Han, J.: Active disturbance rejection control for uncertain multivariable systems with time-delay. *IET Control Theory Appl.* **1**(1), 75–81 (2007)
150. Huang, Y., Xue, W.: Active disturbance rejection control: methodology and theoretical analysis. *ISA Trans.* **53**(4), 963–976 (2014)
151. Chang, X., Li, Y., Zhang, W., Wang, N., Xue, W.: Active disturbance rejection control for a flywheel energy storage system. *IEEE Trans. Ind. Electron.* **62**(2), 991–1001 (2014)
152. Li, S., Yang, J., Chen, W.H., Chen, X.: Disturbance observer-based control: methods and applications. CRC Press (2014)
153. Miklosovic, R., Gao, Z.: A dynamic decoupling method for controlling high performance turbofan engines. *IFAC Proc. Vol.* **38**(1), 532–537 (2005)
154. Goforth, F.J., Zheng, Q., Gao, Z.: A novel practical control approach for rate independent hysteretic systems. *ISA Trans.* **51**(3), 477–484 (2012)
155. Sun, B., Gao, Z.: A DSP-based active disturbance rejection control design for a 1-kW H-bridge DC-DC power converter. *IEEE Trans. Ind. Electron.* **52**(5), 1271–1277 (2005)
156. Zhao, S., Gao, Z.: An active disturbance rejection based approach to vibration suppression in two-inertia systems. *Asian J. Control* **15**(2), 350–362 (2013)
157. Dong, L., Zheng, Q., Gao, Z.: On control system design for the conventional mode of operation of vibrational gyroscopes. *IEEE Sens. J.* **8**(11), 1871–1878 (2008)
158. Wang, J., Li, S., Yang, J., Wu, B., Li, Q.: Extended state observer-based sliding mode control for PWM-based DC-DC buck power converter systems with mismatched disturbances. *IET Control Theory Appl.* **9**(4), 579–586 (2015)
159. Wang, B., Xu, Y., Shen, Z., Zou, J., Li, C., Liu, H.: Current control of grid-connected inverter with LCL filter based on extended-state observer estimations using single sensor and achieving improved robust observation dynamics. *IEEE Trans. Ind. Electron.* **64**(7), 5428–5439 (2017)
160. Lu, J., Golestani, S., Savaghebi, M., Vasquez, J.C., Guerrero, J.M., Marzabal, A.: An enhanced state observer for dc-link voltage control of three-phase AC/DC converters. *IEEE Trans. Power Electron.* **33**(2), 936–942 (2017)
161. Ghosh, R., Narayanan, G.: Generalized feedforward control of single-phase PWM rectifiers using disturbance observers. *IEEE Trans. Ind. Electron.* **54**(2), 984–993 (2007)

162. Nguyen, H.T., Jung, J.W.: Disturbance-rejection-based model predictive control: flexible-mode design with a modulator for three-phase inverters. *IEEE Trans. Ind. Electron.* **65**(4), 2893–2903 (2017)
163. Zhao, Z., Yang, J., Li, S., Yu, X., Wang, Z.: Continuous output feedback TSM control for uncertain systems with a DC-AC inverter example. *IEEE Trans. Circuits Syst. II Express Briefs* **65**(1), 71–75 (2017)
164. Xiong, F., Wu, J., Liu, Z., Hao, L.: Current sensorless control for dual active bridge DC-DC converter with estimated load-current feedforward. *IEEE Trans. Power Electron.* **33**(4), 3552–3566 (2017)
165. Wang, C., Li, X., Guo, L., Li, Y.W.: A nonlinear-disturbance-observer-based DC-bus voltage control for a hybrid AC/DC microgrid. *IEEE Trans. Power Electron.* **29**(11), 6162–6177 (2014)
166. Godbole, A.A., Kolhe, J.P., Talole, S.E.: Performance analysis of generalized extended state observer in tackling sinusoidal disturbances. *IEEE Trans. Control Syst. Technol.* **21**(6), 2212–2223 (2012)
167. Zheng, Q., Chen, Z., Gao, Z.: A practical approach to disturbance decoupling control. *Control Eng. Pract.* **17**(9), 1016–1025 (2009)

Part I

Disturbance Observer Based Control

Methods

Chapter 2

Sliding Mode Control of Three-Phase Two-Level Converters



Abstract According to the number of modulation levels, power converters can be divided into two-level and multi-level converters. Power converters with AC side include single-phase and three-phase converters, and grid-connected power converters are three-phase converters. Although there are various circuit topologies for converters, the three-phase two-level topology is most common in the industrial field due to its topological simplicity and full power range controllability, as well as high reliability, high efficiency and high power capacity [1]. This chapter investigates the grid-connected three-phase two-level power converter, and adopts the disturbance observer based sliding mode control strategy to carry out the current tracking and voltage regulation of the converter. The voltage regulation loop adopts a super twisting sliding mode controller, which is compensated by a disturbance observer. The current control loop is controlled in synchronous reference frame (SRF), and two super twisting sliding mode controllers are used to track the d-axis and q-axis currents. Four different disturbance observers are designed for comparison, including linear observer, second-order sliding mode observer, linear extended state observer and nonlinear extended observer. Then through simulation, the performance of the observers is compared according to the transient response of the DC-link voltage. In order to ensure a fair comparison, the parameters of the observers are adjusted to make the converter have almost the same current distortion level and DC-link voltage steady-state error.

2.1 Mathematical Model and Control Objectives

2.1.1 Mathematical Model

The topology of grid-connected three-phase two-level power converter under investigation is shown in Fig. 2.1. v_{an} , v_{bn} and v_{cn} are three-phase balanced ac input voltages from the grid, i.e., $v_{an} + v_{bn} + v_{cn} = 0$. i_a , i_b and i_c are three-phase grid currents. u_a , u_b and u_c are switching signals of the upper arms, whereas \bar{u}_a , \bar{u}_b and \bar{u}_c are the complimentary switching signals of the lower arms. L is the filtering

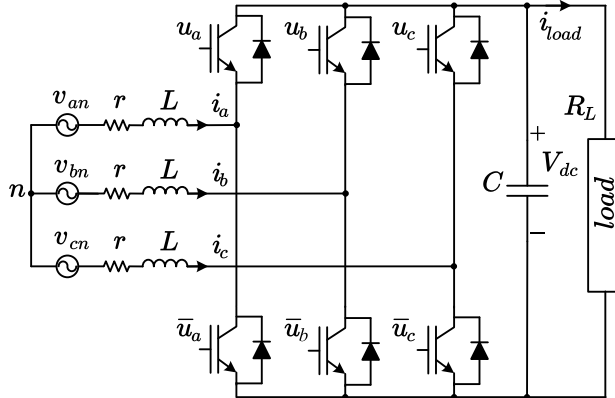


Fig. 2.1 Circuit diagram of grid-connected three-phase two-level power converter

inductor with equivalent series resistance r . C is the dc-link capacitor, whose voltage V_{dc} is to be regulated. R_L is the equivalent load connected to the dc-link, which is assumed to be slow-varying. i_{load} is the current flowing through R_L .

The mathematical model of the converter in natural (a, b, c) frame is as follow [2]:

$$L \frac{di_a}{dt} = -ri_a + v_{an} - \frac{V_{dc}}{3} (2u_a - u_b - u_c), \quad (2.1)$$

$$L \frac{di_b}{dt} = -ri_b + v_{bn} - \frac{V_{dc}}{3} (2u_b - u_a - u_c), \quad (2.2)$$

$$L \frac{di_c}{dt} = -ri_c + v_{cn} - \frac{V_{dc}}{3} (2u_c - u_a - u_b), \quad (2.3)$$

$$C \frac{dV_{dc}}{dt} = i_a u_a + i_b u_b + i_c u_c - i_{load}. \quad (2.4)$$

To facilitate the controller design, following coordinate transformations are often performed on the system (2.1)–(2.4).

(1) Stationary (α, β) frame model

Perform the power-invariant Clarke transform on the system (2.1)–(2.4) as follows,

$$\{\cdot\}_{\alpha\beta} = T_{abc-\alpha\beta} \{\cdot\}_{abc}, \quad T_{abc-\alpha\beta} = \sqrt{\frac{2}{3}} \begin{bmatrix} 1 & -\frac{1}{2} & -\frac{1}{2} \\ 0 & \frac{\sqrt{3}}{2} & -\frac{\sqrt{3}}{2} \end{bmatrix}, \quad (2.5)$$

the system model in the stationary (α, β) frame is obtained as:

$$L \frac{di_{\alpha\beta}}{dt} = v_{\alpha\beta} - \frac{v_{dc}}{2} u_{\alpha\beta} - ri_{\alpha\beta}, \quad (2.6)$$

$$C \frac{d}{dt} \left(\frac{v_{dc}^2}{2} \right) = \frac{v_{dc}}{2} u_{\alpha\beta}^T i_{\alpha\beta} - \frac{v_{dc}^2}{R_L}, \quad (2.7)$$

where $v_{\alpha\beta} = \{v_\alpha, v_\beta\}^T$ are grid voltage, $i_{\alpha\beta} = \{i_\alpha, i_\beta\}^T$ are grid currents, $u_{\alpha\beta} = \{u_\alpha, u_\beta\}^T$ are control signals, which are generated by the controller and then transformed back to u_a, u_b and u_c to be implemented by the modulator [3].

(2) Synchronous reference (d, q) frame model

Perform the power-invariant Park transform on the system (2.1)–(2.4) as follows,

$$\begin{aligned} \{\cdot\}_{dq} &= T_{abc-dq} \{\cdot\}_{abc}, \\ T_{abc-dq} &= \sqrt{\frac{2}{3}} \begin{bmatrix} \cos\omega t & \cos(\omega t - \frac{2}{3}\pi) & \cos(\omega t + \frac{2}{3}\pi) \\ -\sin\omega t & \sin(\omega t - \frac{2}{3}\pi) & \sin(\omega t + \frac{2}{3}\pi) \end{bmatrix}, \end{aligned} \quad (2.8)$$

the system model in the synchronous reference (d, q) frame is obtained as [4]:

$$L \frac{di_d}{dt} = -ri_d + \omega L i_q + v_d - u_d V_{dc}, \quad (2.9)$$

$$L \frac{di_q}{dt} = -ri_q - \omega L i_d + v_q - u_q V_{dc}, \quad (2.10)$$

$$C \frac{dV_{dc}}{dt} = u_d i_d + u_q i_q - i_{load}, \quad (2.11)$$

where v_d, v_q are grid voltage, ω is the grid frequency, i_d, i_q are grid currents, u_d, u_q are control signals. As in the (α, β) frame, the control signals are generated by the controller and transformed back to u_a, u_b and u_c to be implemented by the modulator. It should be noted that, in order to transform the three-phase variables from stationary (a, b, c) frame to synchronous reference (d, q) frame via Park transformation, a phase-lock-loop (PLL) module needs to be included in the control system [5].

2.1.2 Control Objectives

For three-phase two-level power converter, there are normally two control objectives, i.e., (1) regulate the dc-link voltage to its reference, and (2) generate the active and reactive power as required. Therefore, the control problem of power converter includes two aspects as follow:

(1) Voltage regulation problem: the dc-link voltage V_{dc} needs to be regulated to a preset value V_{dc}^* , i.e.,

$$V_{dc} \rightarrow V_{dc}^*. \quad (2.12)$$

(2) Power/current tracking problem: depending on the control strategy, it has following two cases:

- Power tracking: the instantaneous active power p needs to track the reference p^* generated from the voltage control loop, the instantaneous reactive power q needs to track preset value q^* (set $q^* = 0$ to achieve unit power factor), i.e.,

$$p \rightarrow p^*, \quad q \rightarrow q^*. \quad (2.13)$$

- Current tracking: the control of active and reactive power is in nature the control of current, thus the currents needs to track their references to fulfill the power tracking task, i.e.,

– in (α, β) frame:

$$i_\alpha \rightarrow i_\alpha^*, \quad i_\beta \rightarrow i_\beta^*. \quad (2.14)$$

– in (d, q) frame:

$$i_d \rightarrow i_d^*, \quad i_q \rightarrow i_q^*. \quad (2.15)$$

It should be noted that, the instantaneous active power reference p^* is generated from the dc-link voltage regulating process, to ensure V_{dc} to approach V_{dc}^* , whereas the instantaneous reactive power reference q^* is set directly, to achieve a required power factor.

It is worth mentioning that, along with the fulfillment of the above control tasks, the total harmonic distortion (THD) level of grid current must be maintained as low as possible.

Besides of above control tasks, the voltage of grid-connected power converters also needs to be synchronized with that of the utility grid, otherwise the power system goes unstable. To achieve this goal, the phase angle of the grid needs to be obtained. Early calculation methods of phase angle includes cross-zero method and filtering method. The cross-zero method detects the instant that the grid voltage crosses the zero value to obtain the phase angle. This method is the simplest one, but is liable to mistakes when grid voltage fluctuates (such as in voltage dip case and when there exist harmonics). The filtering method is to transform the grid voltage to (d, q) or (α, β) frame, and calculate the phase angle via arc-tangent function. This method is also liable to mistakes when there is voltage fluctuation. The most popular calculation method is the PLL method [6]. As shown in Fig. 2.2, this method works in (d, q) frame. First, set the imaginary axis reference of grid voltage v_q^* to 0; then use a controller (normally PI controller) to regulate v_q to the reference, the generated control signal is the grid frequency ω ; in the end, integrate ω to obtain the phase angle θ .

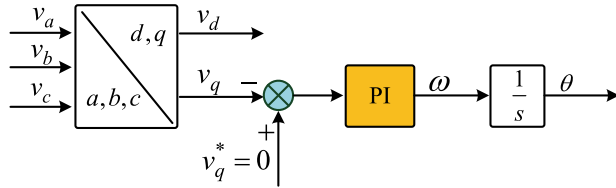


Fig. 2.2 Control diagram of PLL

2.2 Control Scheme

Figure 2.3 shows the control process of three-phase two-level power converter under the VOC mode. The control is implemented in SRF, and the control process is: the sensors measure the three-phase grid voltage v_{an} , v_{bn} and v_{cn} , three-phase grid current i_a , i_b and i_c , and the dc-link voltage V_{dc} ; V_{dc} goes into the controller of voltage regulation loop, which is regulated to reach the reference V_{dc}^* , during this process the active power reference p^* is generated; p^* and the preset reactive power reference q^* are transformed in to current references i_d^* and i_q^* ; the three-phase grid voltage is put into PLL to obtain the voltage vector phase angle θ , which is used to transform the three-phase grid current to (d, q) SRF; the controller of current tracking loop drive i_d and i_q to i_d^* and i_q^* , respectively, during this process the control signals u_d and u_q are generated; u_d and u_q are transformed back to three-phase control signals u_a , u_b and u_b , which are put into the PWM module to make the converter switches take actions.

Based on Fig. 2.3, the overall control diagram is designed, as shown in Fig. 2.4. The voltage regulation loop regulates the dc-link voltage V_{dc} to the reference V_{dc}^* , and is composed of a forward-path controller and a disturbance observer, the controller output signal μ_{dc} and the observer output signal \hat{d} are combined together to form the total control output u , which is actually the active power reference p^* . p^* , q^* , together with grid voltages v_d , v_q are put into the current tracking loop, which generates current references i_d^* , i_q^* ; the current tracking loop adopts two parallel controller to respectively drive the grid currents i_d , i_q to their references i_d^* , i_q^* , and outputs the control signals μ_d , μ_q , which are decoupled via ωL to obtain the final control signals u_d , u_q , i.e., the duty cycle.

Consider the advantage of super twisting algorithm, in this chapter it is adopted by the controller. VOC mode is adopted, i.e., the voltage regulation loop as outer loop, the current tracking loop as inner loop. Both the outer loop and inner loop adopt the super-twisting SMC. To improve the disturbance rejection ability of the outer loop, the disturbance observer is added into the outer loop.

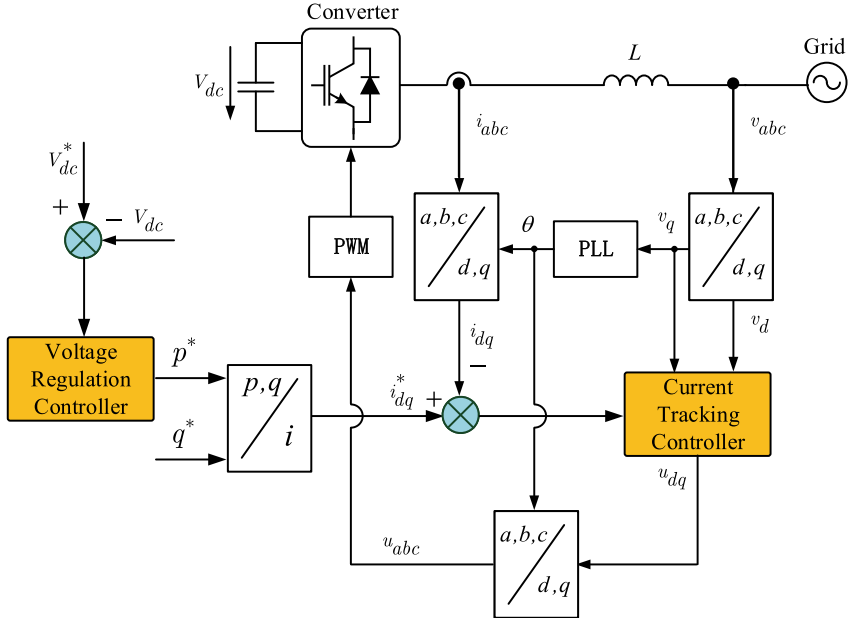


Fig. 2.3 Control process of three-phase two-level power converter

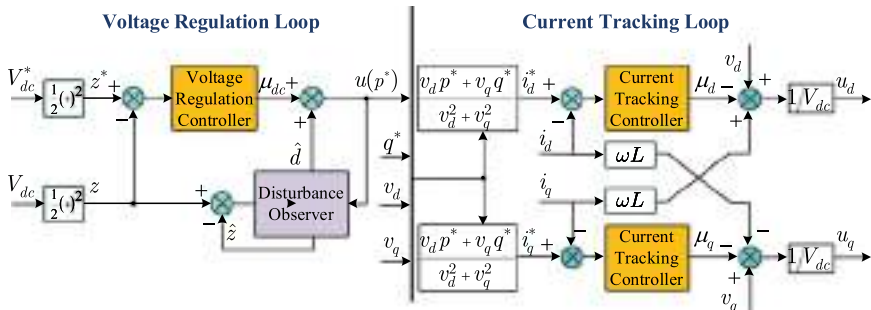


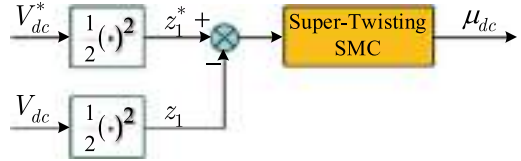
Fig. 2.4 Overall control diagram of three-phase two-level power converter

2.2.1 Voltage Regulation Loop

To demonstrate the advantage of the adoption of disturbance observer, the structure of the voltage regulation loop without disturbance observer is firstly introduced here, as shown in Fig. 2.5. The voltage error is regulated by the super-twisting SMC controller, and the control signal is generated.

Based on Eq. 2.11, the dynamic of the dc-link voltage can be written as:

Fig. 2.5 Voltage regulation loop without disturbance observer



$$C \frac{dV_{dc}}{dt} = \frac{1}{V_{dc}} (p^* - p_{load}), \quad (2.16)$$

where $p^* = v_d i_d^* + v_q i_q^*$, $p_{load} = V_{dc} i_{load}$. Define $(V_{dc}^*)^2 / 2 = z_1^*$, $V_{dc}^2 / 2 = z_1$, $p^* = \mu_{dc}$ as control signal, and $p_{load} = d$ as external disturbance. Obviously, regulating V_{dc} is equal to regulating z_1 . The load power p_{load} can influence the dc-link voltage V_{dc} , and appears as a disturbance to the voltage regulation loop. Equation 2.16 can be written as:

$$C \dot{z}_1 = \mu_{dc} - d, \quad (2.17)$$

Therefore, the super-twisting SMC controller is designed as [7]:

$$\mu_{dc} = \lambda_{vdc} |e_v|^{\frac{1}{2}} \text{sign}(e_v) + \alpha_{vdc} \int_0^t \text{sign}(e_v) dt, \quad (2.18)$$

where $e_v = z_1^* - z_1$.

2.2.2 Observer Design

As shown in Fig. 2.6, a disturbance observer is added in the voltage regulation loop. The disturbance observer estimates the external disturbance d , then estimated disturbance \hat{d} is compensated to the control signal μ_{vdc} , and the control signal after compensation is:

$$u = \mu_{dc} + \hat{d}. \quad (2.19)$$

According to Eq. (2.17), the dynamics of z_1 can be rewritten as:

$$C \dot{z}_1 = u - d. \quad (2.20)$$

In order to the performance of different type of observer, four different type of observers are designed, i.e., linear disturbance observer, sliding mode observer, linear extended state observer, and nonlinear extended state observer. The detailed forms of the observers are as follow:

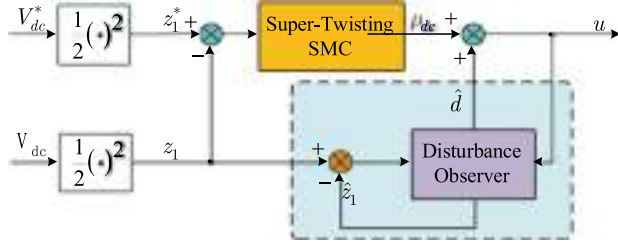


Fig. 2.6 Voltage regulation loop with disturbance observer

(1) Linear disturbance observer

Design a linear disturbance observer (LDO) as:

$$\begin{cases} C\dot{\hat{z}}_1 = u + \beta e_1, \\ e_1 = z_1 - \hat{z}_1, \end{cases} \quad (2.21)$$

where \hat{z}_1 is the estimated value of z_1 . Combining Eqs. (2.20) and (2.21), the dynamic of observation error can be written as:

$$C\dot{e}_1 = -\beta e_1 - d. \quad (2.22)$$

Considering that the load disturbance d is a slow-varying signal, \hat{z}_1 would converge to z_1 with a steady-state error, i.e.,

$$\dot{e}_1 = 0, \quad (2.23)$$

therefore the estimated disturbance value \hat{d} can be calculated as:

$$\hat{d} = -\beta e_1. \quad (2.24)$$

(2) Second-order sliding mode observer

Adopting the concept of designing SMC, a sliding mode observer (SMO) is designed as:

$$\begin{cases} C\dot{\hat{z}}_1 = u + (\lambda_1|e_1|^{\frac{1}{2}}\text{sign}(e_1) + \alpha_1 \int_0^t \text{sign}(e_1) dt), \\ e_1 = z_1 - \hat{z}_1. \end{cases} \quad (2.25)$$

Then the dynamic of observation error can be written as:

$$C\dot{e}_1 = -(\lambda_1|e_1|^{\frac{1}{2}}\text{sign}(e_1) + \alpha_1 \int_0^t \text{sign}(e_1) dt) - d. \quad (2.26)$$

Similar to the above linear observer, taking into account the derivative of observation error in steady state is $\dot{e}_1 = 0$, the external disturbance can be calculated as:

$$\hat{d} = -(\lambda_1 |e_1|^{\frac{1}{2}} \operatorname{sign}(e_1) + \alpha_1 \int_0^t \operatorname{sign}(e_1) dt). \quad (2.27)$$

(3) Linear extended state observer

Following the design process of extended state observer, and taking the external disturbance as an extended state z_2 , the linear extended state observer (LESO) is designed as:

$$\begin{cases} C\dot{\hat{z}}_1 = u - \hat{z}_2 + \beta_1 e_1, \\ \dot{\hat{z}}_2 = -\beta_2 e_1, \\ e_1 = z_1 - \hat{z}_1, \end{cases} \quad (2.28)$$

where \hat{z}_2 is the estimated value of z_2 . Then the dynamic of observation error can be written as:

$$\begin{cases} C\dot{e}_1 = -e_2 - \beta_1 e_1, \\ \dot{e}_2 = h(t) + \beta_2 e_1, \end{cases} \quad (2.29)$$

where

$$\begin{cases} h(t) = \dot{z}_2, \\ e_2 = z_2 - \hat{z}_2. \end{cases} \quad (2.30)$$

Thus the estimated disturbance is:

$$\hat{d} = \hat{z}_2. \quad (2.31)$$

It should be noted that, to ensure the observation error to converge to the equilibrium, the observer parameters β_1 and β_2 must satisfy that the matrix $\begin{bmatrix} -\beta_1/C & -1/C \\ \beta_2 & 0 \end{bmatrix}$ is Hurwitz.

(4) Nonlinear extended state observer

Also take the external disturbance as an extended state z_2 , but design a nonlinear extended state observer (NESO) as:

$$\begin{cases} C\dot{\hat{z}}_1 = u - \hat{z}_2 + \beta_{01} fal_1, \\ \dot{\hat{z}}_2 = -\beta_{02} fal_2, \\ e_1 = z_1 - \hat{z}_1, \end{cases} \quad (2.32)$$

where

$$fal_i(e_1, \alpha_i, \delta) = \begin{cases} |e_1|^{\alpha_i} \operatorname{sign}(e_1), & |e_1| > \delta_i, i \in (1, 2), \\ e_1 / \delta_i^{1-\alpha_i}, & |e_1| \leq \delta_i, i \in (1, 2). \end{cases} \quad (2.33)$$

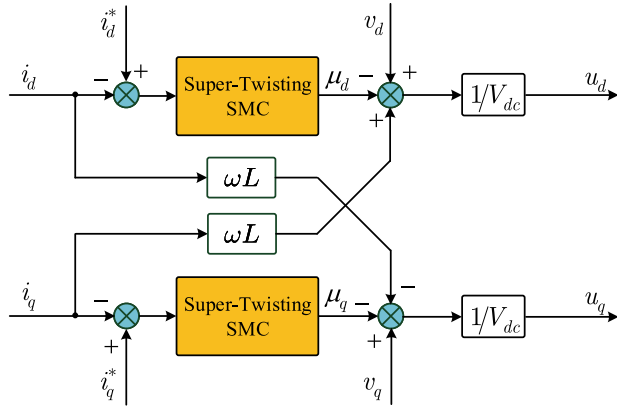


Fig. 2.7 Current tracking loop

Then the dynamic of observation error is

$$\begin{cases} C\dot{e}_1 = -e_2 - \beta_{01}f\alpha l_1, \\ \dot{e}_2 = h(t) + \beta_{02}f\alpha l_2, \end{cases} \quad (2.34)$$

where $h(t)$ and e_2 are the same as defined in Eq. 2.30. Therefore the estimated disturbance \hat{d} is

$$\hat{d} = \hat{z}_2. \quad (2.35)$$

2.2.3 Current Tracking Loop

Figure 2.7 is the current tracking loop based on super-twisting SMC. As can be seen, this chapter adopts the current mode (2.9) and (2.10) in (d, q) SRF. Because the dynamic of the currents are coupled, a decoupled control is necessary.

As mentioned before, the current references are generated by the current tracking loop as follow:

$$i_d^* = \frac{v_d p^* + v_q q^*}{v_d^2 + v_q^2}, \quad i_q^* = \frac{v_q p^* + v_d q^*}{v_d^2 + v_q^2}. \quad (2.36)$$

Further define the error signals of the two axes as:

$$e_{dq} = \begin{bmatrix} e_d \\ e_q \end{bmatrix} = \begin{bmatrix} i_d^* - i_d \\ i_q^* - i_q \end{bmatrix}. \quad (2.37)$$

Therefore the super-twisting SMC controllers of the current tracking loop are designed as [8]:

Table 2.1 System parameters

Parameter	Value	Description
f_s	10	Sampling Rate (kHz)
f_c	10	Control update Rate (kHz)
R_L	100	Load Resistance (Ω)
C	3300	DC Output Capacitor (μF)
L	2.6	Phase Inductor (mH)
f	50	Grid frequency (Hz)
v_{abc}	400	Grid line voltage (V)
V_{dc}^*	750	Capacitor Voltage reference (V)

$$\mu_d = \lambda_d |e_d|^{\frac{1}{2}} \operatorname{sign}(e_d) + \alpha_d \int_0^t \operatorname{sign}(e_d) dt, \quad (2.38)$$

$$\mu_q = \lambda_q |e_q|^{\frac{1}{2}} \operatorname{sign}(e_q) + \alpha_q \int_0^t \operatorname{sign}(e_q) dt. \quad (2.39)$$

Considering Eqs. (2.9) and (2.10), the final output control signals are:

$$u_d = \frac{1}{V_{dc}} (-\mu_d + v_d + \omega L i_q), \quad (2.40)$$

$$u_q = \frac{1}{V_{dc}} (-\mu_q + v_q - \omega L i_d). \quad (2.41)$$

2.3 Simulation Verification

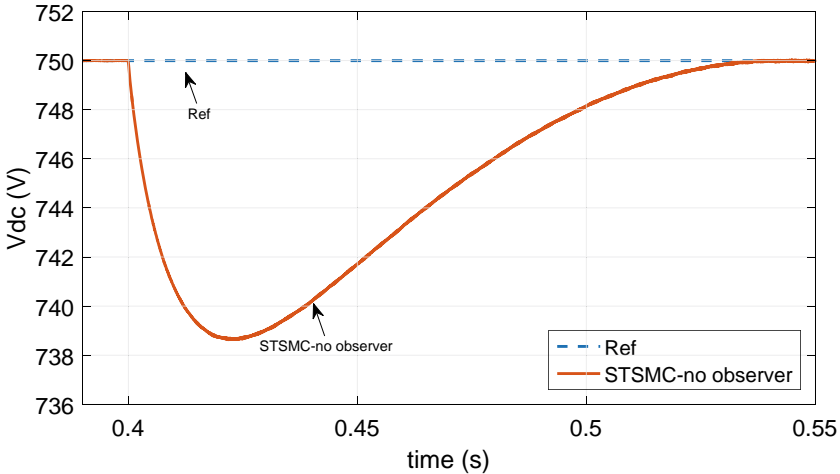
In this section, simulations are carried out to verify the effectiveness of the different type of the disturbance observers and analyze their influence on the control performance. Table 2.1 shows the system parameters for the simulation. The load disturbance is of resistive type, and is connected to the converter dc-link at the time of $t = 0.4$ s, which causes a step disturbance to the system. The reactive current reference i_q^* is set to 0 A to achieve unity power factor.

(1) Super-twisting SMC without observer

To demonstrate the effectiveness of adopting disturbance observer, the control performance of voltage regulation loop with sliding mode control with no observer. The parameters of the super-twisting SMC controller are adjusted to make the converter obtain good dc-link voltage transient response and low current THD. Table 2.2 shows the adopted parameter. Figure 2.8 shows the transient response of dc-link voltage, and the obtained current THD is 2.04%.

Table 2.2 Parameters of super-twisting SMC without observer

Current tracking loop	Voltage regulation loop
$\lambda_d = 20, \alpha_d = 150$	$\lambda_{vdc} = 50, \alpha_{vdc} = 4 * 10^4$
$\lambda_q = 20, \alpha_q = 150$	

**Fig. 2.8** DC-link voltage transient response of super-twisting SMC without observer**Table 2.3** Parameters of super-twisting SMC with observers

Current tracking loop	Voltage regulation loop
$\lambda_d = 20, \alpha_d = 150$	$\lambda_{vdc} = 15, \alpha_{vdc} = 100$
$\lambda_q = 20, \alpha_q = 150$	

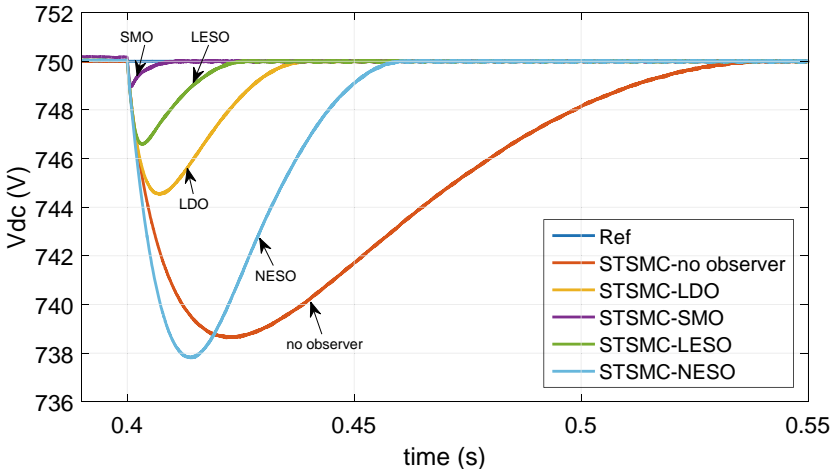
(2) Super-twisting SMC with observers

In this subsection, four different types of disturbance observer are employed to compensate the super-twisting sliding mode controller, to compare their performances. To ensure a fair comparison, the parameters of the super-twisting sliding mode controller are kept the same when working with the observers, and the parameters of the observers are adjusted to make the converter obtain similar steady state performance, i.e., almost the same dc-link voltage steady state error and current THD. The parameters of the super-twisting sliding mode controller and the disturbance observers are shown respectively in Tables 2.3 and 2.4.

Figure 2.9 shows the dc-link voltage transient response with different observers. Figure 2.10 shows that the dc-link voltage steady state errors resulted from the observers are all within 0.05 V. From Fig. 2.9, it can be seen that after the load disturbance is imposed on the system, the second-order SMO obtains better performance than the other three observers, the dc-link voltage drop is only 1 V, and the recover-

Table 2.4 Parameters of observers

LDO	SMO	LESO	NESO
$\beta = 0.8$	$\lambda_1 = 200$	$\beta_1 = 6.6$	$\beta_{01} = 40$
	$\alpha_1 = 200$	$\beta_2 = 3300$	$\beta_{02} = 33000$
			$\alpha_1 = 1$
			$\alpha_2 = 0.5$
			$\delta_1 = \delta_2 = 0.01$

**Fig. 2.9** DC-link voltage transient responses of super-twisting SMC with observers

ing time is 0.01 s; the LESO obtains the second best performance, with 3.4 V dc-link voltage drop and 0.025 s recovering time; the linear observer obtains the third best performance, with 5.5 V dc-link voltage drop and 0.04 s recovering time; the NESO comes up in the forth place, with 12.2 V dc-link voltage drop and 0.06 s recovering time.

For comparison, the result of sliding mode control without observer is also shown in Fig. 2.9, whose dc-voltage drop is similar with that obtained by the NESO. However, with the compensation of NESO, the gains of the super-twisting sliding mode controller and the current THD both decreases significantly. This shows that disturbance observer indeed is capable of improving the performance of the controller.

Due to the reason that this chapter focus on the voltage regulation loop, the current tracking loop remains the same despite which disturbance observer is adopted. Simulation results show that the current tracking performance with different observers keeps the same. Figures 2.11, 2.12 and 2.13 respectively show the tracking performance of i_d , i_q , and grid current under second-order SMO. It can be seen that, the d -axis and q -axis in SRF are tracked, and the grid current waveform is sinusoidal.

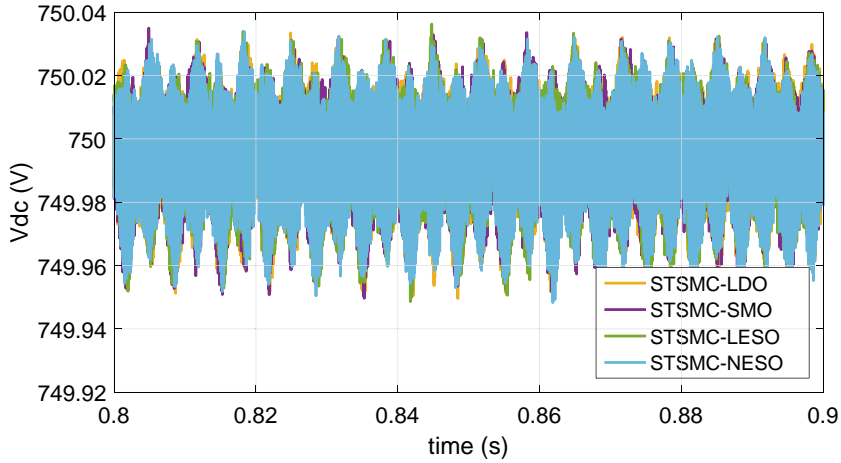


Fig. 2.10 DC-link voltage steady errors of super-twisting SMC with observers

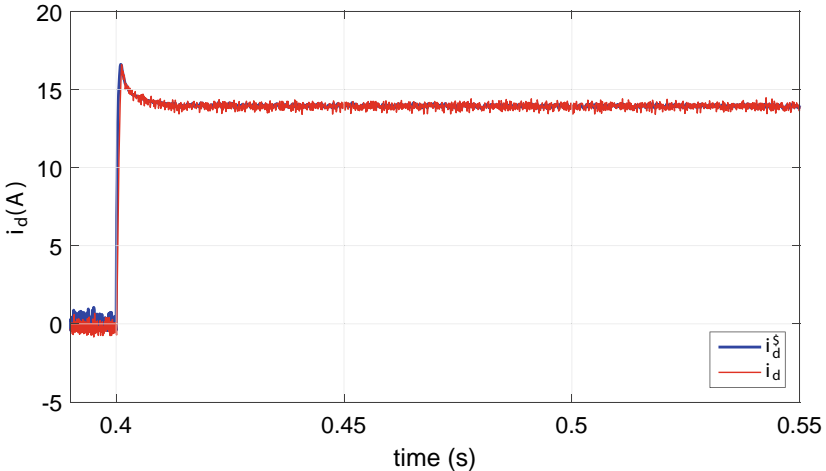


Fig. 2.11 i_d tracking performance

Table 2.5 THD Value of different observers

LDO (%)	SMO (%)	LESO (%)	NESO (%)
0.80	0.80	0.80	0.79

Table 2.5 shows that with the compensation of different observers, the obtained current THD of the converter is almost the same, around 0.80%. Furthermore, the simulation shows that the current harmonic spectrum with different observers are also similar.

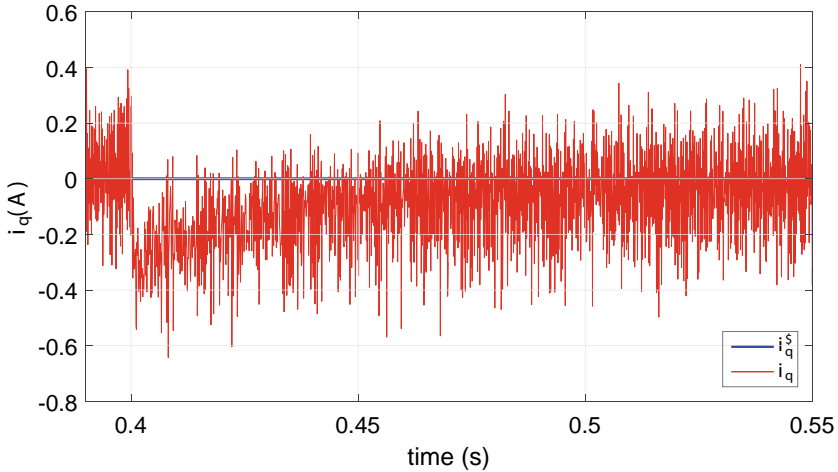


Fig. 2.12 i_q tracking performance

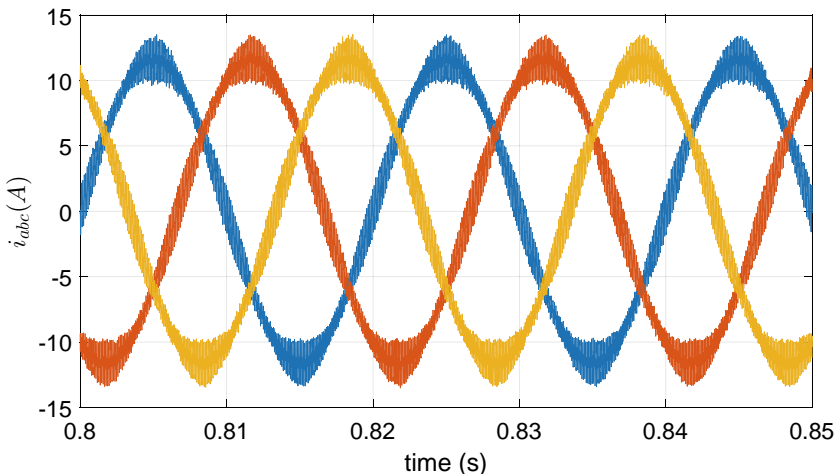


Fig. 2.13 Obtained grid current wave

2.4 Summary

In this chapter, the disturbance observer based sliding mode control strategy is proposed to carry out the current tracking and voltage regulation for three-phase two-level power converter. The voltage regulation loop employs disturbance observer to compensate the super twisting sliding mode controller. The current tracking loop adopts two super-twisting SMC controllers to respectively track the d -axis and q -axis currents. Four different disturbance observers are designed for comparison, including

linear observer, sliding mode observer, linear extended state observer and nonlinear extended state observer. The controllers in current tracking loop remains the same with different observers. The simulation results show that, (1) disturbance observer can not only significantly improve the dc-link voltage transient performance, also can it reduce the current THD; (2) when compensating the super-twisting sliding mode controller, on the condition of obtaining the same dc-link voltage steady state error and current THD, the second-order SMO obtains better disturbance rejection performance than other observers.

References

1. Thounthong, P.: Control of a three-level boost converter based on a differential flatness approach for fuel cell vehicle applications. *IEEE Trans. Veh. Technol.* **61**(3), 1467–1472 (2012)
2. Pan, C.T., Chen, T.C.: Modelling and analysis of a three phase PWM AC-DC convertor without current sensor. *IEE Proc. Electr. Power Appl.* **140**(3), 201–208 (1993)
3. Leon, J.I., Kouro, S., Franquelo, L.G., Rodriguez, J., Wu, B.: The essential role and the continuous evolution of modulation techniques for voltage-source inverters in the past, present, and future power electronics. *IEEE Trans. Industr. Electron.* **63**(5), 2688–2701 (2016)
4. Blasko, V., Kaura, V.: A new mathematical model and control of a three-phase AC-DC voltage source converter. *IEEE Trans. Power Electron.* **12**(1), 116–123 (1997)
5. Vazquez, S., Sanchez, J.A., Reyes, M.R., Leon, J.I., Carrasco, J.M.: Adaptive vectorial filter for grid synchronization of power converters under unbalanced and/or distorted grid conditions. *IEEE Trans. Industr. Electron.* **61**(3), 1355–1367 (2013)
6. Chung, S.K.: A phase tracking system for three phase utility interface inverters. *IEEE Trans. Power Electron.* **15**(3), 431–438 (2000)
7. Levant, A.: Higher-order sliding modes, differentiation and output-feedback control. *Int. J. Control* **76**(9–10), 924–941 (2003)
8. Liu, J., Vazquez, S., Wu, L., Marquez, A., Gao, H., Franquelo, L.G.: Extended state observer-based sliding-mode control for three-phase power converters. *IEEE Trans. Industr. Electron.* **64**(1), 22–31 (2016)

Chapter 3

Proportional-Integral Control of Three-Phase Two-Level Converters



Abstract In Chap. 2, four different types of disturbance observer have been proposed for voltage regulation of a grid-connected power converter. With similar other conditions, the linear disturbance observer (LDO) obtains a relatively good disturbance rejection performance. It is of ease use as there is only one parameter to be adjusted. However, due to this reason, the only way to speed up the observation of the disturbance is to increase this parameter, which leads to severer current THD level in steady state. To solve this problem, this chapter proposes an improved LDO, which has following characteristics:

- Comparing with the LDO in Chap. 2, the proposed LDO has two parameters to adjust its behaviors, one is to improve the system's transient response while not influence the steady state performance, the other is to maintain system's steady state performance. For the converters which are disturbed by external load from time to time, this characteristic is advantageous, due to the reason that the recovering time for the system after being disturbed can be shortened with one parameter, while the grid current THD level in steady state can be maintained low by limiting the other parameter.
- Comparing with nonlinear disturbance observer, LDO maintains the simplicity of the system, which makes the system analysis easier and more convenient for practical engineering use.

In this chapter, the LDO based PI control is proposed to regulate the dc-link voltage of three-phase two-level power converter. The LDO estimates the dc-link load and feeds the estimated value the PI controller in the voltage regulation loop, so as to improve the disturbance rejection ability of the PI controller. The reason of adopting PI control in the voltage regulation loop is to make the loop as a pure linear system, in which way the classical control theory can be used to do the system analysis and parameter tuning. The current tracking loop adopts the conventional SRF-PI control.

This chapter first theoretically analyzes the closed-loop system of voltage regulation loop, which proves that LDO-PI strategy is more effective and advantageous than conventional PI control. Then experiments are carried out on a 5 kW grid-connected power converter, to verify the correctness of the theoretical deduction and converter's

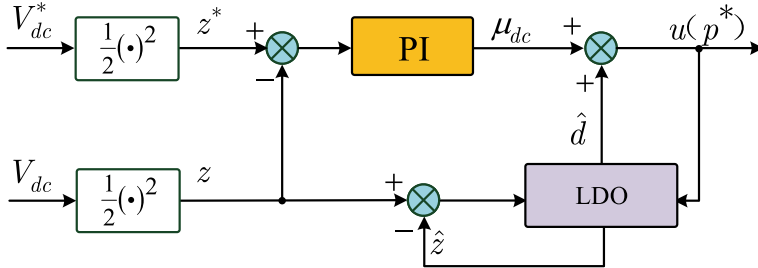


Fig. 3.1 Voltage regulation loop: PI control based on LDO

performance in real application. The experiment results show that, the proposed control strategy can improve the system's transient performance while keep a low current THD level in steady state.

3.1 Control Scheme

Same as in Chap. 2, this chapter adopts VOC mode, i.e., the double loop control consisting of voltage regulation loop and current tracking loop. As mentioned before, this chapter focuses on the observer design for the voltage regulation loop, thus all the controllers in the control loops adopts the PI control most applied in industry.

3.1.1 Voltage Regulation Loop

Figure 3.1 is the control structure of the voltage regulation loop, which consists of a conventional PI controller and an LDO. μ_{dc} is the control output of PI controller, \hat{d} is the estimated external disturbance generated by the LDO, u is the final control output of the voltage regulation loop. Combining (2.16) and (2.17) in Chap. 2 and relative definitions, the dynamic equation of voltage regulation loop can be obtained as:

$$C\dot{z} = u - d = \mu_{dc} + \hat{d} - d, \quad (3.1)$$

where

$$\mu_{dc} = K_{pv}e_z + K_{iv} \int_0^t e_z dt, \quad (3.2)$$

and $e_z = z^* - z$.

3.1.2 Observer Design

To actively reject the impact of dc-link load disturbance, the improved LDO is designed as follows:

$$C\dot{\hat{z}} = K_{ldo}(u + \beta\hat{e}_z), \quad (3.3)$$

$$\hat{e}_z = z - \hat{z}, \quad (3.4)$$

where \hat{z} is the estimated value of z , β and K_{ldo} are observer parameters and $K_{ldo} \geq 1$. Thus the dynamic of observation error can be written as:

$$C\dot{\hat{e}}_z = (1 - K_{ldo})u - K_{ldo}\beta\hat{e}_z - d. \quad (3.5)$$

Considering the load disturbance d is slow-varying, $\dot{\hat{e}}_z = 0$ in steady state, it is obtained that:

$$\beta\hat{e}_z = ((1 - K_{ldo})u - d)/(K_{ldo}). \quad (3.6)$$

From (3.1), it can be seen that when z enters steady state, the final control signal u equals to the load power d , therefore (3.6) changes into $\beta\hat{e}_z = -d$. Based on this fact, the external disturbance can be estimated with following equation:

$$\hat{d} = -\beta\hat{e}_z. \quad (3.7)$$

Until now, the estimated value of external disturbance is obtained and can be compensated to the control signal μ_{dc} generated by the PI controller.

Remark 3.1 It should be noted that, $\dot{\hat{e}}_z = 0$ means that both z and \hat{z} reach their steady state, thus during the transient process of z , the estimated disturbance \hat{d} can approach but can not achieve the actual disturbance d . Therefore, to ensure sufficient compensation to the controller during transient process, the dynamic of \hat{z} needs to be accelerated to provide faster observation of the load. From above analysis, K_{ldo} only affects the observer bandwidth during transient process, while β affects the bandwidth both during transient process and in steady state. Thus, the dynamic of \hat{z} can be accelerated by increasing K_{ldo} or β , or both. ♦

3.1.3 Current Tracking Loop

As mentioned previously, the target of this chapter is to investigate the performance improvement that the disturbance observer can bring to the voltage regulation loop, thus the conventional SRF-PI control is employed in the current tracking loop, which is shown in Fig. 3.2. μ_d and μ_q are the PI control signals to respectively control the d -axis and q -axis current, and the detailed forms are as follow:

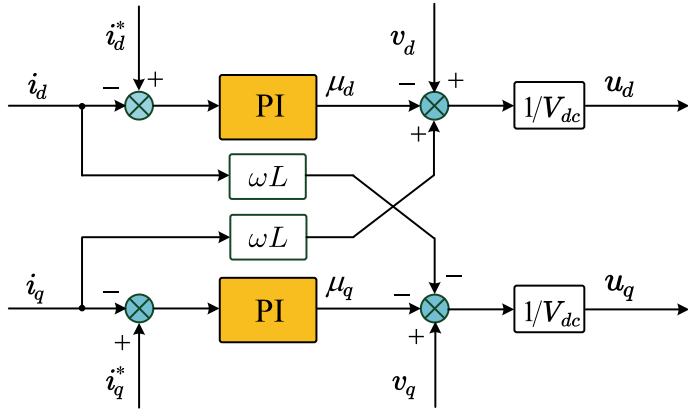


Fig. 3.2 Current tracking loop: PI control

$$\mu_d = K_{pId}e_{id} + K_{iId} \int_0^t e_{id} dt, \quad (3.8)$$

$$\mu_q = K_{pIq}e_{iq} + K_{iIq} \int_0^t e_{iq} dt, \quad (3.9)$$

where

$$e_{id} = i_d^* - i_d, \quad (3.10)$$

$$e_{iq} = i_q^* - i_q. \quad (3.11)$$

Therefore, based on (2.9) and (2.10), the final control signals u_d and u_q are obtained as:

$$u_d = \frac{1}{V_{dc}} (-\mu_d + v_d + \omega L i_q), \quad (3.12)$$

$$u_q = \frac{1}{V_{dc}} (-\mu_q + v_q - \omega L i_d). \quad (3.13)$$

3.1.4 Voltage Loop Analysis

Now that the disturbance observer has been designed, the whole-closed-loop-system analysis of the voltage regulation loop can be carried out, which is to be done via state-space equations to reveal its internal characteristics. Combining the dynamic equations of the PI controller and the LDO, the whole voltage regulation closed loop system can be represented as a three-order model, as follows:

$$\dot{x} = Ax + B\dot{d}, \quad (3.14)$$

where $x = [x_1 \ x_2 \ x_3]^T = [\int e_z dt \ e_z \ e_d]^T$, $e_d = d - \hat{d}$ is the disturbance observation error,

$$A = \begin{bmatrix} 0 & 1 & 0 \\ -\frac{1}{C}K_{iv} & -\frac{1}{C}K_{pv} & \frac{1}{C} \\ K_{lumped}K_{iv} & K_{lumped}K_{pv} & -\frac{\beta}{C} \end{bmatrix},$$

$B = [0 \ 0 \ 1]^T$, $K_{lumped} = \frac{\beta}{C}(1 - K_{ldo})$. Therefore the control target is to make $x = 0$, which means that the dc-link voltage reaches its reference, also the external load is estimated accurately.

The deduction of (3.14) is as follows: according to definition, $\dot{x}_1 = x_2$, considering (3.1)–(3.2),

$$\dot{x}_2 = \dot{e}_z = -\frac{1}{C}(K_{pv}x_2 + K_{iv}x_1 - x_3). \quad (3.15)$$

Then to calculate \dot{x}_3 , with definition, it follows that

$$x_3 = e_d = d - \hat{d} = d + \beta\hat{e}_z,$$

thus

$$\dot{x}_3 = \dot{d} + \beta\dot{\hat{e}}_z = \dot{d} + \frac{\beta}{C}C\dot{\hat{e}}_z, \quad (3.16)$$

considering (3.5),

$$\begin{aligned} C\dot{\hat{e}}_z &= (1 - K_{ldo})(\mu_{dc} + \hat{d}) + K_{ldo}\hat{d} - d \\ &= (1 - K_{ldo})\mu_{dc} - e_d, \end{aligned} \quad (3.17)$$

then (3.16) can be rewritten as

$$\begin{aligned} \dot{x}_3 &= \dot{d} + \frac{\beta}{C}[(1 - K_{ldo})\mu_{dc} - e_d] \\ &= -\frac{\beta}{C}e_d + \frac{\beta}{C}(1 - K_{ldo})\mu_{dc} + \dot{d} \\ &= -\frac{\beta}{C}x_3 + \frac{\beta}{C}(1 - K_{ldo})(K_{pv}x_2 + K_{iv}x_1) + \dot{d}. \end{aligned} \quad (3.18)$$

Then the system state-space Eq. (3.14) is obtained.

From (3.14), it can be seen that, when $K_{ldo} > 1$, the dynamic of x_3 is dependent on $x_i\{i=1,2\}$, and the coefficients contains the parameters of both observer and controller. Therefore, there is interaction between $x_i\{i=1,2\}$ and x_3 , consequently

mutually speed up their convergence. This is due to two reasons: (1) $x_i \{i=1,2\}$ are put into the PI controller which generate a negative feedback to make them converge; (2) they are also put into the LDO to generate an output which is also a negative feedback, and further accelerate their convergence.

On the other hand, comparing with $K_{ldo} = 1$, $K_{ldo} > 1$ also accelerate the dynamic of x_3 , as shown below: when $K_{ldo} = 1$, (3.3) changes into

$$C\dot{\hat{z}} = u + \beta\hat{e}_z, \quad (3.19)$$

then the system state space equation becomes

$$A_1 = \begin{bmatrix} 0 & 1 & 0 \\ -\frac{1}{C}K_{iv} & -\frac{1}{C}K_{pv} & \frac{1}{C} \\ 0 & 0 & -\frac{\beta}{C} \end{bmatrix}.$$

It can be seen that, in this case the dynamic of x_3 is only affected by itself, $x_i \{i = 1, 2\}$ has no influence on x_3 , as a result the dynamic of x_3 slows down. Furthermore, the disturbance observer can only compensate the controller with slowed x_3 , not possible via $x_i \{i = 1, 2\}$, which causes the converging speed of $x_i \{i = 1, 2\}$ to also slow down.

More importantly, as mentioned before, to make the observer better compensate the controller during transient process, the dynamic of \hat{z} needs to be accelerated. However, when $K_{ldo} = 1$, the only way to accelerate \hat{z} dynamic is to increase β , which causes the steady state bandwidth to increase, and leads to severer current THD. Therefore, to accelerate \hat{z} dynamic during transient process, the best way is to increase K_{ldo} , that is, make $K_{ldo} > 1$.

Now test the system state response with different values of K_{ldo} under different load level. The plant parameters are set to $R_L = \{180 \Omega, 120 \Omega, 240 \Omega\}$, $C = 3400 (\mu F)$. The controller and observer parameters are set to $K_{pv} = 0.06$, $K_{iv} = 0.2$, $\beta = 0.02$, $K_{ldo} = \{20, 40, 80\}$. Figure 3.3 shows how state response changes when K_{ldo} increases, with a specified load $R_L = 180 \Omega$, and K_{ldo} is set to $\{20, 40, 80\}$. It can be seen that the larger K_{ldo} is, the faster the state converges. Figure 3.4 shows how state response changes when load increases, with a specified $K_{ldo} = 40$, and $R_L = \{180 \Omega, 120 \Omega, 240 \Omega\}$. It can be seen that the larger R_L is, the faster the state converges.

Remark 3.2 The reason why LDO-PI is more capable of rejecting disturbance than PI is that, the disturbance observer monitors the load disturbance in real time, when load changes, the disturbance observer can track it and compensated the estimated value to the forward-path controller. In contrast, conventional PI controller can not predict load disturbance, and only can generate the control force after the disturbance imposes an impact on the system reference. Therefore, adding disturbance observer enables a pre-control over the disturbance, and a direct attenuation over the influence caused by it, not as conventional PI control, which passively accepts the disturbance impact and takes control action afterwards. ♦

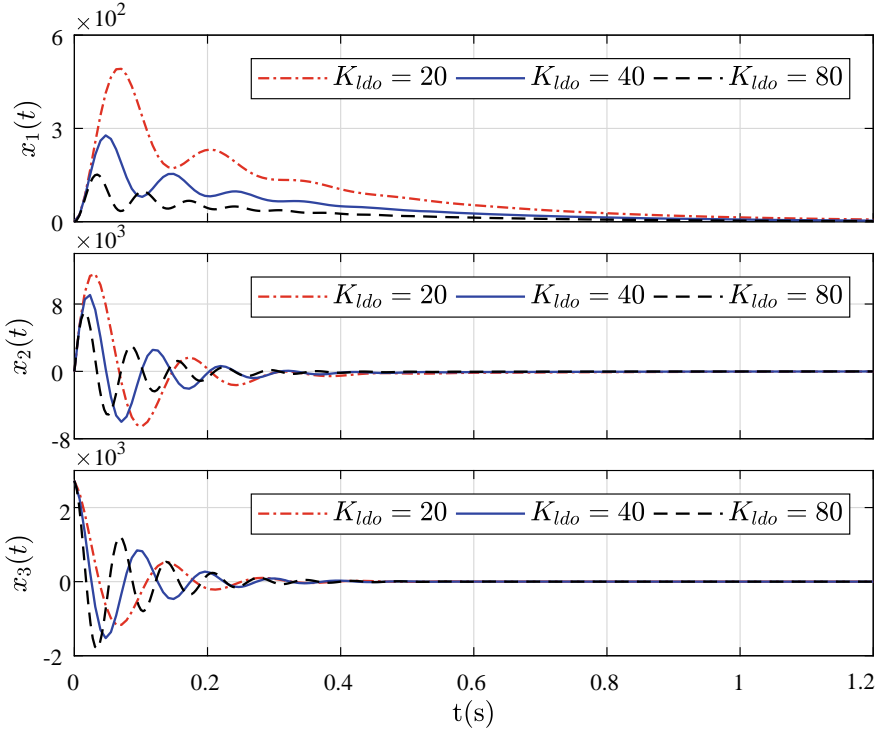


Fig. 3.3 State response with different observer gains

3.2 Experiment Verification

Previous section theoretically proves that LDO-PI obtains better control performance than PI. In this section, experiments are carried out to verify the effectiveness of LDO-PI in real application.

(1) Experiment setup and control parameters

Figure 3.5 is the experiment hardware setup, including a 5kW grid-connected three-phase two-level power converter, a control cabinet, load resistors and measurement instruments such as oscillators, power quality analyzer. The control algorithm is executed by digital signal processor TMS320F28335.

Figures 3.6 and 3.7 are the grid voltage waveform and the harmonic spectrum, which show that there exists certain level of distortion and unbalance in grid voltage. This shall influence the resulted current distortion, due to that there is no compensation strategy considered in current tracking loop.

Table 3.1 is the system parameters, which shows that three load resistors and two dc-link capacitors are used to provide different load cases. The load disturbance type is resistive, and the load resistor shall be abruptly connected to the dc-link at a random

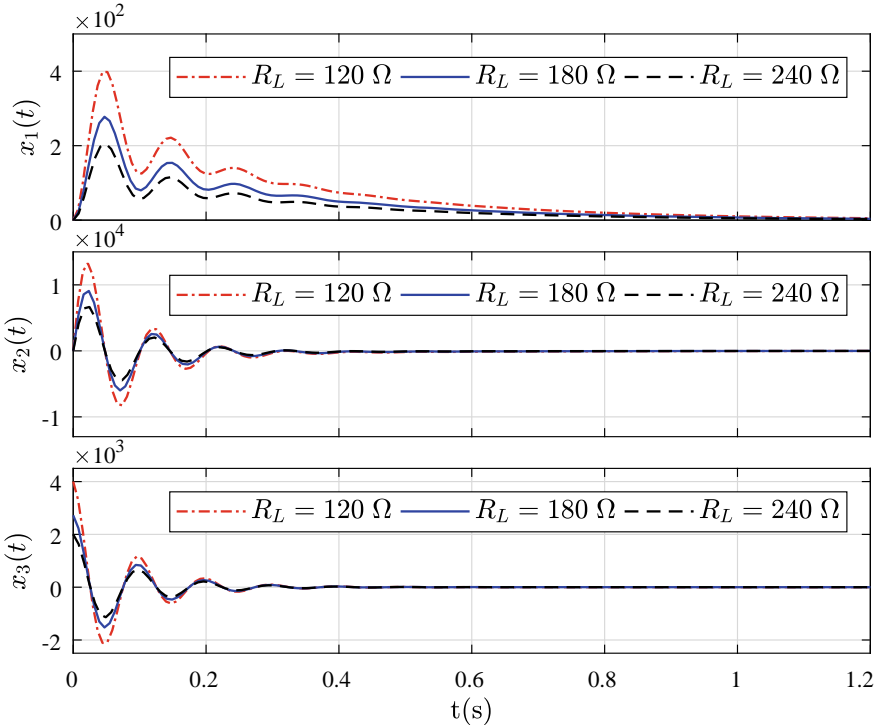


Fig. 3.4 State response under different loads

Table 3.1 System parameters

Parameter	Value	Description
f_s	20	Sampling rate (kHz)
f_{sw}	10	Switching rate (kHz)
R_L	{180, 120, 240}	Load resistance (Ω)
C	{3400, 1700}	DC-Link capacitor (μF)
L	15	Phase inductor (mH)
f	50	Grid frequency (Hz)
v_{abc}	400	Grid line voltage (V)
V_{dc}^*	700	DC-Link voltage Ref. (V)

time, to create a load step. The reactive power reference is set to 0 VAr to achieve unity power factor.

Table 3.2 is the controller parameter, which is tuned according to a nominal load case, i.e., $R_L = 180 \Omega$, $C = 3400 \mu\text{F}$. Setting a nominal load case is reasonable since a nominal operating point needs to be set when designing a power system.

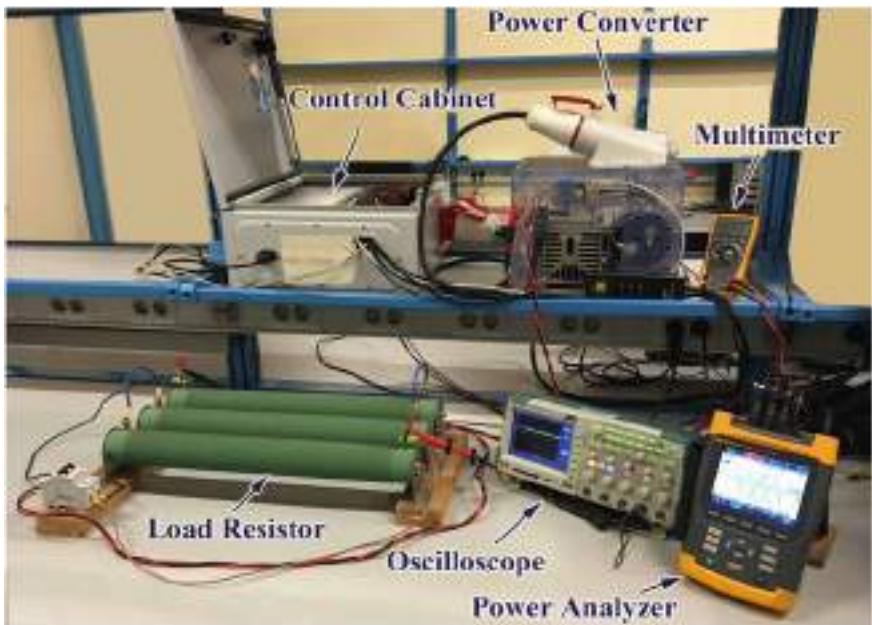


Fig. 3.5 Experiment setup

Fig. 3.6 Grid voltage waveform

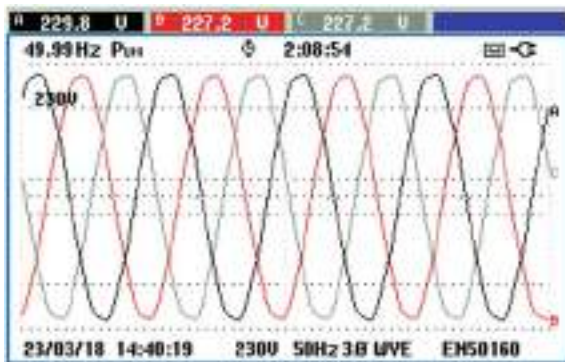


Table 3.2 Control parameters

Current loop conventional PI	Voltage loop proposed strategy	
$K_{pId} = 15$	$K_{pv} = 0.06$	$K_{pv} = 0.06$
$K_{iId} = 400$	$K_{iv} = 0.8$	$K_{iv} = 0.2$
$K_{pIq} = 15$		$\beta = 0.02$
$K_{iIq} = 400$		$K_{ldo} = \{20, 40, 80\}$

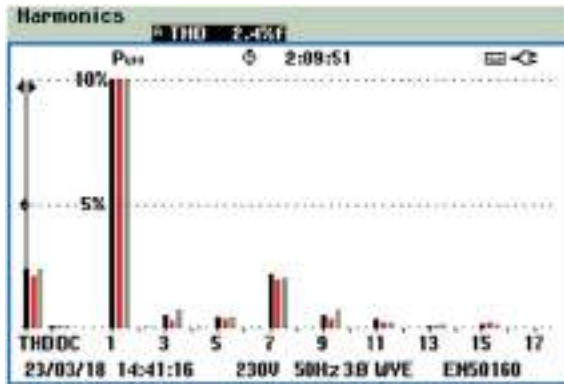


Fig. 3.7 Grid voltage harmonic spectrum

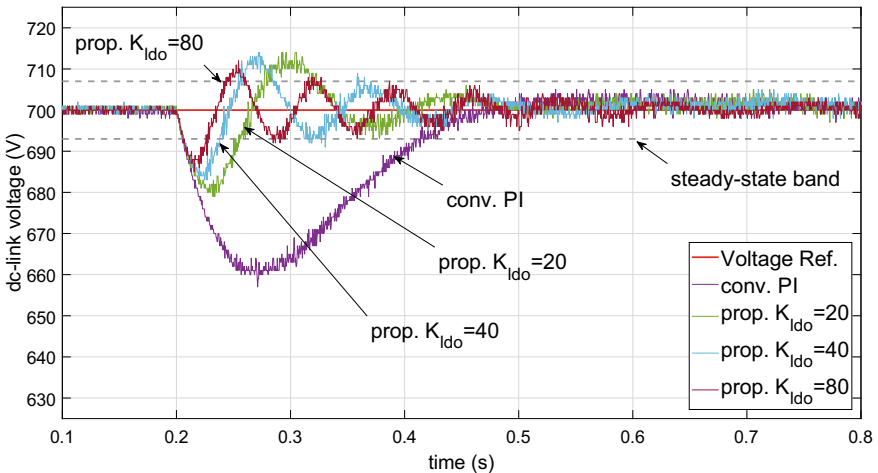


Fig. 3.8 V_{dc} response of nominal load case

(2) Experiment result analysis

(1) Nominal load case ($R_L = 180 \Omega$, $C = 3400 \mu F$)

The load power in nominal case is of middle level, around 2.7 kW.

Figure 3.8 is the dc-link voltage transient response, including LDO-PI strategy ($K_{lido} = 20, 40, 80$) and conventional PI control. It can be seen that, no matter which of the three values K_{lido} takes, the converter obtains better performance with LDO-PI. After the load is connected, comparing with conventional PI, LDO-PI can obtain smaller dc-link voltage drop and less transient time (the transient time here refers to that the dc-link voltage enters a steady-state zone, i.e., reference $\pm 1\%$). With the observer working, the system transient performance is improved significantly, both the voltage drop and the transient time have been reduced by more than half.

Fig. 3.9 Obtained current harmonic spectrum with nominal case: LDO-PI

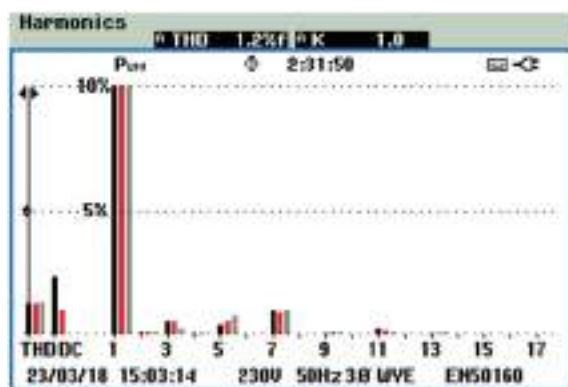
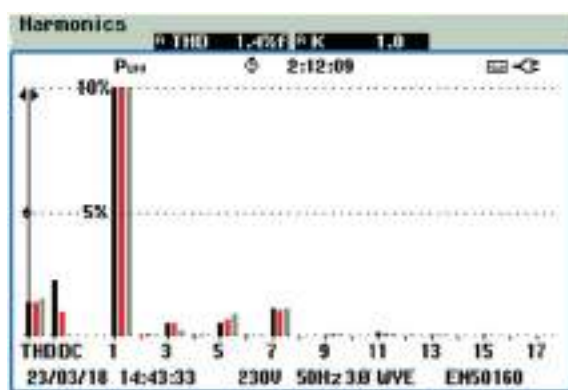


Fig. 3.10 Obtained current harmonic spectrum with nominal case: conv. PI



In the meantime, the current THD with LDO-PI is similar with that of conventional PI. More importantly, it can be noticed that the larger K_{ldo} is, the faster the transient process is, which is consistent with the theoretical analysis in previous section. Figures 3.9 and 3.10 respectively show the grid current harmonic spectrum of LDO-PI ($K_{ldo} = 80$) and conventional PI. It can be seen that LDO-PI maintains the similar harmonic spectrum and THD level. $K_{ldo} = 20$ and $K_{ldo} = 40$ lead to similar harmonic results, and are omitted here.

(2) Small capacitor case ($R_L = 180 \Omega$, $C = 1700 \mu\text{F}$)

Consider that in real application, the dc-link capacitance shall vary. In this case, the dc-link capacitance is reduced to half of the nominal case, to test the robustness of LDO-PI against the capacitance variation.

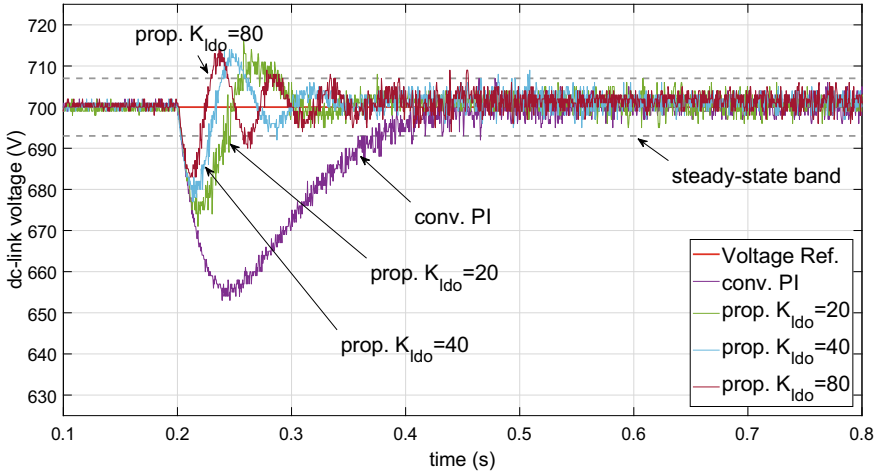


Fig. 3.11 V_{dc} response of nominal load with reduced capacitor

As shown in Fig. 3.11, the experiment results in this case is consistent with that in the nominal case. LDO-PI presents obvious advantage over conventional PI during the dc-link voltage transient process, i.e., the voltage drop and the transient time have been reduced by more than half, meanwhile maintains low current THD level. The current harmonic spectrum in this case is similar with that in nominal case, and is omitted.

The above results show that LDO-PI is robust against large scale variation of dc-link capacitance.

More importantly, comparing Figs. 3.8 and 3.11, it can be seen that, the dc-link voltage transient response of LDO-PI in small capacitor case is still much better than that of PI in nominal case, in terms of much smaller voltage drop and less transient time. It can be concluded that, even the capacitance of dc-link capacitor reduces largely, LDO-PI can still obtain much better performance than conventional PI. Therefore, if LDO-PI is adopted, the converter can operate with smaller dc-link capacitor, and consequently reduces cost, volume and weight of converter.

(3) Large load case ($R_L = 120 \Omega$, $C = \{3400, 1700\} \mu\text{F}$)

As mentioned previously, in real application the load disturbance may vary in large scale. This subsection tests the performance of LDO-PI when the external load is larger than the nominal case, and load power is raised to around 4 kW.

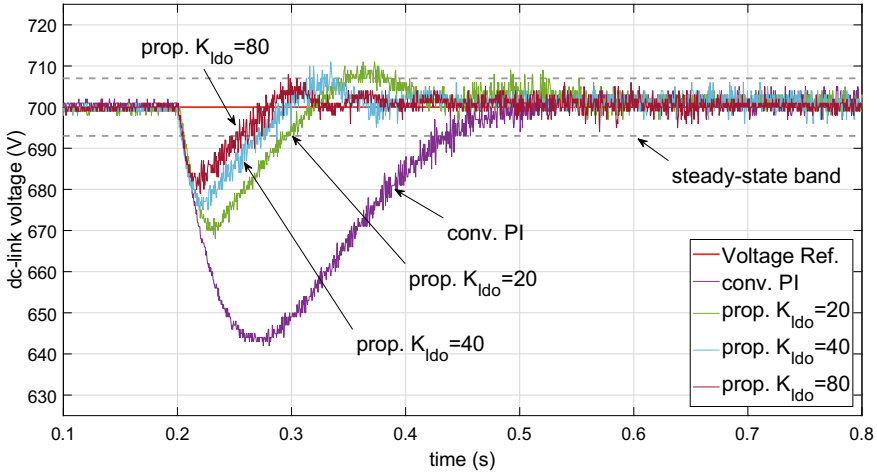


Fig. 3.12 V_{dc} response of large load case

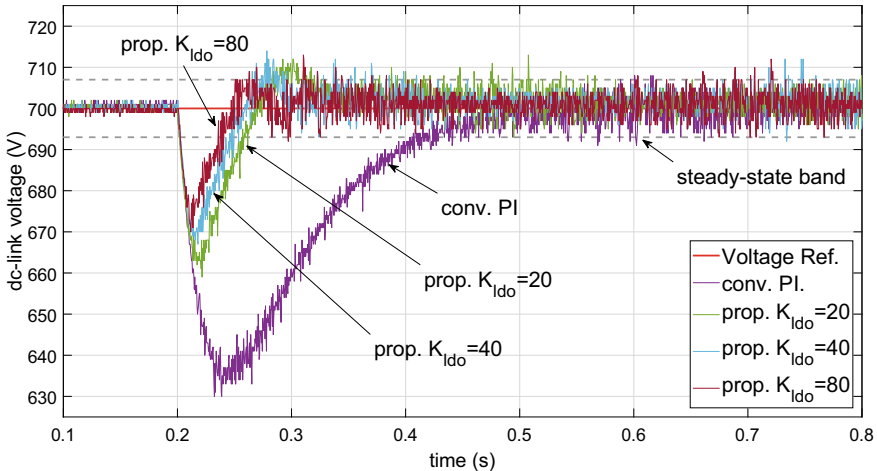


Fig. 3.13 V_{dc} response of large load with reduced capacitor

As shown in Figs. 3.12 and 3.13, LDO-PI maintains the control performance in large load case, and demonstrates an obvious performance improvement than conventional PI. Comparing with nominal load case, the voltage transient response is slower due to the increase of electrical inertia. In this load case, the resulted current THD levels from LDO-PI and conventional PI are similar, around 1.2%, also the obtained harmonic spectrum is similar with that in nominal load case, thus it is omitted.

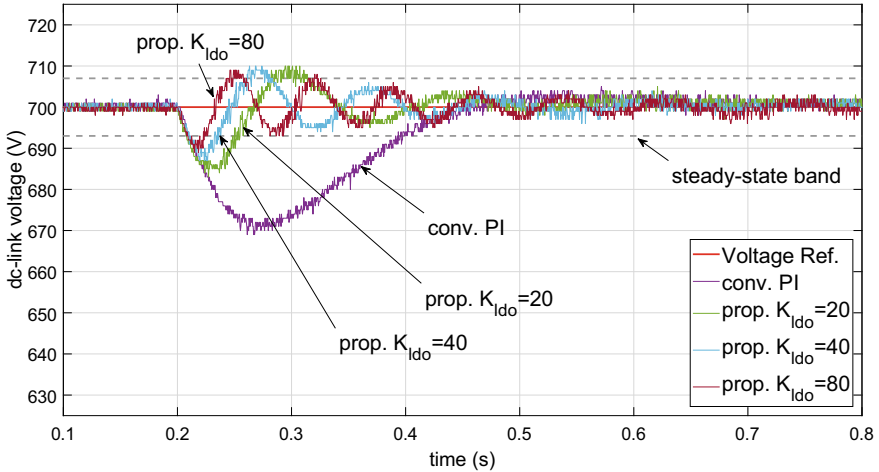


Fig. 3.14 V_{dc} response of small load case

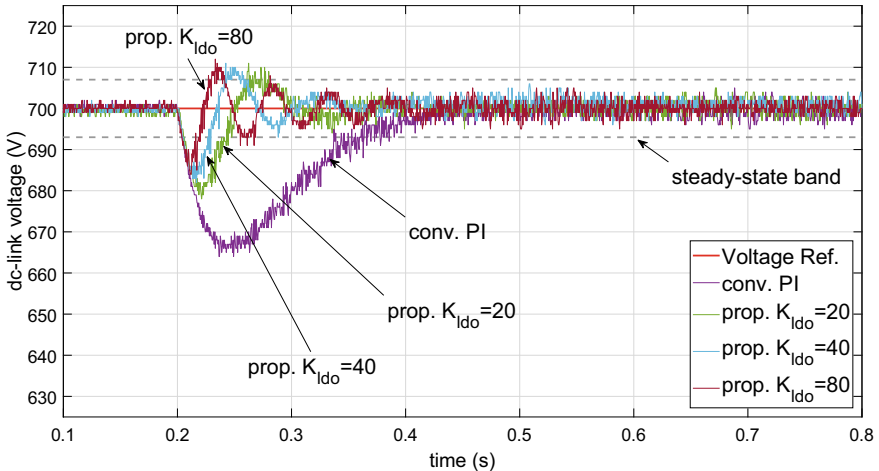


Fig. 3.15 V_{dc} response of small load with reduced capacitor

(4) Small load case ($R_L = 240 \Omega$, $C = \{3400, 1700\} \mu F$)

In real application, the load disturbance may also be smaller than the nominal load. This subsection tests the performance of LDO-PI when the external load is smaller than the nominal case, and load power is raised to around 2 kW.

Figures 3.14 and 3.15 show that LDO-PI also maintains the control performance in small load case.

The experiment results are summarized in Tables 3.3 and 3.4.

Table 3.3 Summary of experiment results with nominal capacitor

$R_L = 180 \Omega$	$C = 3400 \mu\text{F}$ (nominal case)			
	V_{dc} drop (V)	V_{dc} overshoot (V)	Transient time (ms)	Current THD (%)
conv. PI	41	0	260	1.4
$K_{ldo} = 20$	21	13	190	1.4
$K_{ldo} = 40$	18	12	120	1.5
$K_{ldo} = 80$	15	10	70	1.2
$R_L = 120 \Omega$	$C = 3400 \mu\text{F}$			
	V_{dc} drop (V)	V_{dc} overshoot (V)	Transient time (ms)	Current THD (%)
conv. PI	58	0	280	1.1
$K_{ldo} = 20$	31	10	200	1.2
$K_{ldo} = 40$	25	8	140	1.2
$K_{ldo} = 80$	20	6	80	1.2
$R_L = 240 \Omega$	$C = 3400 \mu\text{F}$			
	V_{dc} drop (V)	V_{dc} overshoot (V)	Transient time (ms)	Current THD (%)
conv. PI	32	0	250	1.6
$K_{ldo} = 20$	16	10	120	1.5
$K_{ldo} = 40$	14	10	100	1.6
$K_{ldo} = 80$	11	9	60	1.3

3.3 Summary

This chapter investigates the dc-link voltage regulation problem of grid-connected three-phase two-level power converter. In voltage regulation loop, an improved linear disturbance observer (LDO) is designed, which estimates the external disturbance and compensate the estimated value to the PI controller. After the expression of LDO is obtained, a whole-closed-loop system analysis is carried out for the voltage regulation loop, which theoretically verifies the effectiveness and advantage of LDO-PI. Comparing with the linear observer in Chap. 2, the proposed LDO in this chapter has two parameters, one is to maintain steady state THD, the other is to ensure better transient response. The closed-loop model composed of controller and observer has been established, based on which the stability and state response of the system is analyzed. It can be seen that, as long as $K_{ldo} \geq 1$, the system is stable, and with the increase of K_{ldo} and decrease of load disturbance, the system response speeds up. To test the control performance of LDO-PI in real application, experiments have been carried out on a 5kVA grid-connected power converter. Three different load resistors and two different dc-link capacitors have been used to create different load cases, to test the robustness of LDO-PI. The theoretical analysis and experiment results show that: (1) LDO-PI is robust against the variation in the load and the dc-link capacitor;

Table 3.4 Summary of experiment results with small capacitor

$R_L = 180 \Omega$	$C = 1700 \mu\text{F}$			
	V_{dc} drop (V)	V_{dc} overshoot (V)	Transient time (ms)	Current THD (%)
conv. PI	48	0	220	1.3
$K_{ldo} = 20$	26	16	100	1.3
$K_{ldo} = 40$	23	14	80	1.3
$K_{ldo} = 80$	18	14	60	1.3
$R_L = 120 \Omega$	$C = 1700 \mu\text{F}$			
	V_{dc} drop (V)	V_{dc} overshoot (V)	Transient time (ms)	Current THD (%)
conv. PI	67	0	260	1.1
$K_{ldo} = 20$	40	13	120	1.1
$K_{ldo} = 40$	33	13	100	1.2
$K_{ldo} = 80$	29	10	60	1.1
$R_L = 240 \Omega$	$C = 1700 \mu\text{F}$			
	V_{dc} drop (V)	V_{dc} overshoot (V)	Transient time (ms)	Current THD (%)
conv. PI	35	0	200	1.4
$K_{ldo} = 20$	22	9	80	1.6
$K_{ldo} = 40$	18	11	70	1.6
$K_{ldo} = 80$	16	11	60	1.5

(2) LDO-PI has a big advantage over conventional PI; (3) the larger the observer parameters, the faster the transient process, meanwhile maintains the steady state current THD level; (4) LDO-PI can obtain better performance with smaller capacitor than conventional PI with larger capacitor, if LDO-PI is adopted, the converter can operate with smaller dc-link capacitor, and consequently reduces cost, volume and weight of the converter.

Chapter 4

State Estimation and Control of Three-Phase Two-Level Converters via Sliding Mode



Abstract From the simulation results in Chap. 2, it can be seen that the second-order sliding mode observer (SMO) obtains the best disturbance observation, and offers the best compensation for the sliding mode controller. However, it has similar shortcoming as the linear observer in Chap. 2, i.e., if it needs to accelerate the observation speed, the observer parameters need to be increased, which leads to severer current THD level in steady state. Therefore, following the method in Chap. 3, an improved SMO is proposed in this chapter, which has following characteristics:

- Comparing with the SMO in Chap. 2, the improved SMO has one more tuning parameter, which is used to improve the system's transient response while not influence the steady state performance, while the original two parameters are used to maintain system's steady state performance. In this way, the transient time of the system after it is disturbed can be shortened and the grid current THD level can be kept low.
- Comparing with the improved LDO in Chap. 3, this improved nonlinear SMO has faster converging speed and stronger robustness against system uncertainties.

In this chapter, a sliding mode control strategy based on the improved SMO is proposed to regulate the dc-link voltage of three-phase two-level power converter. In the voltage regulation loop, the improved SMO compensates the adopted sliding mode control. The SMO has similar characteristics as the LDO in Chap. 3, in that it has parameters to tune the transient process and the performance of steady state. Comparing with linear observer, the SMO converges faster and is more robust. The SMO is used to estimates the dc-link load that is abruptly connected and causes voltage fluctuation. The estimated value is used to compensate the controller in the voltage regulation loop, thus the voltage regulation loop obtains stronger robustness against external disturbances, so that the disturbing impact from the load can be greatly reduced. This chapter first proves the stability of voltage regulation loop under SMO-SMC control, via Lyapunov method. Then the effectiveness and advantage of the proposed control strategy is verified via simulation. Afterwards, experiments are carried out on a 5 kW grid-connected power converter. The experiment results show that, comparing with conventional PI control, the proposed SMO-SMC control strategy significantly improves control performance of the voltage regulation loop,

and results in stronger robustness against the operating point variation caused by the changes in external load and dc-link capacitance.

4.1 Control Scheme

Same as in Chap. 3, the cascaded VOC is adopted. Figure 4.1 is the control structure of the voltage regulation loop. Unlike Chap. 3, the controller adopted in this chapter is the ST sliding mode controller, and the observer employs the improved SMO. This chapter focuses on the improvement of voltage control performance, therefore the current tracking loop adopts the conventional PI controller.

4.1.1 Voltage Regulation Loop

As shown in Fig. 4.1, the voltage regulator includes two parts, i.e., the ST sliding mode controller in the forward-path and the SMO employed to estimate the external disturbance. μ_{dc} is the output signal of the ST sliding mode controller, \hat{d} is the output signal of SMO, and u is the final control signal. Same as in Chap. 3, combining (2.16), (2.17) and relevant definitions, the dynamic equation of the voltage regulation loop can be obtained as follows:

$$C\dot{z} = u - d = \mu_{dc} + \hat{d} - d, \quad (4.1)$$

where μ_{dc} is the output signal of the ST sliding mode controller, \hat{d} is the estimated disturbance from SMO. Define the voltage error as follows:

$$e = z^* - z, \quad (4.2)$$

and the ST sliding mode controller can be designed as [1]:

$$\mu_{dc} = \beta_c |e|^{\frac{1}{2}} \text{sign}(e) + \omega_c \int_0^t \text{sign}(e) dt. \quad (4.3)$$

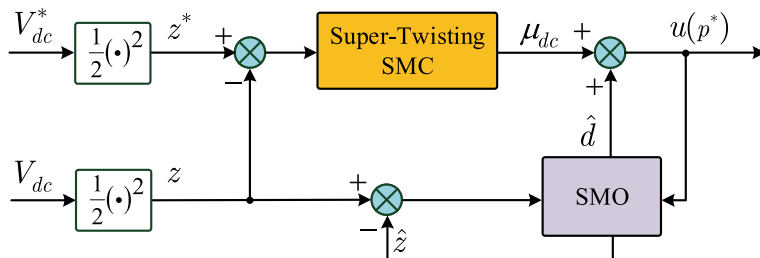


Fig. 4.1 Voltage regulation loop: super-twisting SMC based on SMO

4.1.2 Observer Design

Design the SMO as follows:

$$\begin{cases} C\dot{\hat{z}} = K_o(u + f(\hat{e})), \\ \hat{e} = z - \hat{z}, \end{cases} \quad (4.4)$$

where \hat{z} is the estimated value of z , \hat{e} is the estimation error, K_o is defined as external parameter of SMO, $f(\hat{e})$ is the observer correcting item, which adopts the following form of second-order sliding mode algorithm:

$$f(\hat{e}) = \beta_o |\hat{e}|^{\frac{1}{2}} \operatorname{sign}(\hat{e}) + \omega_o \int_0^t \operatorname{sign}(\hat{e}) dt, \quad (4.5)$$

where β_o and ω_o are defined as internal observer parameters. It can be seen that, the observer dynamic is decided together by K_o , β_o and ω_o . The observer dynamic can be accelerated by increasing any of them.

Therefore the dynamic of observation error can be written as:

$$C\dot{\hat{e}} = (1 - K_o)u - K_o f(\hat{e}) - d. \quad (4.6)$$

According to (4.4), \hat{z} will converge to z , resulting that $\hat{e} = 0$ and $\dot{\hat{e}} = 0$. Based on (4.1), $u = d$ stands in steady state. Therefore, it can be seen that $d = -f(\hat{e})$ in steady state. Considering these facts, the external disturbance is estimated as follows:

$$\hat{d} = -f(\hat{e}). \quad (4.7)$$

Remark 4.1 The (4.7) shows that the estimated disturbance only depends on β_o and ω_o . Considering that in steady state, \hat{d} is the main contributor to the control signal u , thus for the same β_o and ω_o , the current THD level is the same. The aim of introducing K_o is to speed up the dynamic of \hat{z} , i.e., the larger K_o , the faster z is estimated accurately, hence the disturbance is estimated faster, consequently the system convergence is accelerated. The advantage of this observer is that, K_o can be used to speed up the transient process, while β_o and ω_o can be set to small value to maintain low current THD level. ♦

4.1.3 Voltage Loop Analysis

The stability analysis consists of two parts, i.e., the controller stability analysis and the disturbance observer stability analysis.

(1) Controller stability analysis

Assume that z^* is constant, according to (4.1)–(4.2), the error dynamic of the controller can be written as:

$$C\dot{e} = -\mu_{dc} - \hat{d} + d, \quad (4.8)$$

with (4.3), this can be further rewritten as:

$$\begin{aligned} C\dot{e}_1 &= -\beta_c |e_1|^{\frac{1}{2}} \text{sign}(e_1) + e_2, \\ \dot{e}_2 &= -\omega_c \text{sign}(e_1) + h(t), \end{aligned} \quad (4.9)$$

where $h(t) = \dot{d} - \hat{d}$, which is assumed to be bounded, i.e., $|h(t)| \leq \Omega$

Remark 4.2 This assumption is based on two points: (1) \dot{d} is bounded because the load can only vary continuously due to the existence of the dc-link capacitor; (2) $\dot{\hat{d}}$ is also bounded because the observer states will converge to the equilibrium in finite time, which will be proved later. It is worth mentioning that, as finite time convergence is assured, the separation principle is applicable, i.e., the respective convergence of controller and observer can ensure the convergence of the whole system. ♦

Theorem 4.3 If $|h(t)| \leq \Omega$ and the controller parameters satisfy

$$\beta_c > 0, \quad \omega_c > 3\Omega + 2 \left(\frac{\Omega}{\beta_c} \right)^2, \quad (4.10)$$

the controller state can converge to the equilibrium in finite time, and the converging time is no more than $T = \frac{2V^{\frac{1}{2}}(e_0)}{\gamma}$ unit time, where e_0 is the initial state of the controller, $\gamma = \frac{\beta_{\min}^{\frac{1}{2}}\{P\} \min\{\beta_{\min}\{\bar{Q}_1\}, \beta_{\min}\{\bar{Q}_2\}\}}{\beta_{\max}\{P\}}$, where

$$P = \frac{1}{2} \begin{bmatrix} 4\omega_c + \beta_c^2 - \beta_c & \\ -\beta_c & 2 \end{bmatrix},$$

$$\begin{aligned} \bar{Q}_1 &= \frac{\beta_c}{2} \begin{bmatrix} 2\omega_c + \beta_c^2 - 2\Omega - \beta_c - \frac{2\Omega}{\beta_c} & \\ -\beta_c - \frac{2\Omega}{\beta_c} & 1 \end{bmatrix}, \\ \bar{Q}_2 &= \frac{\beta_c}{2} \begin{bmatrix} 2\omega_c + \beta_c^2 - 2\Omega - \beta_c + \frac{2\Omega}{\beta_c} & \\ -\beta_c + \frac{2\Omega}{\beta_c} & 1 \end{bmatrix}. \end{aligned}$$

Proof Construct following Lyapunov function for system (4.9):

$$V(e) = 2\omega_c|e_1| + \frac{1}{2}e_2^2 + \frac{1}{2}(\beta_c|e_1|^{\frac{1}{2}}\text{sign}(e_1) - e_2)^2.$$

Define $\xi^T = [|e_1|^{\frac{1}{2}}\text{sign}(e_1), e_2]$, then $V(e) = \xi^T P \xi$. It should be noted that $V(e)$ is continuous but not differentiable at $e_1 = 0$, but following relation holds:

$$\beta_{\min}\{P\}\|\xi\|_2^2 \leq V(e) \leq \beta_{\max}\{P\}\|\xi\|_2^2,$$

where $\beta_{\min}\{P\}$ and $\beta_{\max}\{P\}$ respectively present the minimum and maximum value of the matrix P . $\|\xi\|_2^2 = |e_1| + e_2^2$ is the Euclidean norm of ξ . Thus the derivative of V is:

$$\dot{V} = -\frac{1}{|e_1|^{\frac{1}{2}}}\xi^T Q \xi + h(t)q^T \xi,$$

where

$$Q = \frac{\beta_c}{2} \begin{bmatrix} 2\omega_c + \beta_c^2 & -\beta_c \\ -\beta_c & 1 \end{bmatrix}, \quad q = \begin{bmatrix} -\beta_c \\ 2 \end{bmatrix}.$$

It can be obtained that:

$$h(t)q^T \xi \leq \max\left\{\frac{1}{|e_1|^{\frac{1}{2}}}\xi^T Q_{h1} \xi, \frac{1}{|e_1|^{\frac{1}{2}}}\xi^T Q_{h2} \xi\right\},$$

where

$$Q_{h1} = \begin{bmatrix} \beta_c \Omega \Omega & 0 \\ \Omega & 0 \end{bmatrix}, \quad Q_{h2} = \begin{bmatrix} \beta_c \Omega - \Omega & 0 \\ -\Omega & 0 \end{bmatrix}.$$

Therefore,

$$\begin{aligned} \dot{V} &\leq \max\left\{-\frac{1}{|e_1|^{\frac{1}{2}}}\xi^T(Q - Q_{h1})\xi, -\frac{1}{|e_1|^{\frac{1}{2}}}\xi^T(Q - Q_{h2})\xi\right\} \\ &= \max\left\{-\frac{1}{|e_1|^{\frac{1}{2}}}\xi^T \bar{Q}_1 \xi, -\frac{1}{|e_1|^{\frac{1}{2}}}\xi^T \bar{Q}_2 \xi\right\}. \end{aligned}$$

It can be seen that, if $\beta_c > 0$, $\omega_c > 3\Omega + 2(\frac{\Omega}{\beta_c})^2$, then \bar{Q}_1 is positive definite, meanwhile, if $\beta_c > 0$, $\omega_c > -\Omega + 2(\frac{\Omega}{\beta_c})^2$, then \bar{Q}_2 is positive definite. Therefore, if the condition (4.10) is satisfied, \dot{V} is negative definite.

According to the deduction in [2], it can be inferred that the controller state shall converge to the equilibrium with no more than $T = \frac{2V^{\frac{1}{2}}(e_0)}{\gamma}$ unit time, where

$$\gamma = \frac{\beta_{\min}^{\frac{1}{2}}\{P\}\min\{\beta_{\min}\{\bar{Q}_1\}, \beta_{\min}\{\bar{Q}_2\}\}}{\beta_{\max}\{P\}}.$$
■

(2) Observer stability analysis

Combining (4.6) and (4.7), the observation error dynamic can be written as:

$$C\dot{\hat{e}} = (1 - K_o)\mu_{dc} - f(\hat{e}) - d, \quad (4.11)$$

which can be further rewritten as

$$\begin{aligned} C\dot{\hat{e}}_1 &= -\beta_o|\hat{e}_1|^{\frac{1}{2}}\text{sign}(\hat{e}_1) + \hat{e}_2, \\ \dot{\hat{e}}_2 &= -\omega_o\text{sign}(\hat{e}_1) + \hat{h}(t), \end{aligned} \quad (4.12)$$

where $\hat{h}(t) = (1 - K_o)\dot{\mu}_z - \dot{d}$. As analyzed earlier, e will converge in finite time, thus $\dot{\mu}_z$ is bounded, hence $\hat{h}(t)$ has some upper limit $\hat{\Omega}$

Construct following Lyapunov function for system (4.12):

$$\hat{V}(\hat{e}) = 2\omega_c|\hat{e}_1| + \frac{1}{2}\hat{e}_2^2 + \frac{1}{2}(\beta_c|\hat{e}_1|^{\frac{1}{2}}\text{sign}(\hat{e}_1) - \hat{e}_2)^2.$$

Then the derivative of \hat{V} is:

$$\dot{\hat{V}} = -\frac{1}{|\hat{e}_1|^{\frac{1}{2}}}\hat{\xi}^T \hat{Q} \hat{\xi} + \hat{h}(t)\hat{q}^T \hat{\xi},$$

where

$$\hat{Q} = \frac{\beta_o}{2} \begin{bmatrix} 2\omega_o + \beta_o^2 & -\beta_o \\ -\beta_o & 1 \end{bmatrix}, \quad \hat{q} = \begin{bmatrix} -\beta_o \\ 2 \end{bmatrix},$$

it can be obtained that

$$\hat{h}(t)\hat{q}^T \hat{\xi} \leq \max\left\{\frac{1}{|\hat{e}_1|^{\frac{1}{2}}}\hat{\xi}^T \hat{Q}_{h1}\hat{\xi}, \frac{1}{|\hat{e}_1|^{\frac{1}{2}}}\hat{\xi}^T \hat{Q}_{h2}\hat{\xi}\right\},$$

where

$$\hat{Q}_{h1} = \begin{bmatrix} \beta_o\hat{\Omega}\hat{\Omega} & 0 \\ \hat{\Omega} & 0 \end{bmatrix}, \quad \hat{Q}_{h2} = \begin{bmatrix} \beta_o\hat{\Omega}-\hat{\Omega} & 0 \\ -\hat{\Omega} & 0 \end{bmatrix}.$$

therefore

$$\begin{aligned}\dot{\hat{V}} &\leq \max\left\{-\frac{1}{|\hat{e}_1|^{\frac{1}{2}}}\hat{\xi}^T(\hat{Q} - \hat{Q}_{h1})\hat{\xi}, -\frac{1}{|\hat{e}_1|^{\frac{1}{2}}}\hat{\xi}^T(\hat{Q} - \hat{Q}_{h2})\hat{\xi}\right\} \\ &= \max\left\{-\frac{1}{|\hat{e}_1|^{\frac{1}{2}}}\hat{\xi}^T\hat{Q}_1\hat{\xi}, -\frac{1}{|\hat{e}_1|^{\frac{1}{2}}}\hat{\xi}^T\hat{Q}_2\hat{\xi}\right\}.\end{aligned}$$

where

$$\begin{aligned}\hat{Q}_1 &= \frac{\beta_o}{2} \begin{bmatrix} 2\omega_o + \beta_o^2 - 2\hat{\Omega} - \beta_o - \frac{2\hat{\Omega}}{\beta_o} \\ -\beta_o - \frac{2\hat{\Omega}}{\beta_o} \\ 1 \end{bmatrix}, \\ \hat{Q}_2 &= \frac{\beta_o}{2} \begin{bmatrix} 2\omega_o + \beta_o^2 - 2\hat{\Omega} - \beta_o + \frac{2\hat{\Omega}}{\beta_o} \\ -\beta_o + \frac{2\hat{\Omega}}{\beta_o} \\ 1 \end{bmatrix}.\end{aligned}$$

It can be seen that, if $\beta_o > 0$, $\omega_o > 3\hat{\Omega} + 2(\frac{\hat{\Omega}}{\beta_o})^2$, then \hat{Q}_1 is positive definite, meanwhile, if $\beta_o > 0$, $\omega_o > -\hat{\Omega} + 2(\frac{\hat{\Omega}}{\beta_o})^2$, then \hat{Q}_2 is positive definite. Therefore, if it holds that

$$\beta_o > 0, \quad \omega_o > 3\hat{\Omega} + 2\left(\frac{\hat{\Omega}}{\beta_o}\right)^2, \quad (4.13)$$

$\dot{\hat{V}}$ is negative definite, then the observer is stable, and its state can converge to the equilibrium in finite time.

4.1.4 Current Tracking Loop

As mentioned before, this chapter focuses on the dc-link voltage control, thus the conventional SRF-PI control is adopted for the current tracking loop. The control structure is shown in Fig. 3.2, and the control signals are:

$$\begin{cases} u_d = \frac{1}{V_{dc}}(-\mu_d + v_d + \omega L i_q), \\ u_q = \frac{1}{V_{dc}}(-\mu_q + v_q - \omega L i_d), \end{cases} \quad (4.14)$$

$$\text{where } \begin{cases} \mu_d = K_{pI_d} + K_{iI_d} \int_0^t e_d dt \\ \mu_q = K_{pI_q} + K_{iI_q} \int_0^t e_q dt \end{cases} \text{ and } e_{dq} = \begin{bmatrix} e_d \\ e_q \end{bmatrix} = \begin{bmatrix} i_d^* - i_d \\ i_q^* - i_q \end{bmatrix}.$$

4.2 Simulation Verification

The system parameter used in simulation is the same as that of the real system for experiments in next section.

Table 4.1 shows the system parameter of power converter. The dc-link voltage reference V_{dc}^* is set to 700 V, the reactive power reference Q^* is set to 0 kVAr to achieve unity power factor. The load disturbance if of resistive type, three load resistors ($R_L = 180 \Omega$, 120Ω and 240Ω) and two dc-link capacitors ($C = 3400 \mu\text{F}$ and $1700 \mu\text{F}$) are used to provide different operating condition for converter.

Table 4.2 shows the parameters of voltage regulation loop and current tracking loop. To demonstrate the advantage of the SMO-based control strategy, the conventional PI control is used as a baseline. The above control parameters are tuned under a nominal operating condition, i.e., $R_L = 180 \Omega$, $C = 3400 \mu\text{F}$, and they are used to test other operating conditions. For brevity, only the simulation under nominal condition is presented here.

The advantage of SMO-SMC is verified in two aspects: (1) both SMO-SMC and PI operate under nominal condition; (2) PI operates under nominal condition while SMO-SMC operates with smaller dc-link capacitance, i.e., $R_L = 180 \Omega$, $C =$

Table 4.1 System parameters

Parameter	Value	Description
v_{abc}	400	Grid line voltage (V)
f	50	Grid frequency (Hz)
L	15	Phase inductor (mH)
f_{sw}	10	Switching rate (kHz)
f_s	20	Sampling rate (kHz)
V_{dc}^*	700	DC-link voltage reference (V)
Q^*	0	Reactive power reference (kVA)
R_L	{180, 120, 240}	Load resistor (Ω)
C	{3400, 1700}	DC-link capacitor (mF)

Table 4.2 Control parameters

Vol. loop PI	Vol. loop SMO-SMC	Cur. loop
$K_{pv} = 0.06$	$\beta_c = 6$	$K_{pId} = K_{pIq} = 15$
$K_{iv} = 0.8$	$\omega_c = 5$	$K_{iId} = K_{iIq} = 400$
	$K_o = 40$	
	$\beta_o = 10$	
	$\omega_o = 20$	

$1700 \mu\text{F}$. The control performance is demonstrated via the dc-link voltage transient response after a load step disturbance.

(1) Nominal condition

As shown in Fig. 4.2, under nominal condition, SMO-SMC demonstrate obvious advantage over conventional PI, in terms of much smaller voltage drop and shorter transient time.

(2) Small capacitor condition

As can be seen from Fig. 4.3, even dc-link capacitance reduces to half, SMO-SMC still obtains better performance than conventional PI. With this fact, for power converters adopting SMO-SMC, the dc-link capacitor can be reduced without influencing its performance, which reduces its cost, volume and weight.

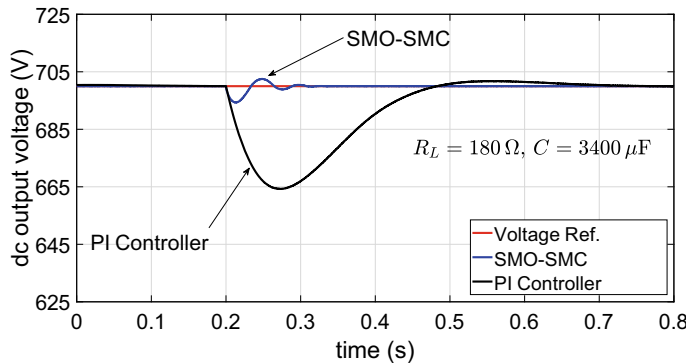


Fig. 4.2 Simulation verification of SMO-SMC: nominal capacitor

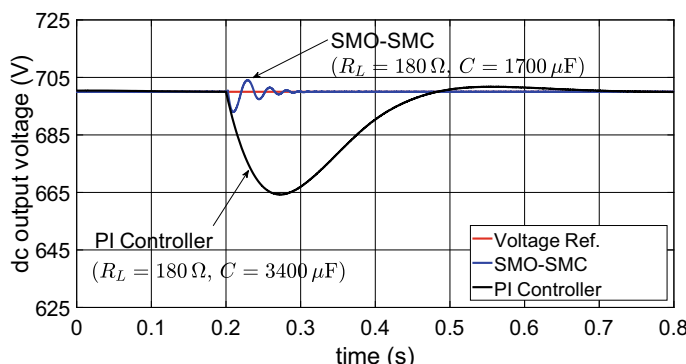


Fig. 4.3 Simulation verification of SMO-SMC: small capacitor

4.3 Experiment Verification

To verify the effectiveness of the proposed SMO-SMC in real application. A series of experiments are performed on a 5 kW grid-connected three-phase two-level power converter. Same as in the simulation section, to demonstrate the advantage of SMO-SMC, the conventional PI control is used as a baseline for comparison. Furthermore, to test the robustness of SMO-SMC, after the experiment under nominal condition, more tests are carried out under other operation conditions.

(1) Experiment setup and control parameters

The experiment hardware is the same as that in Chap. 3, see Fig. 3.5. The parameters of the converter and controller are the same as in previous section, see Tables 4.1 and 4.2. Figures 4.4 and 4.5 are the grid voltage waveform and the harmonic spectrum, which show that there exists certain level of distortion and unbalance in grid voltage. This shall influence the resulted current distortion, due to that there is no compensation strategy considered in current tracking loop.

Fig. 4.4 Grid voltage waveform

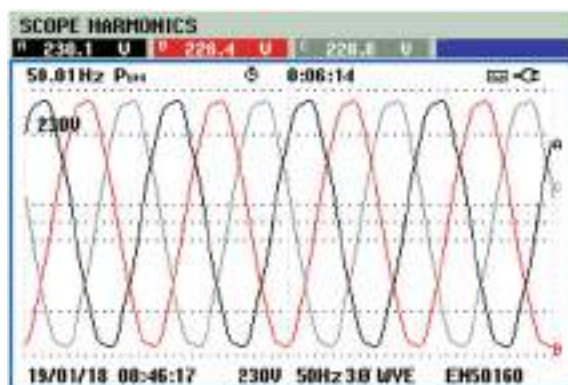
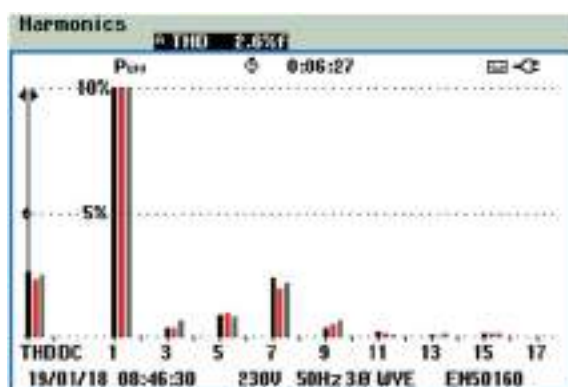


Fig. 4.5 Grid voltage harmonic spectrum



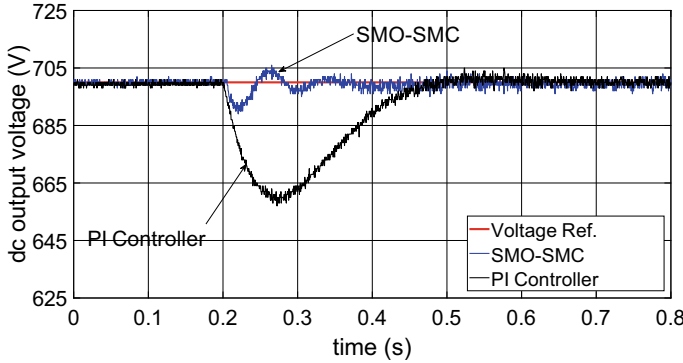


Fig. 4.6 V_{dc} response of nominal condition

(2) Experiment result analysis

(1) Nominal condition ($R_L = 180 \Omega$, $C = 3400 \mu\text{F}$)

In this condition, the external load is of middle level, around 2.7 kW.

Figure 4.6 shows the dc-link voltage transient response after disturbed by a load step. It can be seen that SMO-SMC performs much better than conventional PI control. The voltage drop of SMO-SMC is 10 V, which is only 1/4 of that obtained by PI. Taking 1 % the reference voltage as the steady-state band, i.e., ± 7 V, the voltage overshoot (5 V) of SMO-SMC can be neglected. The transient time of proposed controller is 40 ms, which is much shorter than that of PI controller (230 ms). It is should be noticed that Fig. 4.6 demonstrates a high consistency with Fig. 4.2 obtained by simulation, thus the simulation results are validated by experiments. Therefore the simulation model accurately represents the physical AFE system and is reliable to facilitate the controller design.

Figures 4.7 and 4.8 shows the grid current spectrum obtained by SMO-SMC and PI controller, it can be seen that the current harmonic contents and THD in steady-state for both controllers are almost the same.

From above results, it can be seen that, comparing with conventional PI controller, SMO-SMC can greatly improve the dc-link voltage transient response, in terms of much less voltage fluctuation and much shorter transient time, meanwhile maintains the current THD.

(2) Small capacitor condition

In this subsection, the bulk capacitor ($3400 \mu\text{F}$) in the nominal condition is replaced by a capacitor with only half the capacitance ($1700 \mu\text{F}$), to check the robustness of SMO-SMC against the capacitance change.

As shown in Fig. 4.9, SMO-SMC is robust to the capacitance change, and outperforms PI to a great extent. The voltage drop obtained by SMO-SMC is only 1/3 of that by PI, and the transient time is only 1/10 of PI. Comparing with the nominal

Fig. 4.7 Obtained current harmonic spectrum of nominal condition: SMO-SMC

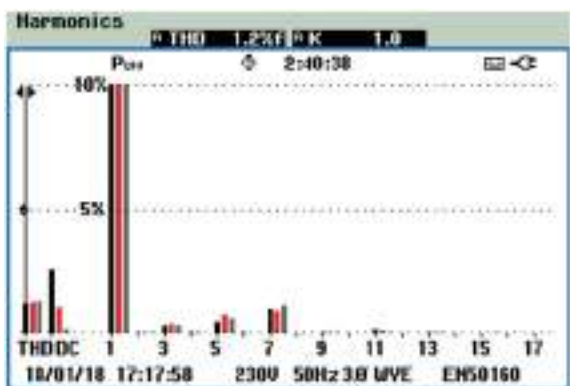
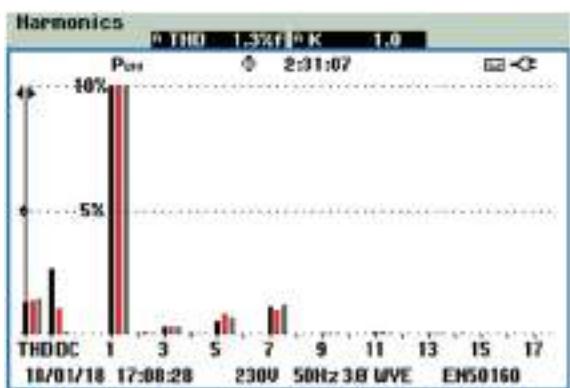


Fig. 4.8 Obtained current harmonic spectrum of nominal condition: conv. PI



condition, for both controllers result in larger drop and shorter transient time, due to the reason that smaller capacitor means smaller electrical inertia.

The THD in steady-state is maintained after capacitor is reduced, and the obtained grid current spectrum is almost the same as that in nominal condition, thus it is omitted here.

Comparing the dc-link voltage response of SMO-SMC in small capacitor condition and that of PI in nominal condition, it can be observed that, SMO-SMC achieves better control performance than PI, which is consistent with the results obtained in the previous simulation section.

(3) Large load condition ($R_L = 120 \Omega$, $C = \{3400, 1700\} \mu\text{F}$)

In this subsection, the external load increases to nearly 4 KVA to test the control performance of SMO-SMC when the external load increases.

Figures 4.10 and 4.11 respectively show the dc-link voltage transient responses for the bulk and the small capacitor. The results are consistent with those under nominal condition, i.e., SMO-SMC demonstrates obvious advantages over PI control. For bulk capacitor, SMO-SMC results in 1/3 the voltage drop and 1/4 the transient time

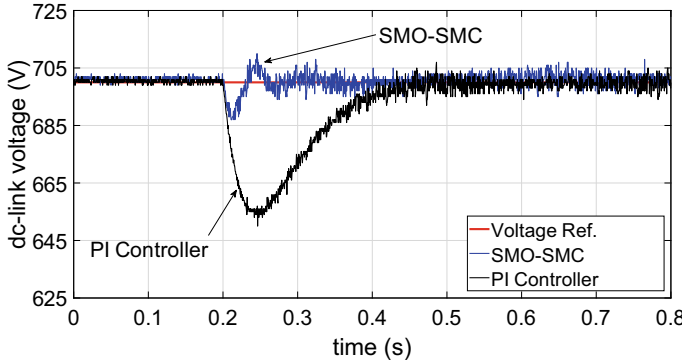


Fig. 4.9 V_{dc} response of nominal load with reduced capacitor

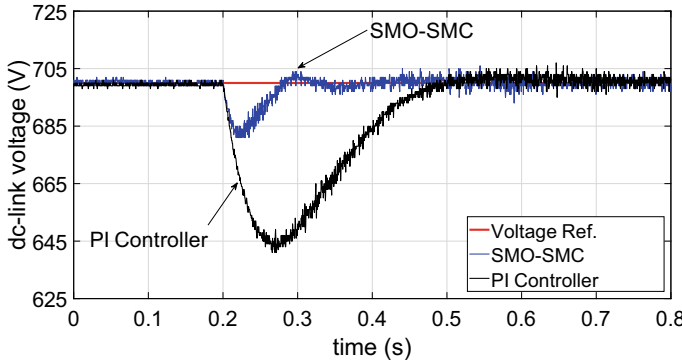


Fig. 4.10 V_{dc} response of large load condition

of PI; for small capacitor, the corresponding data is 1/2 and 1/5. Comparing with the nominal condition, the transient responses are slower due to the load increase.

The obtained grid current THD for the two capacitors are the same, both around 1.1 %. As with the nominal condition, the current THD in steady-state is maintained after capacitor reduction, and the harmonic spectrum is also similar as that in nominal condition. Therefore, it can be seen that, SMO-SMC maintains the performance with increased load.

(4) Small load condition ($R_L = 240 \Omega$, $C = \{3400, 1700\} \mu F$)

In contrast to the previous section, this subsection aims to test the performance of SMO-SMC under small load condition, about 2 KVA.

Figures 4.12 and 4.13 show the dc-link voltage transient responses for the two capacitor. Since the load power is decreased, the transient responses are faster than those under nominal condition. Same with previous test conditions, regardless of the different capacitor values, SMO-SMC achieves a much better performance than PI controller, and the obtained harmonic spectrum is similar as that of nominal condition.

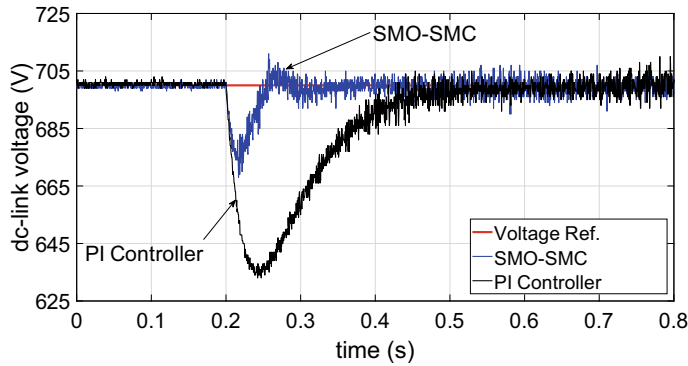


Fig. 4.11 V_{dc} response of large load with reduced capacitor

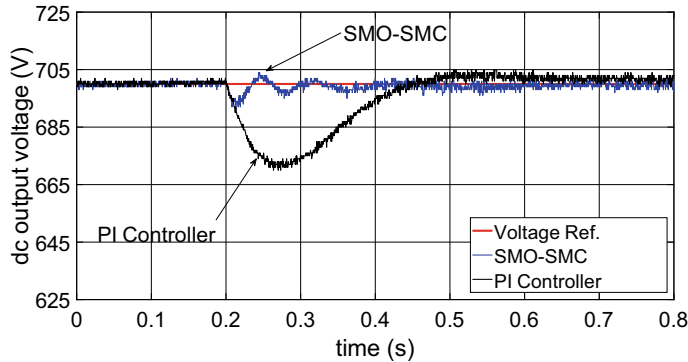


Fig. 4.12 V_{dc} response of small load condition

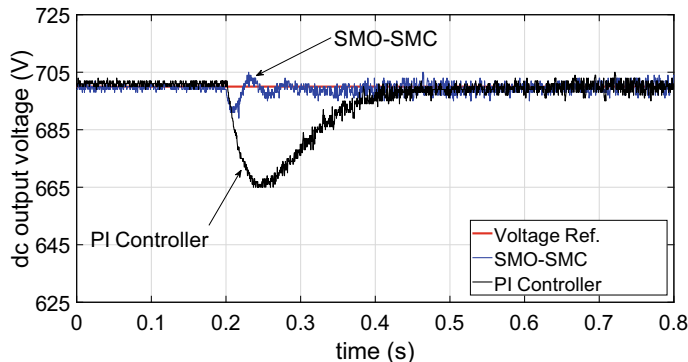


Fig. 4.13 V_{dc} response of small load with reduced capacitor

Table 4.3 Summary of experiment results with bulk capacitor

$R = 180 \Omega$	$C = 3400 \mu\text{F}$ (nominal condition)			
	V_{dc} drop (V)	V_{dc} overshoot (V)	Transient time (ms)	Current THD (%)
SMO-SMC	10	5	40	1.2
PI	41	0	230	1.3
$R = 120 \Omega$	$C = 3400 \mu\text{F}$			
	V_{dc} drop (V)	V_{dc} overshoot (V)	Transient time (ms)	Current THD (%)
SMO-SMC	19	0	60	1.1
PI	58	0	240	1.1
$R = 240 \Omega$	$C = 3400 \mu\text{F}$			
	V_{dc} drop (V)	V_{dc} overshoot (V)	Transient time (ms)	Current THD (%)
SMO-SMC	9	4	30	1.6
PI	29	0	210	1.7

Table 4.4 Summary of experiment results with small capacitor

$R = 180 \Omega$	$C = 1700 \mu\text{F}$			
	V_{dc} drop (V)	V_{dc} overshoot (V)	Transient time (ms)	Current THD (%)
SMO-SMC	14	7	20	1.2
PI	47	0	200	1.3
$R = 120 \Omega$	$C = 1700 \mu\text{F}$			
	V_{dc} drop (V)	V_{dc} overshoot (V)	Transient time (ms)	Current THD (%)
SMO-SMC	31	7	40	1.1
PI	67	0	200	1.1
$R = 240 \Omega$	$C = 1700 \mu\text{F}$			
	V_{dc} drop (V)	V_{dc} overshoot (V)	Transient time (ms)	Current THD (%)
SMO-SMC	10	5	20	1.5
PI	36	0	180	1.7

Summarizing above results, it can be concluded that SMO-SMC has strong robustness against load variation.

The detailed experiment results are summarized in Tables 4.3 and 4.4.

4.4 Summary

In this chapter, the sliding mode control based on an improved sliding mode observer (SMO-SMC) has been proposed to regulate the dc-link voltage of a grid connected three-phase two-level power converter. Comparing with the SMO in Chap. 2, the improved SMO has one more tuning parameter, which is used to improve the transient response while not influence the steady state performance, while the original two parameters are used to maintain the steady state performance. Comparing with the LDO in Chap. 3, this improved nonlinear SMO has faster converging speed and stronger robustness against system uncertainties. The controller for the voltage regulation loop is the super twisting sliding mode controller. The stability of voltage regulation loop under SMO-SMC control has been proved via Lyapunov method, and the effectiveness of SMO-SMC is verified via simulation, which shows that SMO-SMC outperforms conventional PI both under nominal condition and small capacitor condition. At last, experiments are carried out on a 5 kW grid-connected power converter. The experiment results show: (1) comparing with conventional PI control, SMO-SMC significantly improves the performance of the voltage regulation loop while maintains low current THD level; (2) SMO-SMC is strongly robust against the variation in external load and dc-link capacitance.

References

1. Levant, A.: Higher-order sliding modes, differentiation and output-feedback control. *Int. J. Control* **76**(9–10), 924–941 (2003)
2. Moreno, J.A., Osorio, M.: A Lyapunov approach to second-order sliding mode controllers and observers. In: Proceedings of the 47th IEEE Conference on Decision and Control, Cancun, Mexico, pp. 2856–2861 (2008)

Chapter 5

Proportional-Integral Control of Three-Phase Neutral-Point-Clamped Converters



Abstract Two-level converters are widely applied in middle and high voltage fields. In high voltage applications, though the over-voltage problem can be mitigated by using multiple switches in series and/or parallel, this evokes other problems like dynamic and/or static voltage and current sharing problems of the switches, which increases uncertain factors in technology and decreases system stability. To solve this problem, three and higher level converters (i.e., multiple-level converters) have been investigated by researchers, to suit the high-voltage and high-power systems. Multiple level converters can greatly reduce the current THD of the input current, decrease the electromagnetic interference of system, achieve less power loss and improve energy efficiency. Therefore, multiple-level converters is the future trend.

Comparing with two-level converters, multiple-level converters have following merits: they have more modulation levels, which is more similar with the ideal waveform; the increase in modulation level reduces the step variation and harmonic contents of output voltage; the equivalent switching frequency is increased, then reduces power loss and improve efficiency. As show in Fig. 5.1, the more modulation level there is, the more similar is the output voltage to the target waveform. With same switching frequency, the harmonic component of modulated waveform of multiple-level converters is less than that of two-level converters. Vice versa, to achieve similar waveform quality, the switching frequency of multiple-level converters is lower than that of two-level converters. Therefore in high-power applications, the power loss can be greatly reduced and the device span can be extended.

This chapter investigates three-phase neutral-point-clamped (NPC) converter. This type of converter is very popular in industry, and is the most widely used multiple-level converter. It has following merits: (1) Comparing with two-level converters, it can output higher dc voltage and result in less low-order harmonics in output voltage; (2) comparing with higher level converters, it has relatively simple topology, thus it is easier to control, modulate and maintain [1]. With same dc-link voltage, the voltage imposed on power switches is half that of two-level converter, thus the voltage withstand requirements can be reduced.

Inevitably, there is cost for increasing modulation level. Comparing with two-level converter, three-level converter needs more power switches and other devices,

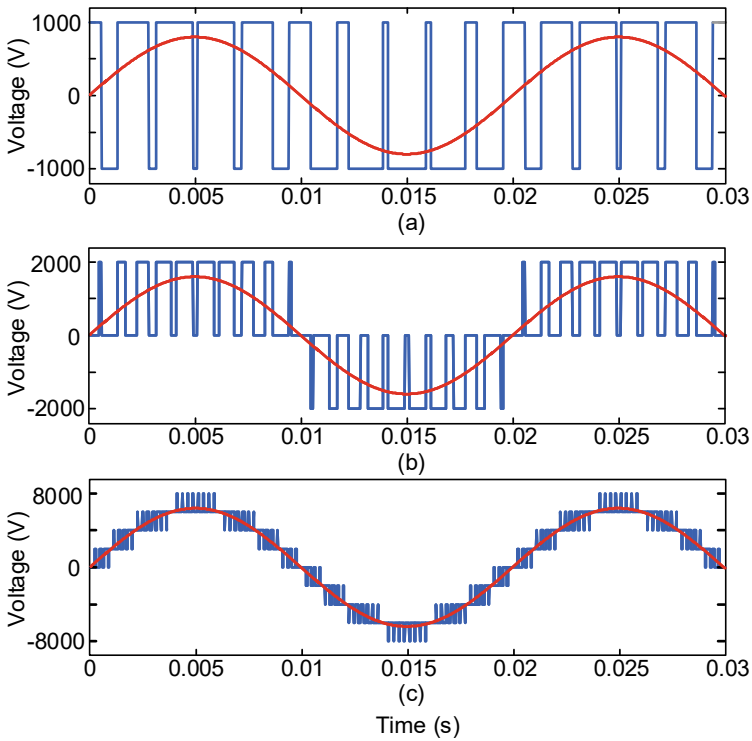


Fig. 5.1 Modulated voltage of **a** two-level, **b** three-level and **c** nine-level converters

leading to cost rise. On the other hand, due to the dc-link capacitor voltage unbalance, additional voltage balance needs to be done.

Due to the influence of circuit component parameter variation, unbalanced load and control algorithm, the circuit would inject/withdraw current from the neutral point, causing the voltage difference between the capacitors. This voltage unbalance will impose low-order or even-order harmonics to the ac voltage, and the accumulation of even-order harmonics would further intensify the unbalance, leading to system instability. Therefore control efforts need to be put on capacitor voltage balance, which mainly has two methods: (1) hardware method, i.e., the voltage is balanced via hardware selection and topology modification; (2) software method, i.e., the voltage is balanced through algorithm optimization. Popular software method is the zero-sequence current injection, which is a voltage balance strategy that is not dependent on modulation technique. To inject the zero-sequence current on the three-phase ac side, 0-axis (in SRF) or γ -axis (in stationary frame) control signal is needed.

Similar with the control methods in previous chapters, the disturbance observer based control strategy is employed for NPC. In this chapter, the LESO is adopted to compensate the controller in voltage regulation loop, to regulate the dc-link voltage

of the converter. The reason of using LESO is: (1) it is an important result of ADRC, its theoretical results are relatively mature and complete, and it is widely adopted both in academia and industry; (2) from the comparison in Chap. 2, LESO presents a fairly good performance. Also for \mathcal{H}_∞ state feedback control which is linear in nature, if LESO is adopted, the whole voltage regulation loop is a linear system.

As capacitor voltage needs to be balanced, NPC needs three control loops. To extend control modes, this chapter investigates NPC control strategies under two control modes, i.e., VOC and DPC.

Figure 5.2 is the control process of NPC under VOC, which includes voltage regulation loop, current tracking loop and capacitor voltage balance loop. It can be seen that, under VOC, NPC has one more capacitor voltage balance loop than the two-level converter. To inject the zero-sequence component to balance the voltage, 0-axis control signal is used in this mode. The control process is: the sensors measure the three-phase grid voltage v_{an} , v_{bn} and v_{cn} , three-phase grid current i_a , i_b and i_c , the dc-link voltage V_{dc} , and the two capacitor voltages V_{c1} and V_{c2} ; V_{dc} goes into the controller of voltage regulation loop, which is regulated to reach the reference V_{dc}^* , during this process the active power reference p^* is generated; p^* and the preset reactive power reference q^* are transformed in to current references i_d^* and i_q^* ; the three-phase grid voltage is put into PLL to obtain the voltage vector phase angle θ , which is used to transform the three-phase grid current to (d, q) SRF; the controller of current tracking loop drive i_d and i_q to i_d^* and i_q^* , respectively, during this process the control signals u_d and u_q are generated; V_{c1} and V_{c2} are put into the capacitor voltage balance loop, to make the voltage difference go zero, and generate control signal u_0 ; u_d , u_q and u_0 are transformed back to three-phase control signals u_a , u_b and u_b , which are put into the PWM module to make the converter switches take actions. Figure 5.3 is the overall control diagram of NPC under VOC.

Figure 5.4 is the control process of NPC under DPC, which includes voltage regulation loop, instantaneous power tracking loop and capacitor voltage balance loop. Different from VOC, in DPC mode the power is tracked directly in (α, β) frame, correspondingly, the γ -axis control signal is generated by the voltage balance loop. The control process is: the sensors measure the three-phase grid voltage v_{an} , v_{bn} and v_{cn} , three-phase grid current i_a , i_b and i_c , the dc-link voltage V_{dc} , and the two capacitor voltages V_{c1} and V_{c2} ; V_{dc} goes into the controller of voltage regulation loop, which is regulated to reach the reference V_{dc}^* , during this process the active power reference p^* is generated, the reactive power reference q^* is set as required; the three-phase grid voltage and current are transformed into (α, β) frame, and the instantaneous active and reactive power p and q are calculated; the controller of power tracking loop drive p and q to p^* and q^* , respectively, during this process the control signals u_α and u_β are generated; V_{c1} and V_{c2} are put into the capacitor voltage balance loop, to make the voltage difference go zero, and generate control signal u_γ ; u_α , u_β and u_γ are transformed back to three-phase control signals u_a , u_b and u_b , which are put into the PWM module to make the converter switches take actions. Figure 5.5 is the overall control diagram of NPC under DPC.

This chapter firstly investigates the performance improvement brought by the LESO under VOC. In voltage regulation loop, LESO estimates the load randomly

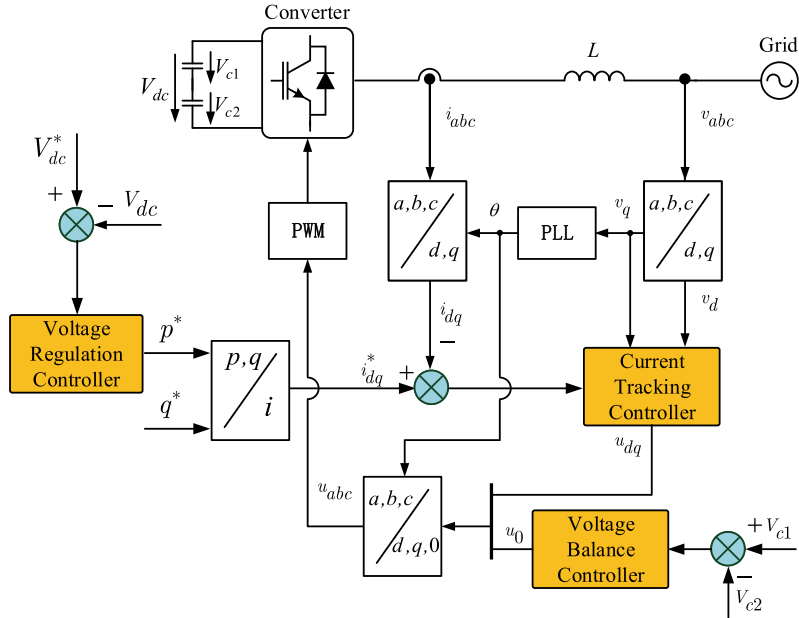


Fig. 5.2 VOC control process of three-phase three-level NPC power converter

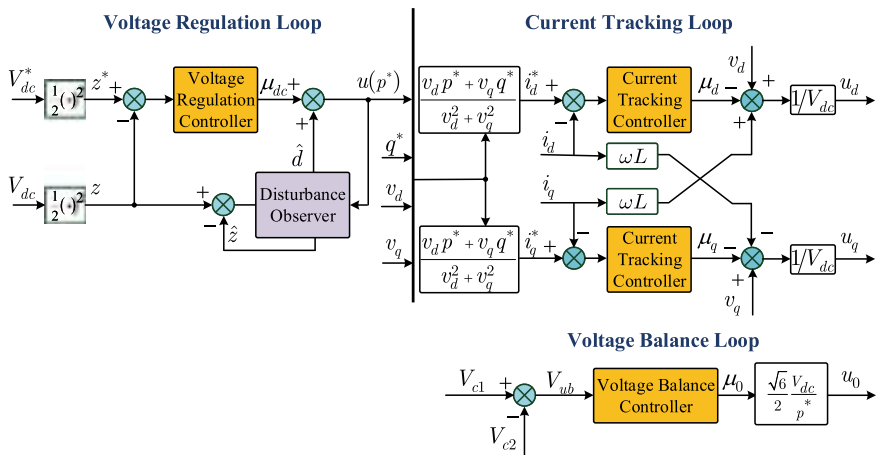


Fig. 5.3 Overall VOC diagram of three-phase three-level NPC power converter

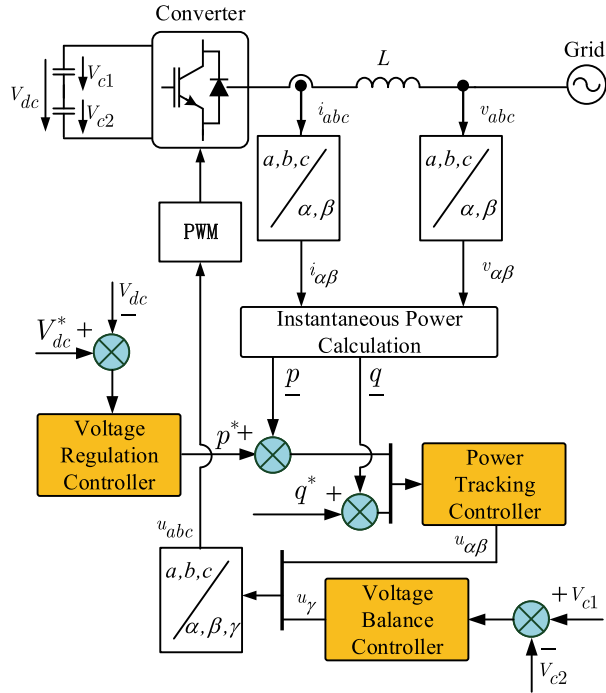


Fig. 5.4 DPC control process of three-phase three-level NPC power converter

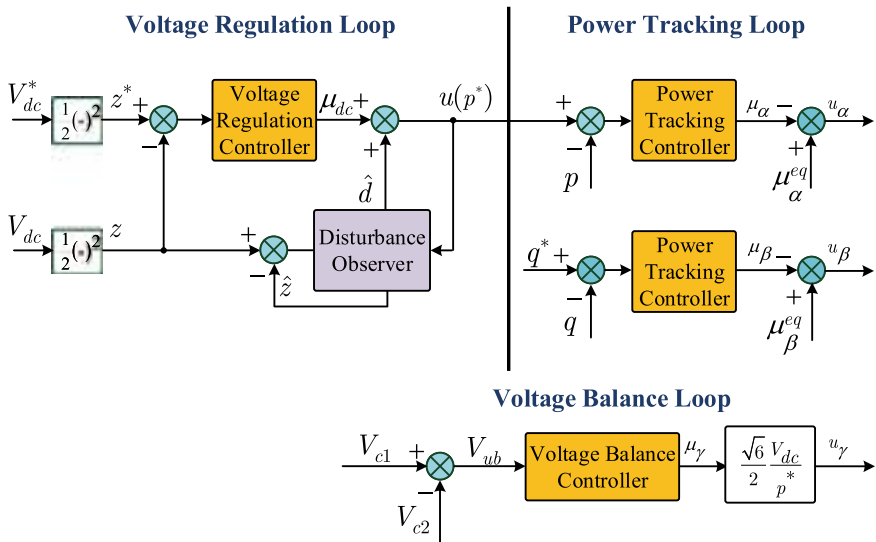


Fig. 5.5 Overall DPC diagram of three-phase three-level NPC power converter

connected to the dc-link, and compensate the estimated value to the PI controller. The effectiveness and advantage of LESO is verified via simulation. To test the robustness of the proposed control strategy, three levels of load have been adopted in simulation, to provide large load variation. The simulation results show: (1) LESO can significantly improve the control performance of voltage regulation loop, in terms of smaller voltage drop and shorter transient time; (2) LESO can improve the robustness of voltage regulation loop against load variation.

After the effectiveness of LESO has been verified under VOC, it is further adopted under DPC. Combining \mathcal{H}_∞ control and adaptive STA method, the \mathcal{H}_∞ based DPC has been proposed. The voltage regulation loop adopts the LESO based \mathcal{H}_∞ control to regulate the dc-link voltage, meanwhile suppress the impact of observation error on output. The instantaneous power tracking loop adopts STA controllers to make the active and reactive power converge to their references. The control design is carried out under stationary (α, β) frame, which does not need the angle information as it does under (d, q) SRF.

In capacitor voltage balance loop, the super-twisting controller based on adaptive estimator is adopted. The estimator can finally be simplified as a resonant filter, to estimate the disturbance signal (composed of base and third-order harmonic) in the dynamic of capacitor voltage difference. The simulation results show that, with this control strategy, the overall dynamic performance of the converter has been significantly improved, the closed-loop system achieves the designated disturbance attenuation level, and the capacitor voltage is balance.

5.1 Mathematical Model and Control Objectives

5.1.1 Converter Model

Figure 5.6 shows the topology of three-phase three-level NPC. v_{an} , v_{bn} and v_{cn} are balanced three-phase grid voltage, which enter the converter through three filtering inductors L . i_a , i_b and i_c are corresponding three-phase grid current. u_{ij} ($i = \{a, b, c\}$, $j = \{1, 2\}$) are switching signals generated by the controller. Two identical capacitors C are put on the two sides of the neutral point N . V_{c1} and V_{c2} are the voltages of upper capacitor and lower capacitor. V_{dc} is the dc-link voltage to be regulated. R_L is the resistive load abruptly connected to the dc-link. i_{load} is load current.

The mathematical model of the circuit in Fig. 5.6 in (a, b, c) natural frame is as follows [2]:

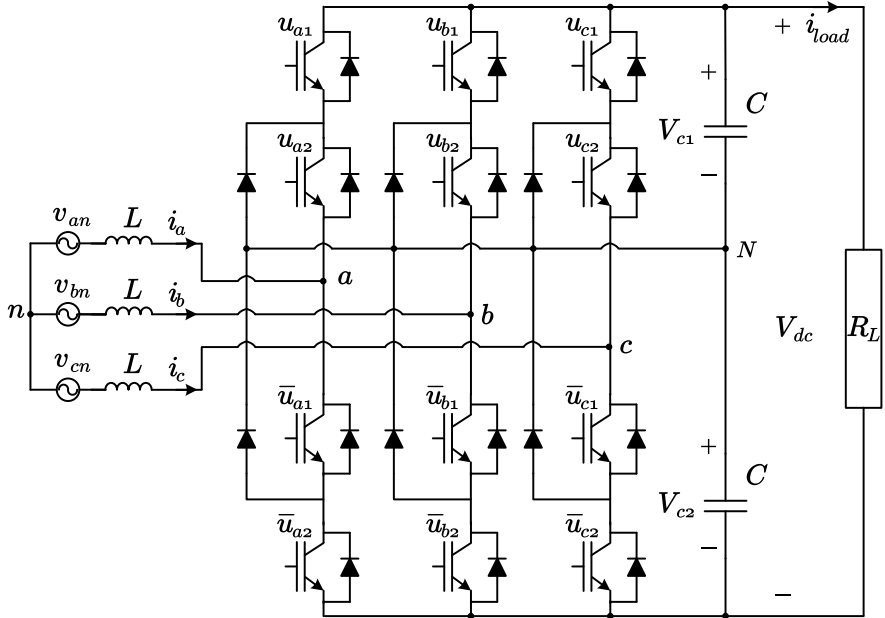


Fig. 5.6 Topology of three-phase three-level NPC

$$L \frac{di_{abc}}{dt} = v_{abc} - \frac{1}{6} \begin{pmatrix} 2 & -1 & -1 \\ -1 & 2 & -1 \\ -1 & -1 & 2 \end{pmatrix} \begin{pmatrix} u_a & u_a^2 \\ u_b & u_b^2 \\ u_c & u_c^2 \end{pmatrix} \begin{pmatrix} V_{dc} \\ V_{ub} \end{pmatrix}, \quad (5.1)$$

$$C \frac{dV_{dc}}{dt} = u_{abc}^T i_{abc} - 2i_{load}, \quad (5.2)$$

$$C \frac{dV_{ub}}{dt} = (u_{abc}^2)^T i_{abc}, \quad (5.3)$$

where $v_{abc} = \{v_{an}, v_{bn}, v_{cn}\}^T$, $i_{abc} = \{i_a, i_b, i_c\}^T$, $u_{abc} = \{u_a, u_b, u_c\}^T$ are duty cycle generated by the controller, $V_{ub} = V_{c1} - V_{c2}$ is the difference of the capacitor voltages.

Similar as two-level converters, to facilitate the controller design, coordinate transform is performed for system (5.1)–(5.3).

(1) Model in stationary (α, β, γ) frame

Perform following Clarke transform to system (5.1)–(5.3),

$$\{\cdot\}_{\alpha\beta\gamma} = T_{abc-\alpha\beta\gamma} \{\cdot\}_{abc}, \quad T_{abc-\alpha\beta\gamma} = \sqrt{\frac{2}{3}} \begin{bmatrix} 1 & -\frac{1}{2} & -\frac{1}{2} \\ 0 & \frac{\sqrt{3}}{2} & -\frac{\sqrt{3}}{2} \\ \frac{1}{\sqrt{2}} & \frac{1}{\sqrt{2}} & \frac{1}{\sqrt{2}} \end{bmatrix}, \quad (5.4)$$

the model in stationary (α, β, γ) frame is obtained [2]:

$$L \frac{di_{\alpha\beta}}{dt} = v_{\alpha\beta} - \frac{v_{dc}}{2} u_{\alpha\beta} + \left[\frac{\frac{1}{2\sqrt{6}}(u_{\beta}^2 - u_{\alpha}^2) - \frac{1}{\sqrt{3}u_{\alpha}u_{\gamma}}}{\frac{u_{\alpha}u_{\beta}}{\sqrt{6}} - \frac{u_{\beta}u_{\gamma}}{\sqrt{3}}} \right] V_{ub}, \quad (5.5)$$

$$C \frac{dV_{dc}}{dt} = u_{\alpha\beta}^T i_{\alpha\beta} - \frac{2}{R_L} V_{dc}, \quad (5.6)$$

$$C \frac{dV_{ub}}{dt} = \frac{2}{\sqrt{6}} [u_{\alpha}^2 - u_{\beta}^2, -u_{\alpha}u_{\beta}] i_{\alpha\beta} + \frac{1}{\sqrt{6}} u_{\alpha\beta}^T i_{\alpha\beta} u_{\gamma}, \quad (5.7)$$

where $v_{\alpha\beta} = \{v_{\alpha}, v_{\beta}\}^T$ is grid voltage, $i_{\alpha\beta} = \{i_{\alpha}, i_{\beta}\}^T$ is grid current, $u_{\alpha\beta} = \{u_{\alpha}, u_{\beta}\}^T$ and u_{γ} are control signals. Same as two-level converter, after control signals are generated, they are transformed back to u_a , u_b and u_c to be implemented by modulator. It can be seen that, as γ -axis control signal is used for balancing capacitor voltages, the stationary coordinate transform performed here is three-axis transform, while for two-level converter it is only two-axis transform.

It should be noted that, when converter operates normally, V_{ub} is close to zero, and can be assumed to be at least one order lower than V_{dc} . On the other hand, the duty cycle $u_{\alpha\beta}$ takes value in the interval $[-1, 1]$, therefore the third term of right side of (5.5) is at least two order lower than the second term. Based on this consideration, (5.5) can be approximated by following equation:

$$L \frac{di_{\alpha\beta}}{dt} = v_{\alpha\beta} - \frac{v_{dc}}{2} u_{\alpha\beta}. \quad (5.8)$$

Next to simplify (5.7) in the view of instantaneous power. Based on the definition of instantaneous active and reactive power p and q [3], it can be obtained that:

$$p = v_{\alpha\beta}^T i_{\alpha\beta}, \quad q = v_{\alpha\beta}^T J i_{\alpha\beta}, \quad J = \begin{bmatrix} 0 & -1 \\ 1 & 0 \end{bmatrix}. \quad (5.9)$$

The dynamic equation of p and q can be expressed as:

$$\begin{aligned} L \dot{p} &= v_{\alpha\beta}^T \left(L\omega q \frac{v_{\alpha\beta}}{\|v_{\alpha\beta}\|^2} + v_{\alpha\beta} - \frac{V_{dc}}{2} u_{\alpha\beta} \right), \\ L \dot{q} &= v_{\alpha\beta}^T J^T \left(-L\omega p \frac{J v_{\alpha\beta}}{\|v_{\alpha\beta}\|^2} - \frac{V_{dc}}{2} u_{\alpha\beta} \right), \end{aligned} \quad (5.10)$$

where $\|v_{\alpha\beta}\|^2 = v_{\alpha\beta}^T v_{\alpha\beta}$.

Let $\dot{p} = 0, \dot{q} = 0$, the following equivalent controller can be obtained:

$$u_{\alpha\beta}^{eq} = \frac{2}{V_{dc}} \left\{ \left(\|v_{\alpha\beta}\|^2 + \omega L q \right) \frac{v_{\alpha\beta}}{\|v_{\alpha\beta}\|^2} - (\omega L p) \frac{J v_{\alpha\beta}}{\|v_{\alpha\beta}\|^2} \right\}. \quad (5.11)$$

Considering that the dynamic of instantaneous power is faster than V_{ub} , let $p = p^*$, $q = q^*$, and put (5.58) into (5.7), it can be obtained that

$$C \frac{dV_{ub}}{dt} = \frac{2p^*}{\sqrt{6}V_{dc}} u_\gamma + \Phi(t), \quad (5.12)$$

where

$$\Phi(t) = \frac{2}{\sqrt{6}} \left[(u_\alpha^{eq})^2 - (u_\beta^{eq})^2, -u_\alpha^{eq} u_\beta^{eq} \right] i_{\alpha\beta}. \quad (5.13)$$

It can be observed that $\Phi(t)$ is composed of base waveform and third harmonic.

Therefore, based on (5.6), (5.8) and (5.12), the simplified dynamic model of NPC is obtained as:

$$\begin{aligned} L \frac{di_{\alpha\beta}}{dt} &= v_{\alpha\beta} - \frac{v_{dc}}{2} u_{\alpha\beta}, \\ C \frac{dV_{dc}}{dt} &= u_{\alpha\beta}^T i_{\alpha\beta} - \frac{2}{R_L} V_{dc}, \\ C \frac{dV_{ub}}{dt} &= \frac{2p^*}{\sqrt{6}V_{dc}} u_\gamma + \Phi(t). \end{aligned} \quad (5.14)$$

(2) Model in $(d, q, 0)$ SRF

Perform following Park transform to the simplified dynamic NPC model (5.14):

$$\{\cdot\}_{dq0} = T_{\alpha\beta\gamma-dq0} \{\cdot\}_{abc}, \quad T_{\alpha\beta\gamma-dq0} = \begin{bmatrix} \cos\omega t & \sin(\omega t) & 0 \\ -\sin\omega t & \cos(\omega t) & 0 \\ 0 & 0 & 1 \end{bmatrix}, \quad (5.15)$$

the model in $(d, q, 0)$ SRF is obtained as:

$$L \frac{di_d}{dt} = \omega L i_q + v_d - \frac{V_{dc}}{2} u_d, \quad (5.16)$$

$$L \frac{di_q}{dt} = -\omega L i_d + v_q - \frac{V_{dc}}{2} u_q, \quad (5.17)$$

$$C \frac{dV_{dc}}{dt} = u_d i_d + u_q i_q - 2i_{load}, \quad (5.18)$$

$$C \frac{dV_{ub}}{dt} = \frac{2p^*}{\sqrt{6}V_{dc}} u_0 + \Phi(t), \quad (5.19)$$

where v_d, v_q are grid voltage, i_d, i_q are grid current, ω is the grid voltage frequency, u_d, u_q and u_0 are control signals, $\Phi(t)$ is the signal composed of base waveform and third harmonic, p^* is the active power reference. It should be noted that, same

as for two-level converters, when converter is modeled in $(d, q, 0)$ SRF, PLL should be included in the controller to provide grid voltage angle to perform Park transform [4].

5.1.2 Control Objectives

For NPC, there are three control targets, including: regulate the dc-link voltage to its reference, generate active and reactive power as required, and balance the capacitor voltages of the dc-link. Therefore, its control problem includes following three aspects:

- Voltage regulation problem: regulate the dc-link voltage V_{dc} to its reference V_{dc}^* , i.e.,

$$V_{dc} \rightarrow V_{dc}^*. \quad (5.20)$$

- Power/current tracking problem:

- Power tracking: the instantaneous active and reactive power p, q track their respective references, i.e.,

$$p \rightarrow p^*, \quad q \rightarrow q^*. \quad (5.21)$$

- Current tracking: the currents track their references, i.e.,

- in (α, β, γ) frame:

$$i_\alpha \rightarrow i_\alpha^*, \quad i_\beta \rightarrow i_\beta^*. \quad (5.22)$$

- in $(d, q, 0)$ SRF:

$$i_d \rightarrow i_d^*, \quad i_q \rightarrow i_q^*. \quad (5.23)$$

- Capacitor voltage balance: ensure there is no difference between the capacitor voltages, i.e.,

$$V_{ub} = 0. \quad (5.24)$$

It can be seen that, the former two control problems are the same as those for two-level converters, the third target is the newly added control problem of NPC.

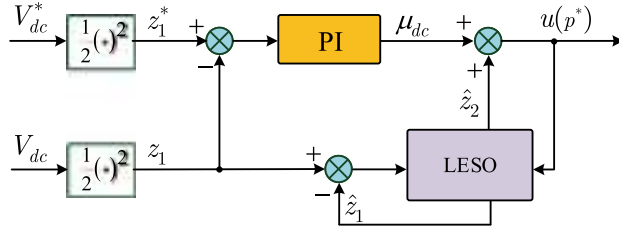


Fig. 5.7 Voltage regulation loop compensated by LESO

5.2 Voltage Oriented Control

5.2.1 Voltage Regulation Loop

As shown in Fig. 5.7, the voltage regulation includes the forward-path controller and a backward-path observer. The observer estimate the external disturbance and compensate the estimated value to the forward-path controller.

(1) PI controller

The forward-path controller adopts the conventional PI algorithm. Considering the NPC dc-link voltage dynamic Eq. (5.18), and following the defining style of two-level converter, define $p^* = v_d i_d^* + v_q i_q^*$, $p_{load} = V_{dc} i_{load}$, it can be obtained that:

$$C \frac{dV_{dc}}{dt} = \frac{1}{V_{dc}} (p^* - 2p_{load}), \quad (5.25)$$

where load power $2p_{load}$ shall disturb V_{dc} , thus it is a disturbance to voltage loop system. Further define $(V_{dc}^*)^2 / 2 = z_1^*$, $V_{dc}^2 / 2 = z_1$, $p^* = \mu_{dc}$ (the control output when there is no compensation from observer), $2p_{load} = d$, and (5.25) can be rewritten as:

$$C \dot{z}_1 = \mu_{dc} - d. \quad (5.26)$$

where z_1 is the item to be controlled, μ_{dc} is the control signal, d is the external disturbance. Therefore PI controller is designed as

$$\mu_{dc} = K_{pv} e_v + K_{iv} \int_0^t e_v dt, \quad (5.27)$$

where $e_v = z_1^* - z_1$. Obviously, z_1 tracking z_1^* is equivalent to V_{dc} tracking V_{dc}^* .

(2) Linear extended state observer (LESO)

The observer adopts the form of LESO. This observer regards the external disturbance d as an extended state z_2 and estimate its value, then compensate this value to the PI controller signal μ_v . Therefore the final output signal of voltage loop is $p^* = u$, and z_1 can be rewritten as

$$C\dot{z}_1 = \mu_{dc} + \hat{z}_2 - z_2. \quad (5.28)$$

Design LESO as:

$$\begin{cases} C\dot{\hat{z}}_1 = u - \hat{z}_2 + \beta_1 e_1, \\ \dot{\hat{z}}_2 = -\beta_2 e_1, \\ e_1 = z_1 - \hat{z}_1, \end{cases} \quad (5.29)$$

The dynamic of observation error is as follows:

$$\dot{e} = Ae + Bh(t), \quad (5.30)$$

$$\text{where } e = [e_1 \ e_2]^T, A = \begin{bmatrix} -\beta_1/C & -1/C \\ \beta_2 & 0 \end{bmatrix}, B = \begin{bmatrix} 0 \\ 1 \end{bmatrix}, h(t) = \dot{z}_2, e_2 = z_2 - \hat{z}_2.$$

To ensure that the observation error can converge to equilibrium, the observer parameters β_1 and β_2 must satisfy that matrix A is Hurwitz.

5.2.2 Current Tracking Loop

The current tracking loop adopts the same SRF-PI control as in Chap. 3, whose control structure is shown in Fig. 3.2. Define current error as:

$$e_{dq} = \begin{bmatrix} e_d \\ e_q \end{bmatrix} = \begin{bmatrix} i_d^* - i_d \\ i_q^* - i_q \end{bmatrix}. \quad (5.31)$$

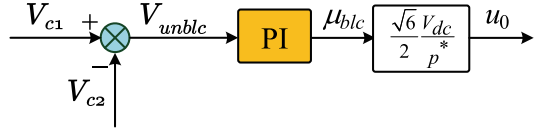
Then the PI controllers for d-axis and q-axis are designed as:

$$\mu_d = K_{pId}e_d + K_{iId} \int_0^t e_d dt, \quad (5.32)$$

$$\mu_q = K_{pIq}e_q + K_{iIq} \int_0^t e_q dt. \quad (5.33)$$

Combining (2.9) and (2.10), the control signals for the two axes currents are:

Fig. 5.8 Capacitor voltage balance control



$$u_d = \frac{1}{V_{dc}} (-\mu_d + v_d + \omega L i_q), \quad (5.34)$$

$$u_q = \frac{1}{V_{dc}} (-\mu_q + v_q - \omega L i_d). \quad (5.35)$$

5.2.3 Voltage Balancing Loop

Figure 5.8 is the voltage balance loop, which adopts conventional PI control. As mentioned before, the control signal for this loop is the 0-axis control signal.

The PI controller output signal is:

$$\mu_0 = K_{pBlc} V_{ub} + K_{iBlc} \int_0^t V_{ub} dt, \quad (5.36)$$

and the final control signal of voltage balance loop is:

$$u_0 = \frac{\sqrt{6}}{2} \frac{V_{dc}}{p^*} \mu_0. \quad (5.37)$$

5.2.4 Simulation Verification

To verify the performance improvement LESO brings to the voltage regulation loop, different load resistors have been adopted for simulation.

The system parameters are in Table 5.1. The load is of resistive type, and is connected to the dc-link at $t = 0.8$ s. The reactive power reference is set to 0 kVAr to achieve unity power factor, thus i_q^* is 0 A.

As shown, the load resistor has three different values to impose disturbance of different levels.

Table 5.2 shows the control parameter, including the PI control parameters of voltage loop, LESO parameters, the PI parameters for current control loop and voltage balance loop.

(1) Load case 1: $R_L = 93.75 \Omega$

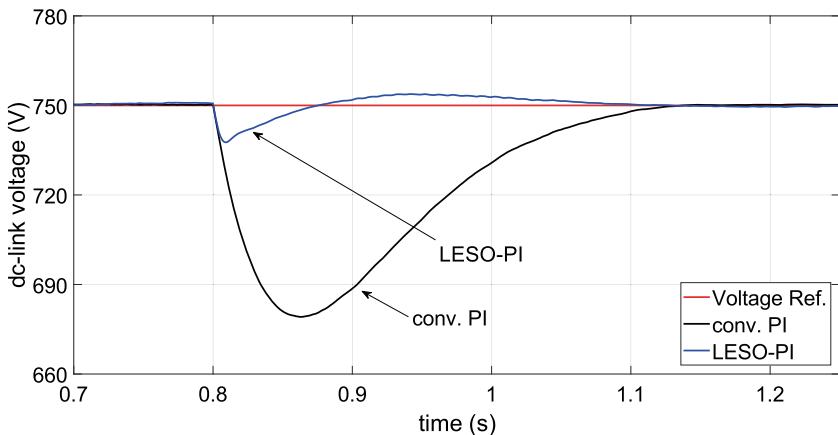
The load disturbance in this case is 6 kW.

Table 5.1 System parameters

Parameter	Value	Description
v_{abc}	380	Source line voltage (V)
f	50	Source frequency (Hz)
L	2	Phase inductor (mH)
C	6000	DC-link capacitor (μF)
V_{dc}^*	750	DC-link voltage reference (V)
R_L	{93.75, 15.625, 7.8125}	Load resistance (Ω)
f_s	6.4	Sampling rate (kHz)
f_c	6.4	Control update rate (kHz)

Table 5.2 Control parameters

Vol. Reg. loop		Cur. Tra. loop	Vol. Bal. loop
PI controller	LESO		
$K_{pv} = 0.06$	$\beta_1 = 8.4$	$K_{pId} = K_{pIq} = 1$	$K_{pBlc} = 0.005$
$K_{iv} = 0.8$	$\beta_2 = 2058$	$K_{iId} = K_{iIq} = 40$	$K_{iBlc} = 10^{-5}$

**Fig. 5.9** DC-link voltage transient response of case 1

The dc-link voltage transient response is shown in Fig. 5.9. As can be seen, when there is only PI controller in the voltage loop, once the load is connected to the dc-link, the voltage drops by 70 V, and recovering time is 0.32 s; when the PI controller is compensated by LESO, the voltage drops only by 12 V, which is only 17.1% of the pure PI control, and the recovering time is 0.28 s, which is slightly faster than pure PI control. Though it can be observed that with LESO, there is a small voltage overshoot about 3.8 V, it is negligible compared with the voltage reference.

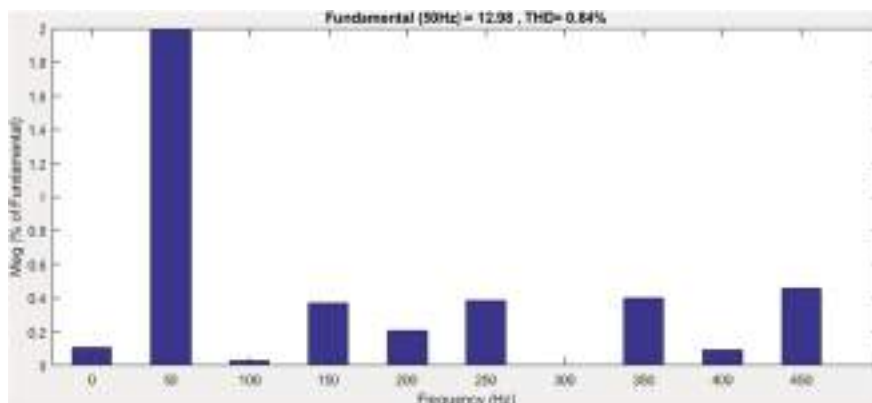


Fig. 5.10 Stead-state current THD of case 1: conv. PI

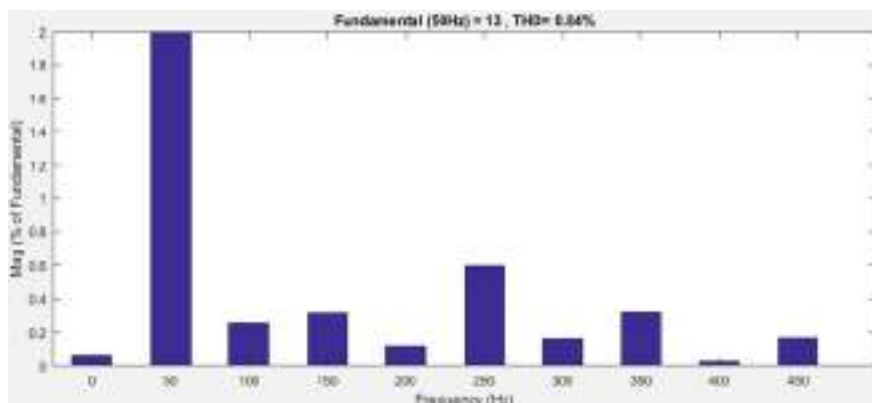


Fig. 5.11 Stead-state current THD of case 1: LESO-PI

Figures 5.10 and 5.11 show current harmonic spectrum and THD in steady-state for pure PI control and PI with LESO, respectively. It can be seen that the obtained THDs are similar. Note that the current harmonic spectrum uses 50Hz as base frequency, as it is the grid voltage frequency of many countries (such as most European countries), the rest of the harmonic frequencies are times of base frequency.

Therefore, it can be concluded that LESO significantly improves the control performance of the voltage loop.

Figure 5.12 is the grid current waveforms obtained with proposed strategy, which are almost sinusoidal and balanced, which demonstrates that the current loop is controlled well.

Figure 5.13 shows the capacitor voltages, which are well regulated to half the dc-link voltage reference, thus the capacitor voltages are balanced.

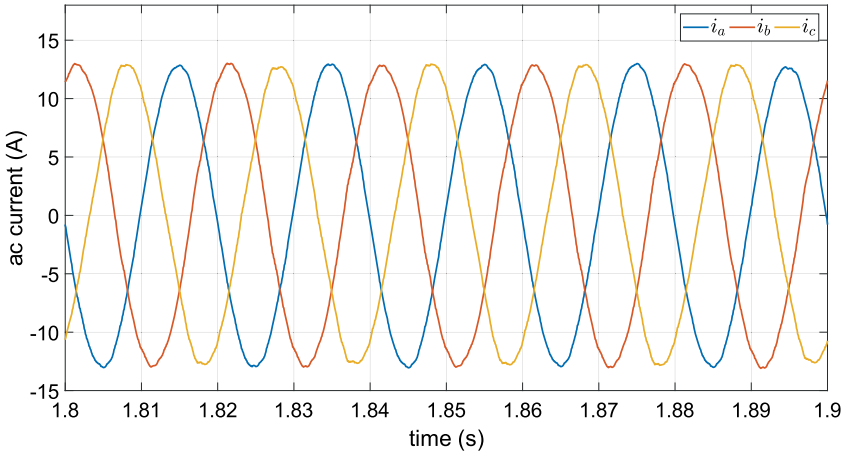


Fig. 5.12 AC currents in steady-state

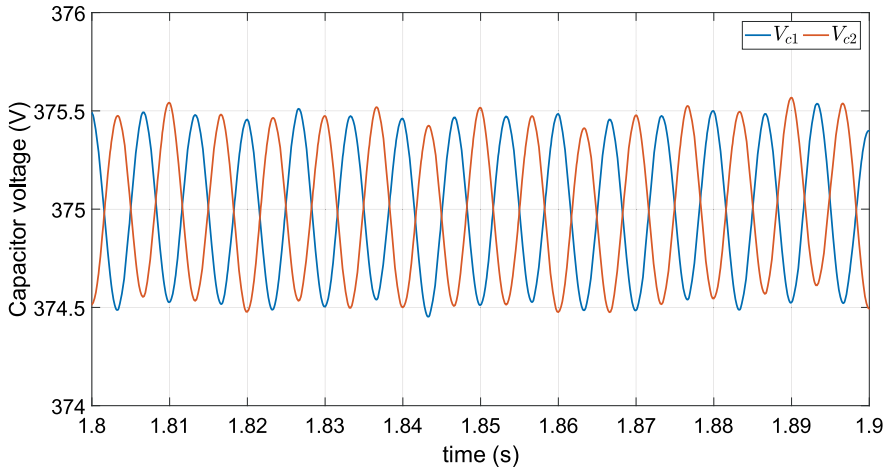


Fig. 5.13 Capacitor voltages

To test the robustness of the proposed control strategy, the simulations are done with increased level of load disturbance.

(2) Load case 2: $R_L = 31.25 \Omega$

In this case, the load disturbance is tripled (from case 1) to 18 kW.

As can be observed From Fig. 5.14, after the load disturbance is tripled, the proposed strategy demonstrates obvious advantage over pure PI control. For pure PI controller, the voltage drop is 120 V, the recovering time is 0.62 s. For the proposed strategy, the voltage drop is 30 V, only one fourth that of pure PI control, and the

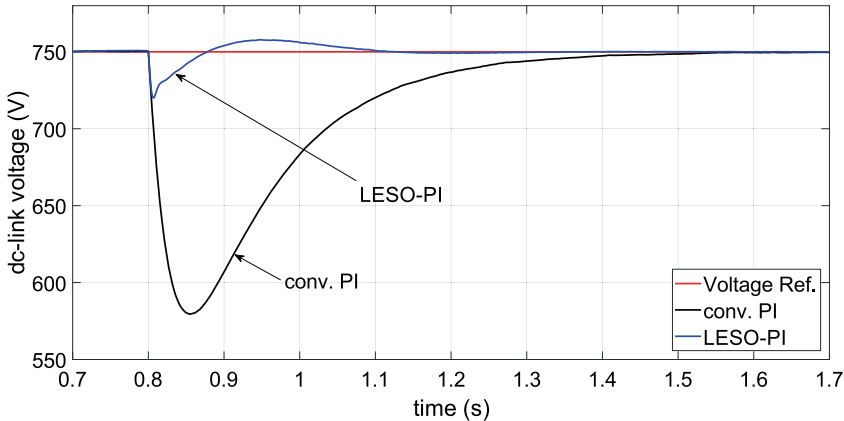


Fig. 5.14 DC-link voltage transient response of case 2

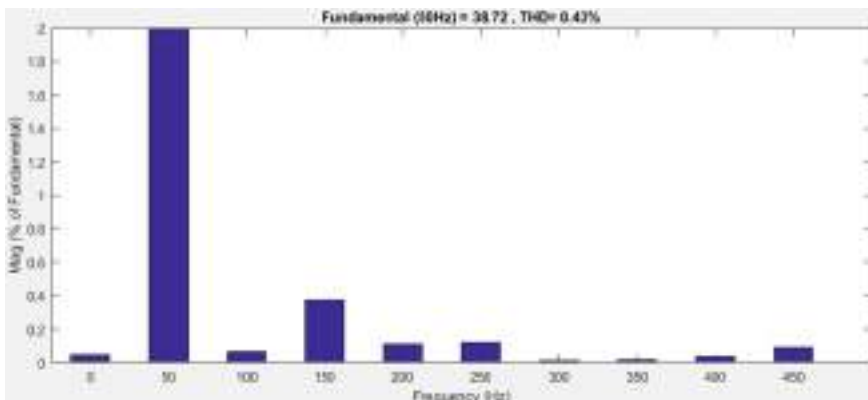


Fig. 5.15 Stead-state current THD of case 2: conv. PI

recovering time is 0.3 s, which is only half that of pure PI control, and the voltage overshoot is 7.8 V, which is rather small.

Comparing with case 1, the voltage drop of proposed strategy increases by 18 V, and the recovering time is similar. However, the voltage drop of PI control increases by 50 V, and the recovering time is doubled.

Figures 5.15 and 5.16 show the obtained current harmonic spectrum and THD for this load level, and the two control strategies result in similar current THD.

These results prove that the PI compensated by LESO is more robust than pure PI control.

(3) Load case 3: $R_L = 15.625 \Omega$

In this case, the load is doubled (from case 2) to 36 kW.

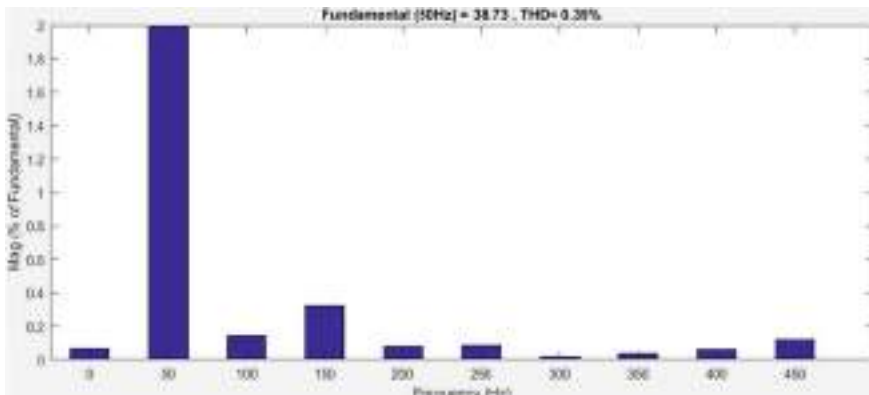


Fig. 5.16 Stead-state current THD of case 2: LESO-PI

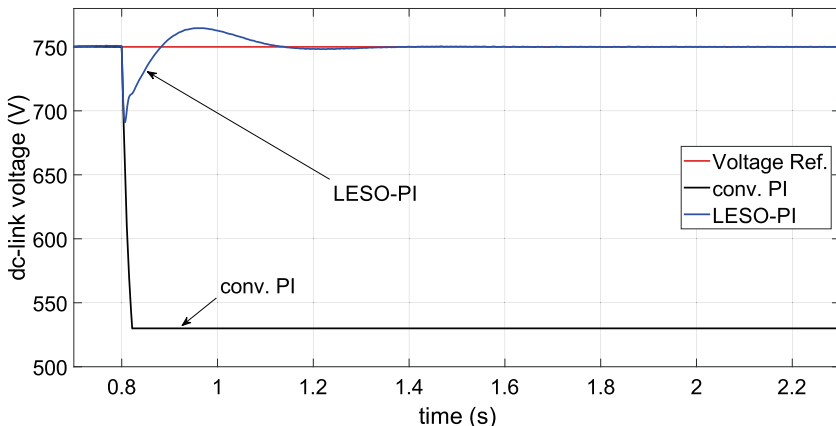


Fig. 5.17 DC-link voltage transient response of case 3

As shown in Fig. 5.17, the proposed strategy outperforms pure PI control, which is consistent with the former two load cases. With this large load disturbance, pure PI controller results in voltage drop of 240 V, which will trip the under-voltage fault. Thus the pure PI controller is no longer functional with this load unless the control parameters are readjusted. However, the proposed observer allows the controller to be functional without changing the parameters, it results in 59 V of voltage drop and relatively small recovering time and voltage overshoot.

Summarizing the above results, it can be observed that: LESO significantly improves the dc-link voltage transient performance, in terms of smaller voltage drop and shorter transient time; after being compensated by LESO, the robustness of PI controller against load variation is greatly improved, first, when disturbance increased to a certain level that pure PI can not work, LESO compensated PI still works and extends the operational range of the converter, second, the recovering time maintains

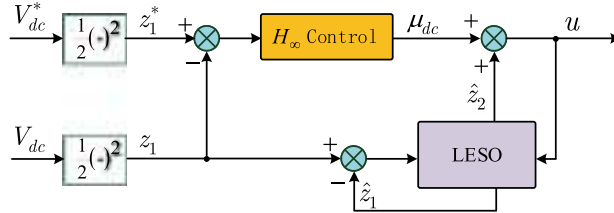


Fig. 5.18 Voltage regulation loop: H_∞ control based on LESO

almost the same as the load disturbance varies in a large range. Next, DPC based on H_∞ control will be carried out on the NPC.

5.3 Direct Power Control

DPC is a famous power converter control strategy developed based on instantaneous power theory [3]. It aims to directly track the reference power based on the active/reactive power error and the voltage vector position, rather than indirectly control the current. Therefore the current tracking loop is no longer needed, thus the control structure is simplified. Also because DPC adopts hysteresis control, it is of strong robustness and fast response.

5.3.1 Voltage Regulation Loop

As shown in Fig. 5.18, the voltage regulation loop adopts the LESO based H_∞ control strategy, which generates the power references and pass them to the power tracking loop.

DPC is usually applied in (α, β) frame, as in this frame the active and reactive power can already be explicitly expressed. Considering (5.6), define $p^* = v_{\alpha\beta}^T i_{\alpha\beta}^*$, $p_{load} = \frac{V_{dc}^2}{R_L}$, and assume that the power loop dynamic is much faster than the voltage loop, the NPC dc-link voltage dynamic can be written as:

$$C \frac{dV_{dc}}{dt} = \frac{1}{V_{dc}} (p^* - 2p_{load}). \quad (5.38)$$

As observed, the dc voltage dynamic in DPC mode is the same as that in VOC mode. Next to design LESO with a new method, to estimate the load disturbance.

(1) LESO design

Define $z_1 = \frac{V_{dc}^2}{2}$ as original system state variable, and extend the load disturbance as a new state variable $z_2 = \frac{2p_{load}}{C}$, then system model (5.38) can be expressed as:

$$\begin{cases} \dot{z}_1 = u - z_2, \\ \dot{z}_2 = h(t), \end{cases} \quad (5.39)$$

where $u = \frac{p^*}{C}$ is the control signal, $h(t)$ is the derivative of z_2 and it is assumed to be bounded. For the extended system (5.39), following LESO with bandwidth parameter is designed [5]:

$$\begin{cases} \dot{\hat{z}}_1 = u - \hat{z}_2 + 2\omega_0 e_1, \\ \dot{\hat{z}}_2 = -\omega_0^2 e_1, \end{cases} \quad (5.40)$$

where $\hat{z} = [\hat{z}_1 \hat{z}_2]^T$ is the estimated value of the state $z = [z_1 z_2]^T$, $e_1 = z_1 - \hat{z}_1$ is the observation error of z_1 , ω_0 is the band-width of LESO. The advantage of using ω_0 to select the observer parameter is that the two same poles can be expressed explicitly.

Define $e_2 = z_2 - \hat{z}_2$, the observation error dynamic can be obtained as follows:

$$\begin{cases} \dot{e}_1 = -2\omega_0 e_1 - e_2, \\ \dot{e}_2 = \omega_0^2 e_1 + h(t). \end{cases} \quad (5.41)$$

Define $\varepsilon_1 = \frac{e_1}{\omega_0}$, $\varepsilon_2 = \frac{e_2}{\omega_0^2}$, then (5.41) can be rewritten as:

$$\dot{\varepsilon} = \omega_0 A \varepsilon + \frac{1}{\omega_0^2} \varphi(t), \quad (5.42)$$

where $\varepsilon = [\varepsilon_1 \varepsilon_2]^T$, A is Hurwitz, $\varphi(t) = [0 \ h(t)]^T$.

Lemma 5.1 [6] For any bounded function $h(t)$, there exists a scalar δ to make $|h(t)| \leq \delta$, then the state estimate of system (5.42) is bounded, i.e.,

$$\|\varepsilon\| \leq \varrho, \quad \varrho = O\left(\frac{1}{\omega_0^\nu}\right), \quad \forall t \geq T, \quad (5.43)$$

where ν is a positive integral, and T is finite time.

(2) H_∞ controller design

Based on \hat{z}_2 , following controller is designed:

$$u = \mu_h(e) + \hat{z}_2, \quad (5.44)$$

where $\mu_h(e) = K e$, K is the controller parameter to be designed, $e = z_1^* - z_1$ is the error of dc-link voltage. The H_∞ control problem is to make the influence index from disturbance observation error e_2 to dc-link voltage error is less than γ :

$$\int_0^{+\infty} e^T(t)e(t)dt \leq \gamma^2 \int_0^{\infty} e_2(t)^T(t)e_2(t)dt. \quad (5.45)$$

To design the H_∞ controller K satisfying above requirements, the following lemma is introduced.

Lemma 5.2 [7] For matrices E and F with appropriate dimension, if

$$E^T F + E F^T < 0,$$

holds, then there exists a scalar $\kappa > 0$, which satisfies:

$$\kappa E^T E + \frac{1}{\kappa} F^T F < 0.$$

Theorem 5.3 For the H_∞ controlled system (10.12), let γ be positive, suppose there exist two positive definite symmetrical matrices P and W , which satisfy

$$\begin{bmatrix} -2W + 1 & P \\ P & -\gamma^2 I \end{bmatrix} \leq 0. \quad (5.46)$$

then system (10.12) is asymptotically stable, and satisfies H_∞ performance index γ , i.e., the dc-link voltage V_{dc} achieves its reference V_{dc}^* . Furthermore, if (5.46) is solvable, then the feasible control parameter is

$$K = W P^{-1}. \quad (5.47)$$

Proof Construct Lyapunov function for system (10.12):

$$V_v(e) = e^T P e. \quad (5.48)$$

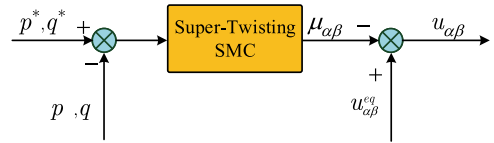
Differentiate the Lyapunov function along the trajectory of system (10.12), then

$$\begin{aligned} \dot{V}_v(e) &= \dot{e}^T P e + e^T P \dot{e} \\ &= -e^T (K^T P + P K) e + e_2^T P e + e^T P e_2. \end{aligned} \quad (5.49)$$

Base on Lemma 5.2, it is obtained that

$$\dot{V}_v(e) \leq e^T (-K^T P - P K + \gamma^{-2} P P) e + \gamma^2 e_2^T e_2. \quad (5.50)$$

Fig. 5.19 Power tracking loop: super-twisting SMC



Define following performance index for system (10.12):

$$\begin{aligned} J(e_2) &= \int_0^\infty (e^T e - \gamma^2 e_2^T e_2) dt \\ &= \int_0^\infty (e^T e - \gamma^2 e_2^T e_2 + \dot{V}_v(x)) dt - (V_v(\infty) - V_v(0)) \\ &\leq \int_0^\infty e^T (-K^T P - PK + \gamma^{-2} PP + I) edt - V(\infty). \end{aligned} \quad (5.51)$$

According to Schur Complement Lemma, (5.46) is equivalent to

$$-2W + \gamma^2 PP \leq 0. \quad (5.52)$$

Thus it can be obtained from (5.46) that

$$J(e_2) \leq \int_0^\infty e^T (-K^T P - PK + \gamma^{-2} PP + I) edt - V(\infty) \leq 0, \quad (5.53)$$

This indicates that for any non-zero observation error e_2 , the system (10.12) achieves the disturbance attenuation index γ . Obviously, if $e_2 = 0$, system is uniformly asymptotically stable. Proof completed. ■

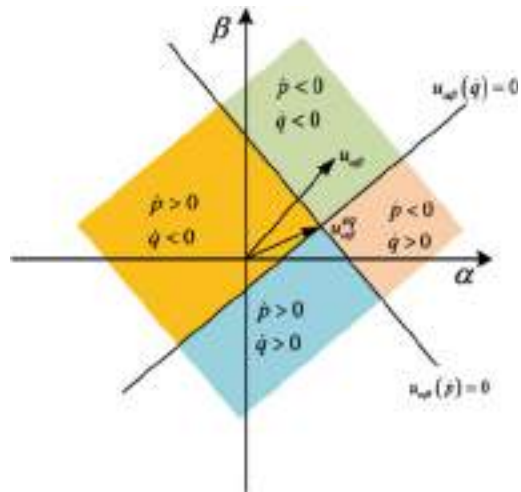
5.3.2 Power Tracking Loop

Figure 5.19 shows the power tracking loop adopting STA. The active power reference p^* is generated by the voltage loop, and the reactive power reference q^* is manually set. The task of power tracking loop is to make the active and reactive power, p and q , to converge to their references.

According to the definition of instantaneous power p and q [3], it can be obtained that:

$$p = v_{\alpha\beta}^T i_{\alpha\beta}, \quad q = v_{\alpha\beta}^T J i_{\alpha\beta}, \quad J = \begin{bmatrix} 0 & -1 \\ 1 & 0 \end{bmatrix}. \quad (5.54)$$

Fig. 5.20 Equivalent control point



According to (7.1), the dynamic equation of p and q can be expressed as:

$$\begin{aligned} L\dot{p} &= v_{\alpha\beta}^T \left(L\omega q \frac{v_{\alpha\beta}}{\|v_{\alpha\beta}\|^2} + v_{\alpha\beta} - \frac{V_{dc}}{2} u_{\alpha\beta} \right), \\ L\dot{q} &= v_{\alpha\beta}^T J^T \left(-L\omega p \frac{J v_{\alpha\beta}}{\|v_{\alpha\beta}\|^2} - \frac{V_{dc}}{2} u_{\alpha\beta} \right), \end{aligned} \quad (5.55)$$

where $\|v_{\alpha\beta}\|^2 = v_{\alpha\beta}^T v_{\alpha\beta}$. Let $\dot{p} = 0, \dot{q} = 0$, two straight lines in (α, β) plane can be obtained,

$$\frac{2}{V_{dc}} \left(\|v_{\alpha\beta}\|^2 + L\omega q \right) \frac{v_{\alpha\beta}}{\|v_{\alpha\beta}\|^2} + d_1 J v_{\alpha\beta} = 0, \quad (5.56)$$

$$-\frac{2}{V_{dc}} (L\omega p) \frac{J v_{\alpha\beta}}{\|v_{\alpha\beta}\|^2} + d_2 v_{\alpha\beta} = 0, \quad (5.57)$$

where d_1, d_2 are the constants to decide these two lines. As shown in Fig. 5.20, the (α, β) plane is divided into four parts by the lines (5.56) and (5.57).

The intersection point of these two lines is the system equilibrium, and satisfies $\dot{p} = 0, \dot{q} = 0$, and the equivalent control signal satisfying this point has following form:

$$u_{\alpha\beta}^{eq} = \frac{2}{V_{dc}} \left(1 + \frac{L\omega q}{\|v_{\alpha\beta}\|^2} \right) v_{\alpha\beta} - \frac{2}{V_{dc}} \frac{L\omega p}{\|v_{\alpha\beta}\|^2} J v_{\alpha\beta}. \quad (5.58)$$

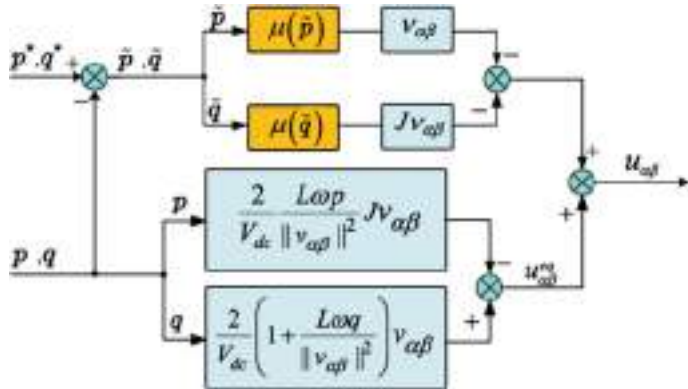


Fig. 5.21 Power tracking loop: detailed diagram

Define error signals as follow:

$$\begin{aligned}\tilde{p} &= p^* - p, \\ \tilde{q} &= q^* - q.\end{aligned}\quad (5.59)$$

Base on the equilibrium (5.58), sliding mode controller $u_{\alpha\beta}$ is designed as:

$$u_{\alpha\beta} = u_{\alpha\beta}^{eq} - \mu(\tilde{p})v_{\alpha\beta} - \mu(\tilde{q})Jv_{\alpha\beta}, \quad (5.60)$$

where $\mu(\tilde{p}), \mu(\tilde{q})$ adopts the following STA:

$$\mu(\tilde{p}) = \lambda_p |\tilde{p}|^{\frac{1}{2}} \text{sign}(\tilde{p}) + \alpha_p \int_0^t \text{sign}(\tilde{p}) dt, \quad (5.61)$$

$$\mu(\tilde{q}) = \lambda_q |\tilde{q}|^{\frac{1}{2}} \text{sign}(\tilde{q}) + \alpha_q \int_0^t \text{sign}(\tilde{q}) dt. \quad (5.62)$$

where $\lambda_p, \alpha_p, \lambda_q, \alpha_q$ are all positive. Figure 5.21 is the detailed control structure of power tracking loop.

Now the stability condition of power loop is to be analyzed. Differentiate the error signals \tilde{p}, \tilde{q} :

$$\begin{aligned}
\dot{\tilde{p}} &= \dot{p}^* - \frac{v_{\alpha\beta}^T}{L} \left[\left(1 + \frac{L\omega q}{||v_{\alpha\beta}||^2} \right) v_{\alpha\beta} - \frac{V_{dc}}{2} u_{\alpha\beta} \right] \\
&= \dot{p}^* - \frac{v_{\alpha\beta}^T}{L} \left\{ \left(1 + \frac{L\omega q}{||v_{\alpha\beta}||^2} \right) v_{\alpha\beta} - \frac{V_{dc}}{2} \left[u_{\alpha\beta}^{eq} - \mu(\tilde{p}) v_{\alpha\beta} - \mu(\tilde{q}) J v_{\alpha\beta} \right] \right\} \\
&= \dot{p}^* - \frac{1}{L} \left[\left(1 + \frac{L\omega q}{||v_{\alpha\beta}||^2} \right) ||v_{\alpha\beta}||^2 - \frac{V_{dc} v_{\alpha\beta}^T}{2} u_{\alpha\beta}^{eq} + \frac{V_{dc} v_{\alpha\beta}^T}{2} \mu(\tilde{p}) v_{\alpha\beta} \right. \\
&\quad \left. + \frac{V_{dc} v_{\alpha\beta}^T}{2} \mu(\tilde{q}) J v_{\alpha\beta} \right], \tag{5.63}
\end{aligned}$$

$$\begin{aligned}
\dot{\tilde{q}} &= \dot{q}^* + \frac{v_{\alpha\beta}^T J^T}{L} \left(L\omega p \frac{J v_{\alpha\beta}}{||v_{\alpha\beta}||^2} + \frac{V_{dc}}{2} u_{\alpha\beta} \right) \\
&= \dot{q}^* + \frac{v_{\alpha\beta}^T J^T}{L} \left\{ L\omega p \frac{J v_{\alpha\beta}}{||v_{\alpha\beta}||^2} + \frac{V_{dc}}{2} \left(u_{\alpha\beta}^{eq} - \mu(\tilde{p}) v_{\alpha\beta} - \mu(\tilde{q}) J v_{\alpha\beta} \right) \right\} \\
&= \dot{q}^* + \frac{1}{L} \left[L\omega p \frac{v_{\alpha\beta}^T J^T J v_{\alpha\beta}}{||v_{\alpha\beta}||^2} + \frac{V_{dc} v_{\alpha\beta}^T J^T}{2} u_{\alpha\beta}^{eq} \right. \\
&\quad \left. - \frac{V_{dc} v_{\alpha\beta}^T J^T}{2} \mu(\tilde{p}) v_{\alpha\beta} - \frac{V_{dc} v_{\alpha\beta}^T J^T}{2} \mu(\tilde{q}) J v_{\alpha\beta} \right]. \tag{5.64}
\end{aligned}$$

Considering $v_{\alpha\beta}^T J^T J v_{\alpha\beta} = ||v_{\alpha\beta}||^2$ and $v_{\alpha\beta}^T J^T v_{\alpha\beta} = 0$, the third terms of (5.63) and (5.64) are calculated as follow:

$$\begin{aligned}
\frac{V_{dc} v_{\alpha\beta}^T}{2} u_{\alpha\beta}^{eq} &= \frac{V_{dc} v_{\alpha\beta}^T}{2} \frac{2}{V_{dc}} \left(1 + \frac{L\omega q}{||v_{\alpha\beta}||^2} \right) v_{\alpha\beta} - \frac{V_{dc} v_{\alpha\beta}^T}{2} \frac{2}{V_{dc}} \frac{L\omega p}{||v_{\alpha\beta}||^2} J v_{\alpha\beta} \\
&= \left(1 + \frac{L\omega q}{||v_{\alpha\beta}||^2} \right) ||v_{\alpha\beta}||^2, \tag{5.65}
\end{aligned}$$

$$\begin{aligned}
\frac{V_{dc} v_{\alpha\beta}^T J^T}{2} u_{\alpha\beta}^{eq} &= \frac{V_{dc} v_{\alpha\beta}^T J^T}{2} \frac{2}{V_{dc}} \left(1 + \frac{L\omega q}{||v_{\alpha\beta}||^2} \right) v_{\alpha\beta} - \frac{V_{dc} v_{\alpha\beta}^T J^T}{2} \frac{2}{V_{dc}} \frac{L\omega p}{||v_{\alpha\beta}||^2} J v_{\alpha\beta} \\
&= -L\omega p \frac{v_{\alpha\beta}^T J^T J v_{\alpha\beta}}{||v_{\alpha\beta}||^2}. \tag{5.66}
\end{aligned}$$

Substitute (5.65) and (5.66) back to (5.63) and (5.64), it can be obtained that

$$\dot{\tilde{p}} = -\frac{V_{dc}}{2L} ||v_{\alpha\beta}||^2 \mu(\tilde{p}) + \dot{p}^*, \tag{5.67}$$

$$\dot{\tilde{q}} = -\frac{V_{dc}}{2L} ||v_{\alpha\beta}||^2 \mu(\tilde{q}) + \dot{q}^*. \tag{5.68}$$

As observed, the active power p and the reactive power q have been decoupled, and the sliding mode controller can directly act on the corresponding error signals \tilde{p} and \tilde{q} .

Next to design control parameters for system (5.67) and (5.68). Let $K = \frac{V_{dc}}{2L} ||v_{\alpha\beta}||^2$, the control parameters adopt following form:

$$\begin{aligned}\lambda_p &= \lambda_0 \Gamma_p / K, & \alpha_p &= \alpha_0 \Gamma_p^2 / K, \\ \lambda_q &= \lambda_0 \Gamma_q / K, & \alpha_q &= \alpha_0 \Gamma_q^2 / K,\end{aligned}\quad (5.69)$$

where $\lambda_0, \alpha_0, \Gamma_p, \Gamma_q$ are positive. Let $\zeta_{p1} = \Gamma_p |\tilde{p}|^{\frac{1}{2}} \text{sign}(\tilde{p})$, then system (5.67) can be rewritten as:

$$\begin{aligned}\dot{\tilde{p}} &= -\lambda_0 \zeta_{p1} + \zeta_{p2}, \\ \dot{\zeta}_{p2} &= -\alpha_0 \Gamma_p^2 \text{sign}(\tilde{p}) + \ddot{p}^*.\end{aligned}\quad (5.70)$$

Let $\zeta_{q1} = \Gamma_q |\tilde{q}|^{\frac{1}{2}} \text{sign}(\tilde{q})$, then system (5.68) becomes:

$$\begin{aligned}\dot{\tilde{q}} &= -\lambda_0 \zeta_{q1} + \zeta_{q2}, \\ \dot{\zeta}_{q2} &= -\alpha_0 \Gamma_q^2 \text{sign}(\tilde{q}) + \ddot{q}^*.\end{aligned}\quad (5.71)$$

Theorem 5.4 For systems (5.70) and (5.71), if there exist two positive scalars δ_p and δ_q , and the second-order derivatives of active and reactive power references p^* and q^* respectively satisfy $|\ddot{p}^*| \leq \delta_p$, $|\ddot{q}^*| \leq \delta_q$, then the condition for the system to converge in finite time is:

$$\begin{aligned}\Gamma_p^2 &> \frac{2\delta_p \lambda_{\max}(Q_1)}{\lambda_{\min}(Q)}, \\ \Gamma_q^2 &> \frac{2\delta_q \lambda_{\max}(Q_1)}{\lambda_{\min}(Q)},\end{aligned}\quad (5.72)$$

where $Q = \lambda_0 \begin{bmatrix} \lambda_0^2 + 2\alpha_0 & -\lambda_0 \\ -\lambda_0 & 1 \end{bmatrix}$, $Q_1 = \begin{bmatrix} \lambda_0 & 1 \\ 1 & 0 \end{bmatrix}$. The converging time is no longer than $T = \max\{T_p, T_q\}$ time unit, where $T_p = \frac{2V_p^{\frac{1}{2}}(\zeta_p(0))}{\gamma_p}$, $T_q = \frac{2V_q^{\frac{1}{2}}(\zeta_q(0))}{\gamma_q}$.

Proof For systems (5.70) and (5.71), construct following Lyapunov functions:

$$V_p(\tilde{p}) = \zeta_p^T P \zeta_p, \quad V_q(\tilde{q}) = \zeta_q^T P \zeta_q, \quad (5.73)$$

where $\zeta_p = [\zeta_{p1}, \zeta_{p2}]^T$, $\zeta_q = [\zeta_{q1}, \zeta_{q2}]^T$, $P = \frac{1}{2} \begin{bmatrix} \lambda_0^2 + 4\alpha_0 & -\lambda_0 \\ -\lambda_0 & 2 \end{bmatrix}$.

First, take derivative of ζ_p, ζ_q :

$$\begin{aligned}\dot{\zeta}_{p1} &= \Gamma_p \frac{1}{2} |\tilde{p}|^{-\frac{1}{2}} \dot{\tilde{p}} = \frac{\Gamma_p}{2|\tilde{p}|^{\frac{1}{2}}} (-\lambda_0 \zeta_{p1} + \zeta_{p2}), \\ \dot{\zeta}_{p2} &= -\frac{1}{|\tilde{p}|^{\frac{1}{2}}} \alpha_0 \Gamma_p^2 |\tilde{p}|^{\frac{1}{2}} \text{sign}(\tilde{p}) + \ddot{p}^* = \frac{\Gamma_p}{2|\tilde{p}|^{\frac{1}{2}}} (-2\alpha_0 \zeta_{p1}) + \ddot{p}^*, \\ \dot{\zeta}_{q1} &= \Gamma_q \frac{1}{2} |\tilde{q}|^{-\frac{1}{2}} \dot{\tilde{q}} = \frac{\Gamma_q}{2|\tilde{q}|^{\frac{1}{2}}} (-\lambda_0 \zeta_{q1} + \zeta_{q2}), \\ \dot{\zeta}_{q2} &= -\frac{1}{|\tilde{q}|^{\frac{1}{2}}} \alpha_0 \Gamma_q^2 |\tilde{q}|^{\frac{1}{2}} \text{sign}(\tilde{q}) + \ddot{q}^* = \frac{\Gamma_q}{2|\tilde{q}|^{\frac{1}{2}}} (-2\alpha_0 \zeta_{q1}) + \ddot{q}^*.\end{aligned}$$

Write it in matrix form as follows:

$$\dot{\zeta}_p = \frac{\Gamma_p}{2|\tilde{p}|^{\frac{1}{2}}} \underbrace{\begin{bmatrix} -\lambda_0 & 1 \\ -2\alpha_0 & 0 \end{bmatrix}}_A \zeta_p + \begin{bmatrix} 0 \\ \ddot{p}^* \end{bmatrix}, \quad \dot{\zeta}_q = \frac{\Gamma_q}{2|\tilde{q}|^{\frac{1}{2}}} \underbrace{\begin{bmatrix} -\lambda_0 & 1 \\ -2\alpha_0 & 0 \end{bmatrix}}_A \zeta_q + \begin{bmatrix} 0 \\ \ddot{q}^* \end{bmatrix}. \quad (5.74)$$

Then take the derivative of the Lyapunov function (5.73) along the trajectory of system (5.74):

$$\begin{aligned}\dot{V}_p &= \zeta_p^T P \dot{\zeta}_p + \dot{\zeta}_p^T P \zeta_p \\ &= \frac{\Gamma_p}{2|\tilde{p}|^{\frac{1}{2}}} \zeta_p^T (A^T P + PA) \zeta_p + 2\zeta_p^T P \begin{bmatrix} 0 \\ \ddot{p}^* \end{bmatrix} \\ &= -\frac{\Gamma_p}{2|\tilde{p}|^{\frac{1}{2}}} \zeta_p^T Q \zeta_p + \kappa^T \zeta_p \ddot{p}^*,\end{aligned} \quad (5.75)$$

$$\begin{aligned}\dot{V}_q &= \zeta_q^T P \dot{\zeta}_q + \dot{\zeta}_q^T P \zeta_q \\ &= \frac{\Gamma_q}{2|\tilde{q}|^{\frac{1}{2}}} \zeta_q^T (A^T P + PA) \zeta_q + 2\zeta_q^T P \begin{bmatrix} 0 \\ \ddot{q}^* \end{bmatrix} \\ &= -\frac{\Gamma_q}{2|\tilde{q}|^{\frac{1}{2}}} \zeta_q^T Q \zeta_q + \kappa^T \zeta_q \ddot{q}^*,\end{aligned} \quad (5.76)$$

where

$$Q = \lambda_0 \begin{bmatrix} \lambda_0^2 + 2\alpha_0 & -\lambda_0 \\ -\lambda_0 & 1 \end{bmatrix}, \quad \kappa = [-\lambda_0 \ 2]^T. \quad (5.77)$$

It can be seen that Q is positive definite. It can be obtained that:

$$\begin{aligned}\kappa^T \zeta_p \ddot{p}^* &\leq \max\left\{\frac{\delta_p}{\Gamma_p |\tilde{p}|^{\frac{1}{2}}} \zeta_p^T Q_1 \zeta_p, \frac{\delta_p}{\Gamma_p |\tilde{p}|^{\frac{1}{2}}} \zeta_p^T Q_2 \zeta_p\right\} = \frac{\delta_p}{\Gamma_p |\tilde{p}|^{\frac{1}{2}}} \lambda_{\max}(Q_1) \|\zeta_p\|_2^2, \\ \kappa^T \zeta_q \ddot{q}^* &\leq \max\left\{\frac{\delta_q}{\Gamma_q |\tilde{q}|^{\frac{1}{2}}} \zeta_q^T Q_1 \zeta_q, \frac{\delta_q}{\Gamma_q |\tilde{q}|^{\frac{1}{2}}} \zeta_q^T Q_2 \zeta_q\right\} = \frac{\delta_q}{\Gamma_q |\tilde{q}|^{\frac{1}{2}}} \lambda_{\max}(Q_1) \|\zeta_q\|_2^2,\end{aligned}$$

where

$$Q_1 = \begin{bmatrix} \lambda_0 & 1 \\ 1 & 0 \end{bmatrix}, \quad Q_2 = \begin{bmatrix} \lambda_0 & -1 \\ -1 & 0 \end{bmatrix}.$$

Considering $\lambda_{\min}(P)\|\zeta_p\|_2^2 \leq V_p \leq \lambda_{\max}(P)\|\zeta_p\|_2^2$ ($\|\cdot\|_2$ is Euclidean norm), thus $-\|\zeta_p\|_2 \leq -\frac{V_p^{\frac{1}{2}}}{\lambda_{\max}^{\frac{1}{2}}(P)}$, further it leads to:

$$\begin{aligned} \dot{V}_p &\leq -\frac{\Gamma_p}{2|\tilde{p}|^{\frac{1}{2}}}\lambda_{\min}(Q)\|\zeta_p\|_2^2 + \frac{\delta_p}{\Gamma_p|\tilde{p}|^{\frac{1}{2}}}\lambda_{\max}(Q_1)\|\zeta_p\|_2^2 \\ &= -\left(\frac{\Gamma_p^2}{2|\zeta_{p1}|}\lambda_{\min}(Q) - \frac{\delta_p}{|\zeta_{p1}|}\lambda_{\max}(Q_1)\right)\|\zeta_p\|_2^2 \\ &\leq -\left(\frac{\Gamma_p^2}{2}\lambda_{\min}(Q) - \delta_p\lambda_{\max}(Q_1)\right)\|\zeta_p\|_2 \\ &\leq -\left(\frac{\Gamma_p^2}{2}\lambda_{\min}(Q) - \delta_p\lambda_{\max}(Q_1)\right)\frac{V_p^{\frac{1}{2}}}{\lambda_{\max}^{\frac{1}{2}}(P)} \\ &= -\gamma_p V_p^{\frac{1}{2}}, \end{aligned} \tag{5.78}$$

$$\begin{aligned} \dot{V}_q &\leq -\frac{\Gamma_q}{2|\tilde{q}|^{\frac{1}{2}}}\lambda_{\min}(Q)\|\zeta_q\|_2^2 + \frac{\delta_q}{\Gamma_q|\tilde{q}|^{\frac{1}{2}}}\lambda_{\max}(Q_1)\|\zeta_q\|_2^2 \\ &= -\left(\frac{\Gamma_q^2}{2|\zeta_{q1}|}\lambda_{\min}(Q) - \frac{\delta_q}{|\zeta_{q1}|}\lambda_{\max}(Q_1)\right)\|\zeta_q\|_2^2 \\ &\leq -\left(\frac{\Gamma_q^2}{2}\lambda_{\min}(Q) - \delta_q\lambda_{\max}(Q_1)\right)\|\zeta_q\|_2 \\ &\leq -\left(\frac{\Gamma_q^2}{2}\lambda_{\min}(Q) - \delta_q\lambda_{\max}(Q_1)\right)\frac{V_q^{\frac{1}{2}}}{\lambda_{\max}^{\frac{1}{2}}(P)} \\ &= -\gamma_q V_q^{\frac{1}{2}}, \end{aligned} \tag{5.79}$$

where $\gamma_p = \frac{\left(\frac{\Gamma_p^2}{2}\lambda_{\min}(Q) - \delta_p\lambda_{\max}(Q_1)\right)}{\lambda_{\max}^{\frac{1}{2}}(P)}$, $\gamma_q = \frac{\left(\frac{\Gamma_q^2}{2}\lambda_{\min}(Q) - \delta_q\lambda_{\max}(Q_1)\right)}{\lambda_{\max}^{\frac{1}{2}}(P)}$. When

the condition (5.72) holds, $\dot{V}_p \leq 0$, $\dot{V}_q \leq 0$, system is stable.

As for the convergence time, consider the solution of differentiation equation $\dot{v} = -\gamma v^{\frac{1}{2}}$, $v(0) = v_0 \geq 0$ is $v(t) = \left(v_0^{\frac{1}{2}} - \frac{\gamma}{2}t\right)^2$, then according to the comparison principle [8], if $V_p(\zeta_p(0)) \leq v_0$, then $V_p(\zeta_p(t)) \leq v(t)$. Therefore, it can be seen from (5.78), $V_p(\zeta_p(t))$ converges in finite time, and the errors \tilde{p} and \tilde{q} respectively

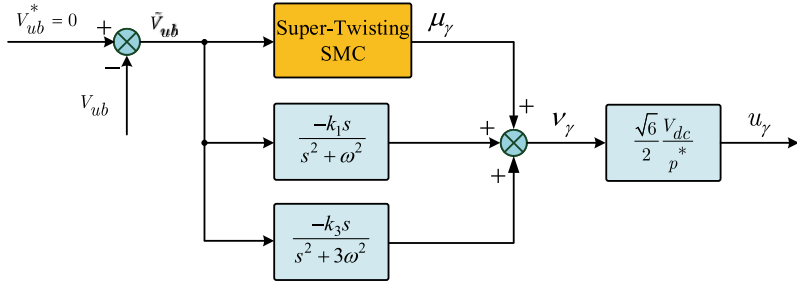


Fig. 5.22 Capacitor voltage balancing loop: super-twisting SMC

converge to the sliding surfaces $\tilde{p} = \dot{\tilde{p}} = 0$ and $\tilde{q} = \dot{\tilde{q}} = 0$. The converging times are respectively no longer than $T_p = \frac{2V_p^{\frac{1}{2}}(\zeta_p(0))}{\gamma_p}$ and $T_q = \frac{2V_q^{\frac{1}{2}}(\zeta_q(0))}{\gamma_q}$ time unit, therefore the converging time of the whole system is no more than $T = \max\{T_p, T_q\}$ time unit. Proof completed. ■

5.3.3 Voltage Balancing Loop

For convenient analysis, the dynamic of capacitor voltage difference is given again here:

$$C \frac{dV_{ub}}{dt} = \frac{2p^*}{\sqrt{6}V_{dc}} u_\gamma + \Phi(t), \quad (5.80)$$

As shown in Fig. 5.22, the voltage balance loop adopts adaptive control based on STA.

Define the error signal as:

$$\tilde{V}_{ub} = V_{ub}^* - V_{ub}. \quad (5.81)$$

Design controller as:

$$v_\gamma = \mu_\gamma(\tilde{V}_{ub}) - \Phi(t), \quad (5.82)$$

$$u_\gamma = \frac{\sqrt{6}V_{dc}}{2p^*} v_\gamma. \quad (5.83)$$

where μ_γ adopts STA, i.e.,

$$\mu_\gamma(\tilde{V}_{ub}) = \lambda_{ub} |\tilde{V}_{ub}|^{\frac{1}{2}} \text{sign}(\tilde{V}_{ub}) + \alpha_{ub} \int_0^t \text{sign}(\tilde{V}_{ub}) dt. \quad (5.84)$$

It can be seen that, control signal u_γ employs $\Phi(t)$ to reject its disturbance. If $\Phi(t)$ can be measured in real time, then with the control signal, the error dynamic becomes:

$$C \frac{d\tilde{V}_{ub}}{dt} = -\mu_\gamma(\tilde{V}_{ub}). \quad (5.85)$$

In this case, if μ_γ can converge, then \tilde{V}_{ub} can converge to the equilibrium. However, in real application $\Phi(t)$ is hard to measure, which is the reason it can hardly rejected. To solve this problem, an adaptive estimator is proposed to estimate its value.

Consider that $\Phi(t)$ is composed of base waveform and third harmonic, its estimated value can be written in following form:

$$\hat{\Phi}(t) = \sum_{n=1,3} \rho_n^T \Psi_n, \quad \rho_n = \begin{bmatrix} \cos(n\omega t) \\ \sin(n\omega t) \end{bmatrix}, \quad \Psi_n = \begin{bmatrix} \Psi_n^r \\ \Psi_n^i \end{bmatrix}. \quad (5.86)$$

Then the system dynamic becomes:

$$C \frac{d\tilde{V}_{ub}}{dt} = -\mu_\gamma(\tilde{V}_{ub}) + \tilde{\Phi}(t), \quad (5.87)$$

$$\tilde{\Phi}(t) = \hat{\Phi}(t) - \Phi(t). \quad (5.88)$$

Next the Lyapunov method is adopted to design the adaptive estimator to estimate $\Phi(t)$. Construct following Lyapunov function:

$$V = \frac{1}{2} C \tilde{V}_{ub}^2 + \sum_{n=1,3} \frac{1}{2k_n} \tilde{\Psi}_n^T \tilde{\Psi}_n. \quad (5.89)$$

Differentiate (5.89) and obtain:

$$\begin{aligned} \dot{V} &= -\mu_\gamma(\tilde{V}_{ub}) \tilde{V}_{ub} + \sum_{n=1,3} \tilde{V}_{ub} \rho_n^T \tilde{\Psi}_n + \sum_{n=1,3} \frac{1}{k_n} \dot{\tilde{\Psi}}_n^T \tilde{\Psi}_n \\ &= -V_1 + \sum_{n=1,3} \tilde{V}_{ub} \rho_n^T \tilde{\Psi}_n + \sum_{n=1,3} \frac{1}{k_n} \dot{\tilde{\Psi}}_n^T \tilde{\Psi}_n, \end{aligned} \quad (5.90)$$

where $V_1 = \mu_\gamma(\tilde{V}_{ub}) \tilde{V}_{ub}$.

First discuss the sign of V_1 . From (5.86), it can be seen that, if the ST control signal μ_γ can make \tilde{V}_{ub} asymptotically stable, then μ_γ and \tilde{V}_{ub} have the same sign, i.e., $V_1 > 0$. Then analyze the convergence of μ_γ . Write (5.84) in following form:

$$\mu_\gamma(\tilde{V}_{ub}) = \lambda_{ub} \xi_1 + \xi_2, \quad (5.91)$$

where $\zeta = [\zeta_1, \zeta_2]^T$, $\zeta_1 = |\tilde{V}_{ub}|^{\frac{1}{2}} \text{sign}(\tilde{V}_{ub})$, $\zeta_2 = \alpha_{ub} \int_0^t \text{sign}(\tilde{V}_{ub}) dt$.

Construct following Lyapunov function for system (5.91):

$$\begin{aligned} V_2(\tilde{V}_{ub}) &= 2\alpha_{ub}\zeta_1^2 + \frac{1}{2}\zeta_2^2 + \frac{1}{2}(\lambda_{ub}\zeta_1 - \zeta_2)^2 \\ &= \zeta^T P \zeta, \end{aligned}$$

$$\text{where } P = \frac{1}{2} \begin{bmatrix} 4\alpha_{ub} + \lambda_{ub}^2 & -\lambda_{ub} \\ -\lambda_{ub} & 2 \end{bmatrix}.$$

Note that $V_2(\tilde{V}_{ub})$ is continuous but not differentiable at $\tilde{V}_{ub} = 0$, but satisfies:

$$\lambda_{\min}\{P\}\|\zeta\|_2^2 \leq V_2(\tilde{V}_{ub}) \leq \lambda_{\max}\{P\}\|\zeta\|_2^2,$$

where $\lambda_{\max/\min}\{P\}$ represents the max./min. value of matrix P , $\|\zeta\|_2^2 = |\zeta_1| + \zeta_2^2$ is the Euclidean norm of ζ . Differentiate V_2 and obtain:

$$\dot{V}_2 = -\frac{1}{|\zeta_1|^{\frac{1}{2}}} \zeta^T Q \zeta \leq -\frac{1}{|\zeta_1|^{\frac{1}{2}}} \lambda_{\min}\{Q\}\|\zeta\|_2^2,$$

where

$$Q = \frac{\lambda_{ub}}{2} \begin{bmatrix} 2\alpha_{ub} + \lambda_{ub}^2 & -\lambda_{ub} \\ -\lambda_{ub} & 1 \end{bmatrix}.$$

It can be seen that, if $\lambda_{ub} > 0$, $\alpha_{ub} > 0$, then Q is positive definite, then $\dot{V}_2 < 0$, and system variable \tilde{V}_{ub} converges to the equilibrium in finite time. Thus in (5.90), $V_1 > 0$, thus if the last two terms can cancel each other, it can be ensured that $\dot{V} < 0$, and the system is asymptotically stable. Based on this consideration, the adaptive law is designed as follows:

$$\dot{\hat{\Psi}}_n \cong \dot{\tilde{\Psi}}_n = -k_n \tilde{V}_{ub} \rho_n^T. \quad (5.92)$$

Following the procedures in [9], the adaptive law (5.92) can further simplified to be following resonant filter to estimate $\Phi(t)$:

$$\hat{\Phi}(t) = \frac{-k_n s}{s^2 + (n\omega)^2} \tilde{V}_{ub}^2, \quad n \in \{1, 3\}. \quad (5.93)$$

To now, the capacitor voltage balance loop as shown in Fig. 5.22 has been obtained.

Table 5.3 System parameters

Parameter	Value	Description
f_1	$1 \cdot 10^6$	Simulation rate (Hz)
f_2	$1 \cdot 10^4$	Control update rate (Hz)
f_3	$1 \cdot 10^4$	Switching frequency (Hz)
R_L	22.5	Load resistance (Ω)
C	3300	DC-link capacitor (μF)
L	2	Filtering inductor (mH)
f	50	Grid voltage frequency (Hz)
v_{abc}	400	Grid line voltage (V)
V_{dc}^*	750	DC-link voltage reference (V)

Table 5.4 Control parameters

Vol. Reg. loop	Pow. Tra. loop	Vol. Bal. loop
$\gamma = 0.1$	$\lambda_p = \lambda_q = 3.5 \cdot 10^{-6}$	$\lambda_{ub} = 0.2$
$K = 75$	$\alpha_p = \alpha_q = 9.0 \cdot 10^{-2}$	$\alpha_{ub} = 10$
$\omega_0 = 400$		$k_1 = 0$
		$k_3 = 1600$

5.3.4 Simulation Verification

This section verifies the effectiveness of LESO- \mathcal{H}_∞ control strategy via simulation, using conventional PI as comparison baseline. Table 5.3 shows the simulation parameter of the converter. To test the robustness of LESO- \mathcal{H}_∞ against load variation and parameter uncertainty, a resistive load step from 0Ω to 22.5Ω is imposed on the system at $t = 0.6$ s, and deviate the filtering inductance by 30% of its nominal value. Table 5.4 shows the control parameter, which satisfies that the power loop dynamic is faster than the voltage loop dynamic. The PI parameters are tuned to obtain good performance.

As shown in Fig. 5.23, $0 \sim 0.25$ s is the converter pre-charging time, and the controller starts operation after pre-charge. It can be seen that, with LESO- \mathcal{H}_∞ control, the dc-link voltage is robust against load variation, and the resulted voltage drop is smaller than of PI, i.e., after load is connected at $t = 0.6$ s, PI results in 50 V voltage drop, while LESO- \mathcal{H}_∞ results in only 30 V voltage drop.

Figures 5.24 and 5.25 show the power tracking performance when there exist load variation and parameter uncertainty. As can be seen, LESO- \mathcal{H}_∞ results in faster dynamic. In steady state, the active power is maintained at 25 kW, and reactive power is maintained at 0 kVAr. Figure 5.26 shows the steady-state error of the instantaneous active and reactive power, which is less than 2%.

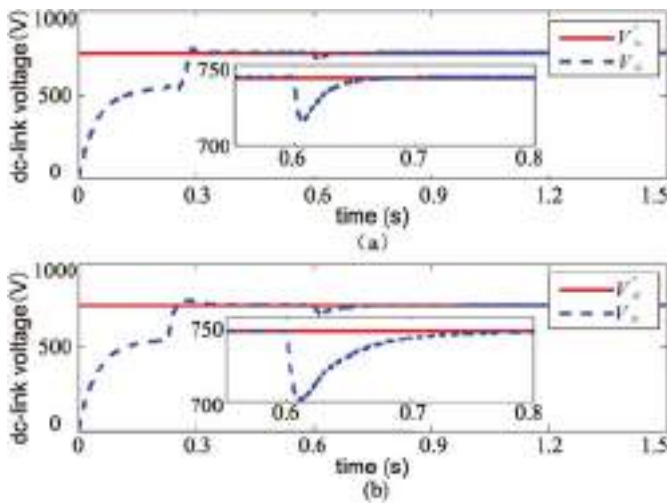


Fig. 5.23 DC-link voltage transient response: **a** LESO- \mathcal{H}_∞ control, **b** PI control

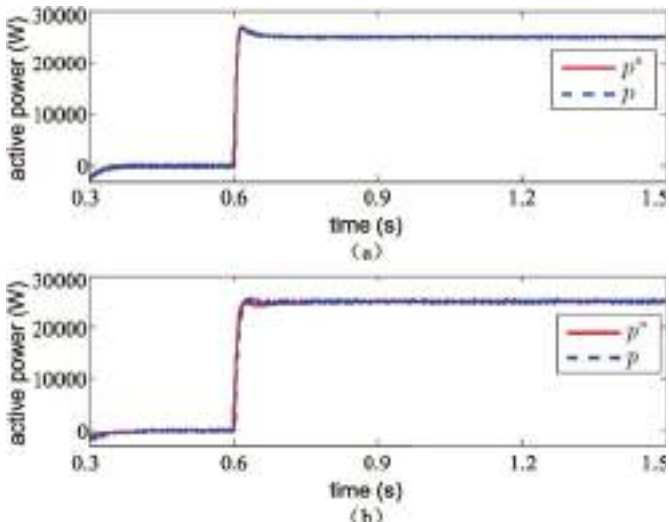


Fig. 5.24 Active power tracking: **a** LESO- \mathcal{H}_∞ control, **b** PI control

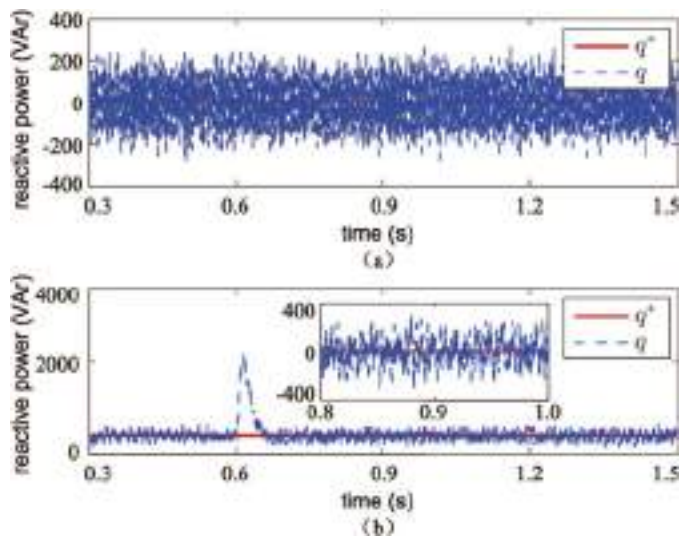


Fig. 5.25 Reactive power tracking: **a** LESO- \mathcal{H}_∞ control, **b** PI control

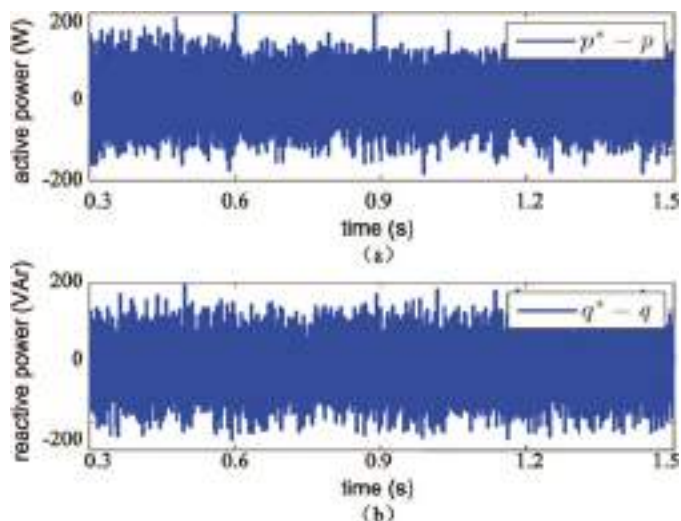


Fig. 5.26 Tracking errors of instantaneous active and reactive power

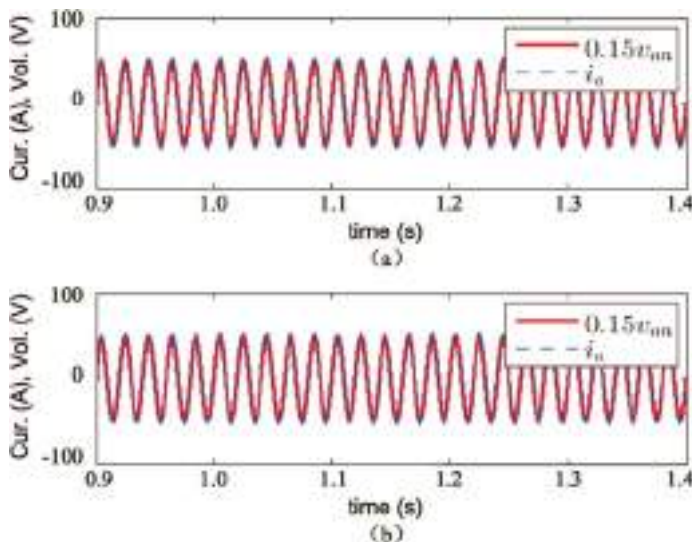


Fig. 5.27 Grid voltage and current: **a** LESO- \mathcal{H}_∞ control, **b** PI control

Figure 5.27 shows grid voltage with one phase (e_a) and corresponding current (i_a). As can be seen, for both LESO- \mathcal{H}_∞ control and PI control, there is no phase offset between the voltage and current, meaning that both control strategies can achieve unity power factor. However, from Fig. 5.28, with LESO- \mathcal{H}_∞ control, the current THD of i_a is obviously reduced, from 2.4% (of PI) to 1%. Figure 5.29 shows the voltage balance result.

5.4 Summary

Based on the work of the three-phase two-level converter, this chapter investigates the advantageous control strategies for three-phase NPC. In order to extend control modes, this chapter carries out the control both in VOC and DPC mode. Firstly, in VOC mode, the performance improvement brought by LESO is verified. The simulation results show that, LESO not only can significantly improve the dc-link voltage transient response, also can it improve the robustness of PI controller against load variation. After that, in DPC mode, the voltage regulation, power tracking and capacitor voltage balance have been carried out. In voltage regulation loop, a \mathcal{H}_∞ control based on LESO has been designed. The LESO estimate the load power in real time to improve the disturbance rejection ability and voltage regulation performance, while the \mathcal{H}_∞ controller ensures that the impact index from the observation error to dc output voltage is less than γ . In power tracking loop, the ST-SMC is adopted to drive the active and reactive power to reach their references. In capacitor voltage

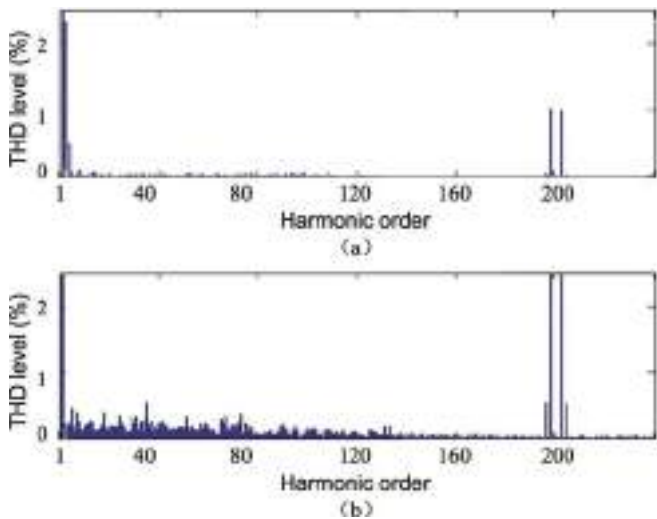


Fig. 5.28 Current harmonic spectrum: **a** LESO- \mathcal{H}_∞ control, **b** PI control

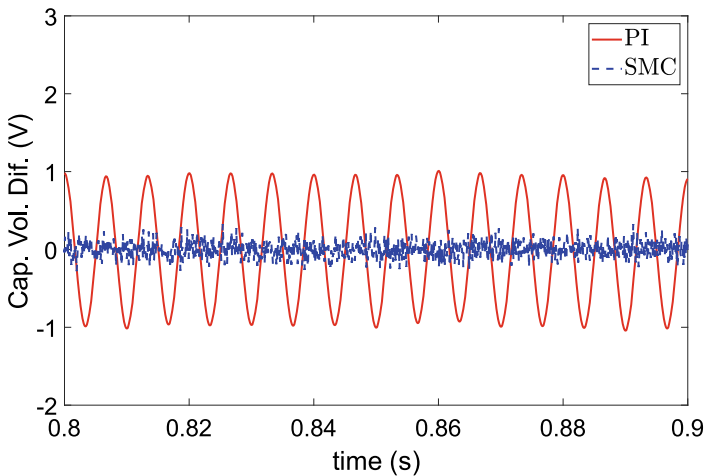


Fig. 5.29 Capacitor voltage difference.eps

balance loop, the ST-SMC based on adaptive estimator is adopted, to eliminate the influence of third harmonic, thus balance the capacitor voltage. The simulation results show that, comparing with PI control, the proposed control strategy obtains better control performance, in terms of robustness against the disturbance and parameter uncertainty, less voltage drop, and balanced capacitor voltage.

References

1. Leon, J.I., Vazquez, S., Franquelo, L.G.: Multilevel converters: control and modulation techniques for their operation and industrial applications. Proc. IEEE **105**(11), 2066–2081 (2017)
2. Portillo, R., Vazquez, S., Leon, J.I., Prats, M.M., Franquelo, L.G.: Model based adaptive direct power control for three-level NPC converters. IEEE Trans. Ind. Appl. **9**(2), 1148–1157 (2012)
3. Akagi, H., Kanazawa, Y., Nabae, A.: Instantaneous reactive power compensators comprising switching devices without energy storage components. IEEE Trans. Ind. Appl. **IA-20**(3), 625–630 (1984)
4. Vazquez, S., Sanchez, J.A., Reyes, M.R., Leon, J.I., Carrasco, J.M.: Adaptive vectorial filter for grid synchronization of power converters under unbalanced and/or distorted grid conditions. IEEE Trans. Ind. Electron. **61**(3), 1355–1367 (2013)
5. Zheng, Q., Chen, Z., Gao, Z.: A practical approach to disturbance decoupling control. Control Eng. Pract. **17**(9), 1016–1025 (2009)
6. Yao, J., Jiao, Z., Ma, D.: Adaptive robust control of DC motors with extended state observer. IEEE Trans. Ind. Electron. **61**(7), 3630–3637 (2013)
7. Doyle, J., Glover, K., Khargonekar, P., Francis, B.: State-space solutions to standard H_2 and H_∞ control problems. In: Proceedings of the 1988 IEEE American Control Conference, Atlanta, GA, USA, pp. 1691–1696 (1988)
8. Khalil, H.K., Grizzle, J.W.: Nonlinear Systems, vol. 3. Upper Saddle River, NJ, Prentice Hall (2002)
9. Escobar, G., Leyva-Ramos, J., Carrasco, J.M., Galvan, E., Portillo, R.C., Prats, M.M., Franqueto, L.G.: Control of a three level converter used as a synchronous rectifier. In: Proceedings of the 35th IEEE Annual Power Electronics Specialists Conference, Aachen, Germany, pp. 3458–3464 (2004)

Chapter 6

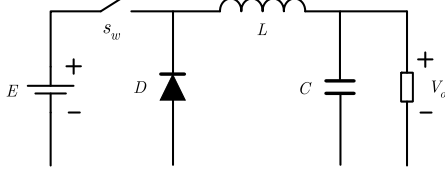
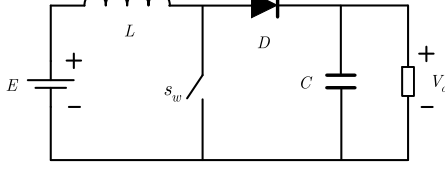
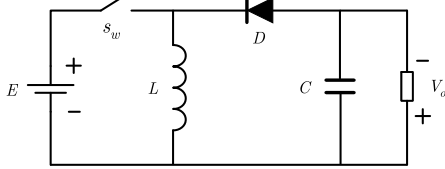
Sliding Mode Control of Buck Converters



Abstract Buck converter is a type of dc/dc power converters, which converts a direct current source from one voltage level to another. They are used for power supplies for office equipments, personal computers, telecommunications equipments, and space-craft power systems, as well as drive control of dc motors [1]. Depending on circuit topology and application, there are many types of dc/dc converters, including buck converter, boost converter, buck-boost converter, Ćuk converter and single-ended primary inductance converter (SEPIC). The buck, boost, and buck-boost converters are basic dc/dc converters, and are usually used for power regulation, whereas Ćuk and SEPIC converter are constructed by combining these basic converters [2]. Buck converter steps down an input voltage to a lower output voltage while boost converter steps up an input voltage to a higher output voltage. Buck-boost, Ćuk and SEPIC converters are able to step up or down an input voltage, depending on the duty ratio of the power switch. Table 6.1 shows the topologies of buck, boost and buck-boost converters, which include a power switch, a diode, an inductor and a capacitor.

This chapter investigates the control strategy for buck converter. A cascaded-control structure is adopted, which include outer voltage regulation loop and inner current tracking loop. The voltage regulation loop consists of second-order sliding mode controller and an extended state observer. The current tracking loop employs a second-order sliding mode controller. The load resistance on the output side affects the system performance and is regarded as an external disturbance, whose impact is asymptotically rejected by estimation of its value via the extended state observer. The effectiveness of proposed strategy is verified by simulation.

Table 6.1 Topologies of three basic converters

Type	Topology	$M(d) = \frac{V_o}{E}$
Buck		d
Boost		$\frac{1}{1-d}$
Buck-boost		$\frac{d}{1-d}$

6.1 Mathematical Model and Control Objectives

6.1.1 Mathematical Model

Figure 6.1 shows the circuit diagram of dc/dc buck converter under investigation. v_{in} is the input dc voltage, L is the filtering inductor with parasitic resistance r , C is the output capacitor, R_L is the equivalent external load. The mathematical model of the buck converter can be expressed as [3],

$$L \frac{di_L}{dt} = -ri_L - v_{out} + uv_{in}, \quad (6.1)$$

$$C \frac{dv_{out}}{dt} = i_L - \frac{v_{out}}{R_L}, \quad (6.2)$$

where i_L is the current flowing through inductor, v_{out} is the dc output capacitor voltage, and u is the control signal.

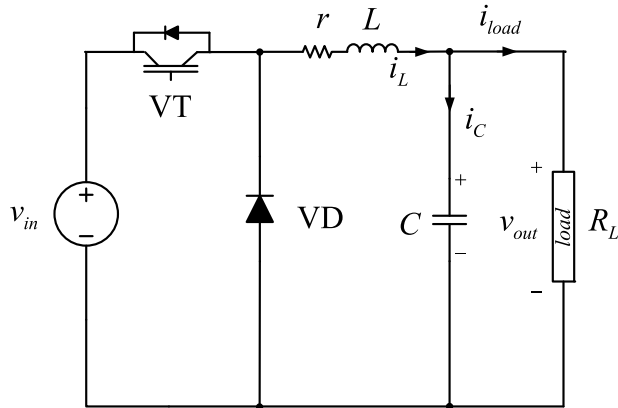


Fig. 6.1 Circuit diagram of dc/dc buck converter

6.1.2 Control Objectives

There are two control objectives for dc/dc buck converter:

- The inductor current i_L should track the reference signal i_L^* calculated in such a way that output DC voltage is driven to a desired value, i.e., $i_L \rightarrow i_L^*$.
- The output dc voltage v_{out} should be regulated to a constant reference v_{ref} , i.e., $v_{out} \rightarrow v_{ref}$.

6.2 Control Scheme

As shown in Fig. 6.2, a disturbance observer based sliding mode control strategy is proposed to control the buck converter. The two-loop cascaded control structure is adopted, which consists of voltage regulation loop and current tracking loop. For the voltage regulation loop, an LESO based super-twisting SMC is adopted to regulate the output voltage to its reference. For current tracking loop, an super-twisting SMC controller is employed to drive the inductor current i_L towards its reference value i_L^* , which is generated by the voltage loop.

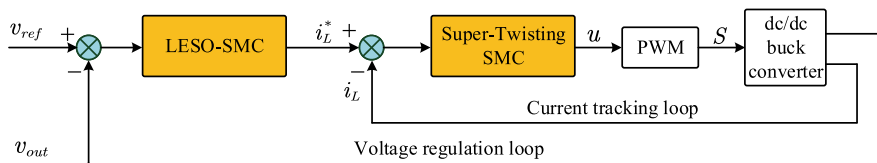


Fig. 6.2 Proposed cascaded control structure

6.2.1 Voltage Regulation Loop

Same as ac-dc converters, the voltage regulation loop of dc/dc converters is the outer loop, and its objective is to regulate the output voltage to a certain desired value. Also it is assumed that the dynamic of inductor current is faster than that of the capacitor voltage dynamic, then the capacitor voltage dynamic can be rewritten as

$$C \frac{dv_{out}}{dt} = i_L^* - i_{load}, \quad (6.3)$$

where load current $i_{load} = \frac{v_{out}}{R_L}$ is considered as an unknown external disturbance, which directly affects the system performance. To reject this undesirable impact, an LESO is adopted to estimate the disturbance and compensate the controller. The LESO is designed as follows:

$$C \dot{\hat{v}}_{out} = i_L^* - \hat{i}_{load} + \eta_1 (v_{out} - \hat{v}_{out}), \quad (6.4)$$

$$\dot{\hat{i}}_{load} = -\eta_2 (v_{out} - \hat{v}_{out}), \quad (6.5)$$

where \hat{v}_{out} and \hat{i}_{load} are respectively the estimated values of v_{out} and i_{load} , η_1 and η_2 are positive parameters to be designed to ensure that \hat{i}_{load} asymptotically converges to its actual value i_{load} . Defining the observation errors $\tilde{v}_{out} = v_{out} - \hat{v}_{out}$ and $\tilde{i}_{load} = i_{load} - \hat{i}_{load}$, their dynamics can be written as

$$C \dot{\tilde{v}}_{out} = -\eta_1 \tilde{v}_{out} - \tilde{i}_{load}, \quad (6.6)$$

$$\dot{\tilde{i}}_{load} = -\eta_2 \tilde{v}_{out} + \dot{\tilde{i}}_{load}. \quad (6.7)$$

The system (6.6) and (6.7) can be further rewritten in compact form as follows:

$$\dot{\varepsilon}(t) = A\varepsilon(t) + \zeta(t) \quad (6.8)$$

$$\text{where } \varepsilon(t) = \begin{bmatrix} \tilde{v}_{out} \\ \tilde{i}_{load} \end{bmatrix}, A = \begin{bmatrix} -\frac{\eta_1}{C} & -\frac{1}{C} \\ \frac{\eta_2}{C} & 0 \end{bmatrix} \text{ and } \phi(t) = \begin{bmatrix} 0 \\ \dot{\tilde{i}}_{load} \end{bmatrix}.$$

The parameters η_1 and η_2 need to be selected to guarantee that matrix A is Hurwitz. Assuming that the load current variation rate \dot{i}_{load} is bounded, the solution of (6.8) is given by

$$\varepsilon(t) = e^{A(t-t_0)} \varepsilon(t_0) + \int_{t_0}^t e^{A(t-\tau)} \zeta(\tau) d\tau, \quad (6.9)$$

where t_0 is the initial time. From the result in [4] that $\|e^{A(t-t_0)}\| \leq ce^{\frac{\lambda_{\max}(A)}{2}(t-t_0)}$ (c is a positive constant), it can be obtained that

$$\begin{aligned}
\|\varepsilon(t)\| &= ce^{\frac{\lambda_{\max}(A)}{2}(t-t_0)} \|\varepsilon(t_0)\| + \int_{t_0}^t e^{\frac{\lambda_{\max}(A)}{2}(t-\tau)} \\
&\quad \times \|\zeta(\tau)\| d\tau, \\
&\leq ce^{\frac{\lambda_{\max}(A)}{2}(t-t_0)} \|\varepsilon(t_0)\| - \frac{2c}{\lambda_{\max}(A)} \sup_{t_0 \leq \tau \leq t} \|\zeta(\tau)\|. \tag{6.10}
\end{aligned}$$

Therefore, it can be concluded that the trajectories of system (6.8) converge in finite time T_0 , i.e., $\|\varepsilon(t)\| \leq \epsilon$, $\forall t \geq T_0 > 0$, where ϵ is a positive constant.

Defining the voltage regulation error $e_v = v_{ref} - v_{out}$, it can be obtained that

$$C \dot{e}_v(t) = -i_L^* + i_{load}. \tag{6.11}$$

Based on the estimated load current \hat{i}_{load} and super-twisting SMC, it yields that

$$i_L^* = u_v(e_v) + \hat{i}_{load}, \tag{6.12}$$

where $u_v(e_v) = \mu_v |\sigma(e_v)|^{\frac{1}{2}} \operatorname{sign}(e_v) + \alpha_v \int_{t_0}^t \operatorname{sign}(e_v) ds$, with positive constants μ_v and α_v . Substituting (6.12) into (6.11) yields that

$$C \dot{e}_v(t) = -u_v(e_v) + \tilde{i}_{load}. \tag{6.13}$$

From (6.13) and (6.10), it can be obtained that regulation error e_v converges to 0 if the parameters μ_v and α_v are selected such that

$$\alpha_v > CH_v, \mu_v^2 \geq 4C^2 H_v \frac{\alpha_v + H_v}{\alpha_v - H_v}, \tag{6.14}$$

in which H_v is positive constant satisfying $\|\dot{\tilde{i}}_{load}\| \leq H_v$. Figure 6.3 shows the structure of voltage regulation loop.

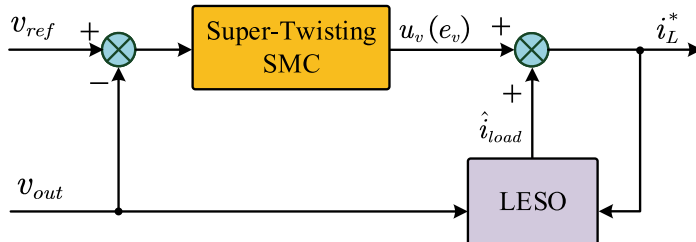


Fig. 6.3 Voltage regulation loop

6.2.2 Current Tracking Loop

The current tracking loop adopts super-twisting SMC controller to make inductor current i_L tracking its reference i_L^* , which is generated by the voltage regulation loop. Define current tracking error $e_i = i_L^* - i_L$, then from (6.1) it can be obtained that

$$\dot{e}_i = \dot{i}_L^* + \frac{r}{L} i_L + \frac{v_{out}}{L} - \frac{v_{in}}{L} u. \quad (6.15)$$

To guarantee that current tracking error converge to equilibrium, an super-twisting SMC controller is designed as follows:

$$u = \frac{L}{v_{in}}(u_i(e_i) + \frac{v_{out}}{L} + \frac{r}{L}i_L), \quad (6.16)$$

where $u_i(e_i) = \mu_i |\sigma(e_i)|^{\frac{1}{2}} \text{sign}(e_i) + \alpha_i \int_{t_0}^t \text{sign}(e_i) ds$. Substituting (6.16) into (6.15), it can be obtained that

$$\dot{e}_i = -u_i(e_i) + \dot{i}_L^*. \quad (6.17)$$

From (6.13) and (6.17), it can be obtained that the tracking error e_i converges to 0 if the parameters μ_i and α_i are selected that

$$\alpha_i > H_v, \mu_i^2 \geq 4H_i \frac{\alpha_i + H_i}{\alpha_i - H_i}, \quad (6.18)$$

where H_i is a positive constant satisfying $\|\ddot{i}_L^*\| \leq H_i$. Figure 6.4 shows the structure of current tracking loop.

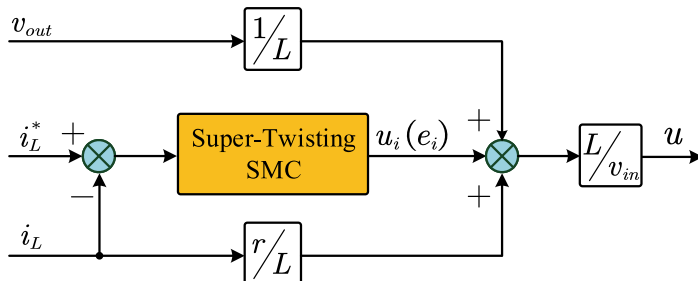


Fig. 6.4 Current tracking loop

6.3 Simulation Verification

Simulations are carried out to verify the effectiveness of the proposed strategy for dc/dc buck converters, using conventional PI as comparison baseline. Table 6.2 shows the system parameters and variables. Table 6.3 show the parameters of PI and the proposed strategy. In order to demonstrate the robustness of the proposed strategy, three types of variations have been added into the system, including load resistance variation, input voltage variation and reference voltage variation.

(1) Load resistance variation

In this case, a load resistance step disturbance is imposed on output link (from 40 to 20 Ω).

Figure 6.5 shows the output voltage dynamic of the buck converter when load varies. As can be seen, both strategies achieve the output voltage reference. However, the transient performance of the proposed strategy is better than conventional PI control, especially in the terms of voltage drop and recovering time. Specifically, the proposed control strategy results in a voltage drop of 0.05 V and a recovering time of 80 ms after load steps at $t = 0.5$ s; while PI control results in a voltage drop of 5 V and a recovering time of 500 ms. This indicates that the proposed control strategy is more robust against load resistance variation than PI. Figure 6.6 shows the inductor current trajectories along with the reference in the presence of load variation. As can be observed that both control methods can drive the inductor current to its reference, yet faster dynamics are achieved with the proposed controller. The transient responses

Table 6.2 System parameters

Parameter	Value	Description
f	$2 \cdot 10^3$	Switching rate (Hz)
R_L	{40, 20}	Load resistance (Ω)
C	4700	Output capacitor (μF)
L	2	Filter inductor (mH)
v_{in}	{300, 250}	Input voltage (V)
v_{ref}	{200, 150}	Output voltage reference (V)

Table 6.3 Control parameters

SMC controller		PI controller	
Cur. Tra. loop	Vol. Reg. loop	Cur. Tra. loop	Vol. Reg. loop
$\mu_i = 1.5$	$\mu_v = 1 \cdot 10^3$	$K_{ip} = 2.0 \cdot 10^5$	$K_{vp} = 0.8$
$\alpha_i = 10$	$\alpha_v = 2 \cdot 10^2$	$K_{ii} = 1.0 \cdot 10^6$	$K_{vi} = 7$
	$\eta_1 = 39.6$		
	$\eta_2 = 1.65 \cdot 10^3$		

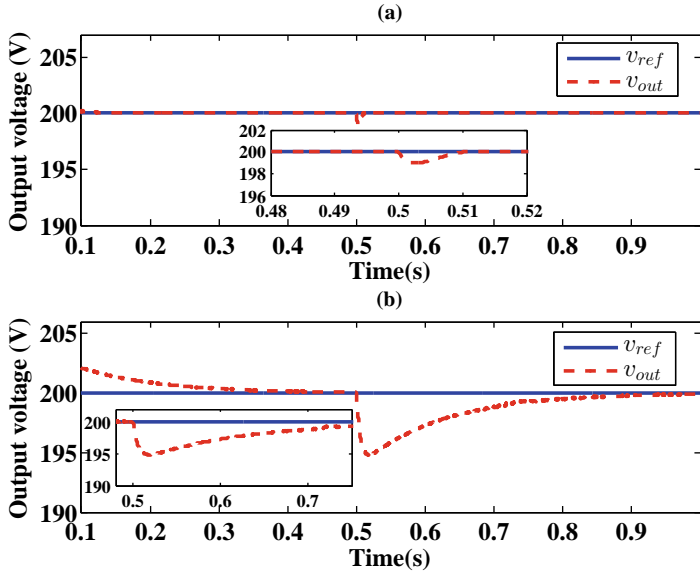


Fig. 6.5 Output voltage regulation: **a** SMC control, **b** PI control

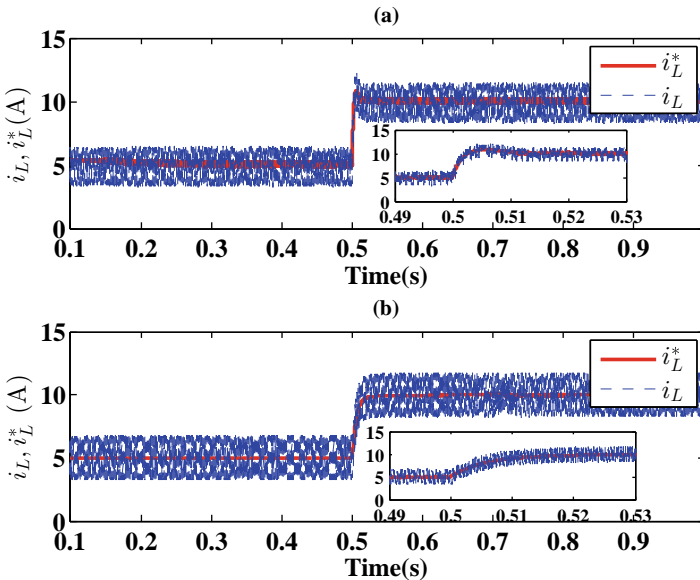


Fig. 6.6 Inductor current tracking: **a** SMC control, **b** PI control

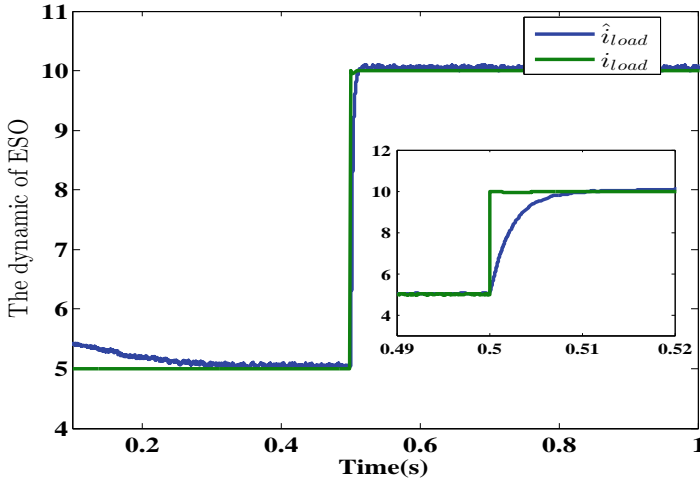


Fig. 6.7 LESO performance

of load current and its corresponding estimation are shown in Fig. 6.7, where load current is accurately estimated by LESO.

(2) Input voltage variation

In this case, the input voltage varies from 300 to 250 V at $t = 0.5$ s.

Figures 6.8 and 6.9 respectively show the transient responses of output voltage and inductor current of when input voltage varies. As can be seen that both strategies can accomplish tasks the voltage regulation and current tracking. However, the performance of the proposed controller is obviously better than PI control, and the input voltage variation barely affects the performance of the proposed controller.

(3) Reference voltage variation

In this case, the reference voltage changes from 200 to 150 V at 0.5 s.

Figure 6.10 shows the output voltage evolution of the buck converter along the reference voltage change. As can be seen that both strategies can achieve the voltage reference, while the proposed scheme results in less overshoot and faster response. Specifically, the proposed control strategy results in a voltage drop of 1 V and a recovering time of 10 ms after the reference voltage steps at $t = 0.5$ s; while PI results in a voltage drop of 3.5 V and a recovering time of 300 ms. Thus proposed control strategy results in faster response with lower overshoot. Figure 6.11 shows that both control laws fulfill the current tracking task, but PI control has a faster response.

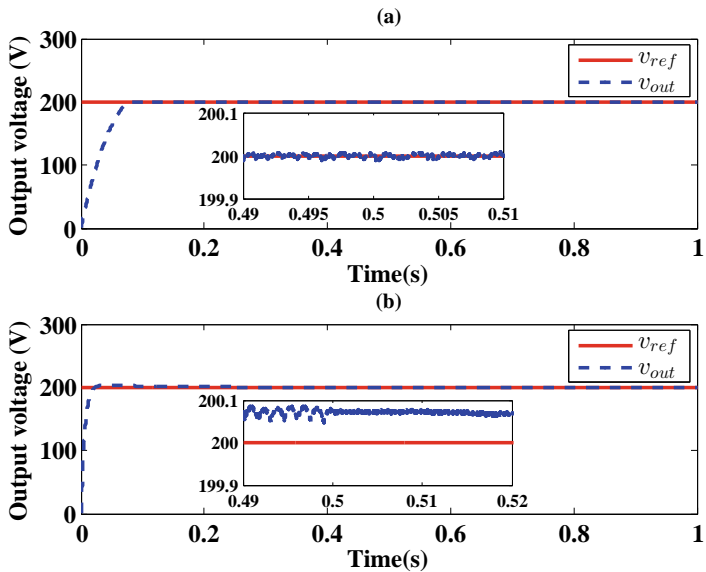


Fig. 6.8 Output voltage regulation: **a** SMC control, **b** PI control

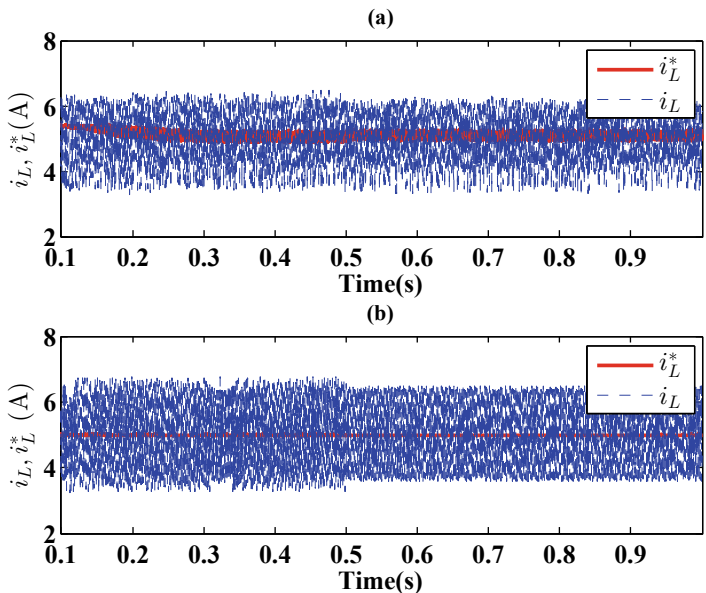


Fig. 6.9 Inductor current tracking: **a** SMC control, **b** PI control

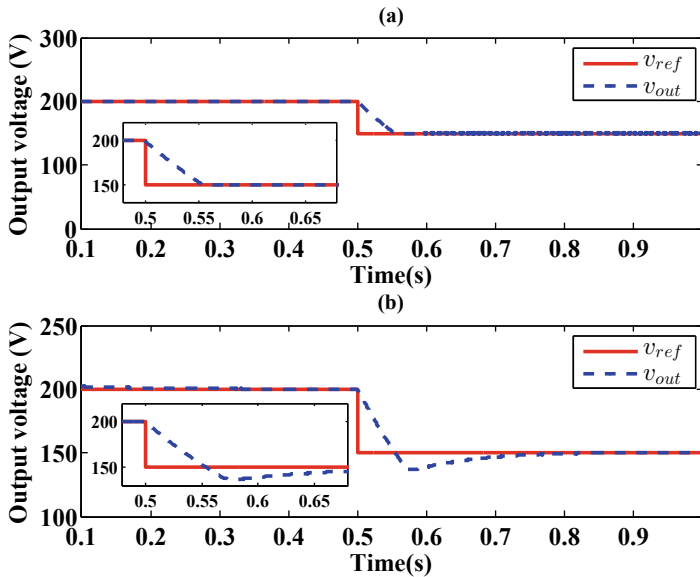


Fig. 6.10 Output voltage regulation: **a** SMC control, **b** PI control

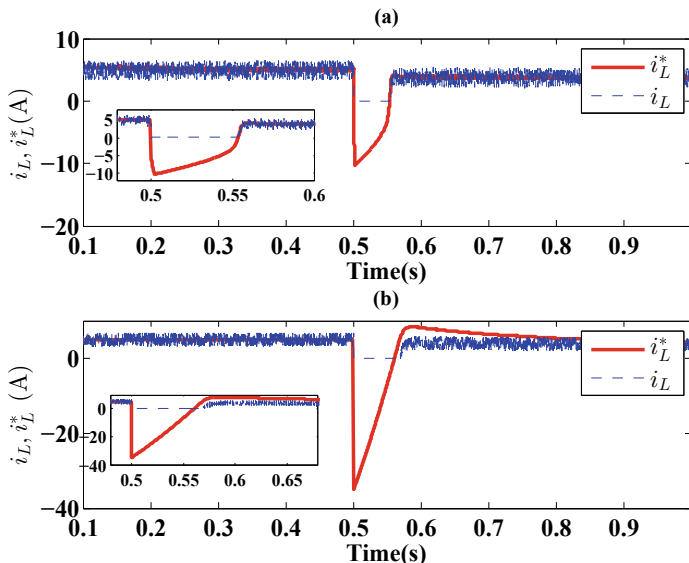


Fig. 6.11 Inductor current tracking: **a** SMC control, **b** PI control

6.4 Summary

This chapter proposed a LESO based SMC strategy for dc/dc buck converters. First, the average model of dc/dc buck converter is established. Based on this model, a cascaded control scheme consisting of two control loops, i.e., output voltage regulation loop and current tracking loop, is designed to fulfill the tasks of output voltage regulation and inductor current tracking. In simulation, three types of variations have been provided to verify the robustness of the proposed controller, including load resistance variation, input voltage variation and reference voltage variation. Simulation results show that the proposed control strategy is effective and outperforms conventional PI control.

References

1. Erickson, R.W., Maksimovic, D.: *Fundamentals of Power Electronics*. Springer Science & Business Media (2007)
2. Tan, S.C., Lai, Y.M., Tse, C.K.: *Sliding Mode Control of Switching Power Converters: Techniques and Implementation*. CRC Press (2018)
3. Utkin, V.: Sliding mode control of DC/DC converters. *J. Franklin Inst.* **350**(8), 2146–2165 (2013)
4. Zhang, W., Branicky, M.S., Phillips, S.M.: Stability of networked control systems. *IEEE Control Syst. Mag.* **21**(1), 84–99 (2001)

Chapter 7

Model Predictive Control of Three-Phase Two-Level Converters



Abstract Due to the finite number of switching combinations of power converters, finite set model predictive control (MPC) is becoming popular control schemes for converter control [1, 2]. It models the converter as a system with finite number of switching states, which can be evaluated online by a cost function and select the switching state that minimizes the cost function. This chapter proposes a model predictive control strategy for three-phase two-level ac/dc power converter. The control is in DPC mode and consists of voltage regulation loop and power tracking loop. The finite-set model predictive control is adopted for power tracking loop to directly drive the active and reactive powers of the system to their reference values with fast dynamics. For voltage regulation loop, a PI controller integrated with an LESO is designed to regulate the dc-link voltage. The effectiveness and advantage of proposed strategy is verified through simulation, using conventional MPC as comparison baseline.

7.1 Control Scheme

The mathematical mode in stationary (α, β) frame is given again here:

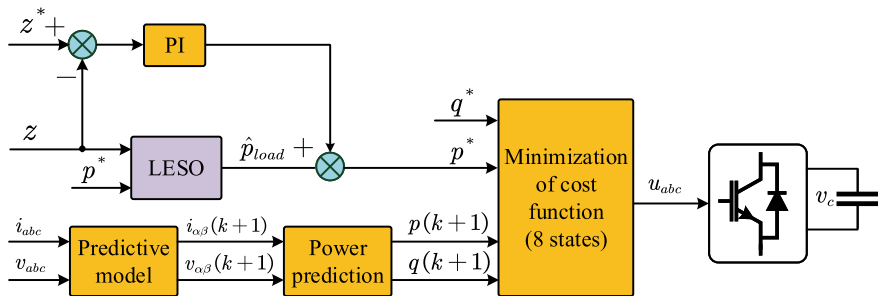
$$\begin{aligned} L \frac{di_{\alpha\beta}}{dt} &= v_{\alpha\beta} - \frac{v_c}{2} u_{\alpha\beta} - ri_{\alpha\beta}, \\ C \frac{dv_c}{dt} &= \frac{1}{2} u_{\alpha\beta}^T i_{\alpha\beta} - \frac{v_c}{R_L}. \end{aligned} \quad (7.1)$$

According to the definition of active and reactive powers p and q [3]:

$$\begin{aligned} p &= v_{\alpha\beta}^T i_{\alpha\beta}, \\ q &= v_{\alpha\beta}^T J i_{\alpha\beta}, \quad J = \begin{bmatrix} 0 & -1 \\ 1 & 0 \end{bmatrix}. \end{aligned} \quad (7.2)$$

Table 7.1 Switch positions in (α, β) model

State	u_1	u_2	u_3	u_α	u_β
U_0	-1	-1	-1	0	0
U_1	1	-1	-1	$2\sqrt{\frac{2}{3}}$	0
U_2	1	1	-1	$\sqrt{\frac{2}{3}}$	$\sqrt{2}$
U_3	-1	1	-1	$-\sqrt{\frac{2}{3}}$	$\sqrt{2}$
U_4	-1	1	1	$-2\sqrt{\frac{2}{3}}$	0
U_5	-1	-1	1	$-\sqrt{\frac{2}{3}}$	$-\sqrt{2}$
U_6	1	-1	1	$\sqrt{\frac{2}{3}}$	$-\sqrt{2}$
U_7	1	1	1	0	0

**Fig. 7.1** Proposed control structure for grid connected power converters

The time derivative of active and reactive powers can be obtained as follow:

$$\begin{aligned} L\dot{p} &= v_{\alpha\beta}^T \left(\omega L q \frac{v_{\alpha\beta}}{|v_{\alpha\beta}|^2} + v_{\alpha\beta} - \frac{v_c}{2} u_{\alpha\beta} \right), \\ L\dot{q} &= v_{\alpha\beta}^T J^T \left(-\omega L p \frac{J v_{\alpha\beta}}{|v_{\alpha\beta}|^2} - \frac{v_c}{2} u_{\alpha\beta} \right), \end{aligned} \quad (7.3)$$

where $|v_{\alpha\beta}|^2 = v_{\alpha\beta}^T v_{\alpha\beta}$.

The possible switch positions in (α, β) coordinate are shown in Table 7.1. The control objectives are to select a switching sequence of the control vector $u_{\alpha\beta}$ such that the output capacitor voltage v_c is regulated to a desired value V_d while keeping unity power factor. Figure 7.1 shows the block diagram of the proposed LESO-based MPC controller.

7.1.1 Voltage Regulation Loop

Same as in Chap. 5, the voltage regulation loop adopts the LESO based PI strategy. As the voltage dynamic is assumed to be much slower than the current dynamic, when the first equation of (7.1) is in stable state, the control signal $u_{\alpha\beta}$ can be obtained as follows [4]:

$$u_{\alpha\beta} = \frac{2}{v_c}(v_{\alpha\beta} - ri_{\alpha\beta}), \quad (7.4)$$

Considering r is rather small and can be neglected, the second equation of (7.1) can be rewritten as

$$C \frac{dv_c}{dt} = \frac{1}{v_c}(p^* - p_{load}), \quad (7.5)$$

where $p_{load} = \frac{v_c^2}{R_L}$. Denoting $z = \frac{v_c^2}{2}$ and $z^* = \frac{V_d^2}{2}$, the voltage dynamic (7.5) can be rewritten as

$$C\dot{z} = u - d(t), \quad (7.6)$$

where $u = p^*$ and $d(t) = p_{load}$, which is considered as an external disturbance. Again, an LESO is designed to estimate p_{load} as follows:

$$\begin{aligned} C\dot{\hat{z}}_1 &= u - \hat{z}_2 + \beta_1(z_1 - \hat{z}_1), \\ \dot{\hat{z}}_2 &= -\beta_2(z_1 - \hat{z}_1), \end{aligned} \quad (7.7)$$

where β_1, β_2 are selected such that $s^2 + \beta_1/Cs + \beta_2/Cs$ is Hurwitz, \hat{z}_1 is an estimate of the output z_1 while \hat{z}_2 is an estimate of the disturbance $d(t)$, i.e., $\hat{z}_1 \rightarrow z_1$ and $\hat{z}_2 \rightarrow d(t)$.

7.1.2 Power Tracking Loop

Predictive control strategy is applied to the power tracking loop based on a discrete-time model, for which the load current derivative $\frac{di_{\alpha\beta}}{dt}$ is replaced by a forward Euler approximation [2]. Thus the predicted instantaneous active and reactive powers p and q can be expressed by

$$\begin{aligned} p(k+1) &= v_\alpha i_\alpha + v_\beta i_\beta, \\ q(k+1) &= v_\alpha i_\beta - v_\beta i_\alpha. \end{aligned} \quad (7.8)$$

Each prediction of $p(k+1)$ and $q(k+1)$ is evaluated by the cost function g , which summarizes the desired behavior of the rectifier, i.e., drive the active and reactive power, p and q , to their references as follows:

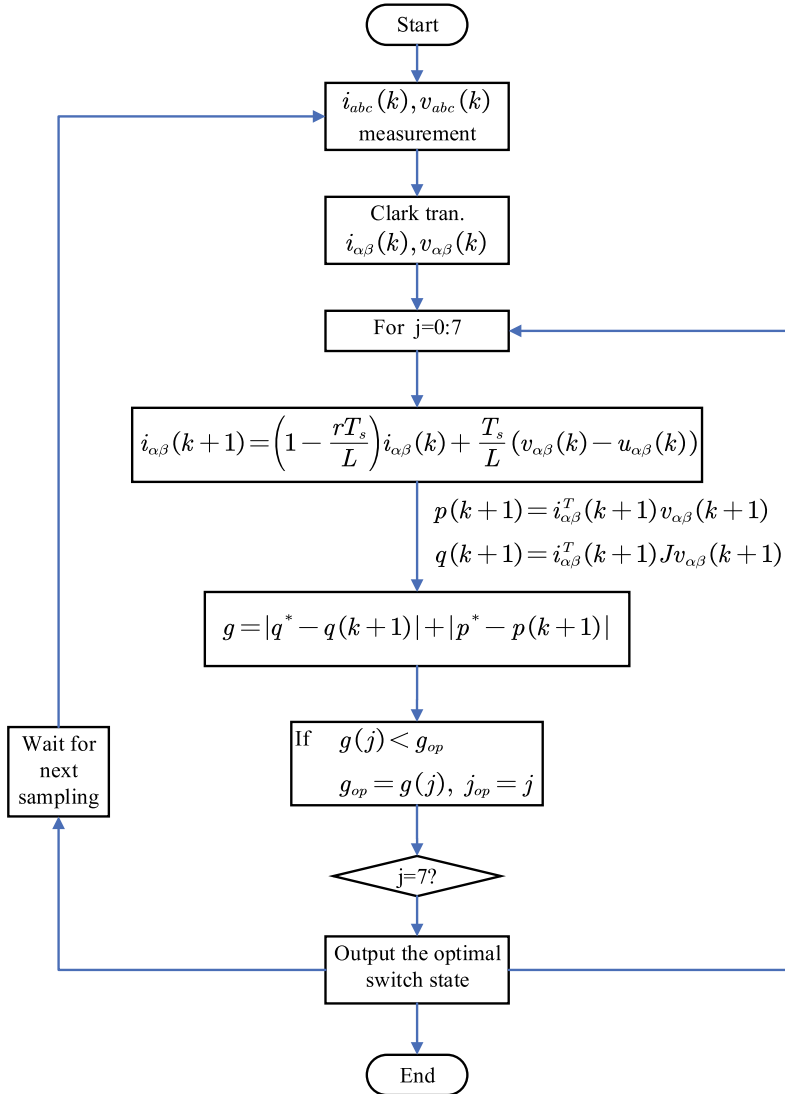


Fig. 7.2 Flow diagram of MPC

$$g = |p(k+1) - p^*| + |q(k+1)|, \quad (7.9)$$

The flow diagram of the proposed control algorithm is shown in Fig. 7.2.

Table 7.2 System parameters

Parameter	Value	Description
L	10	Phase inductor (mH)
v	400	Grid voltage magnitude (V)
C	3300	DC-link capacitor (μF)
f	50	Grid frequency (Hz)
V_d^*	750	Voltage reference (V)
T_s	50	Sampling time (μs)

7.2 Simulation Verification

In this section, simulations are carried out to verify the effectiveness of the proposed LESO-based MPC controller. To assess the proposed control strategy, the conventional MPC is used as a control baseline. Table 7.2 shows the system parameter for simulation. The disturbing load is connected to the system at $t = 0.35$ s.

Figure 7.3 shows the dc-link voltage transient performance when load is connected to the system. As can be seen, the proposed controller results in smaller capacitor voltage overshoot and faster convergence compared with conventional MPC. Specifically, the capacitor voltage drop is 25 V in case of the proposed control while the MPC results in larger value (45 V). Therefore, it can be concluded that the dc-link voltage transient performance is improved by LESO-based MPC. Figures 7.4 and 7.5 show the power tracking performance. As can be seen, the proposed control performs well in tracking the power reference. When the load step is imposed, the proposed controller results in a shorter settling time compared with the MPC. Figure 7.6 shows that the external disturbance (load power) is accurately estimated by LESO.

Figure 7.7 shows one phase current (i_a) along with the corresponding grid voltage (v_{an}), and Fig. 7.4a shows the current harmonic content. As can be seen that both of the controllers result in no phase shift between the input current and corresponding grid voltage and low current distortion. The obtained THD values of the two algorithms are nearly the same, Fig. 7.8a is 1.54% (up to harmonic 40) and Fig. 7.8b is 1.49%, respectively. This is because the power tracking loop of the two strategies adopts the same algorithm.

7.3 Summary

This chapter proposes an LESO-based MPC strategy under DPC mode for three-phase two-level grid connected power converters. The power tracking loop adopts finite set MPC to force the power value p, q to track their reference values with fast dynamics. The voltage regulation loop adopts LESO based PI control to regulate the dc-link voltage, in face of abrupt load disturbance. Comparative simulations have

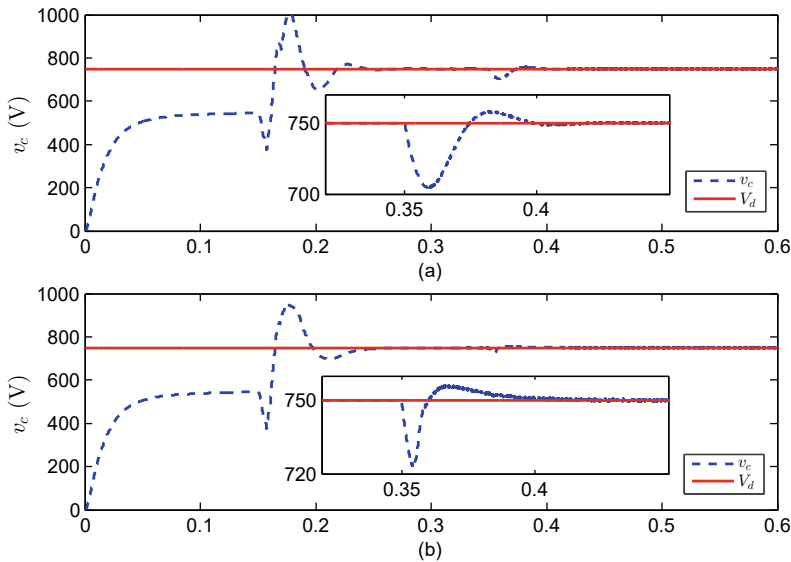


Fig. 7.3 DC-link capacitor voltage: **a** conv. MPC control, **b** LESO-MPC control

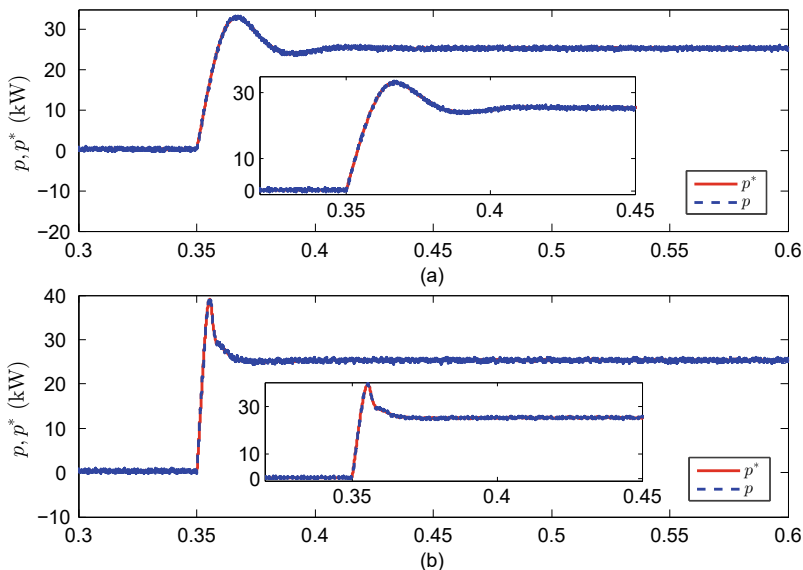


Fig. 7.4 Active power response: **a** conv. MPC control, **b** LESO-MPC control

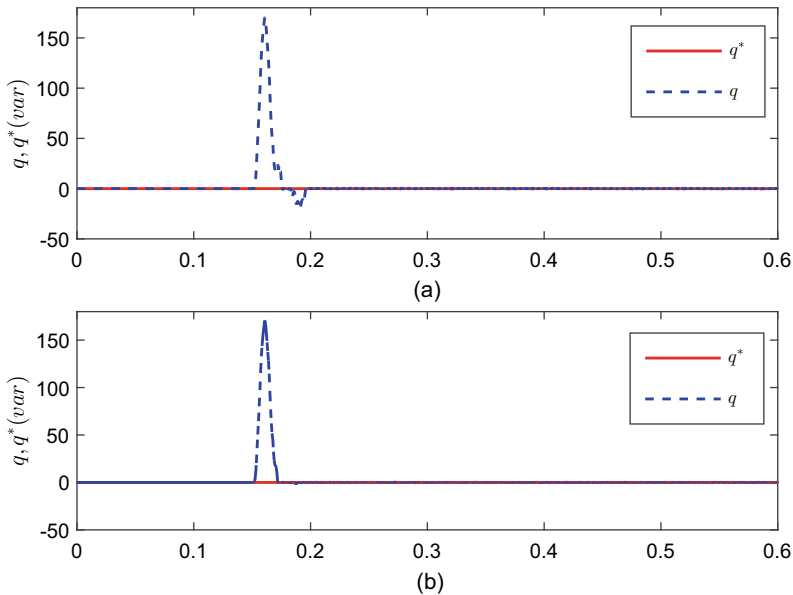


Fig. 7.5 Reactive power response: **a** conv. MPC control, **b** LESO-MPC control

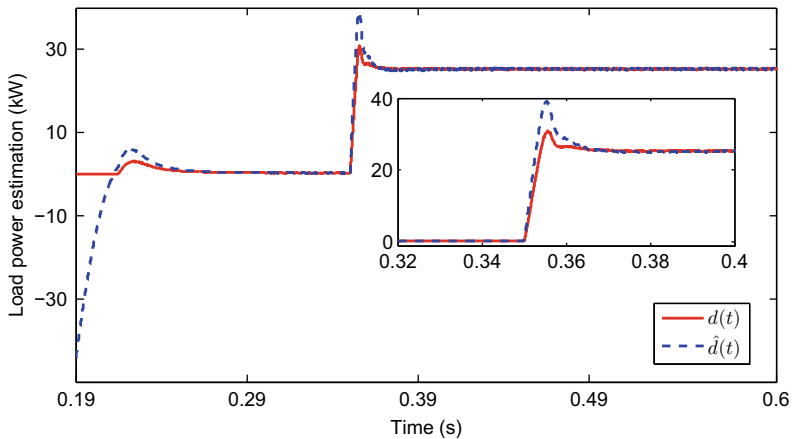


Fig. 7.6 Load estimation

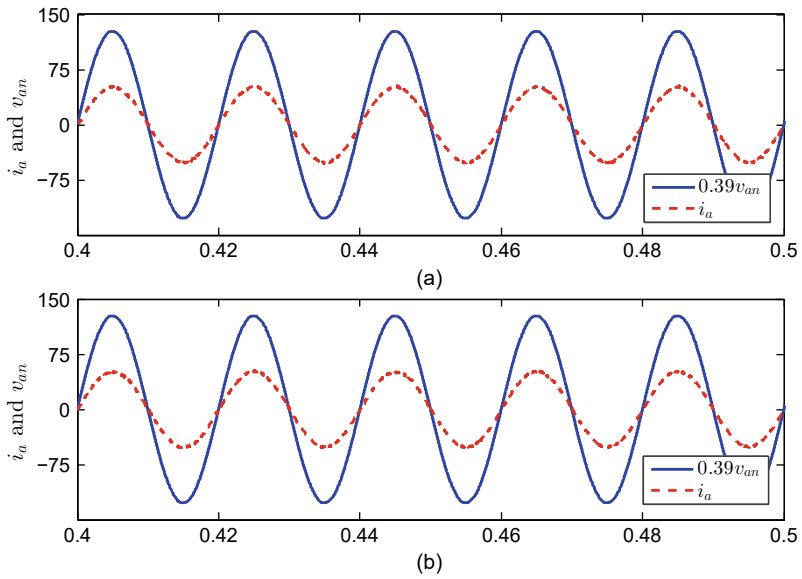


Fig. 7.7 Grid voltage and current: **a** conv. MPC control, **b** LESO-MPC control

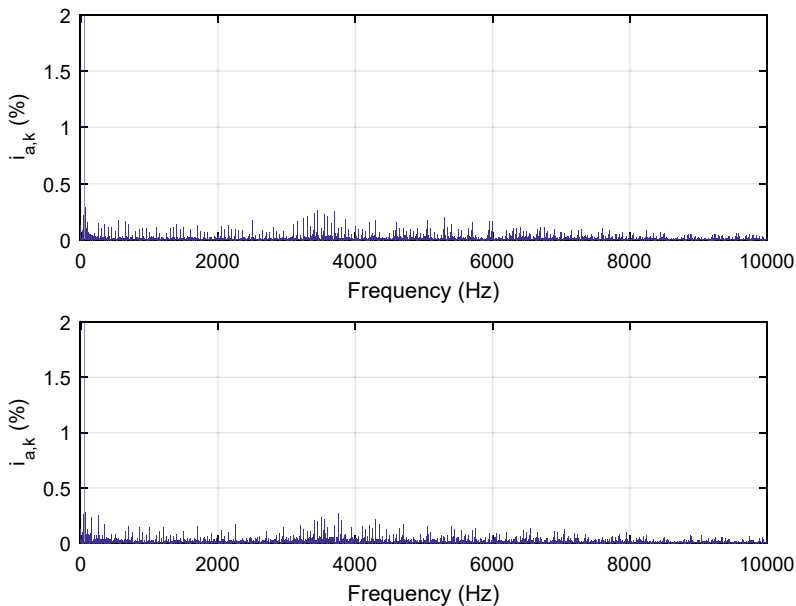


Fig. 7.8 Current harmonic spectrum: **a** conv. MPC control, **b** LESO-MPC control

been carried out to verify the effectiveness of the proposed scheme. The results show that the LESO-based MPC strategy obtains shorter settling time, stronger robustness against external disturbances and parametric uncertainties when compared to conventional MPC control.

References

1. Quevedo, D.E., Aguilera, R.P., Perez, M.A., Cortes, P., Lizana, R.: Model predictive control of an AFE rectifier with dynamic references. *IEEE Trans. Power Electron.* **27**(7), 3128–3136 (2011)
2. Cortes, P., Rodríguez, J., Antoniewicz, P., Kazmierkowski, M.: Direct power control of an AFE using predictive control. *IEEE Trans. Power Electron.* **23**(5), 2516–2523 (2008)
3. Akagi, H., Kanazawa, Y., Nabae, A.: Instantaneous reactive power compensators comprising switching devices without energy storage components. *IEEE Trans. Ind. Appl.* **IA-20**(3), 625–630 (1984)
4. Liu, J., Vazquez, S., Gao, H., Franquelo, L.G.: Robust control for three-phase grid connected power converters via second order sliding mode. In: Proceedings of the 2015 IEEE International Conference on Industrial Technology, Seville, Spain, pp. 1149–1154 (2015)

Part II

Intelligent Control Methods

Chapter 8

Adaptive Control of Buck Converters



Abstract In this chapter, two adaptive control strategies are designed for dc/dc buck converter, i.e., single-loop adaptive control strategy and double-loop adaptive control strategy. As the names imply, single-loop adaptive control strategy has only voltage regulation loop which directly regulate the output voltage, while double-loop adaptive control strategy has voltage regulation loop as outer loop and current tracking loop as inner loop. The single-loop adaptive control strategy is built by adaptive and back-stepping control approach, and the double-loop adaptive control strategy is constructed by adaptive and sliding mode control approach. The purpose of this chapter is to compare and analyze the advantages and disadvantages of the two adaptive control strategies, hence to give a guideline for selecting appropriate control strategy under specific requirements for buck converter.

8.1 Control Scheme

The dc/dc buck converter topology is the same as that in Chap. 6. To facilitate the controller design, the mathematical model is rewritten as follows:

$$\dot{x}_1 = \frac{x_2}{C} - \frac{x_1}{RC}, \quad (8.1)$$

$$\dot{x}_2 = -\frac{x_1}{L} + \frac{v_{in}}{L}u, \quad (8.2)$$

where x_1 denotes the dc output voltage v_{out} , x_2 denotes the inductor current i_L , and u denotes the duty ratio to be generated by the controller. It should be noted that the equivalent resistance r is neglected.

For comparison, two types of adaptive controller are designed for the converter.

8.1.1 Single-Loop Adaptive Control

Define the voltage regulation error as:

$$z_1 = x_1 - x_1^*, \quad (8.3)$$

where x_1^* is the dc output voltage reference. Taking the derivative of (8.3) with respect to (8.1), it can be obtained that

$$\dot{z}_1 = \frac{x_2}{C} - \theta x_1 - \dot{x}_1^*, \quad (8.4)$$

where $\theta = \frac{1}{R_L C}$ is treated as unknown parameter, and the equivalent load R_L is assumed to be slow-varying, that is, $\dot{\theta} \approx 0$. Define $\tilde{\theta} = \hat{\theta} - \theta$, and construct following Lyapunov function for system (8.4):

$$V_{s11} = \frac{1}{2} z_1^2 + \frac{1}{2\eta} \tilde{\theta}^2, \quad (8.5)$$

Taking the time-derivative of (8.5) yields,

$$\dot{V}_{s11} = z_1 \left(\frac{x_2}{C} - \theta x_1 - \dot{x}_1^* \right) + \frac{1}{\eta} \tilde{\theta} \dot{\tilde{\theta}}. \quad (8.6)$$

Based on (8.6), design virtual control α_1 , error variable z_2 and adaptive law $\hat{\theta}$ as follow:

$$\alpha_1 = -k_{s11} z_1 + \dot{x}_1^* + \hat{\theta} x_1, \quad (8.7)$$

$$z_2 = \frac{x_2}{C} - \alpha_1, \quad (8.8)$$

$$\dot{\hat{\theta}} = -\eta z_1 x_1, \quad (8.9)$$

where k_{s11} and η are positive scalars, then (8.6) becomes:

$$\begin{aligned} \dot{V}_{s11} &= z_1 (-k_{s11} z_1 + \hat{\theta} x_1 + z_2 + \dot{x}_1^* - \theta x_1 - \dot{x}_1^*) + \frac{1}{\eta} \tilde{\theta} \dot{\tilde{\theta}} \\ &= -k_{s11} z_1^2 + z_1 z_2 + \tilde{\theta} z_1 x_1 + \frac{1}{\eta} \tilde{\theta} \dot{\tilde{\theta}} \\ &= -k_{s11} z_1^2 + z_1 z_2. \end{aligned} \quad (8.10)$$

As can be seen, to regulate the dc output voltage to its reference, the error vector $z = [z_1, z_2]^T$ needs to be of asymptotic convergence. For this purpose, based on (8.8), the dynamic of z_2 is firstly obtained as follows:

$$\dot{z}_2 = -\frac{x_1}{LC} + \frac{v_{in}}{LC}u - \dot{\alpha}_1. \quad (8.11)$$

Construct following Lyapunov function V_{s12} for the error system $z = [z_1, z_2]^T$,

$$V_{s12} = V_{s11} + \frac{1}{2}z_2^2. \quad (8.12)$$

Taking the derivative of (8.12) yields,

$$\begin{aligned}\dot{V}_{s12} &= -k_{s11}z_1^2 + z_1z_2 + z_2\dot{z}_2 \\ &= -k_{s11}z_1^2 + z_2(z_1 - \frac{x_1}{LC} + \frac{v_{in}}{LC}u - \dot{\alpha}_1).\end{aligned}\quad (8.13)$$

To make $\dot{V}_2 < 0$, the control signal u is designed as:

$$u = \frac{LC}{1.00, 0.00, 0.00} v_{in} (-z_1 + \frac{x_1}{LC} + \dot{x}_1 - k_{s12} z_2). \quad (8.14)$$

Substituting (8.14) into (8.13), it can be obtained that

$$\dot{V}_{s12} = -k_{s11}z_1^2 - k_{s12}z_2^2 \leq 0, \quad (8.15)$$

which means that error system (z_1, z_2) is asymptotically stable, hence the dc output voltage is regulated to its reference. The control structure is shown in Fig. 8.1.

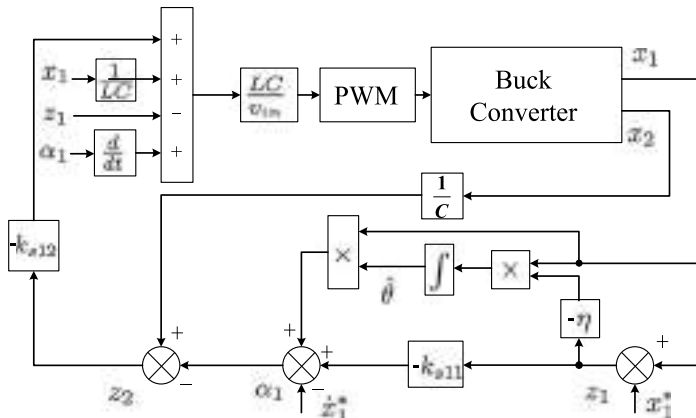


Fig. 8.1 Control structure of single-loop adaptive strategy

8.1.2 Double-Loop Adaptive Control

(1) Voltage regulation loop

The voltage regulation loop aims to regulate the dc output voltage and provide the current reference for the current tracking loop. Assuming that the current dynamic is much faster than the voltage dynamic, the dynamic of z_1 can be obtained as

$$\dot{z}_1 = \frac{x_2^*}{C} - \theta x_1 - \dot{x}_1^*, \quad (8.16)$$

where x_2^* is the reference of x_2 , which is the control signal for the voltage regulation loop. Construct the same Lyapunov function as that in (8.5), and design x_2^* as

$$x_2^* = C(-k_{d1}z_1 + \dot{x}_1^* + \hat{\theta}x_1), \quad (8.17)$$

where k_{d1} is a positive scalar with the same adaptive law as that in (8.9).

(2) Current tracking loop

To track the current reference, the sliding mode controller is employed in this loop. Define the sliding surface as $\tilde{x}_2 = x_2 - x_2^*$, taking its derivative based on (8.2) yields,

$$\dot{\tilde{x}}_2 = -\frac{x_1}{L} + \frac{v_{in}}{L}u - \dot{x}_2^*, \quad (8.18)$$

where $\|\dot{x}_2^*\| \leq \Phi$ is assumed to be a positive constant. Then the sliding mode control signal u is designed to drive the state trajectories onto the sliding surface \tilde{x}_2 in finite time. Construct following Lyapunov function:

$$V_{d12} = \frac{1}{2}\tilde{x}_2^2, \quad (8.19)$$

then its derivative can be obtained as follows:

$$\dot{V}_{d12} = \tilde{x}_2\left(-\frac{x_1}{L} + \frac{v_{in}}{L}u - \dot{x}_2^*\right). \quad (8.20)$$

Design a sliding mode controller as follows:

$$u = -\frac{L}{v_{in}}(c_{d12}\tilde{x}_2 + D_{d12}\text{sign}(\tilde{x}_2) - \frac{x_1}{L}), \quad (8.21)$$

where c_{d12} and $D_{d12} \geq \Phi$ are positive constants. Substituting (8.21) into (8.20) yields,

$$\begin{aligned} \dot{V}_{d12} &= \tilde{x}_2(-c_{d12}\tilde{x}_2 - D_{d12}\text{sign}(\tilde{x}_2) - \dot{x}_2^*) \\ &\leq -c_{d12}\tilde{x}_2^2 - D_{d12}|\tilde{x}_2| - \Phi\tilde{x}_2 \leq 0. \end{aligned} \quad (8.22)$$

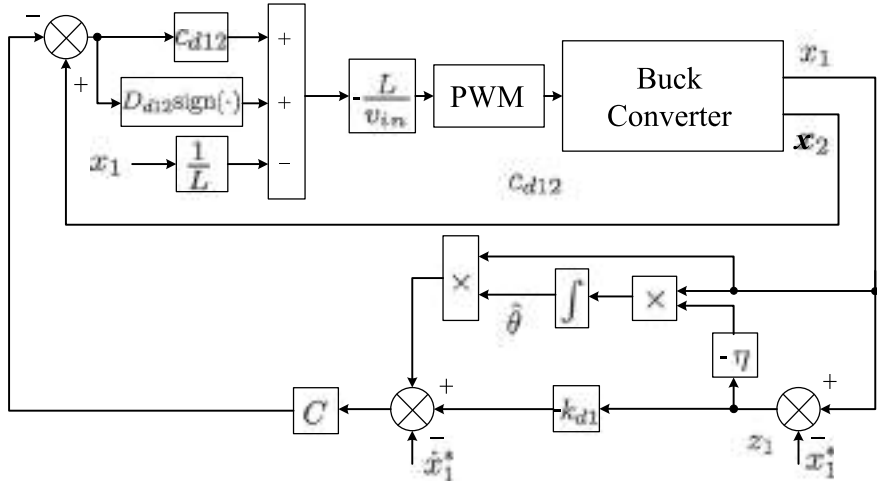


Fig. 8.2 Control structure of double-loop adaptive strategy

Therefore the current reference x_2^* is tracked in finite time. The control structure is shown in Fig. 8.2.

Remark 8.1 Compared with double-loop control strategy, single-loop control strategy has simpler control structure, only needing one loop to regulate the output voltage, which can be easily implemented in practice. Thus, this control method is also called direct output control or voltage-mode control. The double-loop control structure consists of a primary loop and a secondary loop, in which primary loop is the voltage regulation loop to regulate the voltage and secondary loop is the current tracking loop to force the inductor current tracking its reference. This control approach is also named indirect output control. Since this control structure adopts the intermediate measured signal to quickly response the control requirements, it can provide tighter control and improve system dynamic performances. ♦

8.2 Experiment Verification

In this section, the experiments are carried out to compare and analyze the effectiveness of the proposed two adaptive strategies for dc/dc buck converters. The laboratory dc-dc buck converter prototype is shown in Fig. 8.3. The control platform adopts dSPACE 1202. Two types of experiments are performed, including load resistance and reference voltage variations.

The system parameters of the converter are shown in Table 8.1, and the control parameters are shown in Table 8.2.

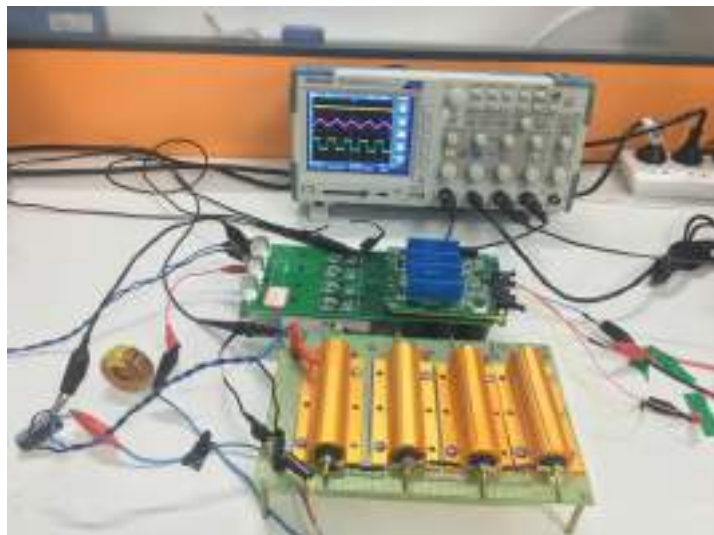


Fig. 8.3 Laboratory prototype of dc-dc buck converter

Table 8.1 System parameters

Parameter	Value	Description
f_s	$10 \cdot 10^3$	Switching rate (Hz)
L	$1.5 \cdot 10^{-3}$	Input inductance (H)
C	$2.0 \cdot 10^{-3}$	Output capacitance (F)
R_L	{20, 10}	Load resistance (Ω)
v_{in}	30	Input voltage (V)
x_1^*	{15, 12}	Reference voltage (V)

Table 8.2 Control parameters

SA	DA	
	Cur. Tra. loop	Vol. Reg. loop
$\eta = 1200$	$c_{d1} = 500$	$k_{d1} = -2.6$
$k_{s11} = -150$	$D_{d12} = 0.05$	$\eta = 120$
$k_{s12} = -200$		

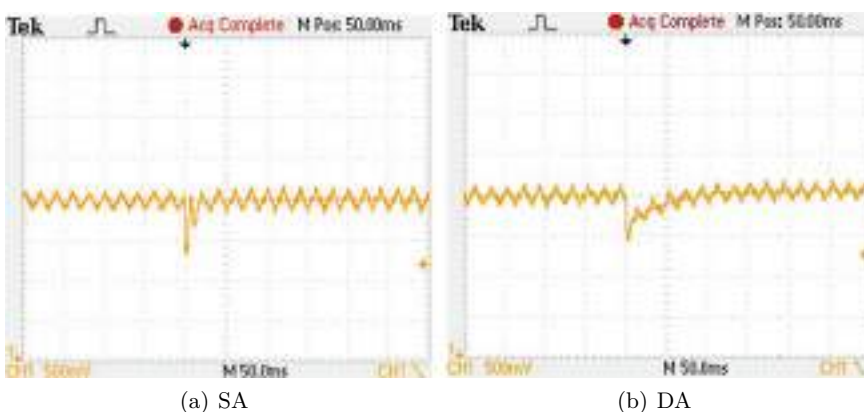


Fig. 8.4 Output voltage with load changes

Table 8.3 Results with load changes

Control strategy	Voltage drop (mV)	Transient time (ms)	Voltage ripple (mV)
SA	680	15	380
DA	550	80	220

(1) Load resistance variation

In this experiment, the reference voltage is kept constant at 15 V and load resistance is changed from 20Ω to 10Ω . Figure 8.4 shows the voltage transient process with the proposed two controllers. As can be observed, both the single and double loop control strategies can regulate the output voltage to its reference 15 V in the presence load changes. The detailed results are shown in the Table 8.3, as can be seen, SA results in faster transient time (15 ms) but larger steady state voltage ripple (380 mV), whereas DA results in less output voltage drop and voltage ripple but slower dynamic response.

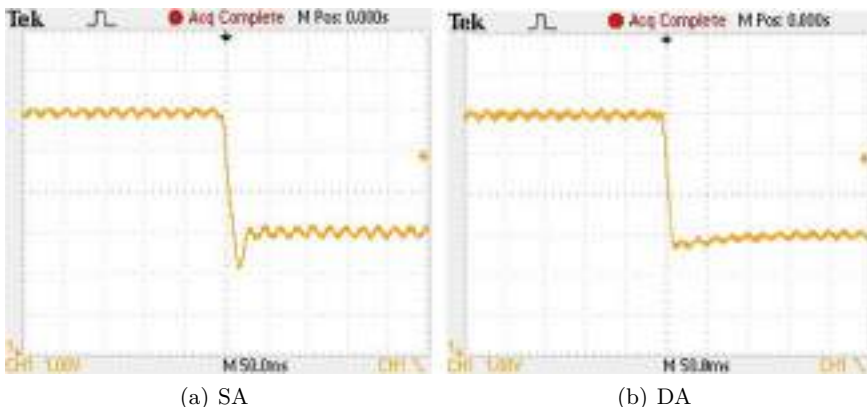
(2) Reference voltage variation

In this experiment, the reference voltage is changed from 15 to 12 V and load resistance is kept at $20\ \Omega$. The control parameters remain the same.

Figure 8.4 shows the voltage transient process with the proposed two controllers. The voltage drop and transient time of the two control strategies when reference voltage changes are presented in Table 8.4. The ripples are the same as in Table 8.3. As can be seen, both proposed control strategies are robust against reference voltage variation and can regulate the output voltage to its new reference. Consistent with previous results, SA results in shorter transient time but larger voltage drop, whereas DA results in lower voltage drop but longer transient time.

Table 8.4 Results with reference voltage changes

Control strategy	Voltage drop (mV)	Transient time (ms)
SA	900	30
DA	300	100

**Fig. 8.5** Output voltage with voltage reference changes

Therefore, depending on specific application requirements, one can choose or switch between the two control strategies (Fig. 8.5).

8.3 Summary

In this chapter, two adaptive control strategies have been designed for dc/dc buck converter, i.e., single-loop and double-loop adaptive control strategies. Two sets of experiments, including load resistance and reference voltage variations, have been conducted to compare and analyze the advantages and disadvantages of the proposed two strategies. Experiment results show that, the single-loop adaptive control strategy results in faster transient process but larger voltage drop and ripple, whereas the double-loop adaptive control strategy results in slower transient process but smaller voltage drop and ripple. Based on these results, one can select or switch the suitable control strategy for real applications.

Chapter 9

Adaptive \mathcal{H}_∞ Control of Three-Phase Two-Level Converters



Abstract This chapter proposes a control strategy consisting of adaptive control and \mathcal{H}_∞ technique for three-phase two-level ac/dc power converters. Cascaded two loop control structure in VOC mode is adopted. For outer voltage regulation loop, an efficient adaptive controller is designed to regulate dc-link output voltage to its reference in the presence of external disturbances. For inner current tracking loop, two \mathcal{H}_∞ controllers are designed in dq SRF to force the grid currents to track their reference values generated from the outer loop. The effectiveness and advantage of proposed strategy is verified through simulation, using sliding mode control as comparison baseline.

9.1 Control Scheme

Rewrite the mathematical model three-phase two-level converter in following form:

$$\dot{i}_{dq}(t) = -\frac{r}{L}i_{dq}(t) - J\omega i_{dq}(t) + \frac{e_{dq}}{L} - \frac{1}{L}u_{dq}v_{dc}(t), \quad (9.1)$$

$$\dot{v}_{dc}(t) = -\frac{1}{R_L C}v_{dc}(t) + \frac{1}{C}u_{dq}^T(t)i_{dq}(t), \quad (9.2)$$

where $i_{dq}(t) = M_{abc}^{dq}i_{abc}(t) = [i_d(t), i_q(t)]^T$, $e_{dq} = M_{abc}^{dq}e_{abc} = [e_d, e_q]^T$, $u_{dq}(t) = M_{abc}^{dq}\sigma = [u_d(t), u_q(t)]^T$, $J = \begin{pmatrix} 0 & -1 \\ 1 & 0 \end{pmatrix}$, M_{abc}^{dq} is the power-invariant transfer matrix.

To facilitate the controller design, following definition and lemma are first given here [1].

Definition 9.1 For following system

$$\begin{aligned} \dot{x}(t) &= Ax(t) + B\omega(t), \\ y(t) &= Cx(t), \end{aligned} \quad (9.3)$$

where $x(t) \in \mathbb{R}^n$ is the state, $y(t)$ is the controlled output, $\omega(t) \in L_2[0, \infty)$ is the disturbance, and A , B and C are real matrices of compatible dimensions, if for $x(0) = 0$ it holds that

$$\int_0^{+\infty} y^T(t)y(t)dt \leq \gamma^2 \int_0^{+\infty} \omega^T(t)\omega(t)dt, \quad (9.4)$$

where γ is a positive scalar, then the system is said to have an \mathcal{H}_∞ performance index γ .

Lemma 9.2 *For matrix M and S of appropriate dimension, then*

$$M^T S + M S^T < 0$$

holds, if and only if there exists a scalar $\kappa > 0$, such that

$$\kappa M^T M + \frac{1}{\kappa} S^T S < 0$$

holds.

9.1.1 Voltage Regulation Loop

In this subsection, an adaptive controller is designed to regulate the dc-link voltage. As in previous chapters, two assumptions are given: (1) the equivalent load resistance R_L is unknown and slow-varying; (2) the dynamic of dc-link voltage v_{dc} is much slower than that of the current i_{dq} .

According to these assumptions and the singular perturbation theory [2], system (9.2) can be written as

$$v_{dc}(t)\dot{v}_{dc}(t) = -\frac{1}{R_L C}v_{dc}^2(t) + \frac{1}{C}v_{dc}(t)u_{dq}^T(t)i_{dq}^*(t). \quad (9.5)$$

Further rewrite the system in following form:

$$\begin{aligned} \dot{x}_1(t) &= \frac{1}{C}p^* - \rho x_1(t), \\ y_1(t) &= x_1(t), \end{aligned} \quad (9.6)$$

where $x_1(t) = \frac{1}{2}v_{dc}^2(t)$, $p^* = v_{dc}u_{dq}^T i_{dq}^*$, $y_1(t)$ is the controlled output and $\rho = \frac{2}{R_L C}$ that can be regarded as an unknown slow-varying disturbance.

Next an adaptive controller p^* is designed to regulate $x_1(t)$ to the reference $x_1^* = \frac{1}{2}(v_{dc}^*)^2$ where v_{dc}^* is the desired reference voltage, which ensures that the dc-link voltage $v_{dc}(t)$ is regulated to its reference v_{dc}^* .

Theorem 9.3 Consider system (9.6) with an adaptive controller

$$p^* = ke_1(t) + Cx_1(t)\hat{\rho}(t), \quad (9.7)$$

where k is positive constant, $e_1(t) = x_1^* - x_1(t)$ is the regulation error; $\hat{\rho}(t)$ is the adaptive law with following dynamic

$$\dot{\hat{\rho}}(t) = \eta x_1(t)e_1(t), \quad (9.8)$$

where η is positive constant. Then the controlled output $y_1(t)$ can asymptotically converge to the reference signal x_1^* , i.e., the adaptive controller (9.7) can regulate the output voltage to its reference v_{dc}^* .

Proof Denote $\tilde{\rho}(t) = \hat{\rho}(t) - \rho$, then according to the first assumption, it can be obtained that

$$\dot{\hat{\rho}}(t) = \dot{\tilde{\rho}}(t). \quad (9.9)$$

Construct the following Lyapunov function:

$$V_1(t) = \frac{1}{2}e_1^2(t) + \frac{1}{2\eta}\tilde{\rho}^2(t). \quad (9.10)$$

Then the derivative of the Lyapunov function (9.10) is

$$\dot{V}_1(t) = e_1(t)\dot{e}_1(t) + \frac{1}{\eta}\tilde{\rho}(t)\dot{\tilde{\rho}}(t). \quad (9.11)$$

From (9.6), (9.7), (9.8) and (9.9), it immediately follows that

$$\begin{aligned} \dot{V}_1(t) &= e_1(t)(-\frac{1}{C}p^* + \rho x_1(t)) + \frac{1}{\eta}\tilde{\rho}(t)\dot{\tilde{\rho}}(t) \\ &= -\frac{1}{C}e_1(t)(ke_1(t) + Cx_1(t)\hat{\rho}(t)) + e_1(t)x_1(t)\rho \\ &\quad + \frac{1}{\eta}\tilde{\rho}(t)\eta x_1(t)e_1(t) \\ &= -\frac{1}{C}ke_1^2(t). \end{aligned} \quad (9.12)$$

According to Lasalle's theorem [3], it can be obtained that the control error $e_1(t)$ converges to 0 as $t \rightarrow \infty$, i.e., the adaptive controller (9.7) can regulate the output voltage to its reference v_{dc}^* . Proof completed. ■

Figure 9.1 shows the structure diagram of the adaptive controller.

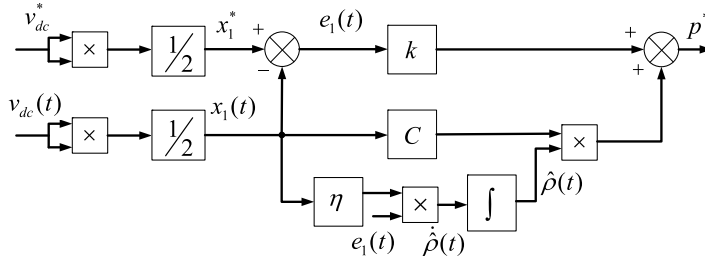


Fig. 9.1 Adaptive controller structure

9.1.2 Current Tracking Loop

In this subsection, an \mathcal{H}_∞ controller is designed to track the ac current. Based on the instantaneous theory [4], the current references are calculated as

$$\begin{cases} i_d^* \\ i_q^* \end{cases} = \frac{1}{e_d^2 + e_q^2} \begin{cases} e_d & e_q \\ e_q & -e_d \end{cases} \begin{cases} p^* \\ q^* \end{cases} = \frac{1}{e_d} \begin{cases} p^* \\ -q^* \end{cases}, \quad (9.13)$$

where p^* and q^* are respectively the instantaneous active and reactive power reference. p^* is generated by the voltage loop to regulate the output voltage, and q^* is a pre-set value, which is usually set to 0 to achieve unity power factor. Denote the current tracking error ε_{qd} ,

$$\varepsilon_{qd}(t) = \begin{cases} \varepsilon_d(t) \\ \varepsilon_q(t) \end{cases} = \begin{cases} i_d^* - i_d(t) \\ i_q^* - i_q(t) \end{cases}. \quad (9.14)$$

Following (9.2), the derivative of ε_{dq} is given by

$$\begin{cases} \dot{\varepsilon}_d(t) \\ \dot{\varepsilon}_q(t) \end{cases} = \begin{cases} \dot{i}_d^* + \frac{r}{L}i_d(t) - \frac{e_d}{L} - \omega i_q(t) \\ \dot{i}_q^* + \frac{r}{L}i_q(t) - \frac{e_q}{L} + \omega i_d(t) \end{cases} + \frac{v_{dc}(t)}{L} \begin{cases} u_d(t) \\ u_q(t) \end{cases}. \quad (9.15)$$

Then, an \mathcal{H}_∞ controller is designed to guarantee that current tracking error converges to zero, as follows:

$$\begin{cases} u_d(t) \\ u_q(t) \end{cases} = \begin{cases} -\frac{L}{v_{dc}(t)}k_d\varepsilon_d(t) + \frac{e_d}{v_{dc}(t)} + \frac{L}{v_{dc}(t)}\omega i_q(t) \\ -\frac{L}{v_{dc}(t)}k_q\varepsilon_q(t) + \frac{e_q}{v_{dc}(t)} - \frac{L}{v_{dc}(t)}\omega i_d(t) \end{cases}, \quad (9.16)$$

where k_d and k_q are \mathcal{H}_∞ controller gains to be designed.

Considering (9.15) and (9.16), it follows that

$$\begin{cases} \dot{\varepsilon}_d(t) \\ \dot{\varepsilon}_q(t) \end{cases} = \begin{cases} -k_d \varepsilon_d(t) + \omega_d(t) \\ -k_q \varepsilon_q(t) + \omega_q(t) \end{cases}, \quad (9.17)$$

where $\omega_d(t) = \dot{i}_d^* + \frac{r}{L} i_d(t)$, $\omega_q(t) = \dot{i}_q^* + \frac{r}{L} i_q(t)$. Note that the parasitic resistance r and \dot{i}_j^* , $j \in \{d, q\}$ viewed as external disturbance are generally unknown, and can not be applied in the controller directly. As can be seen from (9.16) and (9.17), the current tracking errors $\varepsilon_d(t)$ and $\varepsilon_q(t)$ are decoupled, and the controllers for d-axis and q-axis currents can be designed independently. Rewrite the d-axis current tracking error $\varepsilon_d(t)$ as

$$\begin{aligned} \dot{\varepsilon}_d(t) &= -k_d \varepsilon_d(t) + \omega_d(t), \\ y_d(t) &= \varepsilon_d(t), \end{aligned} \quad (9.18)$$

where $y_d(t)$ is the controlled output, and $\omega_d(t)$ is the disturbance input.

Theorem 9.4 Consider the system (9.18) with an \mathcal{H}_∞ controller. For a given positive constant γ_d , if there exist two positive scalars h_d and l_d , such that following inequality holds,

$$\begin{bmatrix} -2l_d & h_d & 1 \\ h_d & -\gamma_d & 0 \\ 1 & 0 & -\gamma_d \end{bmatrix} \leq 0, \quad (9.19)$$

then system (9.18) is asymptotically stable when $\omega_d(t) = 0$ and has an \mathcal{H}_∞ performance less than γ_d , and the \mathcal{H}_∞ controller gain is given by $k_d = \frac{l_d}{h_d}$.

Proof When $\omega_d(t) = 0$, it is obvious that the system (9.18) is asymptotically stable as the controller gain k_d is a positive.

When $\omega_d(t) \neq 0$, define the $h'_d = \gamma_d h_d$, $l'_d = \gamma_d l_d$ and

$$T_d = \begin{bmatrix} \sqrt{\gamma_d} & 0 & 0 \\ 0 & \sqrt{\gamma_d} & 0 \\ 0 & 0 & \frac{1}{\sqrt{\gamma_d}} \end{bmatrix}. \quad (9.20)$$

From (9.19), it can be obtained that

$$T_d \begin{bmatrix} -2l_d & h_d & 1 \\ h_d & -\gamma_d & 0 \\ 1 & 0 & -\gamma_d \end{bmatrix} T_d^T = \begin{bmatrix} -2l'_d & h'_d & 1 \\ h'_d & -\gamma_d^2 & 0 \\ 1 & 0 & -1 \end{bmatrix} \leq 0. \quad (9.21)$$

By the Schur complement, (9.21) is equivalent to

$$\begin{cases} -2l'_d & h'_d \\ h'_d & -\gamma_d^2 \end{cases} + \begin{cases} 1 \\ 0 \end{cases} \begin{bmatrix} 1 & 0 \end{bmatrix} \leq 0, \quad (9.22)$$

that is,

$$\begin{Bmatrix} -2l'_d + 1 & h'_d \\ h'_d & -\gamma_d^2 \end{Bmatrix} \leq 0. \quad (9.23)$$

Applying Schur complement to (9.23) again, the inequality (9.23) holds if and only if,

$$-2l'_d + 1 + (h'_d)^2 \gamma_d^{-2} \leq 0. \quad (9.24)$$

Then, based on (9.21)-(9.24), (9.19) is equivalent to

$$-2l_d + 1 + h_d^2 \gamma_d^{-2} \leq 0. \quad (9.25)$$

On the other hand, construct following Lyapunov function for system (9.18),

$$V_2(t) = h_d \varepsilon_d^2(t). \quad (9.26)$$

Take the derivative of the Lyapunov function (9.26) along the trajectory of system (9.18) and obtain

$$\dot{V}_2(t) = 2h_d \varepsilon_d(t) \dot{\varepsilon}_d(t) = -2h_d k_d \varepsilon_d^2(t) + 2h_d \varepsilon_d(t) \omega_d(t). \quad (9.27)$$

According to Lemma 1, it is obtained that

$$\dot{V}_2(t) \leq -2h_d k_d \varepsilon_d^2(t) + \gamma_d^{-2} h_d^2 \varepsilon_d^2(t) + \gamma_d^2 (\omega_d(t))^2. \quad (9.28)$$

For system (9.18), consider

$$J = \int_0^\infty (\varepsilon_d^2(t) - \gamma_d^2 (\omega_d(t))^2 + \dot{V}_2(t)) dt - (V_2(\infty) - V_2(0)). \quad (9.29)$$

It follows from (9.28) and (9.18) that

$$\begin{aligned} J &= \int_0^\infty (\varepsilon_d^2(t) - \gamma_d^2 (\omega_d(t))^2) dt \\ &\leq \int_0^\infty (-2l_d + \gamma_d^{-2} h_d^2 + 1) \varepsilon_d^2(t) dt - V_2(\infty) \\ &\leq 0, \end{aligned} \quad (9.30)$$

which means that system (9.18) has an \mathcal{H}_∞ performance less than γ_d . Proof completed. ■

Similar to Theorem 9.4, the \mathcal{H}_∞ controller for q-axis current $i_q(t)$ can be obtained.

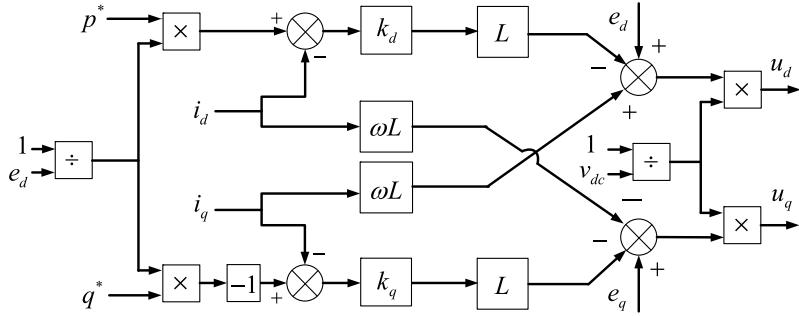


Fig. 9.2 \mathcal{H}_∞ controller structure

Theorem 9.5 Consider the system

$$\begin{aligned}\dot{\varepsilon}_q(t) &= -k_q \varepsilon_q(t) + \omega_q(t), \\ y_q(t) &= \varepsilon_q(t),\end{aligned}\quad (9.31)$$

with an \mathcal{H}_∞ controller. For a given positive constant γ_q , if there exist two positive scalars h_q and l_q , such that following inequality constraint holds,

$$\begin{bmatrix} -2l_q & h_q & 1 \\ h_d & -\gamma_d & 0 \\ 1 & 0 & -\gamma_q \end{bmatrix} \leq 0, \quad (9.32)$$

then system (9.31) is asymptotically stable when $\omega_q(t) = 0$ and has an \mathcal{H}_∞ performance less than γ_q , and the \mathcal{H}_∞ controller gain is given by $k_q = \frac{l_q}{h_q}$.

Figure 9.2 shows the diagram of the \mathcal{H}_∞ controller.

Remark 9.6 In Theorem 9.4 and Theorem 9.5, two \mathcal{H}_∞ controllers have been designed in the current tracking loop to track the current references i_q^* and i_d^* . Note that unlike SMC whose parameter tuning is not easy, \mathcal{H}_∞ control method is of simple control structure and the gains are formulated in terms of linear matrix inequalities which can be efficiently solved by software. ♦

Remark 9.7 From d-axis current tracking error dynamic system (9.18), its transfer function from the disturbance input $\omega_d(t)$ to the output $y_d(t)$ can be represented as $G_d(s) = (s + k_d)^{-1}$, i.e., $y_d(s) = G_d(s)\omega_d(s)$. Then \mathcal{H}_∞ performance can be rewritten as $G_d(s) \leq \gamma_d$, which means the amplifier of the disturbance input $\omega_d(t)$ to the output $y_d(t)$ is less than γ_d . The smaller γ_d is, the better disturbance rejection ability system has. From Theorem 9.4 it can be seen, the \mathcal{H}_∞ problem is a general standard LMI feasibility problem. To obtain the minimum index, the following optimization problem is formed: for $\forall j \in \{d, q\}$,

$$\left\{ \begin{array}{l} \min \quad \gamma_j \\ \text{s.t. } h_j \geq 0, \quad l_j \geq 0, \\ \left[\begin{array}{ccc} -2l_j & h_j & 1 \\ h_j & -\gamma_j & 0 \\ 1 & 0 & -\gamma_j \end{array} \right] \leq 0. \end{array} \right. \quad (9.33)$$

However, it should be noted that there is no need, sometimes even undesirable, to search for the minimum index in practice since the minimum index may lead to high gain for the controller. Thus, it is much easier and more practical to search for sub-minimum index which is very near to the minimum one in the norm sense. ♦

Remark 9.8 It should be pointed that the \mathcal{H}_∞ controllers designed above are actually proportional controllers. However, different from the conventional proportional controller, a specified performance index γ can be selected to make the system reach a certain disturbance rejection level. Moreover, the model used for designing \mathcal{H}_∞ controller is ideal model without considering uncertain parameters, which is inevitable practical systems. Thus in some situations an integral part is added to eliminate the steady-state error to further improve the system performance. The following procedures can be taken to choose the control parameters: first, set the integral gain to zero, and based on a specified \mathcal{H}_∞ performance index γ , calculate the H_∞ controller gain. Second, gradually increase integral gain until any offset is corrected in sufficient time for the process. Then the optimum PI controller is obtained to achieve a desired system performance. ♦

Remark 9.9 Although the integral action can improve the system performance, it also brings lagging effects for the power converter. If the integral parameter is not appropriate, the response time is usually long, even leads to system instability. A fast tracking response can be achieved by proportional controller only, however, there is steady state tracking error in the system without integral term in the controller. Therefore, the \mathcal{H}_∞ performance index γ and integral control gain should be balanced to obtain better transient response with fast convergence rate and high accuracy. ♦

9.2 Simulation Verification

In this section, simulations are carried out to verify the effectiveness of proposed control strategy. The system parameters are shown in Table 9.1.

(1) Comparative result

The adaptive \mathcal{H}_∞ control strategy is compared with the ESO-SOSM strategy proposed in [5], as the ESO-SOSM control strategy has been verified in [5] and demonstrates better performance than the PI controller. The resistance R_L steps from no load to 60Ω at $t = 0.4$ s, then to 30Ω (full load 18.75 kW) at $t = 0.8$ s. The parameters of the proposed and ESO-SOSM controllers are shown in the Table 9.2.

Table 9.1 System parameters

Parameter	Value	Description
f_c	$10 \cdot 10^3$	Switching rate (Hz)
R_L	{30, 60}	Load resistance (Ω)
C	3300	DC-link capacitor (uF)
L	2	Phase inductor (mH)
ω	100π	Grid frequency (rad/s)
E	400	Grid line voltage (V)
V_{dc}^*	750	Voltage reference (V)

Table 9.2 Control parameters

Adaptive \mathcal{H}_∞ controller		ESO-SOSM controller in [5]	
Cur. Tra. loop	Vol. Reg. loop	Cur. Tra. loop	Vol. Reg. loop
$\gamma_d = \gamma_q = 0.2$	$\eta = 5 \cdot 10^{-6}$	$\lambda_d = \lambda_q = 18$	$\beta_1 = 26.4$, $\beta_2 = 2.64 \cdot 10^4$
$k_d = k_q = 21.5052$	$k = 5$	$\alpha_d = \alpha_q = 120$	$\lambda_{dc} = 1$, $\alpha_{dc} = 110$

Figure 9.3 shows the output voltage transient response obtained by the control strategies, as can be seen that both control strategies are able to regulate the dc-link voltages v_{dc} to the reference value 750 V. However, during the load steps, the adaptive \mathcal{H}_∞ control strategy presents the better performance than the ESO-SOSM control, as shown in Fig. 9.4, in terms of less output voltage drop and faster dynamic response. Figure 9.5 and 9.6 show the transient responses of current i_{dq} , both control strategies result in good tracking performance, especially for the current i_d . Figure 9.6 shows that the current i_q is stabilized around 0 A with both control, which means the reactive power is controlled around 0 Var and the power factor is close to unity. More importantly, it should be noticed that for current i_q , the adaptive \mathcal{H}_∞ control strategy has better tracking performance.

Figures 9.7 and 9.8 together show the input currents i_a and corresponding source voltages e_a , from which it can be observed that under both control schemes the sine wave i_a is in phase with the e_a . However, the resulted current THD of the proposed schemes (2.04 %) is slightly less than the ESO-SOSM scheme (3.32 %), as shown in Fig. 9.9. The adaptive law in the external loop is shown in Fig. 9.10.

Table 9.3 compares the results of proposed control strategy, conventional PI, ESO-SOSM strategy in [5], and \mathcal{H}_∞ -SMC strategy in [6], from which it can be observed that the proposed control strategy results in the least voltage drop and lowest current THD level.

(2) Current tracking ability

This subsection is to verify the current tracking ability of proposed approach. The resistance R_L steps from 0 Ω to 30 Ω at $t = 0.4$ s, i.e. the active power steps from

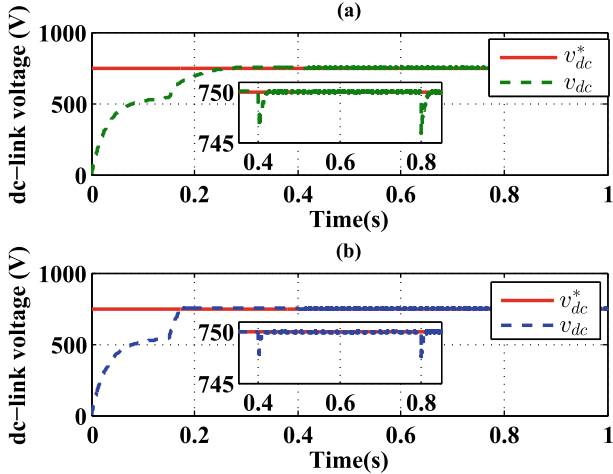


Fig. 9.3 Output voltage response: **a** ESO-SOSM control, **b** Adaptive \mathcal{H}_∞ control

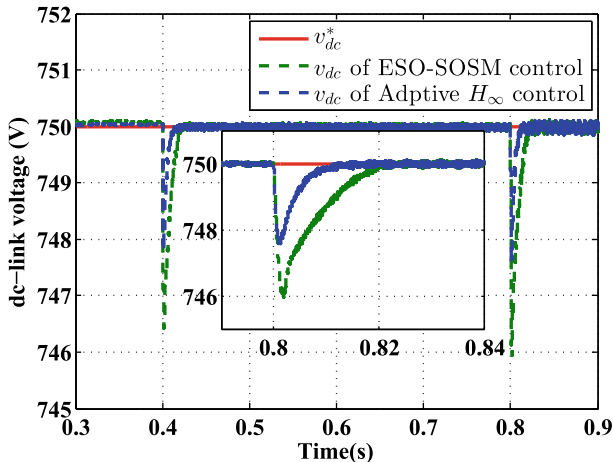


Fig. 9.4 Output voltage response with load steps

0 kW to 18.75 kW at $t = 0.4$ s, and the reactive power command steps from 0 kVar to 15 kVar at $t = 0.5$ s. Figure 9.11 shows the transient responses of instantaneous active power and reactive power, which demonstrate that the powers are tracked. Also it can be noticed that the input current i_a is no longer in phase with the corresponding source voltage e_a in Fig. 9.12. From Fig. 9.13, it can be seen that proposed adaptive \mathcal{H}_∞ control strategy force the current $i_q(t)$ and current $i_d(t)$ to track their references i_q^* and i_d^* , whose errors are within the acceptable level, as drawn in Fig. 9.14, which demonstrate the effectiveness of proposed approach.

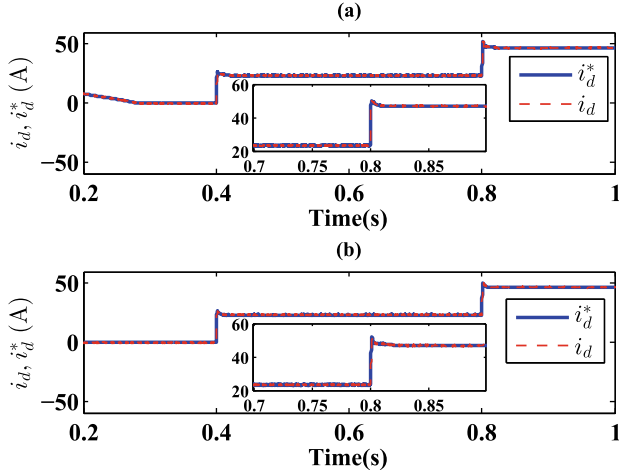


Fig. 9.5 i_d response: **a** ESO-SOSM control, **b** Adaptive \mathcal{H}_∞ control

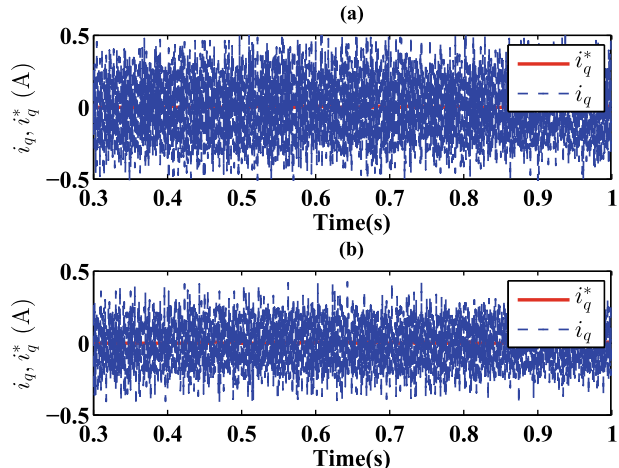


Fig. 9.6 i_q response: **a** ESO-SOSM control, **b** Adaptive \mathcal{H}_∞ control

(3) Robustness test

In this subsection, the parameter uncertainties are introduced, i.e., the filtering inductors L and the dc capacitor C vary by 10% ($\bar{L} = L + 10\% \cdot L$ and $\bar{C} = C + 10\% \cdot C$), also the white gauss noise $f(t) = 0.2 \times (2\pi)^{-\frac{1}{2}} \exp(-\frac{t^2}{2})$, is added to the measured output voltage $v_{dc}(t)$. The resistance R_L steps from no load to 30Ω at $t = 0.5s$, to test the robustness of proposed control strategy. Due to the presence of parameter uncertainties and measurement noises, the disturbance input increases significantly. Therefore, the \mathcal{H}_∞ performance index γ should be appropriately increased

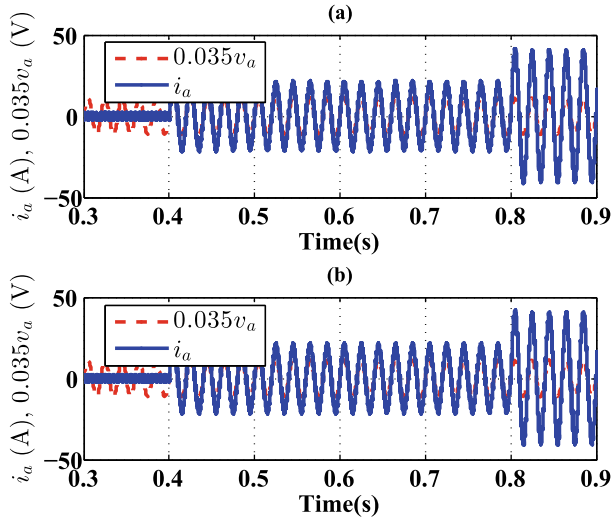


Fig. 9.7 Responses of grid current and grid voltage: **a** ESO-SOSM control, **b** Adaptive \mathcal{H}_∞ control

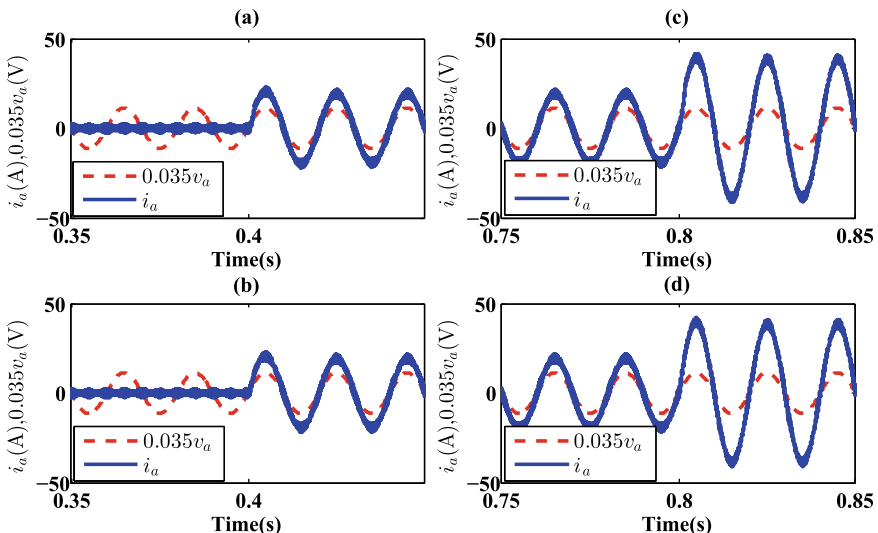


Fig. 9.8 Responses of grid current and grid voltage: **a** ESO-SOSM control at first load step, **b** Adaptive \mathcal{H}_∞ control at first load step, **c** ESO-SOSM control at second load step, **d** Adaptive \mathcal{H}_∞ control at second load step

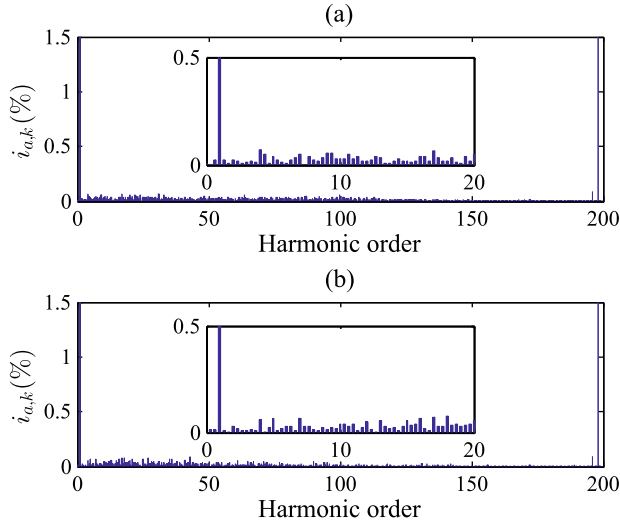


Fig. 9.9 Current THD: **a** ESO-SOSM control, **b** Adaptive \mathcal{H}_∞ control

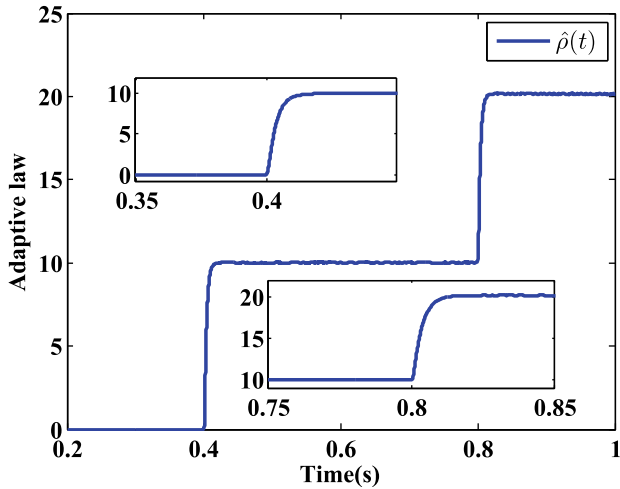


Fig. 9.10 Responses of adaptive law

to $\gamma_d = \gamma_q = 0.3$. By solving the LMI problem, the \mathcal{H}_∞ controllers are obtained as $k_d = k_q = 10.8871$. Based on the Remark 9.9, an integral part $k_{id} = k_{iq} = 1000$ is added to improve the system performance.

A comparison between the control strategy and [5] is carried out. Figure 9.15 shows the output voltage transient response of both control strategies. As can be seen that both control strategies are able to regulate the dc-link voltages under parameter uncertainties, measurement noise and external disturbances. However, similar to

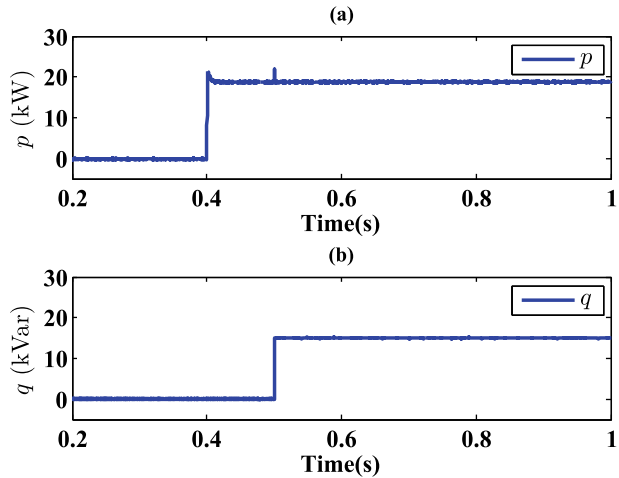


Fig. 9.11 Active power and reactive power responses under adaptive \mathcal{H}_∞ control

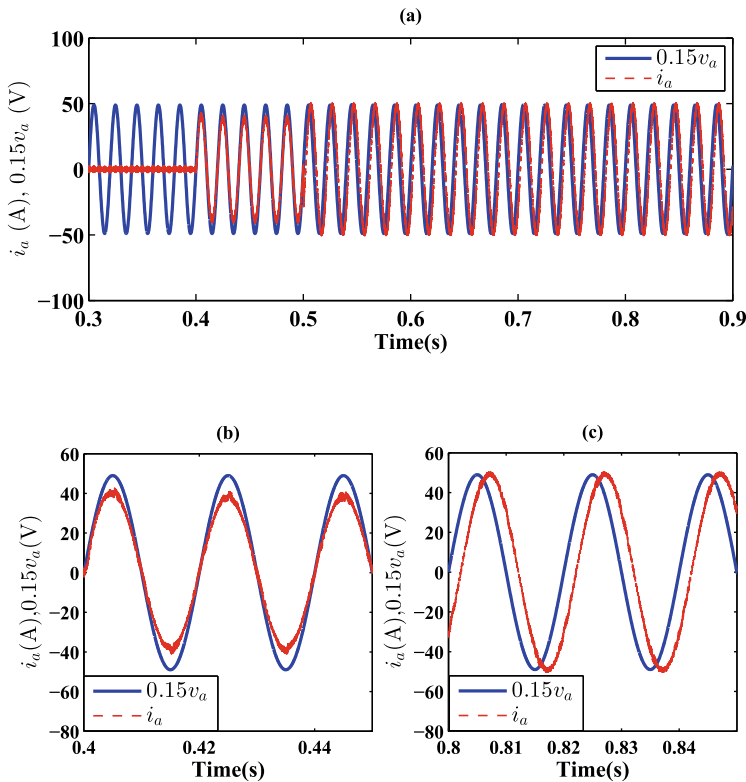
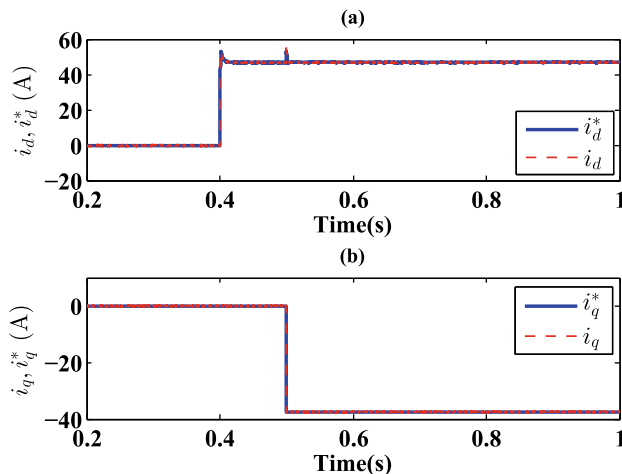


Fig. 9.12 Responses of grid current and grid voltage under adaptive \mathcal{H}_∞ control: **a** from 0.3 to 0.9 s, **b** from 0.4 to 0.45 s; **c** from 0.8 to 0.85 s

Table 9.3 Comparisons of proposed control strategy with other strategies

	PI	ESO-SOSM in [5]	\mathcal{H}_∞ -SMC in [6]	Adaptive \mathcal{H}_∞ control
Cur. Tra. loop	PI	ST-SMC	SMC	\mathcal{H}_∞ control
Vol. Reg. loop	PI	ST-SMC plus ESO	\mathcal{H}_∞ plus ESO	Adaptive control
Phase inductor	2 mH	2 mH	2 mH	2 mH
DC-link capacitor	3300 μ F	3300 μ F	3300 μ F	3300 μ F
Output power	18.75 kW	18.75 kW	18.75 kW	18.75 kW
Output voltage	750 V	750 V	750 V	750 V
Output voltage drop	21 V	4 V	15 V	2.5 V
Current THD	4.90%	3.32%	3.33%	2.04%

**Fig. 9.13** $i_{dq}(t)$ responses under adaptive \mathcal{H}_∞ control strategy

In the first simulation, the proposed adaptive \mathcal{H}_∞ control strategy obtains less output voltage drop and quicker dynamic response when load step is imposed. Figure 9.16 and 9.17 show that the currents track their references with both control strategies. However, due to the existence of parameter uncertainties and measurement noise, current tracking error increases noticeably. The tracking errors of adaptive \mathcal{H}_∞ and ESO-SOSM control strategy are roughly identical. However, compared with the proposed control strategy, the parameter tuning method of ESO-SOSM control strategy is rather complicated in the sense of practical implementation.

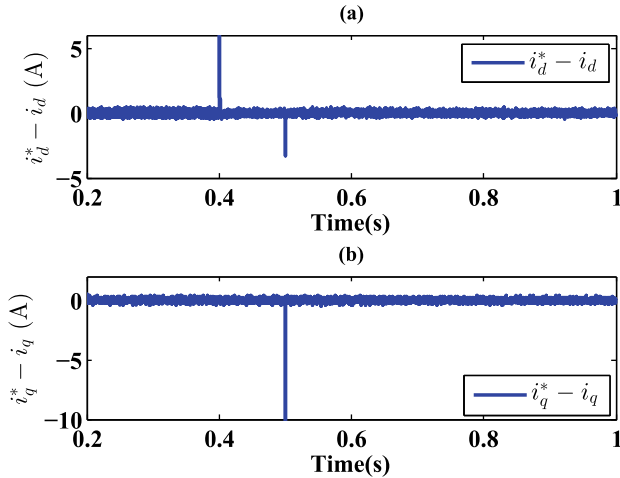


Fig. 9.14 $i_{dq}(t)$ error transients under adaptive \mathcal{H}_∞ control strategy

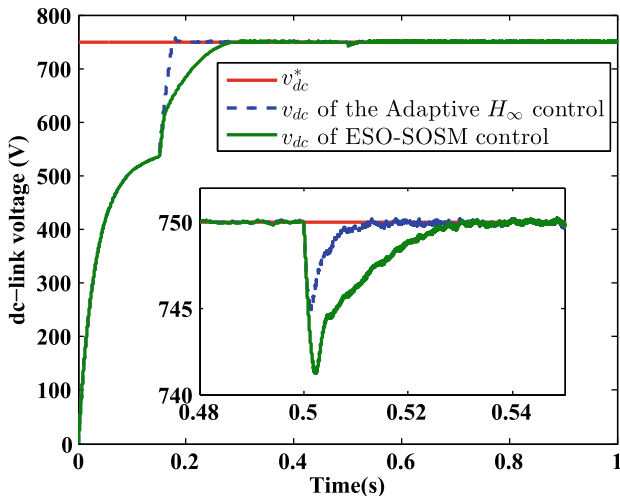


Fig. 9.15 v_{dc} response under parameter uncertainties and external disturbances

9.3 Summary

This chapter proposes adaptive \mathcal{H}_∞ control strategy to carry out the tasks of voltage regulation and current tracking for three-phase grid-connected power converters. Two types of controllers, adaptive controller and \mathcal{H}_∞ controllers are respectively applied in the voltage regulation loop and current tracking loop, to achieve control objectives. The proposed control strategy not only can obtain a desired volt-

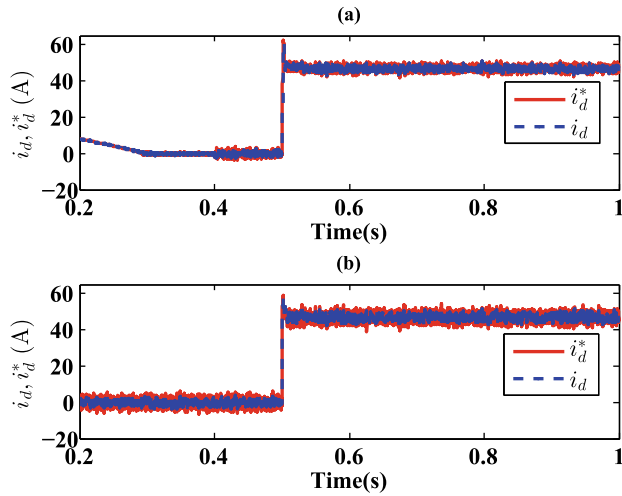


Fig. 9.16 i_d response: **a** ESO-SOSM control, **b** Adaptive \mathcal{H}_∞ control

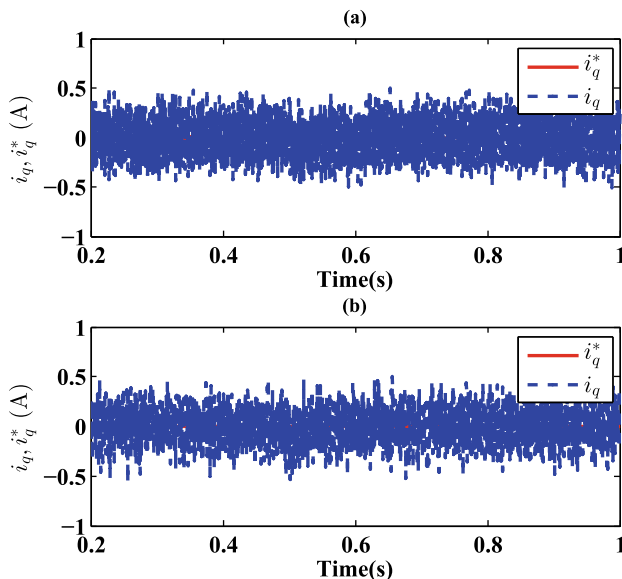


Fig. 9.17 i_q response: **a** ESO-SOSM control, **b** Adaptive \mathcal{H}_∞ control

age or current signals with small harmonic distortion, but also make the structure of controller simple and easy to implement. Simulations has been carried out to verify the advantage of proposed control strategy.

References

1. Doyle, J., Glover, K., Khargonekar, P., Francis, B.: State-space solutions to standard H_2 and H_∞ control problems. In: Proceedings of the 1988 IEEE American Control Conference, Atlanta, GA, USA, pp. 1691–1696 (1988)
2. Khalil, H.K., Grizzle, J.W.: Nonlinear Systems, vol. 3. Prentice Hall, Upper Saddle River, NJ (2002)
3. La Salle, J., Lefschetz, S.: Stability by Liapunov's Direct Method with Applications. Elsevier (2012)
4. Akagi, H., Watanabe, E.H., Aredes, M.: Instantaneous Power Theory and Applications to Power Conditioning. Wiley (2017)
5. Liu, J., Vazquez, S., Wu, L., Marquez, A., Gao, H., Franquelo, L.G.: Extended state observer-based sliding-mode control for three-phase power converters. *IEEE Trans. Ind. Electron.* **64**(1), 22–31 (2016)
6. Yin, Y., Luo, W., Liu, J., Vazquez, S., Wu, L., Franquelo, L.G.: Sliding mode control of three-phase power converters with disturbance attenuation performance. In: Proceedings of the 11th IEEE International Conference on Compatibility, Power Electronics and Power Engineering, Cadiz, Spain, pp. 270–275 (2017)

Chapter 10

Adaptive Sliding Mode Control of Three-Phase Two-Level Converters



Abstract In previous chapters, the parameters of the converter model are assumed to be certain. However in real applications, the converter model is often obtained based on several assumptions, such as that the characteristic of electronic devices does not vary with time. As can be seen, the model obtained in this way is not accurate, and under some conditions its behaviors may have big difference with real system. Therefore, the designed controller needs to be robust against the parameter uncertainty of the mode. Based on this reason, the parameter uncertainty must be taken into account, which may be caused by the filtering inductor L and its series resistance r , grid voltage frequency ω , which can be represented as follow:

$$L = L_0 + \Delta L, r = r_0 + \Delta r, \omega = \omega_0 + \Delta \omega, \quad (10.1)$$

where L_0 , r_0 and ω_0 are nominal values, ΔL , Δr and $\Delta \omega$ are parameter deviation, which can be assumed to be slow-varying signals.

On the other hand, though the super-twisting SMC adopted in previous chapters presents good control performance, it has certain limitation, as it needs to know the upper bound of the external disturbance derivative when selecting control parameters. However, in many real applications, this upper bound (Lipschitz constant) is hard to obtain, thus adaptive super-twisting SMC (ASMC) has been brought up. The ASMC consists of two parts, one part is the typical super-twisting SMC, the other is the PI algorithm [1, 2]. The control parameter of adaptive super-twisting SMC dynamically changes along with the sliding surface, thus the upper bound of the external disturbance derivative is no longer needed [3, 4].

Based on above reasons, this chapter considers both the load variation and the converter parameter uncertainty, and proposes a \mathcal{H}_∞ robust control method based on ASMC, to control the grid-connected three-phase two-level power converter. This chapter adopts VOC control structure. The voltage regulation loop adopts LESO to compensate the \mathcal{H}_∞ controller, to regulate the dc-link voltage to its reference.

The current tracking loop adopts two controllers based on ASMC, to drive the grid currents to their references in finite time. The Lyapunov method is adopted to prove the finite-time convergence of the closed-loop system. Due to the usage of ASMC, the upper bound of the external disturbance derivative is not needed to be provided a priori. The simulation results show that, when there exist load variation and parameter uncertainty, the proposed ASMC- \mathcal{H}_∞ control obtains better control performance and robustness than conventional PI.

10.1 Control Scheme

Based on adaptive control and \mathcal{H}_∞ control technologies, the ASMC based \mathcal{H}_∞ control scheme is design for three-phase two-level power converter. The LESO is employed in voltage regulation loop, and ASMC controller is adopted in current tracking loop.

10.1.1 Voltage Regulation Loop

Figure 10.1 is the voltage regulation loop, in which the controller is designed based on \mathcal{H}_∞ control technology, and the observer adopts LESO. It can be noticed that it is the same as in Chap. 5, the difference is that the output signal in this chapter is the current references. Combining the LESO part in Chap. 2, the dc-link voltage dynamic is give again here:

$$C\dot{z}_1 = u - d. \quad (10.2)$$

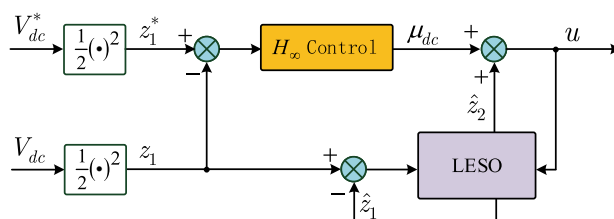


Fig. 10.1 Voltage regulation loop: H_∞ control based on LESO

(1) LESO design

For system (10.2), take the external disturbance as an extended system state, and its derivative is a bounded function $h(t)$, which satisfies:

$$\begin{cases} \dot{z}_1 = u - z_2, \\ \dot{z}_2 = h(t), \end{cases} \quad (10.3)$$

Then LESO can be designed for system (10.3) [5]:

$$\begin{cases} \dot{\hat{z}}_1 = u - \hat{z}_2 + \beta_1 e_1, \\ \dot{\hat{z}}_2 = -\beta_2 e_2, \end{cases} \quad (10.4)$$

where $\hat{z} = [\hat{z}_1 \ \hat{z}_2]^T$ is the estimated value of system state $z = [z_1 \ z_2]^T$, $e_1 = z_1 - \hat{z}_1$ is the observation error of z_1 . Note that e_1 is used in the correction term because z_1 is a measurable output. β_1 and β_2 are positive observer gains to be decided later.

Define $e_2 = z_2 - \hat{z}_2$, from (10.3) and (10.4), the observation error dynamic can be obtained as follows:

$$\begin{cases} \dot{e}_1 = -\beta_1 e_1 - e_2, \\ \dot{e}_2 = \beta_2 e_1 + h(t). \end{cases} \quad (10.5)$$

Then the error dynamic system (10.5) can be simplifies as:

$$\dot{e}_{eso} = A e_{eso} + \psi(t), \quad (10.6)$$

where $e_{eso} = [e_1 \ e_2]^T$, $A = \begin{bmatrix} -\beta_1 & -1 \\ \beta_2 & 0 \end{bmatrix}$. β_1 and β_2 must satisfy that matrix A is Hurwitz and $\psi(t) = [0 \ h(t)]^T$.

Lemma 10.1 Assume that the derivative of external disturbance $d(t)$ is a bounded function $h(t)$, then the observation error e_{eso} is also bounded with some positive scalars ρ and T :

$$\|e_{eso}\| \leq \rho, \quad \forall t \geq T. \quad (10.7)$$

Proof The solution of (10.6) can be written as [6]:

$$e_{eso}(t) = e_{eso}^{(t-t_0)A} e_{eso}(t_0) + \int_{t_0}^t e_{eso}^{(t-\tau)A} \psi(\tau) d\tau, \quad (10.8)$$

where t_0 is the initial instant. With the upper bound $\|e_{eso}^{(t-t_0)A}\| \leq \eta e_{eso}^{-\beta(t-t_0)}$, where η, β are positive, it can be obtained that

$$\begin{aligned} \|e_{eso}(t)\| &\leq \eta e_{eso}^{-\beta(t-t_0)} \|e_{eso}(t_0)\| + \int_{t_0}^t \eta e_{eso}^{-\beta(t-\tau)} \|\psi(\tau)\| d\tau \\ &\leq \eta e_{eso}^{-\beta(t-t_0)} \|e_{eso}(t_0)\| + \frac{\eta}{\beta} \sup_{t_0 \leq \tau \leq t} \|\psi(\tau)\|. \end{aligned} \quad (10.9)$$

With (10.9), it can be seen that $\|e_{eso}\| \leq \rho$, $\forall t \geq T > 0$, where ρ is some positive scalar depending on η , β and $\sup \|\psi(\tau)\|$. Proof completed. ■

(2) Voltage regulation loop design based on H_∞ technology

Define the dc-voltage error as $e = z^* - z$. The \mathcal{H}_∞ control target of voltage loop can be described as: design a controller based on disturbance observation error $e_2(t)$, which satisfies following two requirements:

- The obtained e is asymptotically stable, and the observation error $e_2(t) = 0$;
- With zero initial condition, when exists non-zero observation error $e_2(t) \in l_2[0, \infty)$, the following condition holds:

$$\int_0^{+\infty} e^T(t)e(t)dt \leq \gamma^2 \int_0^\infty e_2(t)^T(t)e_2(t)dt. \quad (10.10)$$

Construct the \mathcal{H}_∞ controller as follows:

$$u = \mu_{dc} + \hat{d}(t), \quad (10.11)$$

where $\mu_{dc} = Ke$, and K is the controller parameter to be designed. Thus the dynamic of dc-link voltage error is

$$\dot{e} = -Ke + e_2(t). \quad (10.12)$$

The \mathcal{H}_∞ control problem is the same as that in Chap. 5, therefore Theorem (5.3) can be adopted to design the H_∞ controller K .

10.1.2 Current Tracking Loop

Figure 10.2 is the current tracking loop designed based on ASMC.

In the current loop, the sliding mode variables are designed as $s_d = i_d^* - i_d$, $s_q = i_q^* - i_q$, differentiate them and obtain:

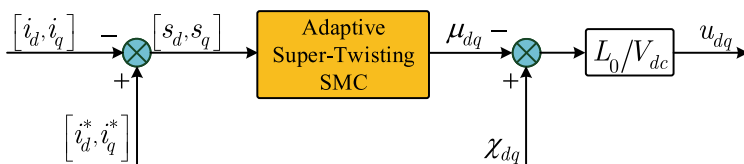


Fig. 10.2 Current tracking loop with adaptive super-twisting SMC

$$\begin{aligned}\dot{s}_d &= \dot{i}_d^* + \frac{r}{L} i_d - \frac{v_d}{L} - \omega i_q + \frac{V_{dc}}{L} u_d, \\ \dot{s}_q &= \dot{i}_q^* + \frac{r}{L} i_q + \omega i_d + \frac{V_{dc}}{L} u_q.\end{aligned}\quad (10.13)$$

Design ASMC control signals u_d, u_q as follow:

$$\begin{aligned}u_d &= \frac{L_0}{V_{dc}} (-\mu_d(s_d) + \chi_d), \\ u_q &= \frac{L_0}{V_{dc}} (-\mu_q(s_q) + \chi_q),\end{aligned}\quad (10.14)$$

where $\chi_d = \frac{v_d}{L_0} - \frac{r_0}{L_0} i_d - \dot{i}_d^* + \omega_0 i_q, \chi_q = -\frac{r_0}{L_0} i_q - \dot{i}_q^* - \omega_0 i_d$, and $\mu_d(s_d), \mu_q(s_q)$ are designed as [1]:

$$\mu_j(s_j) = \lambda_j(t) |s_j|^{\frac{1}{2}} \text{sign}(s_j) + \alpha_j(t) \int_0^t \text{sign}(s_j) d\tau + k_{\lambda_j}(t) s_j + k_{\alpha_j}(t) \int_0^t s_j d\tau, \quad j \in \{d, q\} \quad (10.15)$$

where

$$\begin{aligned}\lambda_d(t) &= \lambda_{d_0} \sqrt{\Gamma_d(t)}, \quad \alpha_d(t) = \alpha_{d_0} \Gamma_d(t), \\ k_{\lambda_d}(t) &= k_{\lambda_{d_0}} \Gamma_d(t), \quad k_{\alpha_d}(t) = k_{\alpha_{d_0}} \Gamma_d^2(t), \\ \lambda_q(t) &= \lambda_{q_0} \sqrt{\Gamma_q(t)}, \quad \alpha_q(t) = \alpha_{q_0} \Gamma_q(t), \\ k_{\lambda_q}(t) &= k_{\lambda_{q_0}} \Gamma_q(t), \quad k_{\alpha_q}(t) = k_{\alpha_{q_0}} \Gamma_q^2(t), \\ \dot{\Gamma}_d(t) &= \begin{cases} \epsilon_d, & \text{if } |s_d| \neq 0 \\ 0, & \text{else} \end{cases}, \quad \dot{\Gamma}_q(t) = \begin{cases} \epsilon_q, & \text{if } |s_q| \neq 0 \\ 0, & \text{else} \end{cases},\end{aligned}\quad (10.16)$$

where $\lambda_{d_0}, \lambda_{q_0}, \alpha_{d_0}, \alpha_{q_0}, k_{\lambda_{d_0}}, k_{\lambda_{q_0}}, k_{\alpha_{d_0}}, k_{\alpha_{q_0}}, \epsilon_d$ and ϵ_q are all positive. Then it is obtained that

$$\begin{aligned}\dot{s}_d &= -\frac{L_0}{L} \mu_d(s_d) + v_d, \\ \dot{s}_q &= -\frac{L_0}{L} \mu_q(s_q) + v_q,\end{aligned}\quad (10.17)$$

where $v_d = \frac{\Delta L}{L} \dot{i}_d^* + \frac{\Delta r}{L} i_d + \frac{L_0 \omega_0 - L \omega}{L} i_q, v_q = \frac{\Delta L}{L} \dot{i}_q^* + \frac{\Delta r}{L} i_q + \frac{L \omega - L_0 \omega_0}{L} i_d$.

As can be seen, when system parameter uncertainty causes current error, the adaptive law shall make the adaptive gains Γ_d, Γ_q increase until the error is eliminated, thus reject the influence caused by the parameter uncertainty.

10.1.3 Stability Analysis

Theorem 10.2 Consider system (2.9)–(2.11) and controller (10.14), assume that for some unknown positive values θ_d , θ_q , following condition holds:

$$\|\dot{v}_d\| \leq \theta_d, \quad \|\dot{v}_q\| \leq \theta_q, \quad (10.18)$$

then the trajectory of system (10.13) converges to $s_d = 0$, $s_q = 0$ in finite time, meanwhile for non-zero observation error $\tilde{d}(t)$, the dc-link voltage V_{dc} will converge to its reference V_{dc}^* with disturbance attenuation level of γ , if the parameters of $\mu_d(s_d)$ and $\mu_q(s_q)$ satisfy following condition:

$$\begin{aligned} 4\alpha_{d_0}k_{\alpha_{d_0}} &> 8\bar{\eta}_0k_{\lambda_{d_0}}^2\alpha_{d_0} + 9\bar{\eta}_0^2\lambda_{d_0}^2k_{\lambda_{d_0}}^2, \\ 4\alpha_{q_0}k_{\alpha_{q_0}} &> 8\bar{\eta}_0k_{\lambda_{q_0}}^2\alpha_{q_0} + 9\bar{\eta}_0^2\lambda_{q_0}^2k_{\lambda_{q_0}}^2, \end{aligned} \quad (10.19)$$

where $\bar{\eta}_0 > 0$, $\epsilon_d > 0$ and $\epsilon_q > 0$.

Proof The proof includes two parts, one is stability analysis of current tracking loop, the other is stability analysis of voltage regulation loop.

Consider the current error dynamic system (10.17) and conditions (10.18), (10.19), assume

$$(1 - \eta_0)L \leq L_0 \leq (1 + \eta_0)L, \quad (10.20)$$

where $0 < \eta_0 < 1$, then system (10.17) can be rewritten as:

$$\begin{aligned} \dot{s}_d &= -\bar{\eta}_0\mu_d(s_d) + v_d, \\ \dot{s}_q &= -\bar{\eta}_0\mu_q(s_q) + v_q, \end{aligned} \quad (10.21)$$

where $(1 - \eta_0) \leq \bar{\eta}_0 \leq (1 + \eta_0)$ are positive constants.

Introduce two state vectors to represent system (10.21):

$$\varepsilon_j = \begin{bmatrix} \varepsilon_{j_1} \\ \varepsilon_{j_2} \\ \varepsilon_{j_3} \end{bmatrix} = \begin{bmatrix} \Gamma_j^{\frac{1}{2}}(t)|s_j|^{\frac{1}{2}}\text{sign}(s_j) \\ \Gamma_j(t)s_j \\ \psi_j \end{bmatrix}, \quad j \in \{d, q\} \quad (10.22)$$

where $\psi_d = -\bar{\eta}_0\alpha_d(t)\text{sign}(s_d) - \bar{\eta}_0k_{\alpha_d}(t)s_d + \frac{d}{dt}\nu_d$, $\psi_q = -\bar{\eta}_0\alpha_q(t)\text{sign}(s_q) - \bar{\eta}_0k_{\alpha_q}(t)s_q + \frac{d}{dt}\nu_q$.

Construct following Lyapunov function for system (10.21):

$$V(s_d, s_q) = \underbrace{\varepsilon_d^T P_d \varepsilon_d}_{V_d} + \underbrace{\varepsilon_q^T P_q \varepsilon_q}_{V_q}, \quad (10.23)$$

where

$$\begin{aligned} P_d &= \frac{1}{2} \begin{bmatrix} 4\bar{\eta}_0\alpha_{d_0} + \bar{\eta}_0^2\lambda_{d_0}^2 & \bar{\eta}_0^2\lambda_{d_0}k_{\lambda_{d_0}} & -\bar{\eta}_0\lambda_{d_0} \\ \bar{\eta}_0^2\lambda_{d_0}k_{\lambda_{d_0}} & \bar{\eta}_0^2k_{\lambda_{d_0}}^2 + 2\bar{\eta}_0k_{\alpha_{d_0}} & -\bar{\eta}_0k_{\lambda_{d_0}} \\ -\bar{\eta}_0\lambda_{d_0} & -\bar{\eta}_0k_{\lambda_{d_0}} & 2 \end{bmatrix}, \\ P_q &= \frac{1}{2} \begin{bmatrix} 4\bar{\eta}_0\alpha_{q_0} + \bar{\eta}_0^2\lambda_{q_0}^2 & \bar{\eta}_0^2\lambda_{q_0}k_{\lambda_{q_0}} & -\bar{\eta}_0\lambda_{q_0} \\ \bar{\eta}_0^2\lambda_{q_0}k_{\lambda_{q_0}} & \bar{\eta}_0^2k_{\lambda_{q_0}}^2 + 2\bar{\eta}_0k_{\alpha_{q_0}} & -\bar{\eta}_0k_{\lambda_{q_0}} \\ -\bar{\eta}_0\lambda_{q_0} & -\bar{\eta}_0k_{\lambda_{q_0}} & 2 \end{bmatrix}, \end{aligned} \quad (10.24)$$

P_d , P_q are symmetrical positive definite matrices, because all the leading principle sub-matrices are positive definite with the condition (10.19).

Differentiate (10.23) along the trajectory of system (10.21), it can be obtained that

$$\begin{aligned} \dot{V} &= -\Gamma_d(t) \left(\frac{\varepsilon_d^T \Omega_{d_1} \varepsilon_d}{|\varepsilon_{d_1}|} + \varepsilon_d^T \Omega_{d_2} \varepsilon_d \right) \\ &\quad + q_{d_1} \frac{d}{dt} \nu_d \varepsilon_d + q_{d_2} \frac{\dot{\Gamma}_d(t)}{\Gamma_d(t)} P_{d_1} \varepsilon_d \\ &\quad - \Gamma_q(t) \left(\frac{\varepsilon_q^T \Omega_{q_1} \varepsilon_q}{|\varepsilon_{q_1}|} + \varepsilon_q^T \Omega_{q_2} \varepsilon_q \right) \\ &\quad + q_{q_1} \frac{d}{dt} \nu_q \varepsilon_q + q_{q_2} \frac{\dot{\Gamma}_q(t)}{\Gamma_q(t)} P_{q_1} \varepsilon_q, \end{aligned} \quad (10.25)$$

where

$$\begin{aligned} q_{d_1} &= [-\bar{\eta}_0\lambda_{d_0} \quad -\bar{\eta}_0k_{\lambda_{d_0}} \quad 2], \quad q_{d_2} = [\varepsilon_{d_1} \quad \varepsilon_{d_2} \quad 0], \\ q_{q_1} &= [-\bar{\eta}_{q_0}\lambda_{q_0} \quad -\bar{\eta}_0k_{\lambda_{q_0}} \quad 2], \quad q_{q_2} = [\varepsilon_{q_1} \quad \varepsilon_{q_2} \quad 0], \end{aligned}$$

meanwhile

$$\begin{aligned} \Omega_{d_1} &= \frac{\bar{\eta}_0\lambda_{d_0}}{2} \begin{bmatrix} \bar{\eta}_0^2\lambda_{d_0}^2 + 2\bar{\eta}_0\alpha_{d_0} & 0 & -\bar{\eta}_0\lambda_{d_0} \\ 0 & 2\bar{\eta}_0k_{\alpha_{d_0}} + 5\bar{\eta}_0^2k_{\lambda_{d_0}}^2 & -3\bar{\eta}_0k_{\lambda_{d_0}} \\ -\bar{\eta}_0\lambda_{d_0} & -3\bar{\eta}_0k_{\lambda_{d_0}} & 1 \end{bmatrix}, \\ \Omega_{d_2} &= \bar{\eta}_0k_{\lambda_{d_0}} \begin{bmatrix} \bar{\eta}_0\alpha_{d_0} + 2\bar{\eta}_0^2\lambda_{d_0}^2 & 0 & 0 \\ 0 & \bar{\eta}_0k_{\alpha_{d_0}} + \bar{\eta}_0^2k_{\lambda_{d_0}}^2 & -\bar{\eta}_0k_{\lambda_{d_0}} \\ 0 & -\bar{\eta}_0k_{\lambda_{d_0}} & 1 \end{bmatrix}, \\ \Omega_{q_1} &= \frac{\bar{\eta}_0\lambda_{q_0}}{2} \begin{bmatrix} \bar{\eta}_0^2\lambda_{q_0}^2 + 2\bar{\eta}_0\alpha_{q_0} & 0 & -\bar{\eta}_0\lambda_{q_0} \\ 0 & 2\bar{\eta}_0k_{\alpha_{q_0}} + 5\bar{\eta}_0^2k_{\lambda_{q_0}}^2 & -3\bar{\eta}_0k_{\lambda_{q_0}} \\ -\bar{\eta}_0\lambda_{q_0} & -3\bar{\eta}_0k_{\lambda_{q_0}} & 1 \end{bmatrix}, \\ \Omega_{q_2} &= \bar{\eta}_0k_{\lambda_{q_0}} \begin{bmatrix} \bar{\eta}_0\alpha_{q_0} + 2\bar{\eta}_0^2\lambda_{q_0}^2 & 0 & 0 \\ 0 & \bar{\eta}_0k_{\alpha_{q_0}} + \bar{\eta}_0^2k_{\lambda_{q_0}}^2 & -\bar{\eta}_0k_{\lambda_{q_0}} \\ 0 & -\bar{\eta}_0k_{\lambda_{q_0}} & 1 \end{bmatrix}. \end{aligned}$$

It can be verified that, with condition (10.19), Ω_{d_1} , Ω_{d_2} , Ω_{q_1} , Ω_{q_2} are all positive definite matrices. Considering $\lambda_{\min}(P_d)\|\varepsilon_d\|^2 \leq V_d \leq \lambda_{\max}(P_d)\|\varepsilon_d\|^2$, $\lambda_{\min}(P_q)\|\varepsilon_q\|^2 \leq V_q \leq \lambda_{\max}(P_q)\|\varepsilon_q\|^2$, (10.25) can be rewritten as

$$\begin{aligned} \dot{V} &\leq -\Gamma_d(t) \frac{\lambda_{\min}(\Omega_{d_1})}{\lambda_{\max}^{\frac{1}{2}}(P_d)} V_d^{\frac{1}{2}} - \Gamma_d(t) \frac{\lambda_{\min}(\Omega_{d_2})}{\lambda_{\max}(P_d)} V_d \\ &+ \theta_d \frac{\|q_{d_1}\|_2}{\lambda_{\min}^{\frac{1}{2}}(P_d)} V_d^{\frac{1}{2}} + \frac{\dot{\Gamma}_d(t)}{2\Gamma_d(t)} \varepsilon_d^T Q_d \varepsilon_d \\ &- \Gamma_q(t) \frac{\lambda_{\min}(\Omega_{q_1})}{\lambda_{\max}^{\frac{1}{2}}(P_q)} V_q^{\frac{1}{2}} - \Gamma_q(t) \frac{\lambda_{\min}(\Omega_{q_2})}{\lambda_{\max}(P_q)} V_q \\ &+ \theta_q \frac{\|q_{q_1}\|_2}{\lambda_{\min}^{\frac{1}{2}}(P_q)} V_q^{\frac{1}{2}} + \frac{\dot{\Gamma}_q(t)}{2\Gamma_q(t)} \varepsilon_q^T Q_q \varepsilon_q \end{aligned} \quad (10.26)$$

where

$$Q_d = \begin{bmatrix} q_{d_3} & 0 & 0 \\ 0 & q_{d_4} & 0 \\ 0 & 0 & q_{d_5} \end{bmatrix}, \quad Q_q = \begin{bmatrix} q_{q_3} & 0 & 0 \\ 0 & q_{q_4} & 0 \\ 0 & 0 & q_{q_5} \end{bmatrix}, \quad (10.27)$$

meanwhile

$$\begin{aligned} q_{d_3} &= 4\bar{\eta}_0 \alpha_{d_0} + \bar{\eta}_0^2 \lambda_{d_0}^2 + \bar{\eta}_0^2 \lambda_{d_0} k_{\lambda_{d_0}} + \bar{\eta}_0 \frac{\lambda_{d_0}}{2}, \\ q_{d_4} &= \bar{\eta}_0 \frac{\lambda_{d_0} + k_{\lambda_{d_0}}}{2}, \\ q_{d_5} &= 2\bar{\eta}_0^3 k_{\alpha_{d_0}} k_{\lambda_{d_0}}^2 + \bar{\eta}_0^2 \lambda_{d_0} k_{\lambda_{d_0}} + \bar{\eta}_0 \frac{k_{\lambda_{d_0}}}{2}, \\ q_{q_3} &= 4\bar{\eta}_0 \alpha_{q_0} + \bar{\eta}_0^2 \lambda_{q_0}^2 + \bar{\eta}_0^2 \lambda_{q_0} k_{\lambda_{q_0}} + \bar{\eta}_0 \frac{\lambda_{q_0}}{2}, \\ q_{q_4} &= \bar{\eta}_0 \frac{\lambda_{q_0} + k_{\lambda_{q_0}}}{2}, \\ q_{q_5} &= 2\bar{\eta}_0^3 k_{\alpha_{q_0}} k_{\lambda_{q_0}}^2 + \bar{\eta}_0^2 \lambda_{q_0} k_{\lambda_{q_0}} + \bar{\eta}_0 \frac{k_{\lambda_{q_0}}}{2}. \end{aligned}$$

It can be obtained from (10.26):

$$\begin{aligned} \dot{V} &\leq -(\Gamma_d(t)\gamma_{d_1} - \gamma_{d_2}) V_d^{\frac{1}{2}} - \left(\Gamma_d(t)\gamma_{d_3} - \gamma_{d_4} \frac{\dot{\Gamma}_d(t)}{\Gamma_d(t)} \right) V_d \\ &- (\Gamma_q(t)\gamma_{q_1} - \gamma_{q_2}) V_q^{\frac{1}{2}} - \left(\Gamma_q(t)\gamma_{q_3} - \gamma_{q_4} \frac{\dot{\Gamma}_q(t)}{\Gamma_q(t)} \right) V_q \\ &\leq -c_{d_1} V_d^{\frac{1}{2}} - c_{d_2} V_d - c_{q_1} V_q^{\frac{1}{2}} - c_{q_2} V_q \end{aligned}$$

$$\begin{aligned} &\leq -\min\{c_{d_1}, c_{q_1}\} \left(V_d^{\frac{1}{2}} + V_q^{\frac{1}{2}} \right) - \min\{c_{d_2}, c_{q_2}\} V \\ &\leq -\min\{c_{d_1}, c_{q_1}\} V^{\frac{1}{2}} - \min\{c_{d_2}, c_{q_2}\} V, \end{aligned} \quad (10.28)$$

where

$$\begin{aligned} c_{d_1} &= \Gamma_d(t)\gamma_{d_1} - \theta_d\gamma_{d_2}, \\ c_{d_2} &= \Gamma_d(t)\gamma_{d_3} - \gamma_{d_4} \frac{\dot{\Gamma}_d(t)}{\Gamma_d(t)}, \\ c_{q_1} &= \Gamma_q(t)\gamma_{q_1} - \theta_q\gamma_{q_2}, \\ c_{q_2} &= \Gamma_q(t)\gamma_{q_3} - \gamma_{q_4} \frac{\dot{\Gamma}_q(t)}{\Gamma_q(t)}, \end{aligned}$$

and

$$\begin{aligned} \gamma_{d_1} &= \frac{\lambda_{\min}(\Omega_{d_1})}{\lambda_{\max}^{\frac{1}{2}}(P_d)}, \quad \gamma_{d_2} = \theta_d \frac{\|q_{d_1}\|_2}{\lambda_{\min}^{\frac{1}{2}}(P_d)}, \\ \gamma_{d_3} &= \frac{\lambda_{\min}(\Omega_{d_2})}{\lambda_{\max}(P_d)}, \quad \gamma_{d_4} = \frac{\lambda_{\max}(\Omega_d)}{2\lambda_{\min}(P_d)}, \\ \gamma_{q_1} &= \frac{\lambda_{\min}(\Omega_{q_1})}{\lambda_{\max}^{\frac{1}{2}}(P_q)}, \quad \gamma_{q_2} = \theta_q \frac{\|q_{q_1}\|_2}{\lambda_{\min}^{\frac{1}{2}}(P_q)}, \\ \gamma_{q_3} &= \frac{\lambda_{\min}(\Omega_{q_2})}{\lambda_{\max}(P_q)}, \quad \gamma_{q_4} = \frac{\lambda_{\max}(\Omega_q)}{2\lambda_{\min}(P_q)}. \end{aligned} \quad (10.29)$$

It can be obtained from (10.16) that, c_{d_1} , c_{d_2} , c_{q_1} , c_{q_2} are positive in finite time. According to the comparison principle [6], the differential inequality (10.28) is of finite time convergence, i.e., ε_d , ε_q will converge to the equilibrium in finite time. Proof completed. ■

10.2 Simulation Verification

In this section, comparative simulation between the proposed ASMC and the linear PI control is performed to validate the effectiveness of the proposed control strategy. Multi-rate simulation is adopted with following considerations:

1. The simulating rate f_1 (representing the continuous converter system) is two orders of the controller updating rate f_2 (representing the discrete controller).
2. The switching rate f_3 of power switches is selected the same as updating rate f_2 .

Table 10.1 shows the simulation parameters. The load disturbance is of resistive type and is connected at $t = 0.6$ s. The filtering inductor is set to vary 20 % around its nominal value in order to verify the robustness of the proposed ASMC- \mathcal{H}_∞ strategy.

Table 10.1 System parameters

Parameter	Value	Description
f_1	$1 \cdot 10^6$	Simulation rate (Hz)
f_2	$1 \cdot 10^4$	Controller evaluation rate (Hz)
f_3	$1 \cdot 10^4$	Pulse width modulator rate (Hz)
r	0.01	Parasitic phase resistance (Ω)
R_L	30	Load resistance ()
C	3300	DC-link capacitor (μF)
L	2	Phase inductor (mH)
f	50	Grid frequency (Hz)
E	400	Grid voltage magnitude (V)
V_{dc}^*	750	Voltage reference (V)

Table 10.2 Control parameters

Adp. ST-SMC controller		PI controller	
Cur. Tra. loop	Vol. Reg. loop	Cur. Tra. loop	Vol. Reg. loop
$\lambda_{d0} = \lambda_{q0} = 6$	$K = 68.66$	$k_{pi_{cd}} = k_{pi_{cq}} = 10$	$k_{pv} = 0.2$
$\alpha_{d0} = \alpha_{q0} = 80$	$\kappa_1 = 0.6 \cdot 10^3$	$k_{ii_{cd}} = k_{ii_{cq}} = 200$	$k_{iv} = 5$
$k_{\lambda_{d0}} = k_{\lambda_{q0}} = 0.2$	$\kappa_2 = 3.6 \cdot 10^5$		
$k_{\alpha_{d0}} = k_{\alpha_{q0}} = 10$			
$\epsilon_d = \epsilon_q = 55$			

During the time period $0 \sim 0.15$ s, the power converter finishes pre-charge, and the controller starts operation after $t = 0.15$ s. The parameters of ASMC- \mathcal{H}_∞ controller and PI controller are given in Table 10.2, which are selected such that the dynamics of the current loop are much faster than that of the voltage loop.

Figures 10.3, 10.4, 10.5, 10.6 and 10.7 show the comparative simulation results between the ASMC- \mathcal{H}_∞ and the PI control. As can be observed, comparing with PI control, the ASMC- \mathcal{H}_∞ results in faster dc-link voltage transient response. Furthermore, when the load is connected at $t = 0.6$ s, the voltage drop obtained from the proposed ASMC- \mathcal{H}_∞ control is much lower than that from PI control, i.e., the ASMC- \mathcal{H}_∞ results in 18 V drop and PI 78 V. Therefore, ASMC- \mathcal{H}_∞ is more capable of recovering the dc-link voltage when disturbed by load variations.

Figures 10.4, 10.4 and 10.5 show the transient responses of the grid currents i_d and i_q when disturbed by load variation and parameter uncertainty. As can be seen, ASMC- \mathcal{H}_∞ achieves faster dynamics than PI. In steady state, the grid current i_d maintains at around 46.5 A, and the grid current i_q maintains at around 0 A which ensures unity power factor. From Figs. 10.4 and 10.5, small current overshoot and fast convergence can be observed, i.e., when the load is connected at $t = 0.6$ s, the grid currents i_d and i_q with ASMC- \mathcal{H}_∞ control converge much faster than that with

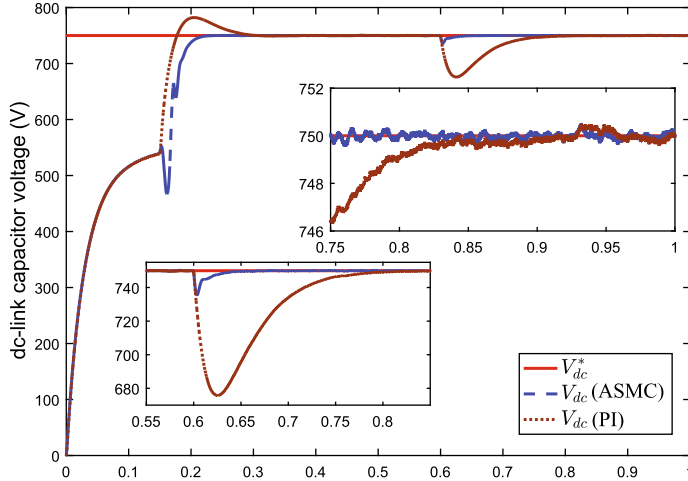


Fig. 10.3 DC-link capacitor voltage transient response

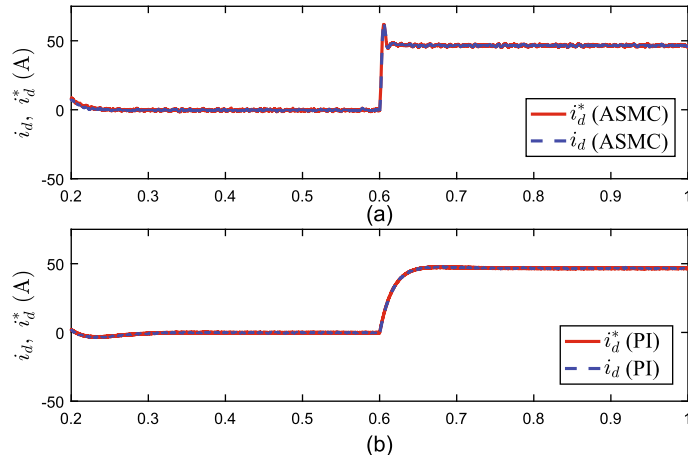


Fig. 10.4 i_d transient response: **a** Adp. ST-SMC, **b** PI control

PI control. Figure 10.6 shows one phase input current i_a along with the corresponding source voltage U_{ga} , as can be seen that both the two controllers can achieve no phase shift between the input phase current and corresponding source voltage. Figure 10.7 shows the evolution of the adaptive-gains $\Gamma_d(t)$ and $\Gamma_q(t)$, which guarantee that the sliding variables s_d and s_q to converge in finite time. The gains in the ASMC expression (10.16) stop increasing when the sliding variables converge to some certain levels.

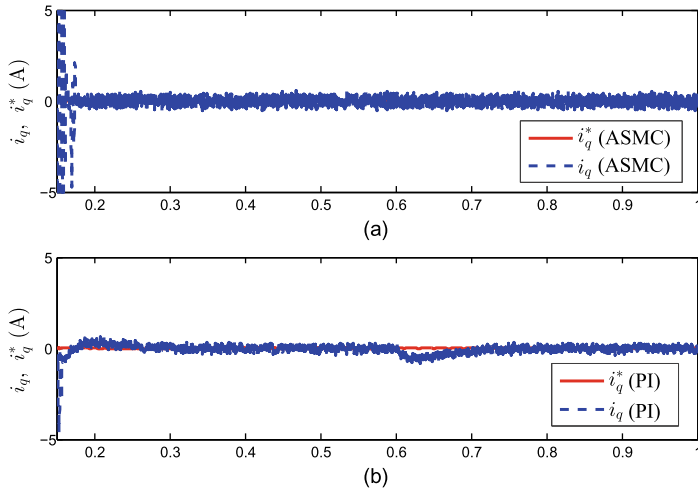


Fig. 10.5 i_q transient response: **a** Adp. ST-SMC, **b** PI control

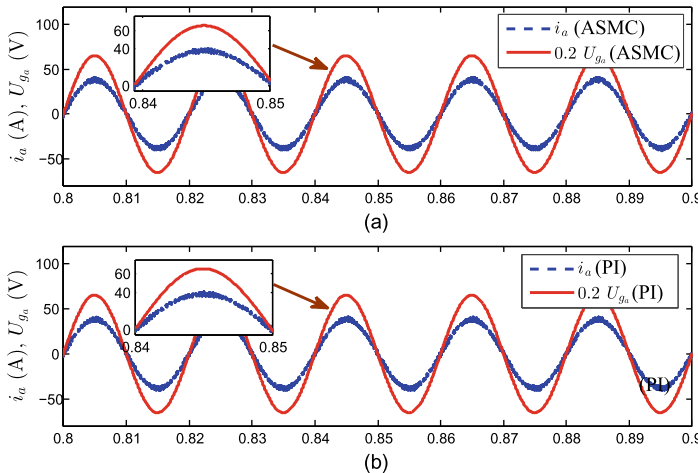


Fig. 10.6 Phase current and source voltage: **a** Adp. ST-SMC, **b** PI control

10.3 Summary

This chapter considers the load variation and parameter uncertainty of the converter system, and proposes the ASMC based \mathcal{H}_∞ robust control strategy. Based on the model in SRF, two-loop cascaded control structure is designed, which includes voltage regulation loop and current tracking loop. The voltage regulation loop adopts the \mathcal{H}_∞ controller combined with LESO, which achieves effective regulation of dc-link voltage in the presence of load variation and measurement noise. In current

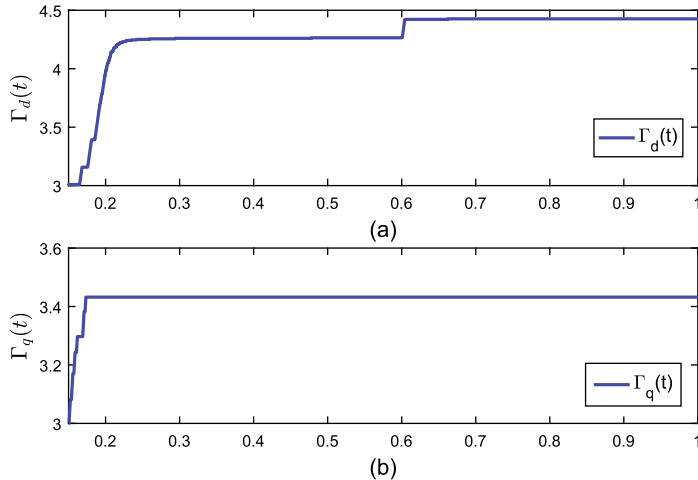


Fig. 10.7 Adaptive gains of Γ_d and Γ_q

tracking loop, two ASMC based controllers have been designed to track the d -axis and q -axis currents. Due to the adoption of ASMC, the upper bound of external disturbance derivative is not needed to know a priori, and the currents can converge to their references. Lyapunov method has been adopted to analyze the stability of the closed-loop and finite time convergence. The effectiveness and advantage of the proposed control method has been verified via simulation. With the help of LESO, ASMC- \mathcal{H}_∞ achieves desired dc-link voltage regulation performance and disturbance attenuation ability. The simulation results show that, comparing with conventional PI control, ASMC- \mathcal{H}_∞ can result in better control performance, in the terms of significantly reduced dc-link voltage drop and shortened recovering time when there exist parameter uncertainty and load variation.

References

1. Moreno, J.A., Osorio, M.: A Lyapunov approach to second-order sliding mode controllers and observers. In: Proceedings of the 47th IEEE Conference on Decision and Control, Cancun, Mexico, pp. 2856–2861 (2008)
2. Laghrouche, S., Liu, J., Ahmed, F.S., Harmouche, M., Wack, M.: Adaptive second-order sliding mode observer-based fault reconstruction for PEM fuel cell air-feed system. *IEEE Trans. Control Syst. Technol.* **23**(3), 1098–1109 (2014)
3. Gonzalez, T., Moreno, J.A., Fridman, L.: Variable gain super-twisting sliding mode control. *IEEE Trans. Autom. Control* **57**(8), 2100–2105 (2011)
4. Kunusch, C., Puleston, P.F., Mayosky, M.A., Riera, J.: Sliding mode strategy for PEM fuel cells stacks breathing control using a super-twisting algorithm. *IEEE Trans. Control Syst. Technol.* **17**(1), 167–174 (2008)

5. Zheng, Q., Chen, Z., Gao, Z.: A practical approach to disturbance decoupling control. *Control Eng. Pract.* **17**(9), 1016–1025 (2009)
6. Khalil, H.K., Grizzle, J.W.: Nonlinear Systems, vol. 3. Prentice Hall, Upper Saddle River, NJ (2002)

Chapter 11

Adaptive Neural Network Control of Three-Phase Neutral-Point-Clamped Converters



Abstract This chapter employs radial basis function (RBF) neural network to approximate the unknown function. For a continuous function $d(x)$ on a compact set \square and ε_m , there exists a RBF neural network $\theta^T \xi(x)$ such that

$$\sup_{x \in \square} |d(x) - \theta^T \xi(x)| \leq \varepsilon_m, \quad (11.1)$$

where $\theta = [\theta_1, \theta_2, \dots, \theta_l]^T$ is the weight vector, and $\xi(x) = [\xi_1(x), \xi_2(x), \dots, \xi_l(x)]^T$ is basis function vector commonly used Gaussian function,

$$\xi_i(x) = \frac{1}{\sqrt{2\pi}\sigma_i} e^{-\frac{1}{2}\left(\frac{\|x-\phi_i\|^2}{\sigma_i}\right)^2}, i = 1, 2, \dots, l, \quad (11.2)$$

where σ_i and ϕ_i are the width and center of the basis function, respectively. It has been proved that in [1, 2] the RBFNN can be used to approximate any smooth nonlinear functions $d(t)$ within arbitrary accuracy. This chapter proposes RBF neural network based control strategy for three-phase three-level neutral-point-clamped (NPC) ac/dc power converter. The control is designed in DPC mode and consists of three loops, including voltage regulation loop, power tracking control loop, and capacitor voltage balance loop. Two RBF neural network based adaptive controllers are designed for power tracking loop, to drive the active and reactive power to their reference values respectively. An adaptive controller is designed to regulate the dc-link voltage where the load is treated as external disturbance. A composite controller consisting of a reduced-order observer is developed for the voltage balance loop to ensure voltage difference between two dc-link capacitors close to zero. The effectiveness and advantage of the proposed control strategy for the NPC power converter are verified through experiments.

11.1 Control Scheme

As mentioned in previous chapters, NPC control structure consists three loops, i.e., voltage regulation loop, current/power tracking loop, and voltage balance loop. In this chapter, DPC mode is adopted. As shown in Fig. 11.1. For voltage regulation loop, an adaptive controller is designed to regulate the dc-link voltage to a constant reference. For power tracking loop, two adaptive sliding mode controllers are designed to guarantee tracking of instantaneous active and reactive power towards their references. For the voltage balance loop, an \mathcal{H}_∞ controller based on reduced-order observer is designed to eliminate the unbalance of the capacitor voltages.

11.1.1 Voltage Regulation Loop

In this subsection, an adaptive controller will be designed to regulate the sum of capacitor voltages x_1 to the reference value x_1^* . Assume that the equivalent load resistance R_L is unknown and slow-varying, i.e., $\dot{R}_L \approx 0$, and the dynamics of instantaneous power are much faster than the voltage dynamic, the x_1 dynamic can be rewritten as

$$\dot{x}_1 = -\frac{2}{R_L C}x_1 + \frac{1}{C}i_{\alpha\beta}^{*\text{T}}u_{\alpha\beta}, \quad (11.3)$$

where $i_{\alpha\beta}^*$ is the reference of inductor current $i_{\alpha\beta}$. Then it follows that

$$\dot{z}_1 = -\eta z_1 + \frac{2}{C}p^*, \quad (11.4)$$

where $z_1 = \frac{1}{2}x_1^2$ is a new state variable, $p^* = \frac{x_1}{2}i_{\alpha\beta}^{*\text{T}}u_{\alpha\beta}$ is the active power reference, and $\eta = \frac{4}{R_L C}$ is the unknown parameter. Define the regulation error as

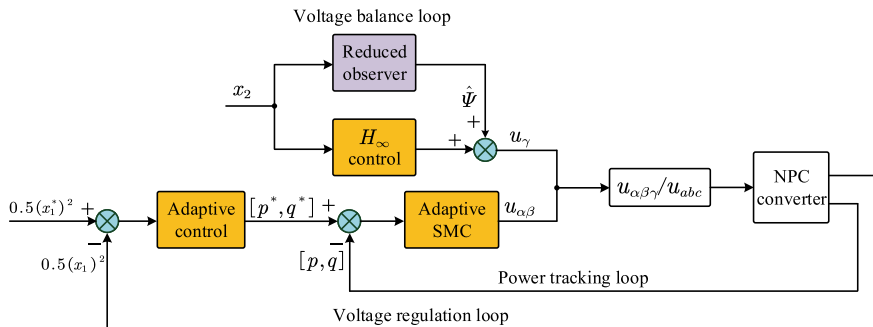


Fig. 11.1 Control diagram

$$e_z = z_1 - z_1^*, \quad (11.5)$$

where $z_1^* = \frac{x_1^{*2}}{2}$. With (11.4), it follows that

$$\dot{e}_z = \dot{z}_1 = -\eta z_1 + \frac{2}{C} p^*. \quad (11.6)$$

Next, an efficient adaptive controller will be designed to regulate x_1 to its reference x_1^* . Construct a Lyapunov function as follows:

$$V_1(t) = \frac{1}{2} e_z^2 + \frac{1}{2\lambda} \tilde{\eta}^2, \quad (11.7)$$

where λ is a positive constant, $\tilde{\eta} = \hat{\eta} - \eta$, $\hat{\eta}$ is the adaptive law to be designed.

Take the derivative of (11.7) along the trajectory of system (11.6) as follows:

$$\dot{V}_1 = e_z(-\eta z_1 + \frac{2}{C} p^*) + \frac{1}{\lambda} \tilde{\eta} \dot{\tilde{\eta}}. \quad (11.8)$$

Design following adaptive controller and adaptive law:

$$p^* = -k_{vs} e_z + \frac{C}{2} z_1 \hat{\eta}, \quad (11.9)$$

$$\dot{\hat{\eta}}(t) = -\lambda z_1 e_z. \quad (11.10)$$

Substituting (11.9) and (11.10) into (11.8), it yields that

$$\begin{aligned} \dot{V}_1 &= -\eta z_1 e_z - \frac{2}{C} k_{vs} e_z^2 + \hat{\eta} z_1 e_z - \tilde{\eta}(t) z_1 e_z, \\ &= -\frac{2}{C} k_{vs} e_z^2. \end{aligned} \quad (11.11)$$

According to the Lasalle's theorem [3], it can be concluded that the regulation error $e_z(t)$ converges to 0 as $t \rightarrow \infty$, that is, the adaptive controller is able to regulate x_1 to x_1^* . The control structure of voltage regulation loop is shown in Fig. 11.2.

11.1.2 Power Tracking Loop

To carry out DPC, the NPC model in stationary α, β, γ frame is adopted as follows [4]:

$$\dot{i}_\alpha = \frac{1}{L} v_\alpha - \frac{1}{2L} x_1 u_\alpha + \frac{1}{2\sqrt{6}L} x_2 (u_\beta^2 - u_\alpha^2) - \frac{1}{\sqrt{3}L} x_2 u_\alpha u_\gamma, \quad (11.12)$$

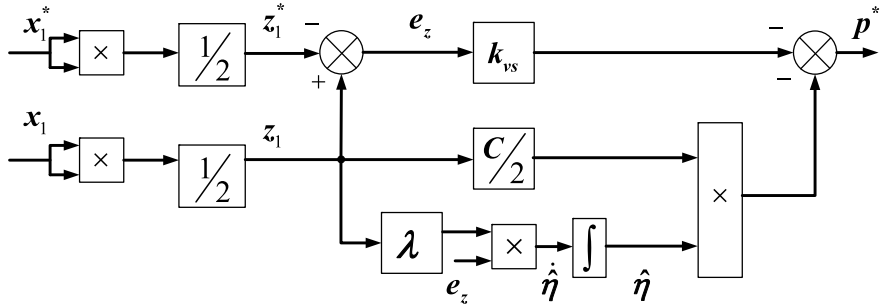


Fig. 11.2 Adaptive controller in the voltage regulation loop

$$\dot{i}_\beta = \frac{1}{L} v_\beta - \frac{1}{2L} x_1 u_\beta + \frac{1}{\sqrt{6} L} x_2 u_\alpha u_\beta - \frac{1}{\sqrt{3} L} x_2 u_\beta u_\gamma, \quad (11.13)$$

$$\dot{x}_1 = -\frac{2}{R_L C} x_1 + \frac{1}{C} i_{\alpha\beta}^T u_{\alpha\beta}, \quad (11.14)$$

$$\dot{x}_2 = \frac{2i_{\alpha\beta}^T u_{\alpha\beta} u_\gamma}{\sqrt{3} C} + \frac{1}{\sqrt{6} C} [(u_\alpha^2 - u_\beta^2) i_\alpha - 2u_\alpha u_\beta i_\beta], \quad (11.15)$$

where $v_{\alpha\beta} = [v_\alpha, v_\beta]^T$ is the grid source voltage, $i_{\alpha\beta} = [i_\alpha, i_\beta]^T$ is the grid current, $x_1 = v_{c1} + v_{c2}$ is the sum of capacitor voltages, $x_2 = v_{c1} - v_{c2}$ is the difference of capacitor voltages, and $u_{\alpha\beta\gamma} = [u_\alpha, u_\beta, u_\gamma]^T$ is the average duty cycle.

Based on the instantaneous theory [5], instantaneous active and reactive powers p, q are defined as,

$$\begin{aligned} p &= v_\alpha i_\alpha + v_\beta i_\beta, \\ q &= v_\alpha i_\beta - v_\beta i_\alpha. \end{aligned} \quad (11.16)$$

Assume that the grid source voltages are balanced and the difference of capacitor voltages x_2 is close to zero, the dynamics of active and reactive power can be obtained by taking the derivative of (11.16) as follow:

$$\begin{aligned} \dot{p} &= -\frac{1}{2L} v_{\alpha\beta}^T u_{\alpha\beta} x_1 + \omega q + \frac{1}{L} \|v_{\alpha\beta}\|^2, \\ \dot{q} &= -\frac{1}{2L} v_{\alpha\beta}^T J^T u_{\alpha\beta} x_1 - \omega p, \end{aligned} \quad (11.17)$$

where $J = \begin{bmatrix} 0 & -1 \\ 1 & 0 \end{bmatrix}$. Then the equilibrium point of the system (11.17) can be obtained as [6]:

$$u_{\alpha\beta}^{eq} = \frac{2}{x_1} \left\{ \left(1 + \frac{\omega L q}{\|v_{\alpha\beta}\|^2} \right) v_{\alpha\beta} - \left(\frac{\omega L p}{\|v_{\alpha\beta}\|^2} \right) J v_{\alpha\beta} \right\}. \quad (11.18)$$

Next, two adaptive sliding mode controllers will be designed to track the instantaneous active and reactive power via RBF neural network technology. Define the tracking errors as

$$\begin{aligned} e_p &= p^* - p, \\ e_q &= q^* - q. \end{aligned} \quad (11.19)$$

With (11.17), it follows that

$$\begin{aligned} \dot{e}_p &= -\omega q + \frac{v_{\alpha\beta}^T x_1}{2L} u_{\alpha\beta} - \frac{\|v_{\alpha\beta}\|^2}{L} + \dot{p}^*, \\ \dot{e}_q &= \omega p + \frac{(J v_{\alpha\beta})^T x_1}{2L} u_{\alpha\beta} + \dot{q}^*. \end{aligned} \quad (11.20)$$

Note that above system is an ideal model without considering uncertain parameters, which are inevitable in practical applications caused by parametric uncertainties, measurement errors and unknown disturbances, etc. Therefore, it is necessary to establish more accurate model by taking into account these uncertainties, as follows:

$$\begin{aligned} \dot{e}_p &= -(\omega + \Delta_\omega)q + \left(\frac{1}{2L} + \Delta_L\right)v_{\alpha\beta}^T x_1 u_{\alpha\beta} \\ &\quad - \left(\frac{1}{L} + \Delta_L\right)\|v_{\alpha\beta}\|^2 + \dot{p}^*, \\ \dot{e}_q &= (\omega + \Delta_\omega)p + \left(\frac{1}{2L} + \Delta_L\right)(J v_{\alpha\beta})^T x_1 u_{\alpha\beta} + \dot{q}^*, \end{aligned} \quad (11.21)$$

where Δ_ω and Δ_L are the parametric uncertainties. Then (11.21) can be rewritten as,

$$\begin{aligned} \dot{e}_p &= -\omega q + \frac{v_{\alpha\beta}^T x_1}{2L} u_{\alpha\beta} - \frac{\|v_{\alpha\beta}\|^2}{L} + d_p(t), \\ \dot{e}_q &= \omega p + \frac{(J v_{\alpha\beta})^T x_1}{2L} u_{\alpha\beta} + d_q(t), \end{aligned} \quad (11.22)$$

where

$$\begin{aligned} d_p(t) &= -\Delta_\omega q + \Delta_L v_{\alpha\beta}^T x_1 u_{\alpha\beta} - \Delta_L \|v_{\alpha\beta}\|^2 + \dot{p}^*, \\ d_q(t) &= \Delta_\omega p + \Delta_L (J v_{\alpha\beta})^T x_1 + \dot{q}^*. \end{aligned} \quad (11.23)$$

Next, on the basis of equilibrium point (11.18), the control signal $u_{\alpha\beta}$ against parametric uncertainties to drive the active and reactive power tracking their desired values are designed as,

$$u_{\alpha\beta} = u_{\alpha\beta}^{eq} - \mu(e_p)v_{\alpha\beta} - \mu(e_q)J v_{\alpha\beta}, \quad (11.24)$$

where $\mu(e_p)$ and $\mu(e_q)$ are the adaptive sliding mode controllers to be designed. Substituting (11.24) into (11.22), one can obtain that

$$\begin{aligned}\dot{e}_p &= -\frac{x_1}{2L} \|v_{\alpha\beta}\|^2 \mu(e_p) + d_p(t), \\ \dot{e}_q &= -\frac{x_1}{2L} \|v_{\alpha\beta}\|^2 \mu(e_q) + d_q(t).\end{aligned}\quad (11.25)$$

Utilizing the RBFNN to approximate the unknown function $d_p(t)$ and $d_q(t)$, the approximate expressions are

$$\begin{aligned}d_p(t) &= \theta_p^{*\text{T}} \xi + \varepsilon_p, \quad |\varepsilon_p| \leq \varepsilon_{mp}, \\ d_q(t) &= \theta_q^{*\text{T}} \xi + \varepsilon_q, \quad |\varepsilon_q| \leq \varepsilon_{mq},\end{aligned}\quad (11.26)$$

where $\theta_p^{*\text{T}}$ and $\theta_q^{*\text{T}}$ are the ideal weight vector, ε_p and ε_q are the approximation errors, and ε_{mp} and ε_{mq} are their upper bounds, respectively.

Therefore, two adaptive sliding mode controllers with RBFNN approximating unknown functions are designed as

$$\begin{aligned}\mu(e_p) &= k_p e_p + \frac{2L}{x_1 \|v_{\alpha\beta}\|^2} [\hat{\theta}_p^T \xi + \varepsilon_{mp} \text{sign}(e_p)], \\ \mu(e_q) &= k_q e_q + \frac{2L}{x_1 \|v_{\alpha\beta}\|^2} [\hat{\theta}_q^T \xi + \varepsilon_{mq} \text{sign}(e_q)],\end{aligned}\quad (11.27)$$

where k_p and k_q are positive constants, $\hat{\theta}_p$ and $\hat{\theta}_q$ are estimation of ideal weight vectors θ_p^* and θ_q^* , respectively. Applying adaptive sliding mode controllers (11.27) into system (11.25), the error dynamics become

$$\begin{aligned}\dot{e}_p &= -\frac{x_1}{2L} \|v_{\alpha\beta}\|^2 k_p e_p - \hat{\theta}_p^T \xi - \varepsilon_{mq} \text{sign}(e_p) + d_p(t), \\ \dot{e}_q &= -\frac{x_1}{2L} \|v_{\alpha\beta}\|^2 k_q e_q - \hat{\theta}_q^T \xi - \varepsilon_{mq} \text{sign}(e_q) + d_q(t).\end{aligned}\quad (11.28)$$

Construct following Lyapunov function for system (11.28),

$$V_{pq} = \frac{1}{2} e_p^2 + \frac{1}{2} e_q^2 + \frac{1}{2\gamma_p} \tilde{\theta}_p^T \tilde{\theta}_p + \frac{1}{2\gamma_q} \tilde{\theta}_q^T \tilde{\theta}_q,\quad (11.29)$$

where $\tilde{\theta}_p = \hat{\theta}_p - \theta_p^*$, $\tilde{\theta}_q = \hat{\theta}_q - \theta_q^*$. Then it can be obtained that

$$\dot{V}_{pq} = e_p \dot{e}_p + e_q \dot{e}_q + \frac{1}{\gamma_p} \tilde{\theta}_p^T \dot{\tilde{\theta}}_p + \frac{1}{\gamma_q} \tilde{\theta}_q^T \dot{\tilde{\theta}}_q.\quad (11.30)$$

With (11.26) and (11.28), it can be obtained that

$$\begin{aligned}
\dot{V}_{pq} = & -\frac{x_1}{2L} \|v_{\alpha\beta}\|^2 k_p e_p^2 - e_p \hat{\theta}_p^T \xi - \varepsilon_{mp} |e_p| + e_p \theta_p^{*\text{T}} \xi \\
& - \frac{x_1}{2L} \|v_{\alpha\beta}\|^2 k_q e_q^2 - e_q \hat{\theta}_q^T \xi - \varepsilon_{mq} |e_q| + e_q \theta_q^{*\text{T}} \xi \\
& + \frac{1}{\gamma_p} \tilde{\theta}_p^T \dot{\tilde{\theta}}_p + \frac{1}{\gamma_q} \tilde{\theta}_q^T \dot{\tilde{\theta}}_q + \varepsilon_p e_p + \varepsilon_q e_q \\
\leq & -\frac{x_1}{2L} \|v_{\alpha\beta}\|^2 k_p e_p^2 - \frac{x_1}{2L} \|v_{\alpha\beta}\|^2 k_q e_q^2 - e_p \tilde{\theta}_p^T \xi \\
& - e_q \tilde{\theta}_q^T \xi - (\varepsilon_{mp} - \varepsilon_p) |e_p| - (\varepsilon_{mq} - \varepsilon_q) |e_q| + \frac{1}{\gamma_p} \tilde{\theta}_p^T \dot{\tilde{\theta}}_p \\
& + \frac{1}{\gamma_q} \tilde{\theta}_q^T \dot{\tilde{\theta}}_q. \tag{11.31}
\end{aligned}$$

Design the adaptive law as

$$\begin{aligned}
\dot{\tilde{\theta}}_p &= \gamma_p e_p \xi, \\
\dot{\tilde{\theta}}_q &= \gamma_q e_q \xi. \tag{11.32}
\end{aligned}$$

Then the derivative of the Lyapunov function becomes

$$\begin{aligned}
\dot{V}_{pq} \leq & -\frac{x_1}{2L} \|v_{\alpha\beta}\|^2 k_p e_p^2 - \frac{x_1}{2L} \|v_{\alpha\beta}\|^2 k_q e_q^2 \\
& - (\varepsilon_{mp} - \varepsilon_p) |e_p| - (\varepsilon_{mq} - \varepsilon_q) |e_q|. \tag{11.33}
\end{aligned}$$

According to Lasalle's theorem [3], it can be concluded that the tracking errors $e_p(t)$ and $e_q(t)$ converge to 0 as $t \rightarrow \infty$, i.e., the adaptive sliding mode controllers can force instantaneous active and reactive power p, q to track their references.

The control structure of power tracking loop is shown in Fig. 11.3.

11.1.3 Voltage Balancing Loop

To balance the capacitor voltages, an \mathcal{H}_∞ controller based on reduced-order observer is designed. Regarding the assumption that the power dynamics are much faster than the voltage dynamic, the dynamic of (11.15) becomes

$$\dot{x}_2 = \frac{4p^*}{C\sqrt{3x_1}} u_\gamma + \frac{1}{C} \psi(t), \tag{11.34}$$

where $\psi(t)$ is considered as disturbance. According to [7], the disturbance $\psi(t)$ mainly consists of third harmonics and can be expressed as

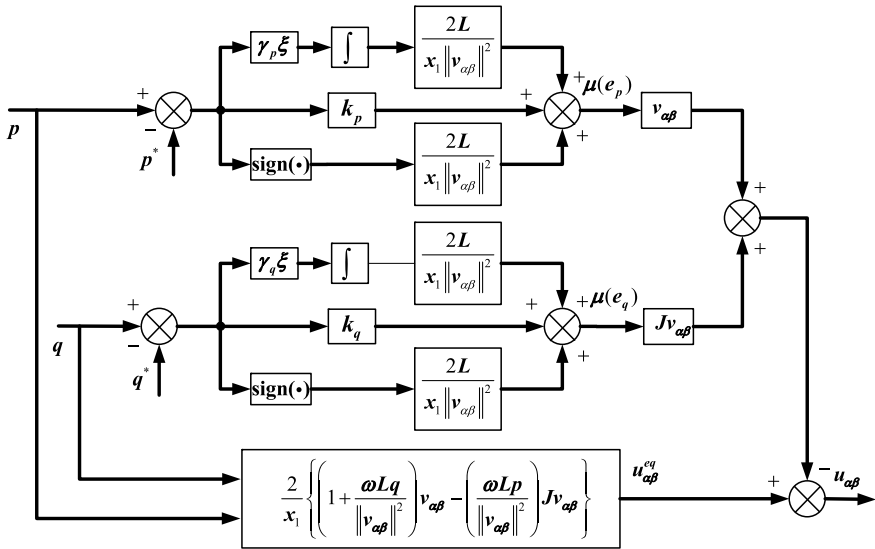


Fig. 11.3 Adaptive sliding mode controller structure based on the RBF neural network technology

$$\psi(t) = \chi \sin(3\omega t + \varphi), \quad (11.35)$$

where χ and φ are the constant values.

Next, a reduced-order observer will be designed to estimate the disturbance $\psi(t)$. Adding two new state variables, $\psi(t)$ and its time derivative x_ψ to the system, the augmented system can be obtained as

$$\begin{aligned} \dot{x}_2 &= \frac{h}{C} u_\gamma + \frac{1}{C} \psi, \\ \dot{\psi} &= x_\psi, \\ \dot{x}_\psi &= -9\omega^2 \psi, \end{aligned} \quad (11.36)$$

where $h = \frac{4p^*}{\sqrt{3}x_1}$. Express this system in state-space form as follows:

$$\begin{aligned} \dot{x} &= Ax + Bu_\gamma, \\ y &= Ex, \end{aligned} \quad (11.37)$$

where $x = [x_2, \psi, x_\psi]^T$,

$$A = \begin{bmatrix} 0 & \frac{1}{C} & 0 \\ 0 & 0 & 1 \\ 0 & -9\omega^2 & 0 \end{bmatrix}, \quad B = \begin{bmatrix} \frac{h}{C} \\ 0 \\ 0 \end{bmatrix}, \quad E = \begin{bmatrix} 1 \\ 0 \\ 0 \end{bmatrix}^T$$

are constant matrices.

Then system (11.37) can be rewritten as

$$\begin{bmatrix} \dot{\bar{x}}_1 \\ \dot{\bar{x}}_2 \end{bmatrix} = \begin{bmatrix} A_{11} & A_{12} \\ A_{21} & A_{22} \end{bmatrix} \begin{bmatrix} \bar{x}_1 \\ \bar{x}_2 \end{bmatrix} + \begin{bmatrix} B_1 \\ B_2 \end{bmatrix} u_\gamma, \\ y = \bar{x}_1, \quad (11.38)$$

where

$$A_{11} = [0], A_{12} = \left[\frac{1}{C} \ 0 \right],$$

$$A_{21} = \begin{bmatrix} 0 \\ 0 \end{bmatrix}, A_{22} = \begin{bmatrix} 0 & 1 \\ -9\omega^2 & 0 \end{bmatrix}$$

As can be observed from (11.38), \bar{x}_1 can be directly obtained from the measurable output y , and \bar{x}_2 needs to be estimated, for which following reduced-order state observer is designed:

$$\begin{aligned} \dot{\varepsilon} &= F\varepsilon + Gy + Hu_\gamma, \\ \dot{\hat{x}}_2 &= M\varepsilon + Ny, \end{aligned} \quad (11.39)$$

where F, G, M and N are the observer gains to be designed.

Denote observation error $e_\psi = \bar{x}_2 - \hat{x}_2$, then its dynamic is

$$\dot{e}_\psi = (A_{22} + LA_{12})e_\psi. \quad (11.40)$$

The observation error $e_\psi \rightarrow 0$ if and only if $A_{22} + LA_{12}$ is Hurwitz. According to the result of [8], it can be obtained that if there exists a positive matrix P such that

$$(A_{22} + LA_{12})^T P + P(A_{22} + LA_{12}) \leq 0, \quad (11.41)$$

then $A_{22} + LA_{12}$ is Hurwitz. The equation (11.41) is equivalent to

$$A_{22}^T P + PA_{22} + WA_{12} + A_{12}^T W^T \leq 0, \quad (11.42)$$

where $W = PL$. This equation is standard linear matrix inequality which can be efficiently solved by calculation software to obtain the matrices P and Q , and $L = P^{-1}Q$.

Defining $\varepsilon = \hat{x}_2 + Ly$, it yields that

$$\begin{aligned} \dot{\varepsilon} &= \dot{\hat{x}}_2 + L\dot{y} \\ &= (A_{22} + LA_{12})\hat{x}_2 + L(A_{11}y + B_1u_\gamma) \\ &\quad + A_{21}y + B_2u_\gamma + (B_2 + LB_1)u_\gamma, \end{aligned} \quad (11.43)$$

and the observer gains can be obtained as

$$\begin{aligned} F &= A_{22} + LA_{12}, \\ G &= (A_{21} + LA_{11}) - (A_{22} + LA_{12})L, \\ H &= B_2 + LB_1, \\ M &= I, \\ N &= -L. \end{aligned} \quad (11.44)$$

Using the estimated disturbance $\psi(t)$, an \mathcal{H}_∞ controller is designed as

$$u_\gamma = \frac{C}{h}(k_b x_2 + \frac{1}{C}\hat{\psi}), \quad (11.45)$$

where k_b is the \mathcal{H}_∞ controller gain to be designed.

Substituting (11.45) into (11.34), it yields that

$$\dot{x}_2 = -k_b x_2 + \frac{1}{C}\varsigma(t), \quad (11.46)$$

where $\varsigma(t)$ consisting of observation error and other harmonics is the disturbance. According to the result of [9], following condition is presented to calculate the admissible \mathcal{H}_∞ controller.

For a given constant ϱ , if there exist positive scalars w_b and j_b , such that

$$\begin{bmatrix} 2w_b + 1 & \frac{1}{C}j_b \\ \frac{1}{C}j_b & -\varrho^2 \end{bmatrix} \leq 0, \quad (11.47)$$

then the system satisfies following conditions:

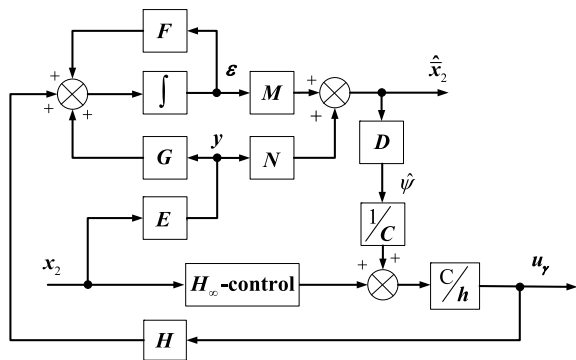
- the difference of capacitor voltages $x_2 = v_{c1} - v_{c2}$ converges to zero as $t \rightarrow \infty$ in the absence of disturbance;
- under zero-initial condition, the following inequality

$$\int_0^{+\infty} x_2^T x_2 dt \leq \varrho^2 \int_0^{+\infty} \varsigma^T \varsigma dt, \quad (11.48)$$

holds in the presence of disturbance input $\varsigma(t)$.

Moreover, if scalars w_b and j_b are feasible, the \mathcal{H}_∞ gain is obtained as $k_b = \frac{w_b}{j_b}$. The control structure of voltage balance loop is shown in Fig. 11.4, where $D = [1, 0]$.

Fig. 11.4 \mathcal{H}_∞ controller structure based on the reduced-order observer



11.2 Experiment Verification

In order to verify the effectiveness and advantage of proposed control strategy, the experimental comparisons using a NPC prototype between the proposed and conventional PI control strategy are provided in this section. Figure 11.5 shows the NPC prototype.

The system parameters are shown in Table 11.1 and the TMS320VC33 floating point digital signal processor board is used to execute control algorithm.



Fig. 11.5 Laboratory prototype of three-phase three-level NPC power converter

Table 11.1 System parameters

Parameter	Value	Description
f_c	$11.2 \cdot 10^3$	Switching rate (Hz)
e_{abc}	400	Grid line voltage(V)
L	1.2	Phase inductor (μ H)
C	1100	DC-link capacitor (μ F)
R_L	{120,60}	Load resistance (Ω)
x_1^*	750	Voltage reference(V)

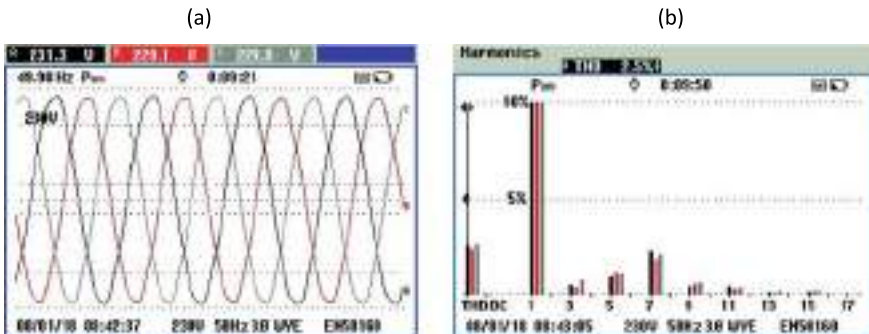


Fig. 11.6 Grid voltage: **a** waveform, **b** harmonic spectrum

Table 11.2 Control parameters

ANN controller

Pow. Tra. loop	Vol. Reg. loop	Vol. Bal. loop
$k_p = k_q = 1.6 * 10^{-7}$	$k_{vs} = 0.15$	$L = [-0.8701, -1.79 * 10^3]^T$
$\gamma_p = \gamma_q = 8.0 * 10^{-4}$	$\lambda = 2.0 * 10^{-7}$	$k_b = 1.08 * 10^3, \varrho = 4.5$
$\varepsilon_{mp} = \varepsilon_{mq} = 5.0 * 10^{-5}$		

PI controller

Pow. Tra. loop	Vol. Reg. loop	Vol. Bal. loop
$k_{pp} = k_{pq} = 3.54 * 10^{-5}$	$k_{vs} = 0.12$	$k_{pb} = 0.15$
$k_{ip} = k_{iq} = 3.54 * 10^{-2}$	$k_{iv} = 5$	$k_{ib} = 3$

As shown in Fig. 11.6, the grid voltage is distorted and unbalanced to some extend. Since the controlled design assumes balanced grid voltage, this allows to test the robustness of the proposed controller under a more realistic environment.

The resistance R_L steps from no load to the half load (4.6875 kW) then to full load (9.375 kW), and the reactive power is set to 0 VAr. Table 11.2 shows the control parameters of proposed and PI control strategy.

Figure 11.7a, b show the dynamics of v_{c1} and v_{c2} , with proposed and PI control strategy measured by oscilloscope, respectively. As observed from Fig. 11.8a, c, both control strategies regulate the dc-link output voltage x_1 to the reference 750 V despite the load variation. However, the proposed control scheme results in better performance, in terms of faster dynamic response and less output voltage drop, especially during the transient process. Figure 11.8b, d show the responses of the capacitor voltage difference, it can be seen that, compared with PI control, the obtained voltage by proposed strategy is smaller and close to zero.

Figure 11.9 shows the active and reactive power responses. As can be observed that both control strategies can drive the active and reactive power p, q to track their references. Note that both control strategy can guarantee that the generated active power steps from 4.6875 kW to 9.375 kW when load changes, meanwhile

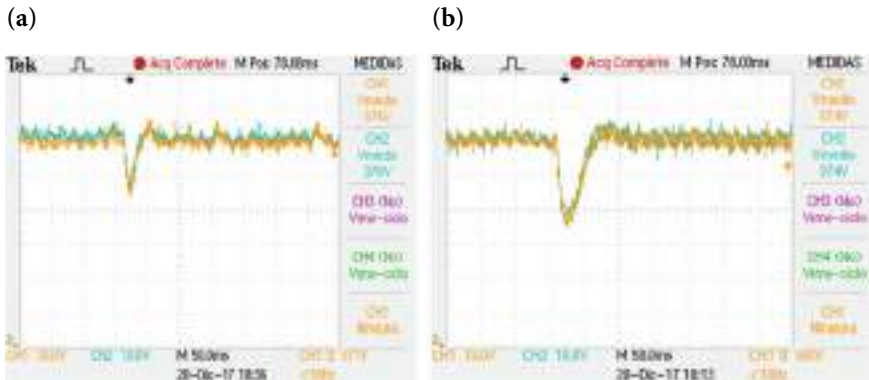


Fig. 11.7 v_{c1} and v_{c2} responses: **a** ANN control, **b** PI control

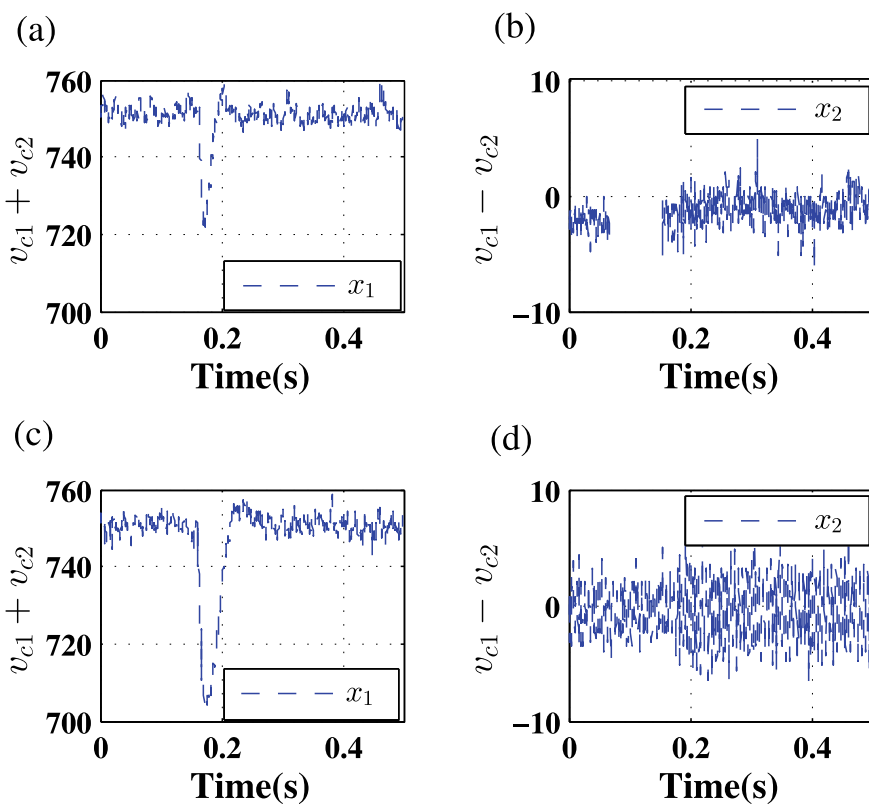


Fig. 11.8 x_1 and x_2 responses: **a, b** ANN control, **c, d** PI control

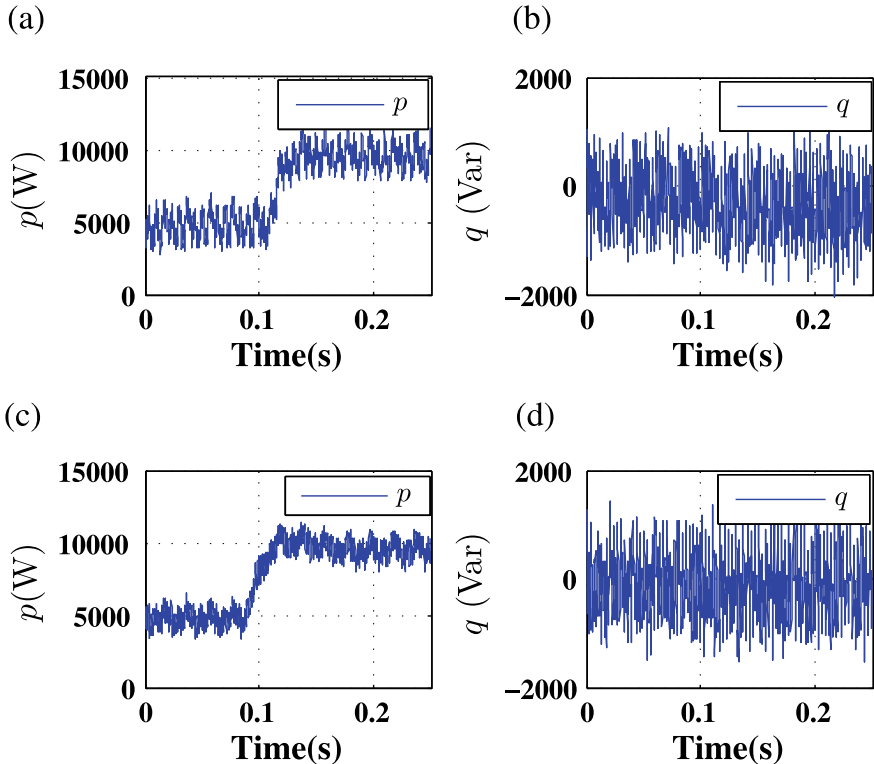


Fig. 11.9 p and q responses: **a, b** ANN control, **c, d** PI control

the generated reactive power maintains at 0 VAr. This indicates that both control strategies are robust to the load change. Moreover, since reactive power is kept close to 0 VAr to achieve unity power factor, the grid source voltage is in phase with the corresponding current (phase c voltage and current), as shown in Fig. 11.10a, c. The dynamics of three phase current achieved with both control strategies are shown in Fig. 11.10b, d, and it can be seen from Fig. 11.11a, c that the current total harmonic distortion (THD) of the both schemes has the same values. In fact, as can be seen in Fig. 11.11b, d, active and reactive power of both control strategies are also almost the same. Therefore, the experimental result demonstrates that the dc-link voltage and capacitor voltage difference obtained by proposed control strategy is better than that of PI control.

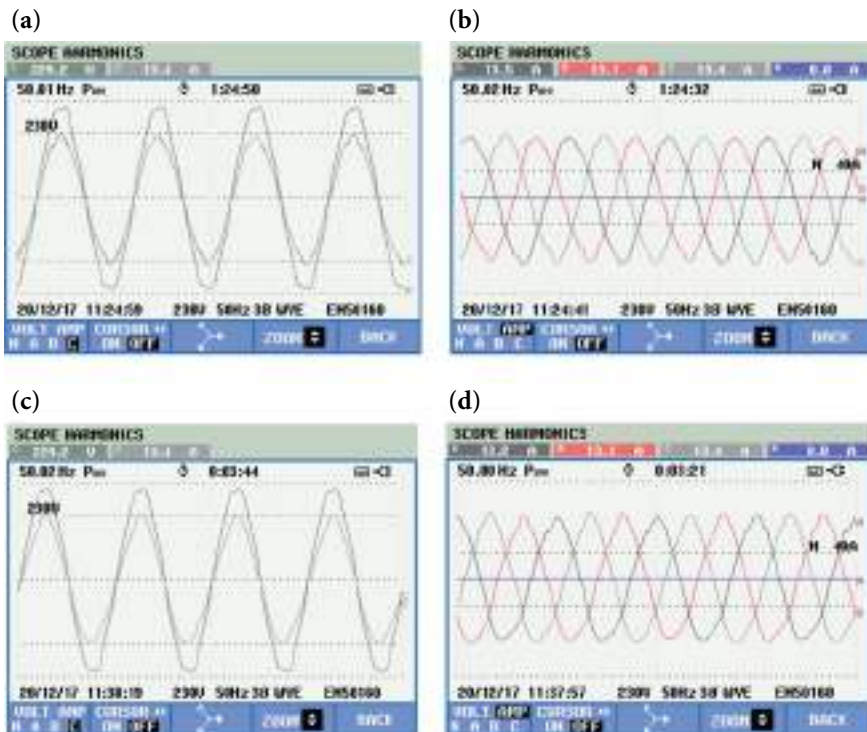


Fig. 11.10 Grid voltage and current responses: **a, b** ANN control, **c, d** PI control

11.3 Summary

This chapter proposes RBF neural network based control strategy for three phase three-level neutral-point-clamped (NPC) power converter under DPC mode. In voltage regulation loop, an adaptive controller has been developed to regulate dc-link output voltage. In power tracking loop, two adaptive sliding mode controllers have been designed via RBF neural network technology to deal with the model uncertainties of the system. In voltage balance loop, an \mathcal{H}_∞ controller based on reduced-order observer is established to eliminate the voltage unbalance voltages between two dc-link capacitors. Experiments have been carried out on an NPC converter prototype, and the results show that compared with the PI control, the dc-link voltage obtained by proposed control strategy has smaller voltage drop and remarkably shorter transient time, and the capacitor voltage difference is smaller and close to zero. With these results, the devices of injecting a zero-sequence voltage and feed forward compensation can be omitted with the employment of proposed control strategy, thus reduce the weight, size and cost of the power converter. Furthermore, the proposed control strategy is more robust against the load change, which is of significant advantage in practice.

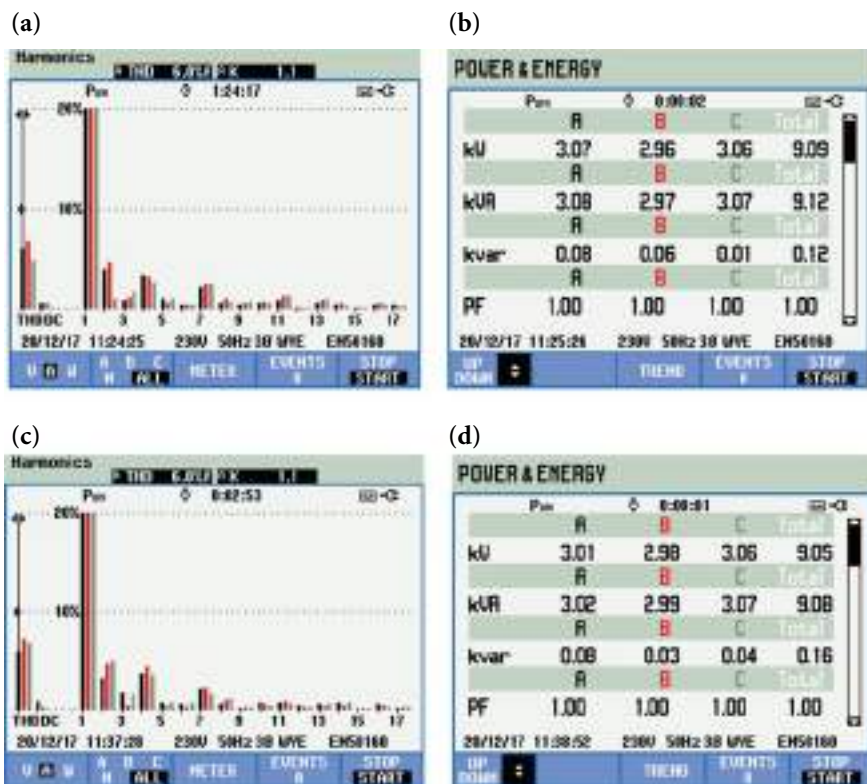


Fig. 11.11 Current harmonic spectrum, active and reactive power and power factor: **a, b** ANN control, **c, d** PI control

References

1. Liu, X., Cao, J.: Robust state estimation for neural networks with discontinuous activations. *IEEE Trans. Syst. Man Cybern.: Cybern.* **40**(6), 1425–1437 (2010)
2. Liu, N., Fei, J.: Adaptive fractional sliding mode control of active power filter based on dual RBF neural networks. *IEEE Access* **5**, 27590–27598 (2017)
3. Shevitz, D., Paden, B.: Lyapunov stability theory of nonsmooth systems. *IEEE Trans. Autom. Control* **39**(9), 1910–1914 (1994)
4. Portillo, R., Vazquez, S., Leon, J.I., Prats, M.M., Franquelo, L.G.: Model based adaptive direct power control for three-level NPC converters. *IEEE Trans. Ind. Inf.* **9**(2), 1148–1157 (2012)
5. Akagi, H., Watanabe, E.H., Arede, M.: Instantaneous Power Theory and Applications to Power Conditioning. Wiley (2017)
6. Vazquez, S., Liu, J., Gao, H., Franquelo, L.G.: Second order sliding mode control for three-level NPC converters via extended state observer. In: Proceedings of the 41st Annual Conference of the IEEE Industrial Electronics Society, Yokohama, JP, pp. 5118–5123 (2015)
7. Umbria, F., Gordillo, F., Gomez-Estern, F., Salas, F., Portillo, R.C., Vazquez, S.: Voltage balancing in three-level neutral-point-clamped converters via Luenberger observer. *Control Eng. Pract.* **25**, 36–44 (2014)

8. Gahinet, P., Nemirovskii, A., Laub, A. J., Chilali, M.: The LMI control toolbox. In: Proceedings of the 33rd IEEE Conference on Decision and Control, Lake Buena Vista, FL, USA, vol. 3, pp. 2038–2041 (1994)
9. Doyle, J., Glover, K., Khargonekar, P., Francis, B.: State-space solutions to standard H_2 and H_∞ control problems. In: Proceedings of the 1988 IEEE American Control Conference, Atlanta, GA, USA, pp. 1691–1696 (1988)

Chapter 12

Conclusion and Further Work



This chapter draws conclusions on the book, and points out some possible research directions related to the work done in this book.

12.1 Conclusion

The focus of the book has been placed on advanced control methodologies for power converters (including three-phase two-level ac/dc power converter, three-phase NPC ac/dc power converter, dc/dc buck converter, etc.) Specifically, several research problems have been investigated in detail.

1. For three-phase two-level ac/dc power converter, disturbance observer based control methods have been investigated. First, disturbance observer based SMC strategy has been proposed, for which four different disturbance observers, including linear disturbance observer (LDO), sliding mode observer (SMO), linear and non-linear extended observer (LESO and NESO) have been designed to compensate the sliding mode controller in the voltage regulation loop. The results show that the disturbance observer can significantly improve the control performance, and the compensation capabilities of different observers have been compared. Based on this, an LDO based PI control strategy has been proposed, for which an improved LDO has been designed. The effectiveness and advantages of this strategy have been verified through experiments carried out using a 5 kW three-phase two-level power converter connected to the grid. To further improve the system robustness and convergence speed, an SMO based SMC control strategy has been investigated, for which an improved SMO has been designed. The stability of voltage regulation loop have been proved via Lyapunov method. The effectiveness and

superiority of this control strategy have been validated by both simulation and experiments.

2. Based on the research work of three-phase two-level converter, the disturbance observer based control methods have been further investigated for three-phase NPC converters by designing controllers in VOC and DPC modes. First, the capability of LESO to improve the system control performance (including the transient response and robustness) has been verified in VOC mode. Based on this, the DPC control strategy has been designed by combining LESO, \mathcal{H}_∞ technique, super-twisting SMC and adaptive control, i.e., the voltage regulation loop adopts LESO based \mathcal{H}_∞ controller to regulate the dc-link voltage while suppressing the impacts of disturbance estimation error on output voltage, the power tracking loop employs super-twisting SMC to drive the active/reactive power their references, the capacitor voltage balancing loop uses adaptive super-twisting SMC controller to effectively suppress the third harmonic disturbance.
3. Regarding the disturbance observer based control for dc/dc buck converter, an LESO based SMC strategy has been proposed for the average model. Cascaded control structure has been adopted to fulfill the tasks of output voltage regulation and inductor current tracking. Simulations have been conducted to verify effectiveness of this strategy, specifically, the robustness has been tested with three types of variations, which are load resistance variation, input voltage variation and reference voltage variation. Further, adaptive control strategies have been investigated. Two strategies have been designed, i.e., single-loop and double-loop adaptive control strategies. Two sets of experiments, including load resistance and reference voltage variations, have been conducted to compare and analyze the advantages and disadvantages of the two adaptive strategies, which provides a guidance for selecting appropriate control strategy for real applications.
4. To facilitate the self-tuning ability of the system, adaptive control strategies have been investigated for three-phase two-level power converter. First, an adaptive \mathcal{H}_∞ control strategy has been proposed, which adopts adaptive control for the voltage regulation loop and \mathcal{H}_∞ control for the current tracking loop. This strategy is of simple structure and results in desirable control performance. Further, an adaptive super-twisting SMC-based \mathcal{H}_∞ control strategy is proposed. The \mathcal{H}_∞ control technique is adopted in the voltage regulation loop to attenuate the impact of disturbance estimation error on voltage output, whereas two adaptive super-twisting SMC controllers are employed in the current tracking loop to address the parameter uncertainty of the converter system. By using adaptive super-twisting SMC, the time derivative of external disturbance is not required a priori for SMC design.
5. Apart from the disturbance observer based control and adaptive control strategies, neural network based control and model predictive control (MPC) methods also have been investigated for power converters. First, an radial basis function (RBF) neural network based DPC control strategy for three-phase NPC power converter has been proposed, for which the adaptive sliding mode controllers of power tracking loop has been designed via RBF neural network technology to deal with the model uncertainties. Second, an LESO-based MPC strategy under DPC mode

for three-phase two-level power converter has been proposed, which generates the optimal switching state by minimizing the cost function while obtains disturbance rejection ability.

12.2 Further Work

Related topics for the future research work are listed below:

1. Regarding the control strategies proposed in this book, the stability condition of closed loop system is mostly obtained via Lyapunov method, and the observer and controller parameters obtained are rather conservative which need further exhaustive trial and error process to find appropriate parameters. Therefore, some systematic parameter tuning methods need to be investigated in the future.
2. The types of power converter covered in this book include three-phase two-level power converter, three-phase NPC power converter, and buck converter, which constitute a small part of existing power converters. In the future, more types of power converters will be taken into consideration, such as flying capacitor converter, cascaded H-bridge converter, multi-level modulated converter, etc.
3. This book focus on single converter control, and future work will consider networked multiple converter control. In this case, the communication induced control problems such as communication burden, information attack, need to be addressed. To reduce the communication burden, event-triggered control is an effective solution. To target the information attack, cyber-physical system control needs to be investigated.